Spring 2009

Phenotype characterization of lung structure in inbred mouse strains using multi modal imaging techniques

Jacqueline Thiesse Namati
University of Iowa

PHENOTYPE CHARACTERIZATION OF LUNG STRUCTURE IN INBRED MOUSE STRAINS USING MULTI MODAL IMAGING TECHNIQUES

by

Jacqueline Thiesse Namati

An Abstract

Of a thesis submitted in partial fulfillment
of the requirements for the Doctor of
Philosophy degree in Biomedical Engineering
in the Graduate College of
The University of Iowa

May 2009

Thesis Supervisor: Professor Geoffrey McLennan

ABSTRACT

Research involved in modeling human lung disease conditions has provided insight into disease development, progression, and treatment. In particular, mouse models of human pulmonary disease are increasingly utilized to characterize lung disease conditions. With advancements in small animal imaging it is now possible to investigate the phenotypic differences expressed in inbred mouse strains *in vivo* to investigate specific disease conditions that affect the lung.

In this thesis our aim was to generate a comprehensive characterization of the normative mouse lung phenotypes in three of the most utilized strains of mice, C57BL/6, A/J, and BALB/c, through imaging techniques. The imaging techniques that we utilized in this research included micro-CT, a custom Large Image Microscope Array (LIMA) system for 3D microscopy, and classical histology. Micro-CT provided a non-destructive technique for acquiring *in vivo* and fixed lung images. The LIMA 3D microscopy system was utilized for direct correspondence of the gold standard histology images as well as to validate the anatomical structures and measurements that were extracted from the micro-CT images. Finally, complete lung histology slices were utilized for assessment of the peripheral airspace structures that were not resolvable using the micro-CT imaging system.

Through our developed imaging acquisition and processing strategies we have been able to successful characterize important phenotypes in the mouse lung that have not previously been known as well as identify strain variations. These findings will provide the scientific community with valuable information to be better equipped and capable of pursuing new avenues of research in investigating pulmonary disease conditions that can be modeled in the mouse.

Abstract Approved: _____

Thesis Supervisor

_____

Title and Department

_____

Date

PHENOTYPE CHARACTERIZATION OF LUNG STRUCTURE IN INBRED MOUSE STRAINS USING MULTI MODAL IMAGING TECHNIQUES

by

Jacqueline Thiesse Namati

A thesis submitted in partial fulfillment
of the requirements for the Doctor of
Philosophy degree in Biomedical Engineering
in the Graduate College of
The University of Iowa

May 2009

Thesis Supervisor: Professor Geoffrey McLennan

Graduate College
The University of Iowa
Iowa City, Iowa

CERTIFICATE OF APPROVAL

_____

PH.D. THESIS

_____

This is to certify that the Ph.D. thesis of

Jacqueline Thiesse Namati

has been approved by the Examining Committee
for the thesis requirement for the Doctor of Philosophy
degree in Biomedical Engineering at the May 2009 graduation.

Thesis Committee: _____
Geoffrey McLennan, Thesis Supervisor

_____
Joseph M. Reinhardt

_____
Joseph Zabner

_____
Eric A. Hoffman

_____
Kenneth Moore

To my grandmother Rosa Hunter who is an inspiration for all women. May you always know the footprint you have left for generations to come.

Science without religion is lame. Religion without science is blind.
Albert Einstein
New York Times Magazine

ACKNOWLEDGMENTS

Where do I begin? There are so many people deserving of gratitude and appreciation for their influence during my "P.H.D." journey. First, I would like to thank my advisor and, more importantly, mentor Professor Geoffrey McLennan who taught me that this process is not just about research outcomes but about the entire "pathway to discovery". At the start of this journey, I would have never imagined that while I was making scientific discoveries I would also be uncovering my true self. Thank you for your enthusiasm, support, and wisdom in all things related to the lung, medicine, and engineering (to name only a few). I feel so fortunate that I was a part of the "Lab of Oz"—my home away from home!

To my remarkable parents, Marilyn and Bryon Thiesse, you will never know how much your hard work and ambition have inspired me. I am so proud to have you as my parents! Thank you for providing me with the foundation for academic excellence, creating an environment of learning in our home, and—without expectations—always giving your love and support. I would not have been able to reach this milestone in my life without you! Oh, and Dad, I think I now understand that there is a lot more to engineering than I told you when I was 16. Remember?

I also want to thank the members of my committee: Joseph Reinhardt, Eric Hoffman, Joseph Zabner, and Kenneth Moore. Your valuable guidance, interest and participation in this project have helped to make it the best that it could be. I look forward to working and interacting with you in the future. Thank you to all of the staff at the Central Microscopy Research Facility. I learned a lot from you while I was working as an undergraduate in the core and I learned even more while I was a graduate student. A special thank you to Katherine Walters for her patience and excitement in working with me and our difficult LIMA samples! Also, thank you to the I-CLIC staff, especially

Janice Cook-Granroth and Jered Sieren for making sure that I always had everything I needed to run a successful micro-CT experiment.

I would also like to thank the members of the McLennan group including Kimberly Glynn and Christine McLennan. The smooth running of this lab would not be possible without all that you do! Thank you for all of the hard work you put in to facilitate our success! To the other students of the lab, Amanda Smith, Vincent Wagner, and Andrew Stessman, who have contributed to the success of this project, I must say thank you for all of your hard work! Amanda, I hope your hand gets some much needed rest!

There are not enough words to express the gratitude I feel for my ladies, Melissa Suter and Jessica de Ryk! We have had some really great times in the lab. Our lunches, amongst the lung dust, are unforgettable! Thank you Melby for always being generous with your time and experience. We have really missed you around here the last couple of years. I am looking forward to our great adventures in the near future! This brings me to Jess, who has been in the lab with me through all the successes and failures of this research. Thank you for your wisdom and being honest, sincere, and a friend who I can always count on. Our tea "parties" in the morning really helped to get me through the roadblocks that I've hit during this time. I am really going to miss you!

Finally, I would like to thank my husband Eman Namati for doing his graduate research at the University of Iowa! I can't imagine what my life would be like had you chosen a different path. Thank you for tolerating my intensity all day long at work and still wanting to come home with me at the end of the day. ☺ Your unwavering support and love have made this all possible. Thank you for opening my eyes and heart to all the great things this world has to offer, including science! I love you!

TABLE OF CONTENTS

LIST OF TABLES

LIST OF FIGURES

CHAPTER 1

INTRODUCTION

The genetic revolution has created a wealth of information, such as the entire mouse genome, which allows us to manipulate and study disease conditions that can be correlated back to the human [1]. Utilizing genetic models for human disease has and is continuing to generate great insight into the genetic basis of disease and, in particular, has been an important component of pulmonary research [2-5]. Inbred mouse strains have been useful because they have predictable genetics and the resulting phenotypic characteristics can be used to analyze important pulmonary diseases such as cystic fibrosis, emphysema, and asthma. The inbred mouse strains most commonly utilized in research are the C57BL/6, A/J, and BALB/c mice which were developed in the first third of the twentieth century.

In addition to the genetic revolution, there has been an equally important revolution in digital imaging. Integrating information from the genetic and digital imaging disciplines has the potential to uncover previously unknown structure and function relationships in dynamic organ systems. Based on currently understood genotypes we can further examine the expressed phenotypes in the pulmonary system of mice using new small animal imaging systems. In particular, micro computed tomography(micro-CT) has created advances in imaging of these small animals and can now be used for cancer detection, monitoring efficacies of drugs in disease treatment, and phenotype characterization [6-12]. Ultimately, through the use of micro-CT, we can examine the phenotypic differences expressed in inbred mouse strains *in vivo* to investigate specific disease conditions that affect the lung.

However, it is uncertain what anatomical structures can be discerned through the use of *in vivo* micro-CT imaging with the resolution of current commercial systems. In addition, micro-CT systems are not considered the gold standard for assessing anatomical

structures. Therefore, direct correlation of the micro-CT imaged lung to histology would prove extremely valuable for the investigation of the normal mouse lung. Multi-modal imaging systems combining micro-CT, 3D microscopy, and classical histology would accomplish this important correlation for the characterization and quantification of anatomical structures of the entire mouse lung. The 3D microscopy system, the Large Image Microscope Array (LIMA), has been developed for the correlation of CT images to ground truth histology as well as to validate anatomical structures and measurements extracted from CT. We utilize these systems to visualize and quantify the expressed lung phenotypes in the C57BL/6, A/J, and BALB/c mouse strains, including both airway and parenchyma structures.

We hypothesize that the 'normal' mouse lung consists of a spectrum of characteristics and significant differences in the lung structures between the C57BL/6, A/J, and BALB/c inbred mouse strains exist . Furthermore, we propose that through the utilization of novel imaging approaches for investigating the lungs of small animals, we will for the first time, provide a comprehensive phenotypic characterization for many of the normal lung structures in these mouse strains.

The following specific aims were developed in order to test our hypothesis and satisfy the development of the phenotype characterization of the normal mouse lung in three inbred mouse strains.

Specific Aim 1: *Development of an image acquisition sequence for collection of the in vivo micro-CT, ex vivo micro-CT, LIMA, and histology datasets of the mouse lung.* A specific imaging sequence needs to be developed that overcomes and minimizes difficulties that occur while collecting datasets from multiple imaging modalities as well as between the living animal and the corresponding fixed tissue sample. This involves developing an *in vivo* mouse lung micro-CT protocol, successful lung tissue fixation, *ex vivo* micro-CT imaging with lung stabilization, LIMA imaging, and finally histological processing protocols. In addition, image registration techniques need to be employed to

align and compare the image information at regions of interest between the multi-modal datasets. Through the collection of these datasets information relating the lung structures of the C57BL/6, A/J, and BALB/C mice from the *in vivo* down to the corresponding histology can be extracted.

Specific Aim 2: *Define the smallest anatomical structure of the mouse lung that can be resolved using the Siemens Micro-CAT II micro-CT system.* The micro-CT system used in these studies was configured with a pixel size of 28 µm. However, the resolving power of the system in this configuration is closer to 50 µm. With the reported alveolar size of the mouse to be in the range of 30-40 µm, it is unlikely that under ideal conditions (i.e. a fixed and non moving lung) we are able to discern alveoli in the micro-CT images. Therefore we will utilize complimentary imaging systems to verify the smallest anatomical structure of the mouse lung that we can resolve using micro-CT. This includes the LIMA system which, for our application, has a resolution of approximately 10x greater in the x-y plane than the micro-CT. However, due to the depth of field inherent in the bright field LIMA images it is difficult to distinguish the anatomical structures of the parenchyma. Therefore, we will also develop a lighting technique that will increase the surface contrast to facilitate defining the parenchymal structures.

Specific Aim 3: *Characterize the normal mouse lung anatomy including the lobes and tracheobronchial tree in the C57BL/6, A/J, and BALB/c inbred mouse strains using in vivo micro-CT.* Utilizing *in vivo* micro-CT imaging we will image the living mouse lung during a breath hold of 10, 20, and 30 cmH_2O pressure. Manual segmentation of the lung, lobes and airways at each pressure will be performed and quantitative measurements will be extracted and compared. The development of a mouse airway nomenclature will be developed to further facilitate the comparison of airway structures. In addition, we will verify measurements that are obtained in the micro-CT datasets through the use of the "ground truth" pathology LIMA images. In addition, the

manual segmentation will provide a means of validation for development of future automated segmentation algorithms.

Specific Aim 4: *Assess the lung parenchyma airspace in the C57BL/6, A/J, and BALB/c strains.* In addition to macroscopic measurements such as the airway dimensions, parenchyma airspace measurements will also be made from image datasets utilizing the corresponding histology images. Although *in vivo* measurements are ideal, limitations in the current hardware of the Siemens Micro-CAT II micro-CT system prevents imaging of the alveoli in the mouse lung. However, *ex vivo* analysis of the lung parenchyma will be completed using the respective histology image data.

In Chapter 2 a discussion of the background information that is important for understanding the major topics covered in this work is given. This includes an overview of the structure and function of the lung, the known normal mouse lung anatomy to date, how mouse models of human disease have been developed and their implications for the pulmonary system, imaging techniques used for the mouse lung including micro-CT and microscopy, analysis techniques used for the airways and alveoli, and finally the significance and innovation that is provided by this body of work.

Chapter 3 presents the experimental methods and imaging technologies that were developed and utilized for this research. This spans from animal handling, anesthesia protocols, and micro-surgical techniques to undertaking *in vivo* imaging of mice using the micro-CT system. In addition, Chapter 3 discusses the development of a tissue fixation protocol that can be used for successful *ex vivo* imaging on the micro-CT, the Large Image Microscope Array (LIMA) imaging system, and gold-standard histology. Also discussed is the development of the Bright Field Segmentation Tomography (BFST) system, developed specifically for increasing the surface contrast of lung tissue by reducing the depth of field of the LIMA system.

Chapter 4 focuses on the image processing, analysis and registration techniques that were implemented for visualization and quantification of the normal lung structures

in the C57BL/6, A/J, and BALB/c mice. For each imaging modality, including *in vivo* and *ex vivo* micro-CT, LIMA, and histology, processing and analysis was completed for extraction of lung parameters. This included segmentation of the entire lung, individual lobes, and the airway tree as well as identification of the airspaces of the parenchyma (alveolar ducts and alveoli). In order to compare image information between datasets multi-modal registration techniques were employed and described in this chapter.

Throughout Chapter 5 a characterization of the normal lung phenotypes that were discovered through our novel imaging methodologies in the C57BL/6, A/J, and BALB/c mice is presented. This includes an anatomical and volume analysis of the lobar structures, visualization and quantification of the airway tree, assessment of the peripheral airspace, and results from pulmonary function tests in each of these three strains of mice.

Finally, in Chapter 6, a complete synopsis of this work and the impact that this research will have on the greater scientific community is presented. In addition, a discussion of the future directions that could further benefit lung disease research is offered.

CHAPTER 2

BACKGROUND

2.1 Structure and Function of the Lung

An essential organ for the survival of air-breathing animals is the lung. Its respiratory functioning fulfills the vital role of gas exchange—facilitating the oxygenation of the blood while carbon dioxide is removed [13]. In addition, the lung functions to metabolize some compounds, filter materials from the circulation that are undesired, maintain pH balance, and act as a blood reservoir [13].

These physiologic functions are served through the structural architecture of the lung, and although this seems to differ between animals many structural components remain consistent. In reptiles, birds, and mammals respiration takes place through a sequence of steps where air is brought into the lung through the airways. In mammals, the lungs are divided into the right and left lung and, depending on the animal; contain a varying number of lobes on each side. In this case, the airway system enters and further divides to feed both sides of lung through a series of channels: the trachea, main bronchi, bronchioles, and the smaller terminal branches of the respiratory tree until the alveoli are reached, **Figure 2.1** and **Figure 2.2**. In the human lung, the terminal branches of the respiratory tree are the respiratory bronchioles. However, in the mouse lung the terminal branches of the respiratory tree are the terminal bronchioles which lead straight into the alveolar ducts, **Figure 2.3**, and there are no respiratory bronchioles.

Although the airways are the conduits for transporting air, the location for gas exchange in mammals is in the alveoli, which comprise of the majority of the surface area of the lung. This exchange occurs across the thin alveolar membrane between the alveoli and the fine network of capillaries that cover them. Oxygen diffuses into the bloodstream and the carbon dioxide diffuses into the alveoli for expiration.

2.2 Mouse Models of Human Disease and Implications for the Pulmonary System

The mouse (*Mus musculus*) has become the most widely used animal model of human disease for many reasons including their close physiologic and genetic relationship with humans as well as their defined, understood, and easily manipulated genetic makeup. The study of mouse genetics began in the early 1900's with the development of the first inbred strain. Since then more than 465 inbred strains have been developed through a minimum of twenty consecutive generations of brother x sister matings, at which stage the inbred line has attained homozygosis at nearly every locus [14, 15]. The most commonly used inbred mouse strains used in research have been inbred for more than 200 generations [16-18]. **Table 2.2**, modified from The Laboratory Mouse, illustrates the commonly used inbred mouse strains for biomedical research and their applications for research.

The mouse, like the human, naturally develops many diseases that affect the immune, endocrine, nervous, cardiovascular, pulmonary, and other complex physiological systems [19]. Through the use of novel breeding techniques, including the development of standard inbred, congenic, and recombinant crosses, many traits have been isolated that are useful in the study of disease conditions. For instance, congenic mouse strains are developed through transferring a segment of chromosome that is of interest from one strain to another through 10 or more successive backcross matings. At the production of each generation, selection for the donor chromosome segment occurs [14]. Recombinant crosses, on the other hand, are created by crossing two different inbred strains of mice. The consequent offspring, known as the F2 generation, are systematically inbred at random. During inbreeding the genes from the parents follow segregation and reassortment laws resulting in fixed combinations in the new strain [14, 16, 20]. With further advances in genetic technologies the production of custom mouse models for research of specific diseases continues.

Additionally, techniques used to manipulate the mouse genome for biomedical research, include transgenic and embryonic stem (ES) cell knockout technology. Transgenic models are used to promote gene function, while knockout models are used to ablate gene function [16]. Utilizing transgenic technology, the mouse genetics are manipulated by injecting a gene of interest, known as a transgene, into the pronucleus of a recently fertilized single cell embryo. The transgene is then incorporated into the mouse chromosomes at random locations and during embryonic divisions this additional DNA is passed on to all cells in the growing mouse. The resulting mice born through this procedure can potentially pass the transgene through the complete germline to establish a permanent transgenic line [21].

Knockout models, on the other hand, are created by injecting blastocysts with embryonic stem cells that have been isolated and modified through replacement of an endogenous gene with a homologous DNA segment. The resulting mice are chimeric—they have cells derived from both the implanted ES cell and the host—with some tissues and cells expressing the targeted gene while others are not.

With the advent of novel methodologies a multitude of disease models have been developed. However, for the scope of this work we are interested in the possible applications of using the mouse to model lung disease. There is now an array of mouse models available for lung diseases such as asthma, chronic obstructive pulmonary disease (COPD), and cancer. Asthma models are produced by creating the airflow obstruction characteristics seen in asthma patients—inflammation with lymphocyte and eosinophil infiltration of the bronchial mucosa, epithelial desquamation, goblet cell hyperplasia, and submucosa thickening. Many models have been developed to display these characteristics and the standard protocols involve sensitization and subsequent challenges. The most commonly used mouse strain for these protocols is the BALB/c [2, 16, 22, 23]. COPD models are more challenging to create because usually the disease develops over long time spans from epi-genetic factors and the accelerated lifespan of the

mouse (1 mouse year = 30 human years) limits the amount of time disease can be studied. However, there are mice that develop airspace enlargement, characteristic of emphysema. These include tight skin (Tsk +/-), pallid, blotchy, klotho and beige mice [5, 16]. Finally, there are lung cancer models in use for studying the human condition including spontaneous models of adenomas in the A/J and SWR strain; carcinogen induced squamous cell carcinomas; and many transgenic models [4].

There are other practical benefits to using the mouse for biomedical research besides the ability to manipulate their genetics in a controlled fashion. Mice are small and easy to house, they are relatively inexpensive so multiple experiments can be carried out with ease, and they have short gestation periods which allows multiple generations to be acquired in a short period of time. In addition, there are certain factors that can be controlled in the mouse such as sex, age, and environmental exposures that are not easily controllable in human studies. However, some issues arise with the development of the mouse strains including the inability to completely model all variables of a human disease condition, sterility, offspring that are non viable or cannot live into adulthood for completion of the research study, no germline transmission, no transgene expression, and no evident phenotype despite transgene expression [21]. Albeit there are problems in using the mouse, the advantages are still providing important information for biomedical research and in conjunction with the genome and phenome project the addition of imaging to reliably and quantitatively phenotype the normal and disease mouse will be of substantial importance.

2.3 Normal Mouse Lung Anatomy

Knowledge of the normal mouse lung anatomy is still in its infancy and to date has been accomplished primarily through observational and histological techniques. In addition, some characteristics have been made based on functional testing [22, 24-30] and anatomical studies through casting of the airways [26, 27, 31-35]. The total lung capacity

of the mouse has been reported as 1 ml with 4 lobes in the right mouse lung and a single left lung. In the mouse, 18% of the lung is comprised of parenchymal tissue while 11% is composed of airway [31]. It has also been found that the airways have: a relatively large lumen traversing to the base of the lung, fewer airway generations (13-17), and a monopodial versus dichotomous branching pattern. Additionally, the mouse lung has no bronchial circulation and there is no cartilage in the conducting airways beyond the mainstem bronchi. The alveoli in mice are smaller than in humans and the reported size varies greatly between investigators depending upon the strain studied and the technique utilized to measure these structures. Irvin reported the alveoli to be around 80 microns, Mitzner reports alveolar size varying in inbred strains from 34.0-45.0 microns, and The Laboratory Mouse reports the alveolar size to vary between 39.0 and 69.0 microns [16, 31, 36].

Other characteristics of the mouse lung anatomy include a thin pleura that is strong enough to be inflated to pressures beyond the 30 cmH_2O (up to 80cmH_2O has been reported) [33] that is sometimes associated with mouse total lung capacity. In addition, the mouse has very few and maybe no sub-mucosal glands while it has a very high number of Clara cells [31]. In **Figure 2.4**, modified from the National Institute of Allergy and Infectious Diseases: National Institutes of Health, the major components of the lung anatomy are schematically depicted and labeled.

A large collection of preliminary information is available regarding the anatomy of the mouse lung. However, the *in vivo* anatomy of the lung has yet to be characterized. **Table 2.1** summarizes and compares what has been reported in the literature on the differences between the mouse and the human anatomical structures of the lung.

In addition to the reported values for lung structures, it has been found that a common pattern of branching occurs in the rodent lung. In both the right and left lungs, side bronchi project off of the main bronchi in three rows: the ventral row which consists of the longest branches and runs into the ventral periphery of the lungs, the dorsal row

which consists of smaller branches that supplies lung tissue adjacent to the vertebral column, and the medial row which feeds the lung directed toward the posterior region of the mediastinum [34, 35].

To date, there is limited information regarding anatomical differences between inbred mouse strains. Oldham and Phalen were interested in finding if there were toxicologically significant differences between two inbred mouse strains at equivalent ventilation rates and examined the airway anatomy using casting techniques. They revealed differences including average airway diameter and branch length between the BALB/c and B6C3F1 mice [32]. Soutier examined the differences in alveolar size between the C3H/HeJ, C57BL/6, and A/J strains and found significant differences between them. The alveoli were reported to be the largest in the C3H/HeJ mice (45 µm), the A/J strain were found to be smaller (38 µm), and the alveoli in the C57BL/6 were the smallest(35 µm) [36]. In addition, researchers have utilized inbred mice strains extensively for inhalation toxicology studies and many findings have indicated that different mouse strains respond differently to common inhaled spasmogens including (carbachol and serotonin) through examination of lung mechanical responses including respiratory system resistance and compliance measurements [2, 32, 37] . These strain-related variations have previously been attributed to differences in metabolism or tissue sensitivity. However, further examination needs to be completed to uncover whether these measured differences can be attributed to biochemical effects or even anatomical traits[32]. To date there has not been research that has analyzed both the airways and the alveoli in the same study under the same conditions using standardized methodologies.

2.4 Small Animal Micro-Computed Tomography (micro-CT) Imaging

The demand for imaging small animals has brought about a new discipline known as preclinical imaging. Micro-CT is a technique used in this discipline that provides a

means of using X-ray energy to create high resolution data sets through a minimally invasive system for screening small animals. Of particular interest, is screening mouse models for drug discovery, cancer detection and monitoring, and genomics applications. Such a non-invasive system can provide a means for longitudinal studies, which is a major advantage in mouse model research. Also, in genomics research, one can create a disease model to study a genetically expressed variation without terminating or destroying the animal [8, 9] which is important since development of specific mouse genetic studies can be labor intensive and very expensive.

Micro-CT systems consist of an X-ray source, a detector array that converts X-ray energy to an electronic signal, and a stage that rotates the specimen within a stationary scanner or rotates the scanner around the stationary specimen [8]. When scanning live animals, the use of a specimen holder that is stationary and does not rotate during the scanning process is the preferred approach. Many different commercial makes and models of micro-CT scanners are now available with each offering different advantages. **Table 2.3** lists commonly used commercial scanners along with some of their specifications. Note that the field of view and resolution range depends primarily on the installed detector array; therefore the highest resolution cannot be attained while using the largest field of view and a tradeoff needs to be made. In order to successfully acquire high quality images through micro-CT systems, underlying specifications need to be understood so that appropriate physics and technological accommodations are met. High resolution images depend on the X-ray source, focal spot size, detector element size, system geometry, and X-ray flux. The scan speed is dependent upon the X-ray source power output, the detector sensitivity and readout speed, and gantry rotation speed. Since, micro-CT systems are not standardized scan speed comparisons are difficult to make [38].

Methodologies utilizing micro-CT for *in vivo* imaging of the pulmonary system have been limited by factors including resolution, rapid movements in the respiratory and

cardiovascular systems of mice that cause motion artifacts, radiation dosage that may hinder longitudinal studies, and the length of scan time. These limitations have been met by researchers in various ways including the development of ventilation and gating techniques. Namati et al. developed the Intermittent Iso-pressure Breath Hold (IIBH) ventilation technique that acquires X-ray projections while the animal undergoes a forced breath hold. The images produced *in vivo* utilizing the IIBH technique show the lung microstructure with improved resolution and reduction of motion artifacts compared to other gating techniques of the spontaneously breathing mouse [39, 40]. In addition, it has been found that the length of time required to scan a living animal can be reduced through the use of multiple X-ray source and detector arrays, as was developed by the Bioimaging Research Inc. (BIR) for their commercial micro-CT system. The concern for radiation dosage has been addressed by investigators using *in vivo* respiratory-gated small animal lung imaging. They reported that the average dosage for each scan to be 0.15 Gy, while it is considered that a total body radiation dose of 5-6.7 Gy is lethal for a small rodent [6, 8, 12]. From these reported dose calculations, it would be reasonable to scan the animal without expecting short term damage due to ionizing radiation. However, if longitudinal studies were to take place, with special consideration to tumor studies, the long term effect of radiation dosage on the animal needs to be assessed carefully[41].

Although the micro-CT is being used for many *in vivo* imaging applications, it was initially utilized for analyzing small fixed tissue specimens. Micro-CT systems, including synchrotron based systems, have been used to study the intact structures of the mouse lung [10]. However, microscopy techniques are still the gold standard for assessing fixed tissue specimens and therefore quantitative measurements comparing micro-CT to microscopy images is increasingly important.

2.5 Microscopy Based Imaging of the Lung

Techniques using microscopy have been used as the gold standard for assessing the morphology of the lung. However, analysis of the lung utilizing 2D microscopy based techniques does not completely characterize the 3D nature of the airways including: airway diameter, length, and branching angle and the 2D descriptions suffer because of their small sample size relative to the overall organ of interest. Therefore, with the advent of whole organ microscopy extending into 3D we can evaluate the lung morphology of the mouse in a more complete fashion [42, 43].

2.5.1 Histology

Histology is the study of tissues and how these tissues make up organs. The four basic tissue types that make up organs are: epithelial, connective, muscular, and nervous. These tissue types are comprised of cells and extracellular matrix and therefore need to be examined under a microscope. In order to generate sections that can be viewed under the microscope, the tissue needs to be fixed so that the cellular architecture is preserved. For light microscopy procedures, the tissue is also embedded in a solid medium, usually paraffin, so that it is supported and does not tear or distort extensively during sectioning. Since most tissue samples are colorless, these fine sections that result need to under go staining to increase the contrast of the underlying cellular structures.. Many techniques for staining tissues have been developed in order to allow the tissues to stand out under the microscope as well as to differentiate between tissue and cell types. These stains are usually acidic or basic and react with ionizable radicals of the tissues to form electrostatic linkages [44]. Parts of the tissues that stain with basic dyes are considered basophilic and those that stain with acidic dyes are acidophilic. For example, nucleic acids react with basic dyes such as hematoxylin, touidine blue or methylene blue, due to its acidic composition. On the other hand, mitochondria, secretory granules, and collagen react with acid dyes such as eosin, orange G, and acid fuschsin. Of all the stains that are

currently utilized, of which we only mention a few, hematoxylin and eosin is by far the most common.

Morphology of the *ex vivo* mouse lungs has been studied on fixed tissue specimens using the light microscope. This involves embedment of the fixed specimen in paraffin or resin, cutting tissue sections, placing the sections on slides, and staining the tissue. Digitized microscopy slides on the light microscope have been used to assess airway wall thickness and luminal dimensions. These cross-sectional airway measurements are then compared to remodeled airways that have undergone changes in response to certain diseases such as asthma. The use of microscopy imaging techniques has also aided in the measurement of alveoli through stereologic techniques such as the mean linear intercept and mean chord length metrics. Research has shown notable differences in alveolar size between inbred mouse strains. More specifically, researchers investigated hematoxylin and eosin (H&E) stained tissue sections from the C3H/HeJ, C57BL/6, and A/J mouse strains and concluded that there was a significant difference in alveolar size ranging from 34.0-45.0 microns [36]. In addition, the average number of alveoli in an entire mouse lung has been estimated by histology techniques at 12-13 million in the C57BL/6 mouse through unbiased stereology techniques used by Ochs [45].

However, research assessing the airway structure throughout the entire mouse lung is lacking because of the 3D nature of the airways. Therefore the development of 3D histology would contribute greatly to the current techniques used for assessment of lung structures and provide a new “gold standard” for assessing disease characteristics.

2.5.2 Large-Scale Image Microscope Array (LIMA) Imaging

Novel developments in 3D microscopy yield important new information to complement non-invasive imaging strategies, such as computed tomography (CT). The

LIMA system was created to provide a “ground truth” for comparison to CT datasets because the image content that is acquired through it is not dependent upon reconstruction algorithms. In addition, the LIMA system bridges the gap between non-destructive 3D imaging systems such as micro-CT and destructive 2D histology imaging and provides additional image content such as color and fluorescence. When a tissue of interest is imaged on multiple systems such as micro-CT, LIMA, and histology the resulting images can be spatially registered, resulting in a 3D map of anatomical structures that can provide functional insight.

The LIMA system consists of many components, **Figure 2.5**; including a modified microtome and tissue stage, a custom built vibrating knife assembly, a stereomicroscope with an attached charge coupled device (CCD)camera, and a XYZ gantry all on top of a vibration free optical table. The modified Leica SM2500 microtome involved the incorporation of a stepper motor control and a stage locking mechanism. This assured that the tissue stage would move at a constant rate resulting in a uniform cutting speed throughout the sectioning process. By replacing the manual control with an electronic control, the tissue stage was also interfaced with a computer for automation. The stage locking is also computer controlled and following every section the stage is brought back to its starting location and locked into place [46].

The knife assembly was re-designed as a large-scale vibrating blade, in order to smoothly section soft tissue without the need for tissue embedment. The knife assembly includes an adjustable bracket which allows the knife to adjust to varying levels to accommodate tissue samples of different sizes—up to a whole human lung. In addition, it was found experimentally that the knife needed to be modified so it was capable of cutting through tissues of different densities. High frequency was effective for the majority of tissues, but some difficulty was experienced while sectioning both the delicate lung structure and dense airway walls. Therefore, the vibrating blade was

designed to vibrate at both high and low frequencies. Using this system, sections are reliably cut and can be saved for further histological processing [46].

The optical train used in the LIMA system includes a Leica MZ16FA (Leica Microsystems GmbH, Germany) stereomicroscope connected to a 1x plan achromatic objective and a JenOptik C12 (Jenoptik GmbH, Germany) cooled scientific camera. This microscope carrier and camera couple was chosen because it is adaptable for use in bright field and dark field fluorescent microscopy of stained and non-stained specimens. To remove the "stereo" angle and create a perpendicular line of sight for the acquired images, a Leica axial shift adapter was mounted between the objective and the stereoscope. In addition the magnification of the microscope varies from 7.11x to 115x—resulting in a maximum resolution of 420 line pairs using the described setup. Digital images are acquired through the CCD camera which contains a 1300x1030 pixel array with a pixel pitch of 6.7 μm. Image data that is acquired by the camera is transferred by a Firewire IEEE 1394 interface to the computer [46].

During image acquisition, the vibratome stage is locked into place and the blade vibration is stopped. However, image acquisition is highly sensitive to vibration. Therefore, the LIMA system is positioned on a vibration free table to minimize environmental vibrations. The microscope and CCD camera coupling is controlled above the sectioned tissue surface through a Velmex Bislide (Velmex, New York) parallel-coupled gantry system. Control of the gantry motion is automated via three computer-interfaced stepper motors [46].

Application of the LIMA system for imaging of the mouse lung would provide important 3D microscopic information for assessing the anatomical structures and would provide a means for direct correlation between micro-CT and histology.

2.6 Airway Analysis Techniques

2.6.1 Airway Casting

In the mouse, prior to the use of 3D imaging techniques, airway structures were examined using lung casts. Initial studies examined the morphology of the bronchial tree in different species of rodents including: Micromys minutus, Mus musculus, and Rattus norvegicus [34, 35]. These studies examined primarily the generalized nomenclature for over 40 species of rodents as well as the relationship between airway dimensions and body size. Further advancements were made in analyzing the cast of the laboratory mouse using manual caliper morphological measurements including: airway length, airway diameter, and branching angle [32]. Specifically, Oldham and Phalen created lung casts of the BALB/c and B6C3F1 mice—with notable differences in the airway anatomy. The resulting casts, **Figure 2.6**, demonstrate the differences in airway structure between the two inbred mouse strains examined in this study [32].

Casting methods have shed light on the morphology of the mouse lung, yet they are intensive and inherit processing and subjective analysis errors. The process of casting may also cause a distortion in the airway shape resulting in the inaccuracy of measurements. Due to the variation in methods used between investigators, casting used to study the lung is subject to measured discrepancies in the airway morphology. Finally, one additional drawback to casting is the limitation in studying any differences between the airway structure and the supporting structure of the parenchyma.

2.6.2 Airway Segmentation

Airway segmentation from image datasets is important for visualization and quantitative analysis for studying lung anatomy and function. Manual tracings from an expert have been the gold standard for validation purposes and through the use of tracing tablet computer systems with custom software, such as the Pulmonary Analysis Software Suite (PASS), segmented data can be systematically created. However, manual tracings

are very time consuming and exhibit variability between experts. Therefore, automated airway segmentation techniques are needed to provide a faster routine for identifying airway conduits and ideally are more repeatable.

There have been many techniques developed for the use of segmenting human airways in conventional CT scans. These include: fuzzy connectivity, region growing methods, mathematical morphology methods, and hybrid methods combining both region growing and morphology [47-49].

Although automated airway segmentation algorithms have been developed for analysis of the human airway tree from CT images, direct translation of these algorithms for extracting the mouse airway tree has not been trivial. Micro-CT systems vary from conventional CT in image quality and inconsistencies in CT values (density resolution) with respect to reasonable dosage [6]. Therefore, an adapted algorithm for the automated segmentation of the mouse airways is necessary and 3D airway segmentation based on grayscale morphology is being created by Shi [50]. Otherwise, to date, the only airway segmentation from micro-CT images acquired of the mouse have been on manually segmented *in vivo* data sets and through segmentation and skeletonization of micro-CT scans of airway casts [42, 43, 51].

2.7 Alveoli Analysis Techniques

Limitations in resolution for *in vivo* imaging systems has and continues to prevent the ability to image and quantify the alveoli in the living human or animal. However, researchers have developed techniques for quantifying the alveoli from samples of lung tissue that have been fixed. These techniques include unbiased stereology, mean chord length, and mean linear intercept.

Unbiased stereology of the lung is a methodology used to quantify its physical properties in three-dimensional space through measurements made on 2D tissue sections [52, 53]. It is systematic technique that places emphasis on the importance of fixation,

sampling, and processing. The sampling technique that has been most widely accepted for lung stereology is the cascade sampling process described in detail by Ochs, [45, 53]. This methodology applies systematic random sampling where the lung is cut into horizontal slices with a specified thickness starting from a random location. The total volume of the lung[V(lung)] is then calculated as the product of the slice thickness and the cut area of all slices. To calculate an estimated volume fraction of the lung parenchyma within the lung, [V_v(par/lung)] point counting is completed at a low magnification using light microscopy. In a similar manner, except at a medium light microscopic magnification, the volume fraction of alveolar septum [V_v(alvsep/par)] within the parenchyma is estimated. Finally, using a medium electron microscopic magnification the volume fraction of the type II cells [V_v(typeII/alvsep)] within alveolar septum can be estimated. From these calculated values the total volume of the parenchyma, alveolar septum or type II cells can be obtained. In addition, unbiased stereology can be used to estimate the total number of alveoli in a lung through identification of the free ends of the alveolar septae which contribute to the 2D network of alveolar openings in 3D [45].

Frequently used methods for analysis of the alveoli on paraffin processed histology slices includes the mean linear intercept technique and mean chord length technique. Mean linear intercept measures the airspace chord lengths in addition to the wall thickness whereas mean chord length measures the airspace chord lengths and does not include the wall thickness in its metrics [36, 54, 55]. Both are performed in a similar fashion where sampled regions containing alveolar tissue and not containing large airways or blood vessels are used. The peripheral airspace (PAS) is measured by a straight line that is taken at random and the alveolar cord is the distance that is in between two walls. From a binary black and white image this corresponds to white regions being airspace and black regions consisting of the alveolar wall.

Currently within the field of lung morphometric analysis there is discordance regarding techniques which are suitable for assessment of the alveoli [56].

2.8 Significance and Innovation

Within pulmonary research the development of mouse models has provided insight into disease development, progression, and treatment options. However, for a more complete understanding of the differences in normal and diseased structures it is necessary to fully evaluate the lung phenotypes expressed in healthy inbred mouse strains. The goal of this research is to provide a characterization of the normal lung in the three most commonly utilized mouse strains through the use of multi-modality image datasets obtained from micro-CT, the LIMA bright field and BFST system, and histological processing. Micro-CT was chosen because it provides non-destructive and non-invasive high resolution anatomical imaging with the potential for longitudinal *in vivo* studies. In order to accurately correlate the micro-CT anatomical measures to traditional gold-standard histology, we have incorporated the use of the LIMA system to bridge the gap between micro-CT and histology. This comprehensive, multi-dimensional imaging strategy has never been done before and applied to the same mouse.

In vivo imaging of the mouse lung is still in its early stages of development and characterization of the mouse lung from *in vivo* micro-CT extending to traditional histology has not been completed. This characterization includes adaptation of a nomenclature for the mouse airways, quantification of the airway structures including lung and airway volumes, major and minor diameters of the airways, as well as branch lengths. In addition, analysis of the alveolar air space in these mouse strains will be provided through the use of LIMA BFST imaging and subsequent histology. The development of 3D datasets characterizing the mouse lung will be valuable in many fields including toxicology studies of particulate flow, longitudinal studies of disease, and the improved development of pharmaceutical treatments. In addition, the availability of

the lung phenotypes developed from these imaging systems will play an important role in the incorporation of novel quantitative image information into databases which present phenotypes of mice, such as the Mouse Phenome Project [57].

It is our hope that through the completion of this research project new information relating the genetic differences between mouse strains and the expressed lung phenotypes will be more closely examined. We believe that notable differences should be discerned between the normal and diseased lung structures and they will provide insight into structure and function, thereby extending knowledge of human disease conditions. In addition, through this analysis we speculate that structural differences between mouse strains will affect the future modeling of lung disease in the mouse.

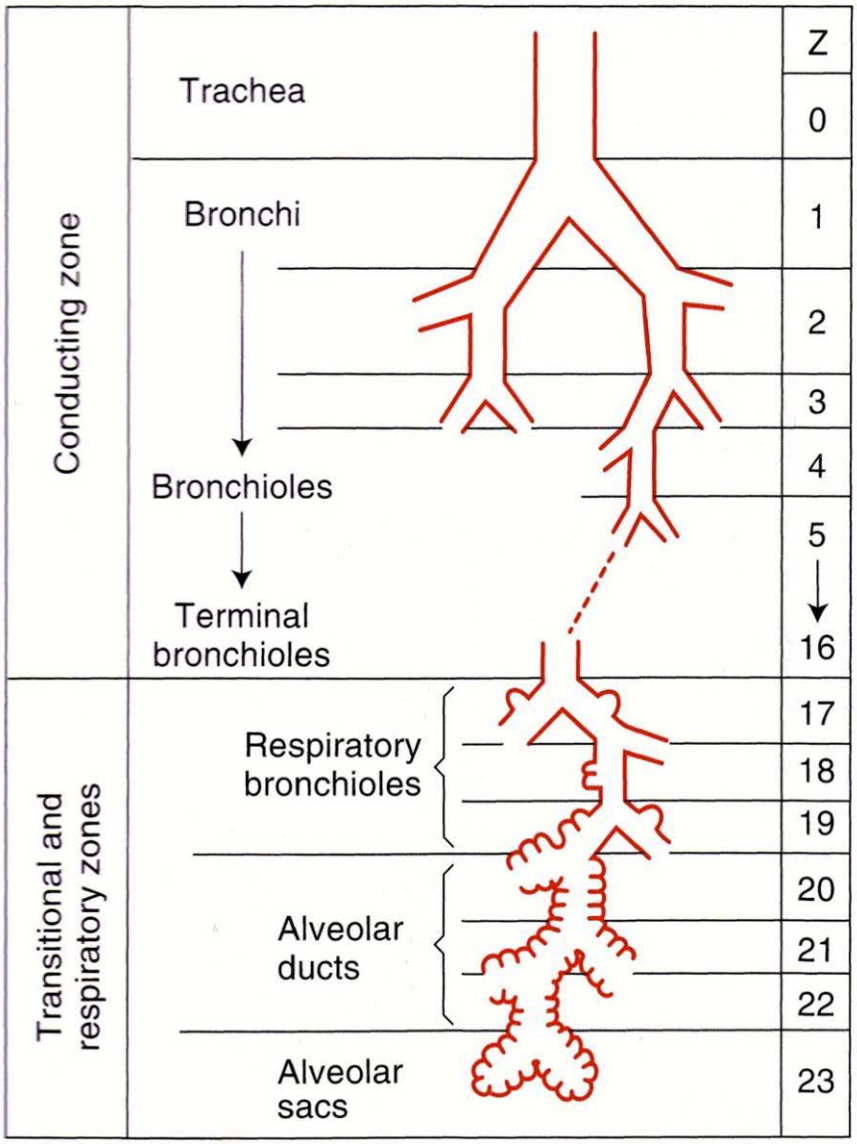

Figure 2.1: Breakdown of the human airway system. According to Weibel, the dichotomous branching system of the human airways can be categorized into two major zones: the conducting and transitional and respiratory. The major bronchi, bronchioles, and terminal bronchioles make up the conducting zone, while the respiratory bronchioles, alveolar ducts, and alveolar sacs make up the transitional and respiratory zones.

Reproduced from West. 2005 [13]

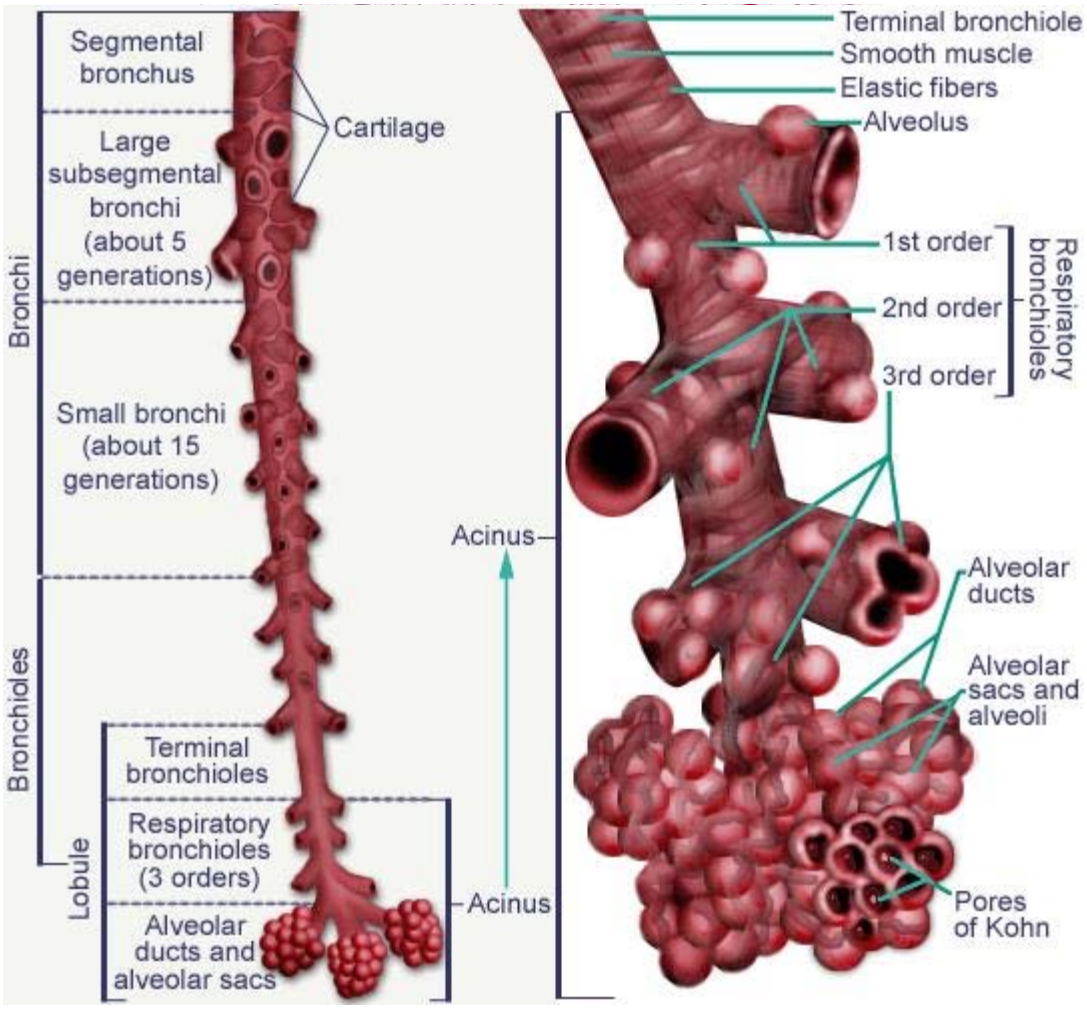

Figure 2.2: Anatomical schematic of the terminal regions of the pulmonary system. From a terminal bronchiole two respiratory bronchioles originate with alveolar buds. In addition, the alveolar ducts, alveolar sacs, and individual alveoli are depicted.

Reproduced from McGill Molson Informatics Project. 2006 [58]

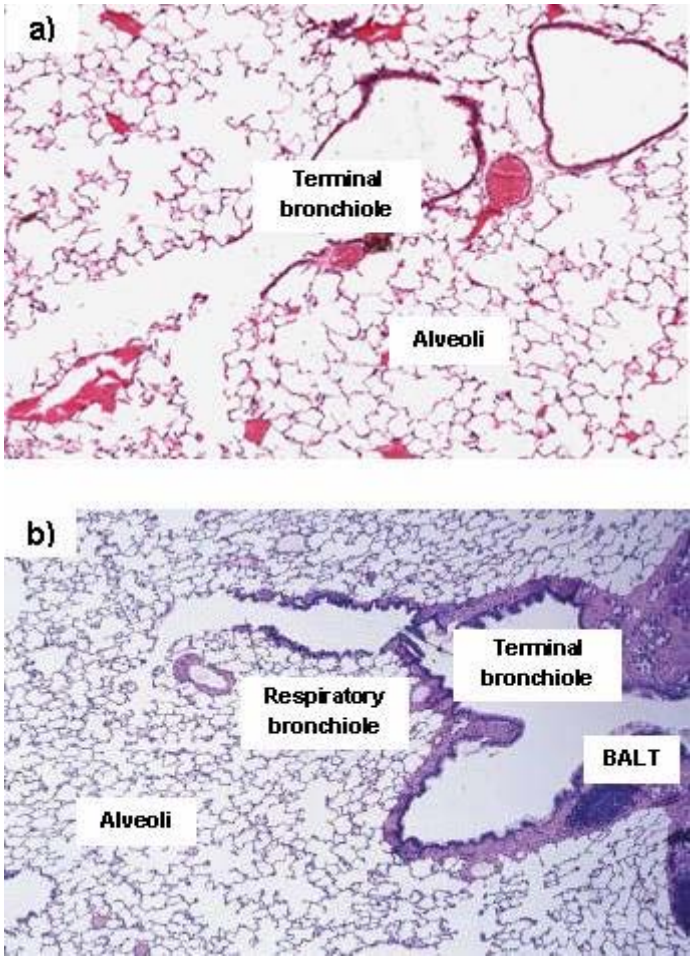

Figure 2.3: Histology micrographs of the lung.
a) In the mouse, the terminal bronchiole feeds directly into the alveolar duct.
b) In the human, the terminal bronchiole is followed by a respiratory bronchiole branch which is continuous with an alveolar duct and many alveoli.

Image in panel b) reproduced from Junqueira and Carneiro. 2005 [44]

	Mouse	Human
Lobe Anatomy	4 lobes on right 1 lobe on left	3 lobes on right 2 lobes on left
% Parenchyma by volume	18%	12%
Airway generations	Maybe 13-17	17-21
Main bronchus diameter	1 mm	10-15 mm
Bronchioli diameter	0.1-0.5 mm	<1 mm
Terminal bronchioli diameter	0.1 mm	0.6 mm
Respiratory bronchioli diameter	Not existent	0.5 mm
Alveoli diameter	Varies from 0.035-0.080mm	0.2-0.4 mm
Bronchial Circulation	No	Yes

Table 2.1: Reported anatomical differences between the mouse and human lung.

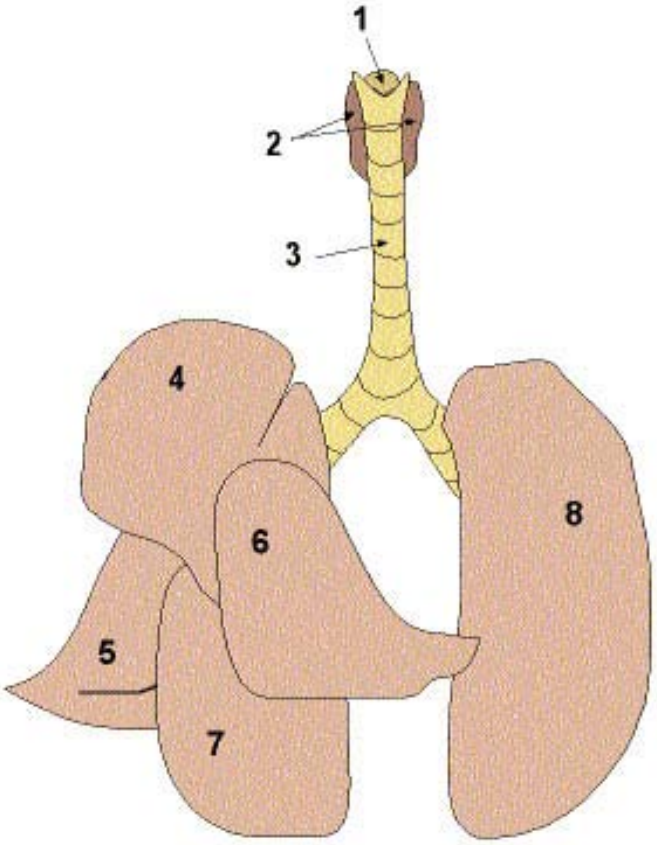

Figure 2.4: **Gross Anatomy of the Mouse Lung.** This generalized schematic of the mouse lung consists of four lobes in the right lung and the single left lung. The numbers are associated with the following labels:

1. Larynx
2. Thyroids
3. Trachea
4. Apical Lobe
5. Azygous Lobe
6. Cardiac Lobe
7. Diaphramatic Lobe
8. Left Lobe.

Reproduced from NIH. 2006 [59]

Parent Strain	Origin	Commonly used substrains	Research Applications
A	Cold Spring Harbor albino crossed with a Bagg albino L.C. Stron, Bussey Institute	A/J, A/He, A/WySn	General purpose, cancer, immunology, sensorineural, and developmental biology research. High susceptibility to carcinogen-induced lung adenomas.
AKR	Detwiler stock, Norristown PA H. Furth, Rockefeller Institute	AKR/J	Cancer Research(high leukemia strain)
BALB/c	Albino stock H.Bagg, Memorial Hospital, NY	BALB/c, BALB/cAn, BALB/cBy	General purpose, immunology research, neurodevelopmental defects
C3H	Bagg albino female crossed with a DBA male L.C. Strong, Bussey Institute	C3H/He, C3H/HeOu, C3H/HeSn	General purpose, cancer research, sensorineural research
C57BL	Lathrop stock C.C. Little, Bussey Institute	C57BL/6, C57BL/6By, C57BL/Ei, C57BL/10, C57BL/10Sn	General purpose, cardiovascular biology research, background strain for most transgenes, spontaneous or targeted mutations
DBA	Coat color stock C.C. Little, Bussey Institute	DBA/1, DBA/1Lac, DBA/2	General purpose, DBA/2: Cardiovascular biology, neurobiology, often contrasted with C57BL/6. DBA/1: autoimmunity and arthritis
NOD	Outbred Jc1:ICR S. Makino, Shionogi Research Laboratories	NOD/LtJ, NOD/MrkTac, NOD/Shi	Type 1 diabetes research, autoimmunity research
NZB	Outbred mice from Imp. Cancer Research Fund M. Bielschowsky, University of Otago Medical School	NZB/B1NJ	Autoimmunity research
SWR	Swiss mice from A. de Coulon of Lausanne, Switzerland C.J. Lynch, Rockefeller Institute	SWR/J	General purpose, cancer research, metabolic disease research, autoimmunity research

Table 2.2: Commonly used inbred mouse strains, origins, and research applications.

Source: H. Hedrich, *The Laboratory Mouse*: Elsevier Academic Press, 2004.

	Siemens (Imtek)	Skyscan	Scanco	Stratec
Scanner Name	Inveon CTmodule	1076	vivaCT 40	XCT Research SA+
Detector Array	3072x2048 4000x4000	4000x2300	2048x2048	12 detectors
Field of View	Up to 100mm	Up to 68mm	Up to 145 mm	Up to 50mm
Resolution	>15 microns	9-35 microns	16 microns	70-300 microns
Reconstruction (512x512x768)	Real time	Nrecon 4 PC cluster ~40s	Not specified	Not specified
Comments	Multimodality Integration; gating	Gating; physiologic monitoring	Visualization and measurement software	Accommodates wide range of sizes

Table 2.3: Commercial preclinical imaging systems.

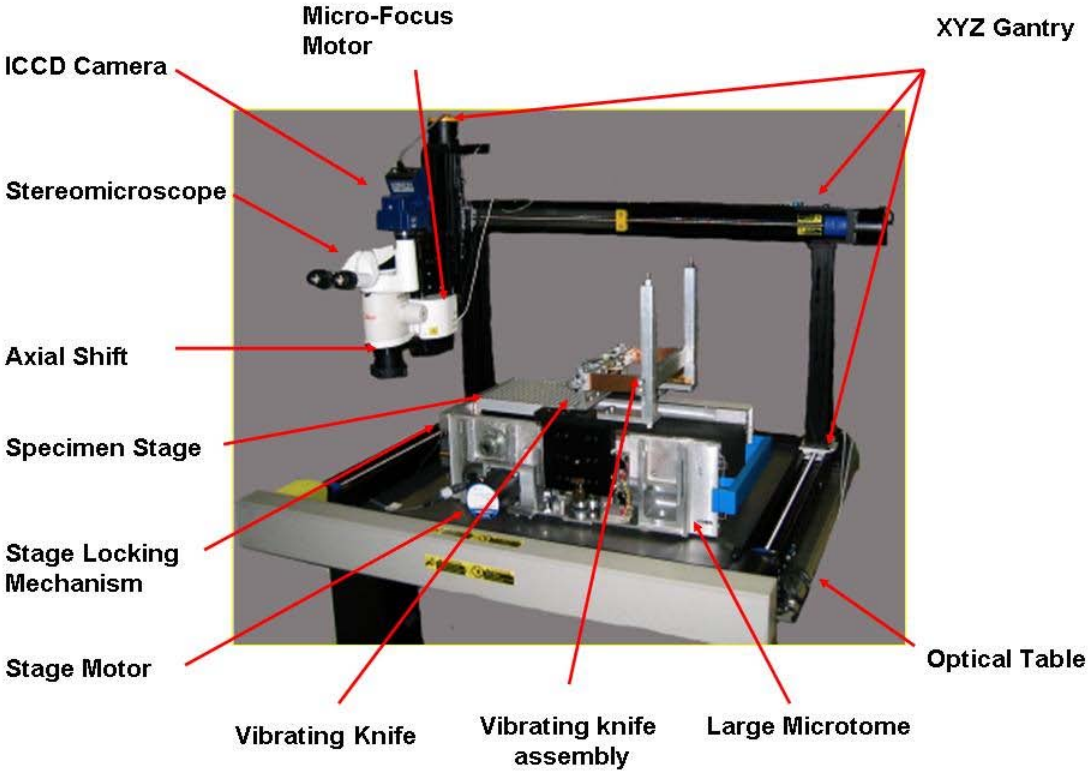

Figure 2.5: The Large Image Microscope Array (LIMA) system. This 3D pathology system is capable of sectioning tissue samples at varying thickness and imaging the cut surface on the remaining tissue block. The various components of the system are shown (in black) and their respective locations are indicated (in red).

Figure 2.6: **Mouse airway casts.** Variation in casts can be seen between the two strains: BALB/c (left) and B6C3F1 (right).

Reproduced from Oldham and Phalen. 2002 [32]

CHAPTER 3

IMAGE ACQUISITION METHODS

3.1 Image Acquisition Sequence

The development of a process model, **Figure 3.1**, for acquiring both the *in vivo* and *ex vivo* image datasets was necessary for successful characterization of the mouse lung anatomy in the C57BL/6, A/J, and BALB/c mice. The specific imaging sequence was developed in order to overcome and minimize difficulties that occur while collecting datasets from multiple imaging modalities as well as between the living animal and the corresponding fixed tissue sample. To begin with, *in vivo* micro-CT imaging is performed. The information extracted from this imaging technique serves as the basis for the closest anatomical representation of the lung that exists in the living mouse. Following *in vivo* scanning the lungs are inflation fixed and dried. The e*x vivo* specimen undergoes micro-CT imaging and subsequent LIMA imaging. Each section imaged on the LIMA system is removed for histological processing. The LIMA system is essential because it is a 3D microscopy system which acquires registered slices, and can serve as the reference between micro-CT and traditional histology. A summary of the imaging modalities that are used is available in **Table 3.1** and a schematic demonstrating the whole *ex vivo* process is displayed in **Figure 3.2**. Experimental procedures have been developed for use of each of these systems and analysis has been performed on the resulting datasets. **Table 3.2** provides a synopsis of the time required to generate the image datasets from the beginning of the *in vivo* imaging through histology for a single mouse.

3.2 *In Vivo* Micro-CT Imaging

In vivo micro-CT image acquisition is the first step in the 3D lung characterization and is extremely valuable because the lung can be imaged live, non-invasively, and it is a non-destructive imaging modality.

3.2.1 Animal Preparation

In order to conduct experimentation using mice a proposal for humane treatment of animals must be approved through the Institutional Animal Care and Use Committee (IACUC). Following approval, design of *in vivo* imaging involves: handling of animals, development of appropriate anesthesia protocols, applying micro-surgical techniques, and utilization of physiologically appropriate ventilation for gating purposes.

Three normal mouse strains are being utilized in the characterization of the normal mouse lung including the: C57BL/6, A/J, and BALB/c. These mouse strains were chosen because they are the oldest inbred mouse strains and the most commonly used in research. The image datasets that were acquired came from mature mice between 20-22 weeks of age.

The anesthesia protocol that was developed for the *in vivo* mouse imaging included an initial sedation of inhaled 2-3% isofluorane, after which each mouse was weighed. To fully anesthetize the mouse an intra-peritoneal injection was given with a dose of 87.5mg/kg ketamine and 12.5mg/kg xylazine. The initial sedation using isofluorane was used to avoid as much stress to the mouse as possible prior to the study which was especially important prior to lung function testing [26]. The ketamine-xylazine mixture served as the surgical anesthesia in addition to the analgesic agent. The plane of anesthesia using this lasted for approximately 20-30 minutes which allowed for enough time to get the mouse prepared to be connected to the ventilator. Side affects of the ketamine-xylazine include bradycardia, hypotension, respiratory depression, and hypothermia. These conditions were taken into account during monitoring of the mouse and modifications to the *in vivo* protocol included the addition of heat lamps to prevent hypothermia of the mouse during scanning.

Following a non-responsive pedal reflex test, a microsurgical tracheotomy was performed, figure 5. The mouse was then connected to a computer controlled ventilator, which consists of a modified Scireq (Montreal, Quebec) Flexivent system controlled via

Labview (National Instruments, Austin, TX). In order to achieve minimal motion, respiratory paralysis was necessary and completed through the administration of 0.1 mg/kg pancuronium. A concentration of 1-2% of isofluorane maintained the anesthesia throughout the imaging phase. All animals were housed and treated in accordance with the University of Iowa Animal Research Committee guidelines.

3.2.2 Computer-controlled ventilation for measuring respiratory mechanics in the mouse

The ventilator system, *flexiVent* (SCIREQ, Montreal, Quebec), that is used for the *in vivo* micro-CT imaging is capable of generating measurements of lung mechanics in the mouse lung. As with our micro-CT imaging, there is a trade-off that is made in order to acquire these measures of the lung. For instance, in our *in vivo* micro-CT imaging protocol we anesthetize, paralyze, ventilate, and perform gating which introduces unnatural physiological conditions in the mouse and could ultimately introduce bias in the lung function and structure. However, without these control conditions we would not acquire the same quality of images and therefore could not extract the same anatomical features. Similarly, while generating measurements of respiratory mechanics in the mouse there is a spectrum of conditions that can be controlled. This spectrum has been termed the "*Phenotyping Uncertainty Principle*" [60] and relates the least invasive and most precise procedures used in lung function measures to unrestrained plethysmography and the forced oscillation technique, respectively. Since we are imaging the mice at the most precise end of the spectrum we would like to make sure lung function measures are also generated under similar conditions. The *flexiVent* utilizes the forced oscillation technique to generate measures of lung mechanics where the mouse is connected to the ventilator via a tracheostomy tube and the *flexiVent* applies:

- Sinewave oscillations in flow to determine resistance and elastance
- Broad-band oscillations in flow to determine impedance

- Step changes in volume to determine the pressure-volume curve

Prior to imaging, we collected measures of the resistance (R) and elastance (E) of the lung to compare functional parameters of the mouse lung to the structural features such as the airway tree that were extracted from the micro-CT images using a custom script.

3.2.3 *In Vivo* Respiratory Gated Micro-CT

The Siemens Micro-CAT II (Siemens Pre-Clinical Solutions, Tennessee), scanner was used for the *in vivo* micro-CT imaging completed in this research. It consists of a Kevex (Thermo Electron Corp., Waltham, MA) micro-focus X-ray source that has a variable range of voltage potential and current that can produce anywhere from 0-130 kVp and 0-500 µA. The detector is made up of a phosphor screen connected to an intensified 3072 x 2048 CCD, with a 32 µm pixel pitch size, through a fiber-optic taper. In addition, the X-ray source and detector are attached to a gantry slide so that the distance between the X-ray source, detector, and object can be varied. For optimized imaging of the mouse lung the distance between the X-ray source, the object, and the detector was placed so that the lung would have a maximized magnification and fit entirely within the field of view.

Micro-CT imaging of the mouse lung using the Micro-CAT II scanner was found to contain extensive ring artifacts that are problematic when performing quantitative analysis. The primary cause for ring artifacts in the reconstructed images are due to small differences in the sensitivity of adjacent detector elements [11]. There are two possible solutions for reducing ring artifacts. One approach is hardware based where the detector sensitivities are reduced. The second approach is processing of either the raw sinograms or the reconstructed transverse images. Both methods were evaluated and a post reconstruction ring artifact reduction algorithm was implemented. Through further investigation it was found that a substantial reduction could be achieved through careful calibration and maintenance of the micro-CT scanner prior to and during the scanning.

This included maintaining a consistent temperature in the micro-CT room during scanning, performing an X-ray conditioning step, and acquiring calibration images in the form of serial X-ray source on and off images prior to each individual scan. The maintenance of temperature aids in reducing fluctuations in the detector element sensitivities, while the X-ray source conditioning ramped the tube into a steady state condition. Finally, the acquisition of bright and dark field calibration images prior to each mouse accounted for the remaining detector insensitivities that were most relevant to the current scan. This is opposed to performing a single calibration step at the beginning of the day, where the detector and X-ray source have yet to reach a steady state, and therefore future mouse scans increasingly inherit dramatic ring artifacts.

All mice were placed supine onto a polysterene bed and mounted on the micro-CT carbon fiber stage. During imaging, the mouse was monitored via ECG and temperature sensors using a BioVet C1 data acquisition system (Supertron Technologies, Newark, NJ). A healthy and stable cardiac rate for the anesthetized mouse is anywhere between 150 and 250 beats per minute [61]. If for any reason the heart rate dropped below these levels the mouse was assessed and adjustments were made to the isofluorane percentage to try to bring the heart rate back to a stable level.

For the *in vivo* image acquisition, a trade-off was made between the acquisistion time to perform each scan, the reconstructed image resolution, and the amount of radiation that the mice were exposed to. From these three requirements the following settings were decided upon for all scans that were completed *in vivo*: an output of 60kVp and 500µa, an exposure time of 500ms, and a total of 720 projections over 200 degrees (half-scan). With these parameters, each scan takes approximately 45 minutes to complete and exposes the mouse to approximately 85 Rad (cGy) of radiation. In addition, when intubated the animals can be successfully revived. The resulting image dataset from these scans takes approximately 30 minutes to reconstruct using a 28 micron

isotropic voxel size and generates an image dataset of 1526 pixel x 1526 pixel x 1024 pixel in size. The field of view represented in this image set is 43 x 43 x 28 mm.

For the *in vivo* lung imaging, the projections were acquired using a custom gating and breath hold technique called the Intermittent Iso-pressure Breath Hold [40] which provides higher resolution images for *in vivo* lung imaging. This was made possible through the use of a computer-controlled ventilator and the development of a gating program that could trigger the scanner to take projections while the ventilator was stopped and a constant forced airway pressure was induced. IIBH, more specifically, consists of a unique breathing sequence that involves three phases: (1) slightly hyperventilated breathing at 90 br min-1 and 20 ml kg-1 for a total of 4-5 seconds, (2) two deep breaths, and (3) apnea for about 5 seconds while a forced airway pressure is induced and the micro-CT scanner is triggered to capture multiple angles of view. Since a total of 720 projections are required for a complete *in vivo* lung scan and 4 projections are captured during each complete IIBH breathing sequence, the gating process where a breath-hold is induced occurs approximately 180 times. The images that have been obtained for the C57BL/6, A/J, and BALB/c mice using this technique demonstrates the high image quality that can be obtained for the pulmonary system of small animals using the IIBH technique instead of spontaneous breathing, **Figure 3.3**

A total of three *in vivo* scans were acquired using the breath-hold technique at 10, 20, and 30 cmH_2O for each mouse. Since the mouse cannot be told to hold a deep breath it has been extremely challenging to define the total lung capacity for the mouse. Researchers have tried to define this pressure empirically through pressure and volume relationships and have not yet been able to present a definite answer. They have found that the mouse lung can be inflated past 80 cmH_2O without damage [33]. Therefore, we are not defining a total lung capacity for the mouse; instead we have assessed the *in vivo* lung at multiple pressures and fixed the lung tissue at 20cmH_2O—a pressure that has been accepted to fully inflate the lung. Complete analysis of the *in vivo* and *ex vivo* lung

phenotypes for the C57BL/6, A/J, and BALB/c mice have been completed at 20cmH_2O pressure using the *in vivo* micro-CT, *ex vivo* micro-CT, LIMA, and histology imaging. Additionally, lung metrics at 10 and 30 cmH_2O using the breath-hold technique have also been extracted from the *in vivo* micro-CT scans. An in depth comparison of the lung volume and airway dimensions that exist between breath-hold pressures within each mouse strain has been completed to assess the distensibility of the lungs between the inbred mouse strains we have investigated.

3.3 Tissue Excision and Fixation

"Every fixation for light and electron microscopy produces an artifact, in the best sense of the word, which represents some aspects as faithfully as possible but at the expense of others. We therefore have to live with the 'failed dream of the physiological fixation'"[3, 45].

Many fixation techniques are utilized to preserve the lungs for *ex vivo* imaging using microscopy and micro-CT. For preservation of the tissue following *in vivo* micro-CT imaging, the lung is excised and fixed using a modified Heitzman fixation solution. This fixative is intended to conserve radio-density while maintaining necessary histopathology for accurate pathologic and radiologic comparisons. Therefore, the lungs are fixed with a fixation mixture consisting of 25% Polyethylene Glycol 400 (FisherChemicals, New Jersey), 10% Ethyl Alcohol (190 Proof, 95%) (Pharmco Products, Connecticut), 10% Formaldehyde Solution (FisherChemicals, New Jersey) and 55% laboratory distilled water [62]. Since there are many fixation techniques, experimentation and a review of previously used methodologies was completed. Testing done by Blumler et al. showed that immersion fixation without instillation through the trachea did not allow sufficient subsequent inflation of the lung [63]. Based on a review by Renne et al. researchers using formalin lung fixation techniques were surveyed in order to develop an accepted and more standardized protocol for the fixation of lung

specimens. Seven out of the eight members surveyed used intratracheal instillation and normally removed the lungs from the thoracic cavity prior to fixation unless they were quantitative studies. In addition, gravity instillation was used in quantitative studies versus filling until full expansion of the lobes in qualitative studies. All eight of the responding members (including the member who did not use instillation fixation) agreed unanimously that intratracheal instillation provided the best preservation of airways and alveolar walls—in addition to maximizing visualization of the lung parenchyma. The single member who did not use intratracheal instillation noted that there is the disadvantage of inducing artifacts [64]. However, based on the study the sub-committee of the Society of Toxicologic Pathology expressed the opinion that the advantages of intratracheal instillation for the fixation of lung tissue outweighed the disadvantages and they strongly recommend this method for quantitative studies involving the alveoli [64].

Based on the previous techniques accepted for formalin fixation, we modified our fixation technique using the Heitzman solution. The fixation fluid is applied intratracheally through a gravity feed system at a constant specified pressure of 20cmH_2O for a total of 18-24 hours for mice. Initially, the fixation is performed within the thoracic cavity for approximately thirty minutes for full inflation and fixation of the air spaces. The effect of the chest wall mechanics on the lung is ignored since previous reports have found that the chest wall compliance is 6-7 times greater compared to the compliance of the lung. It has also been found that strain-specific phenotypes in lung mechanics are not influenced by the chest wall [30, 65]. After the lung is removed from the chest, the trachea remains connected to the gravity feed system and is immersed in the fixation mixture for the remaining time. Placing the lung in the fixative ensures that areas inaccessible via the airways are fixed through diffusion. The lung is then disconnected from the fixation apparatus and air-dried at the same pressure that the tissue was fixed at 20cmH2O for 48 hours in a heated drying oven set to 60 degrees Celsius. Using this method there is minimal reduction in lung volume during fixation; and the lung density as

measured by the CT scan before and after fixation, is preserved. **Figure 3.4**, shows the set-up used for fixation of the mouse lung.

In addition, **Figure 3.5** shows the differences in size between lungs fixed using the methodology with the Heitzman solution versus 10% neutral buffered formalin. The experimentation was completed on two A/J mice of the same age and using the same instillation protocol. An image slice obtained from the micro-CT demonstrating the differences in internal lung structures between the modified Heitzman fixed lung and the 10% neutral buffered formalin fixed lung is shown in **Figure 3.6**. The fixation protocol and the scanning parameters for the micro-CT were constant for both lungs, revealing that the differences seen in the images are a result of the fixative used. It is clear that the Heitzman technique is superior for our experimentation.

3.4 *Ex Vivo* Fixed Lung Micro-CT Imaging

Because no single imaging system can provide all the information available within the specimen it is important to utilize complimentary imaging systems to characterize the lung in 3D. Micro-CT imaging provide radiodensity image information. *Ex vivo* micro-CT allows fixed lung investigation without motion artifacts and can be correlated to the lung structures in 3D microscopy techniques. Therefore, following tissue fixation the lung is re-imaged on the micro-CT.

Prior to imaging the fixed lung specimen, the development of an apparatus was needed to maintain the lung in the same imaging plane for micro-CT and subsequent LIMA imaging. The system that has been used to orient the lung, **Figure 3.7**, consists of a fine 22 gauge plastic wire fed through a catheter directed through the heart—to prevent disruption of lung tissue. The lung is stabilized by two wooden dowels connecting two polyethylene end plates that fit directly onto the micro-CT specimen stage. The system further translates to the LIMA, without changing the imaging plane through the attachment of one end plate to the stage base plate of the LIMA system.

The Siemens Micro-CAT II scanner (Siemens Pre-Clinical Solutions, Tennessee) was used for *ex vivo* micro-CT imaging. The scanner settings have been changed to 60kVp, 368μA, and 2250ms in order to acquire higher resolution images through the decrease in the X-ray power output (reduction of the focal spot size) and the increase in the exposure time (increase the dynamic range and hence increase the signal to noise ratio). The images were reconstructed using 28 micron isotropic voxel size generating an image dataset of 1536 pixel x 1536 pixel x 1024 pixel in size. The field of view represented in this image set is 43 x 43 x 28 mm.

3.5 The LIMA System

Although the LIMA system and traditional histology are destructive imaging systems they are important for the development of the 3D characterization of the entire mouse lung because they contain image information not found in the micro-CT. Traditional histology, consisting of extremely thin 2D stained tissue samples, has been the gold standard for assessing normal and diseased lung structures. However, because of the loss of precise spatial information in standard processing of histology samples the tissue slices cannot be accurately correlated to the 3D micro-CT data. Therefore, the use of the LIMA system is essential because it is a 3D microscopy system which acquires registered slices, allowing correspondence between micro-CT and traditional histology. In addition, the LIMA system can provide image information such as color and fluorescence.

3.5.1 Tissue Embedment

In order to section the lung from apex to base using the LIMA system without disrupting the tissue, an external embedment step needed to be incorporated. Extensive experimentation evaluating multiple materials including resin, paraffin, foam, and agarose was completed. However, due to limitations in the embedment material, including artifacts from the paraffin and foam, agarose was chosen. Testing of the best

preparation for agarose was made and the resulting methodology for preparation included: using low gel temperature biological grade agarose mixed with distilled water and heated in a microwave on high for approximately 60 seconds. The agarose was allowed to cool down to 10 degrees above the gelling temperature and then poured into a custom embedment container which houses the mouse lung in the correct orientation with respect to the *ex vivo* micro-CT scan. The container was placed in a refrigerator where the agarose gelled and cooled until it was completely set (approximately 2 hours). The embedment container is made up of a stack of plates surrounding the embedded material that is sequentially removed during the sectioning process. This is important for supporting the agar and the lung during sectioning. Error! Reference source not found.Error! Reference source not found. shows the embedment process with the orientation device and the dynamic embedment container with lung tissue embedded in agarose. Using this technique we have been able to section on the LIMA system in a repeatable fashion and are able to process the slices successfully for generation of histology slides.

3.5.2 Bright Field LIMA Imaging

Following the embedment procedure, imaging and sectioning is performed on the LIMA system. The LIMA system is capable of high resolution imaging from 0.7 µm to 12 µm depending on the level of magnification used. However, a trade-off between resolution and the time required for acquisition needed to be made. For this project, it was found that a magnification of 20x, producing a resolution of 4.2 µm, was suitable for analysis of the lung structures as well as acquisition time.

The agarose embedded lung was attached to the base plate of the LIMA system and the entire lung was imaged and sectioned. The sequence for capturing the LIMA images consists of the microscope moving through an automated raster scan creating a montage of images of the top surface of the tissue specimen. At 20x magnification we

acquired 36 subtile images (6x6) at individual image sizes of 1300x1050 pixels. The image tiles were acquired with a 15% overlap in the horizontal and vertical directions for subsequent image processing to form a composite image of the tissue surface, **Figure 3.9**. Following imaging, the sectioning equipment is turned on and the base plate moves towards the knife, resulting in a tissue section of 500 µm thickness. This cycle is repeated and occurs sequentially through the lung in an automated process. Using the LIMA system for microscopy image acquisition, spatial relationships between sequential slices are maintained and spatial correlation can be made with the micro-CT. In addition, the resulting slice from the LIMA can be processed using traditional histological techniques.

The LIMA and histological datasets consisted of approximately 40 slices per lung, based on a sectioning thickness of 500 µm. In comparison, the image datasets obtained from the micro-CT have approximately 600 image slices.

3.5.3 Bright Field Segmentation Tomography (BFST) LIMA Imaging

The images obtained using the standard LIMA bright field ring illumination provide valuable information regarding the lung and airway structures. However, the nature of the lung parenchyma makes it difficult to distinguish the very top surface of tissue from the surrounding tissue structures using this illumination, especially at high magnifications. In order to distinguish these structures, a custom made ring illumination attached to the LIMA microscope, known as Bright Field Segmentation Tomography (BFST), was designed and developed. The BFST extracts surface details from highly sculptured specimens through oblique illumination using a series of collimated light sources. The BFST illumination technique in conjunction with the Leica microscope provides a novel system that can detect subtle surface features.

The illumination device was constructed from an aluminum ring with eight bright white LED's placed around the base of the ring, **Figure 3.10**. The aluminum was coated in opaque black to prevent reflection and other optical disturbances within the system. In order to achieve consistent illumination the LED's were placed with even separation according to DS = 360/N, where N is the number of LED's used and DS is the degree of separation. Since eight LED's were used, they were placed at 45-degree separation measured from the center of the ring and were set in holes drilled to fit their diameter of 3.25 mm. Setscrews were added to hold the LED's in position to provide consistency of illumination intensity and viewing. The system was integrated for automated control by the LIMA acquisition system.

Incorporation of the images from the LIMA using BFST provides a methodology for producing images that can be analyzed for assessment of the lung parenchyma and can verify the lung structures that can be resolved in the prior micro-CT image datasets. An example of the BFST technique on a sample of fixed mouse lung tissue at 60x magnification demonstrates that the interaction of light and shadows produces an image with increased contrast, and the affect of decreasing the depth of field provides more defined top surface edges, **Figure 3.9**.

3.6 Histology

The 500 µm sections that were removed following imaging of the tissue block on the LIMA system were further processed utilizing traditional histology techniques. Each slice was wrapped in biopsy paper and placed within histology cassettes. They were then placed in a paraffin processor where each tissue slice was infiltrated with paraffin. The slices were subsequently embedded in a paraffin block for sectioning in such a manner to ensure the section laid flat on the base of the paraffin embedding container. Each 500 µm slice was re-sectioned at a finer increment of 5 µm using a paraffin microtome. The

resulting sections were placed on slides and stained with Hemoatoxylin and Eosin (H&E).

The microscope slides were digitized with a ScanScope automated slide digitizer. This system was utilized because it could image an entire stained mouse lung section and maintain focus across the field of view in un even samples using a dynamic focusing system. The slides were scanned using a 20x objective which resulted in images with a pixel size of 0.504 µm.

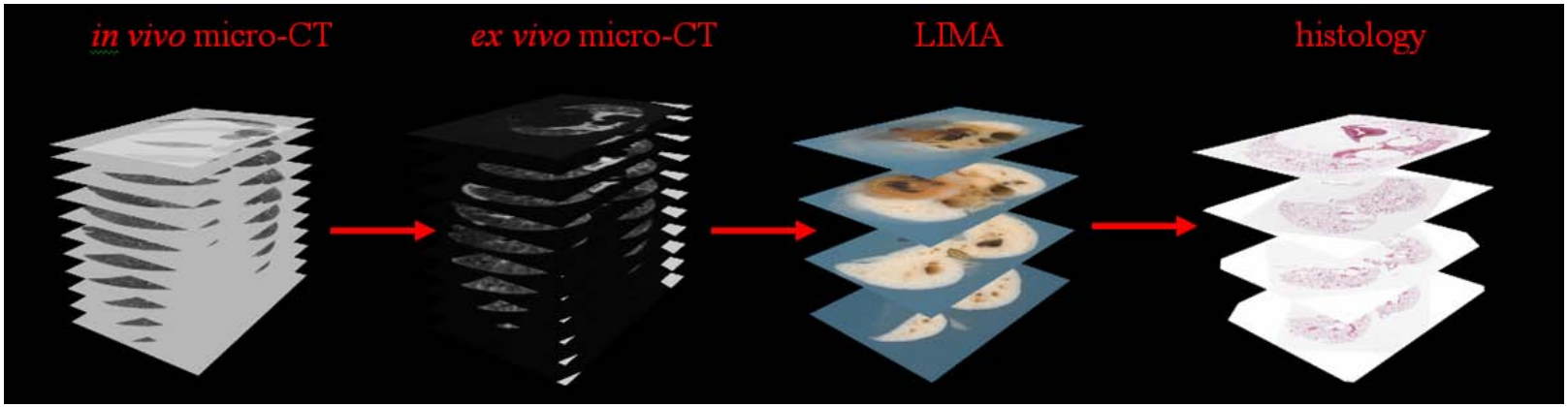

Figure 3.1: The Image Acquisition Sequence: The imaging modalities used in this research include non-destructive micro-CT and destructive LIMA and histology imaging. Starting with *in vivo* micro-CT anatomical structures within the living animal are evaluated. Once the tissue is harvested *ex vivo* micro-CT can be used for assessment of the fixed lung and directly correlated to.

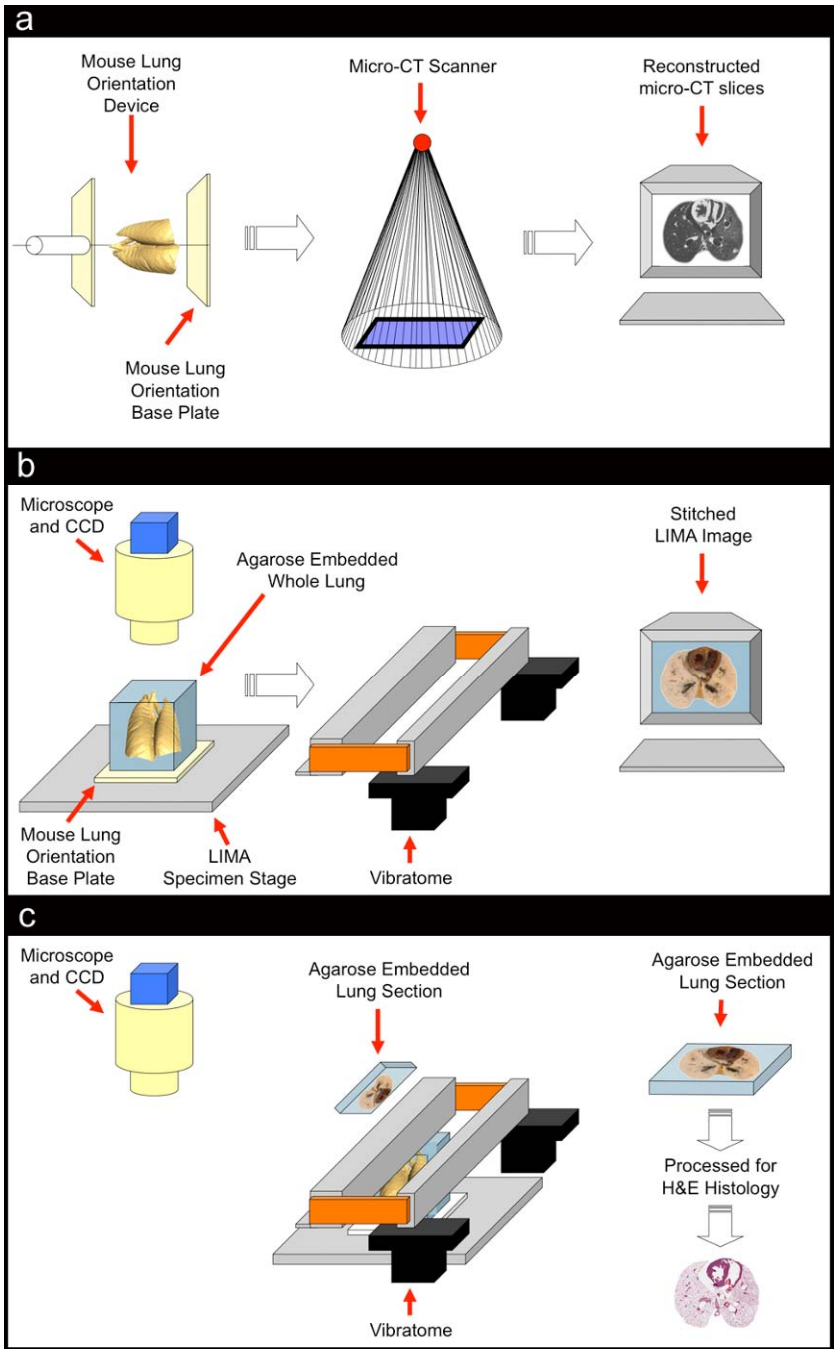

Figure 3.2: *Ex vivo* imaging process from micro-CT through histology. a) The mouse lung is suspended between two base plates custom fit for the Micro-Cat II bed and micro-CT imaged. b) The base plate from the orientation device is connected to the LIMA specimen stage to maintain the same imaging plane. The lung is agarose embedded and imaged. c) The vibratome sections the lung and the slice is histology processed.

	Application	Image Content	Resolving Power	Voxel Dimensions
***In vivo* micro-CT**	• Non-invasive imaging • Longitudinal studies • Physiological studies	• Radiodensity	~55µm	28 x 28 x 28µm
***Ex vivo* micro-CT**	• Fixed tissue imaging • High resolution • Increased signal/noise ratio	• Radiodensity	~40µm	28 x 28 x 28µm
LIMA	• 3D pathology • Enables accurate micro-CT—histology registration	• Gross pathology • Color • BFST • Fluorescence	4.2µm (20x magnification)	4.2 x 4.2 x 250µm
Histology	• Ground truth • Cellular information	Cellular & Subcellular	2.5µm (20x objective)	2.5 x 2.5 x 5µm

Table 3.1: Summary of imaging modalites.

Process	Time required (hours)
In vivo micro-CT imaging	
animal preparation -anesthesia -tracheostomy	0.75
scanning -3 scans at: 10, 20, 30 cmH_2O	2.25
reconstruction -3 reconstructed datasets	1.5
Lung fixation	
in situ inflation fixation	0.5
excision	0.25
immersion fixation	24
Ex vivo micro-CT imaging	
scanning -1 scan with increased exposure	1
reconstruction -1 reconstructed dataset	0.5
LIMA imaging	
agarose embedment	2
35 bright field slices	5
3 BFST at apex, mid, and base	2
photoshop stitching	3
Histological processing	
paraffin processing	14
paraffin embedment	3
sectioning	8
staining	0.5
slide digitizing	5
TOTAL	**73.25**

Table 3.2: Acquisition time required for collection of the raw image data for a single mouse lung.

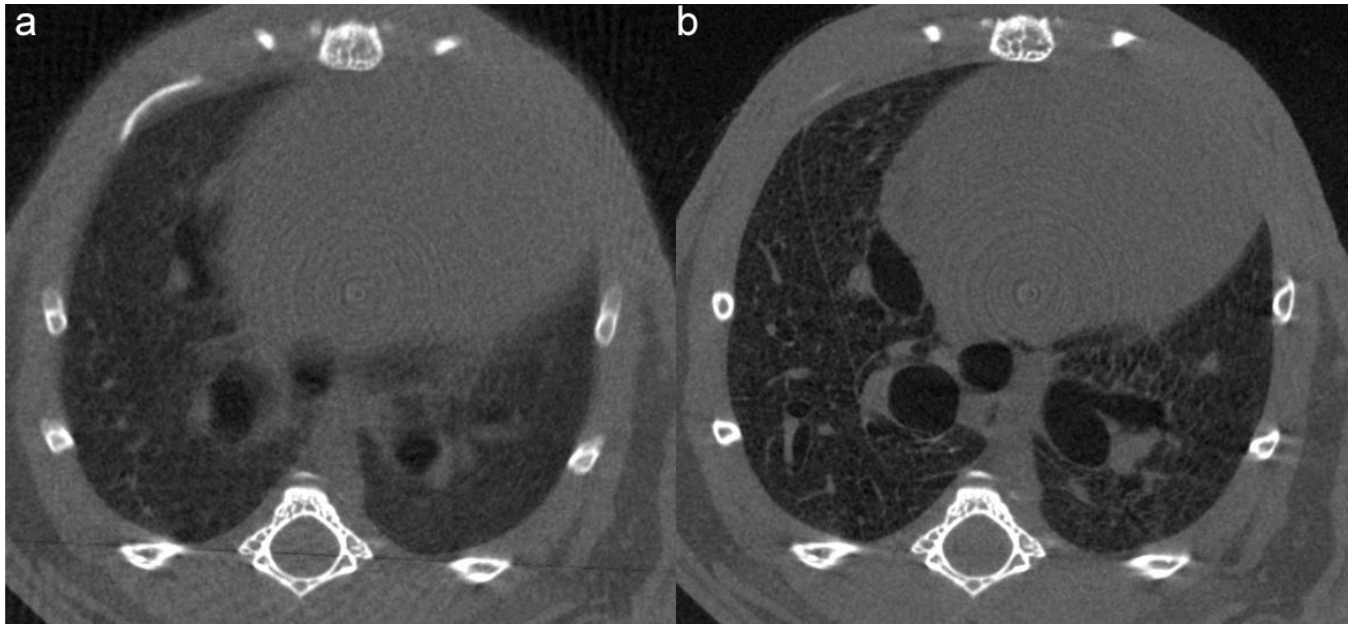

Figure 3.3: Comparison of a spontaneous breathing mouse and IIBH ventilated mouse *in vivo* micro-CT image. a) The spontaneous breathing mouse micro-CT image demonstrates the poor image quality due to the motion artifact caused by normal mouse respiration. b) The IIBH ventilated mouse micro-CT image by comparison has significant decrease in motion artifact and clear airway and lung boundaries that can be extracted.

Figure 3.4: *In situ* fixation system setup. The fixation system consists of constant pressure monitoring through the pressure transducer and the dynamic gravity feed system.

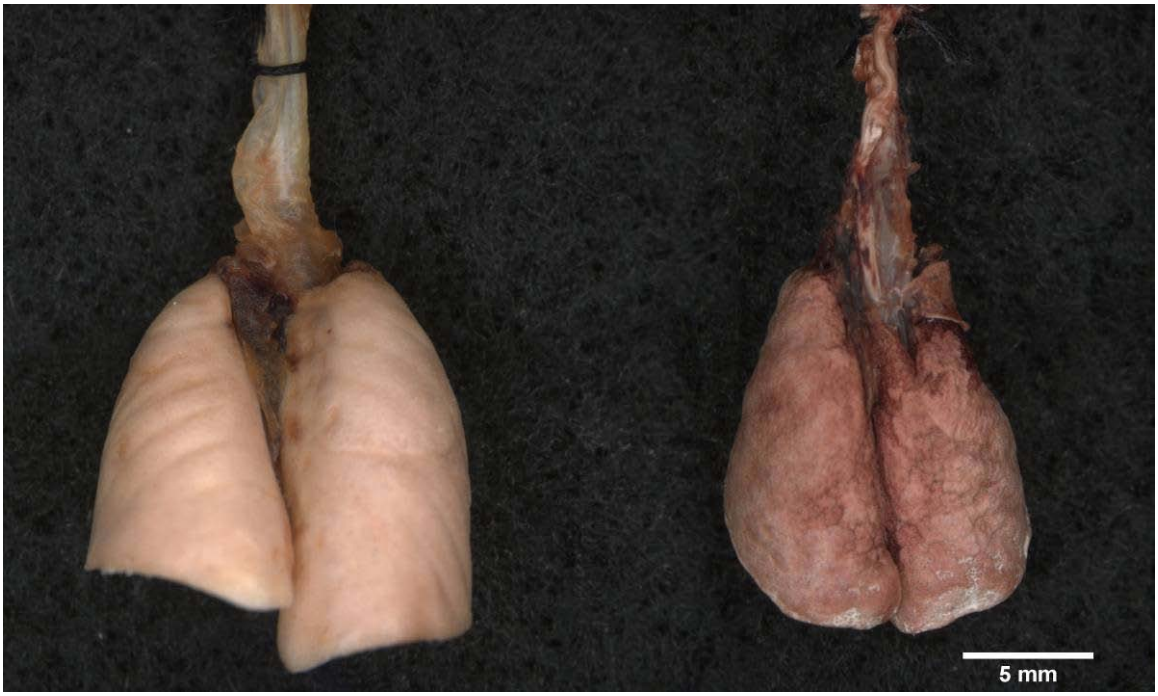

Figure 3.5: In situ lung fixation comparison. Using our in situ fixation setup two lungs from the A/J strain were harvested. The modified Heitzman solution was used for the left lung and a 10% neutral buffered formalin solution for the right lung.

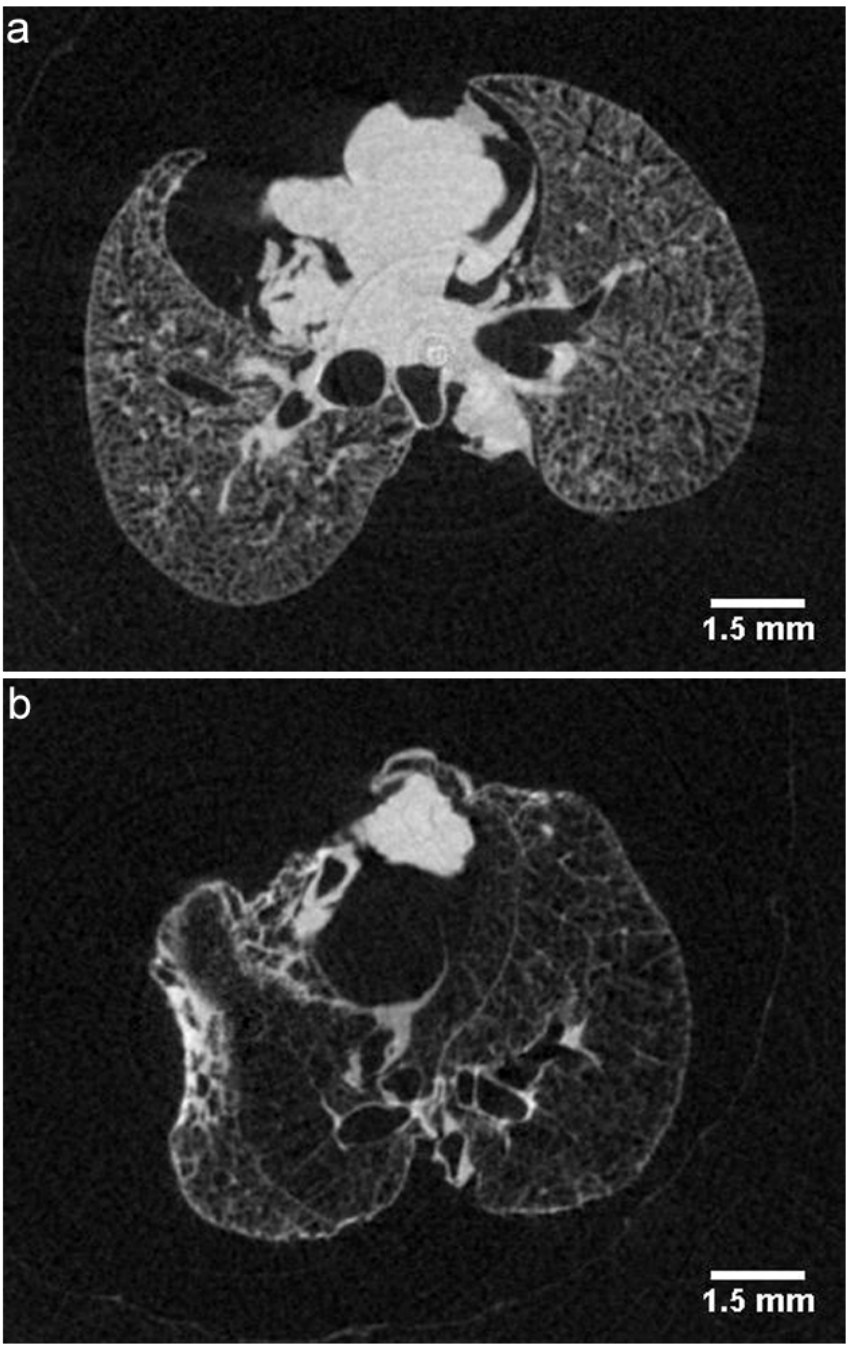

Figure 3.6: Comparison of fixation techniques using micro-CT. a) Performing installation fixation and air drying of the specimens demonstrates that the lung fixed with the Heitzman solution has less distortion and shrinkage than b).the lung fixed with 10% neutral buffered formalin

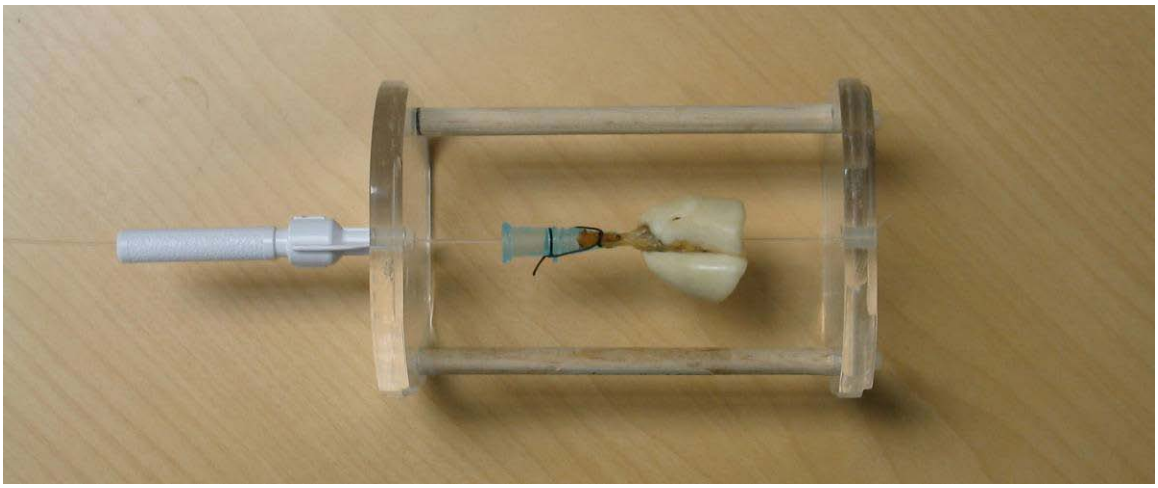

Figure 3.7: Orientation and lung stabilization apparatus for fixed lung imaging. The above apparatus prevents the lung from shifting during micro-CT scanning and can be connected directly to the LIMA specimen stage for sectioning.

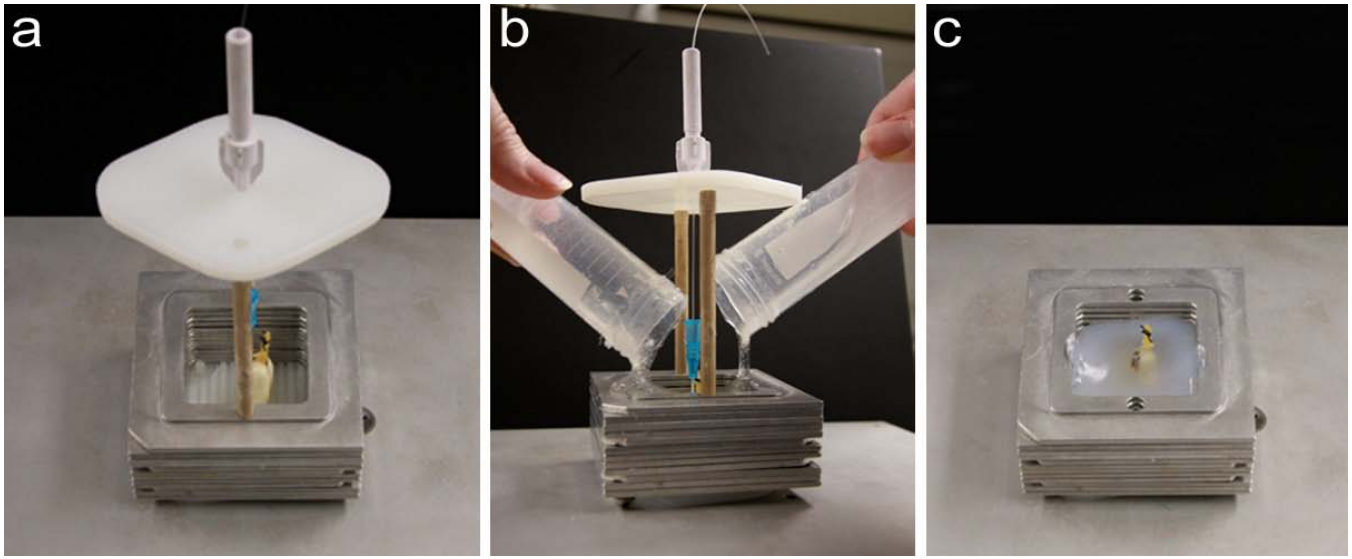

Figure 3.8: Agarose embedment container. a) Lung within embedment container while still attached to orientation device prior to embedment, b) agarose embedment, and c) agarose embedded lung with orientation device removed

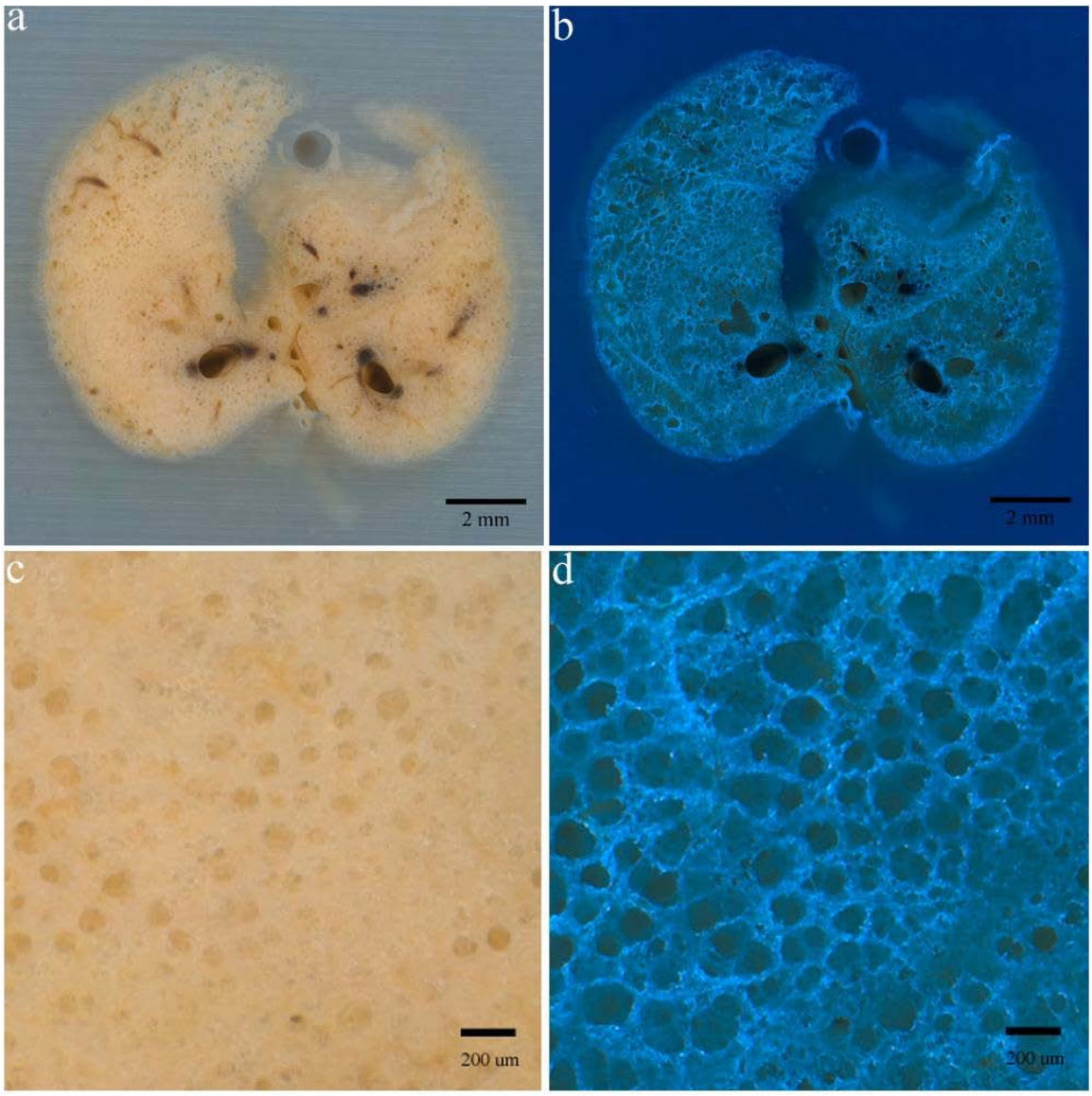

Figure 3.9: Composite bright field and BFST LIMA images of mouse lung embedded in agarose. Example tissue surface that is imaged via the LIMA system. a) A single composite image of the bright field LIMA consists of 36 subtile images (20x) while the b) BFST consists of 144 subtile images (60x). The images have been resized and can be zoomed into to reveal smaller structures c) in the bright field and d) BFST images.

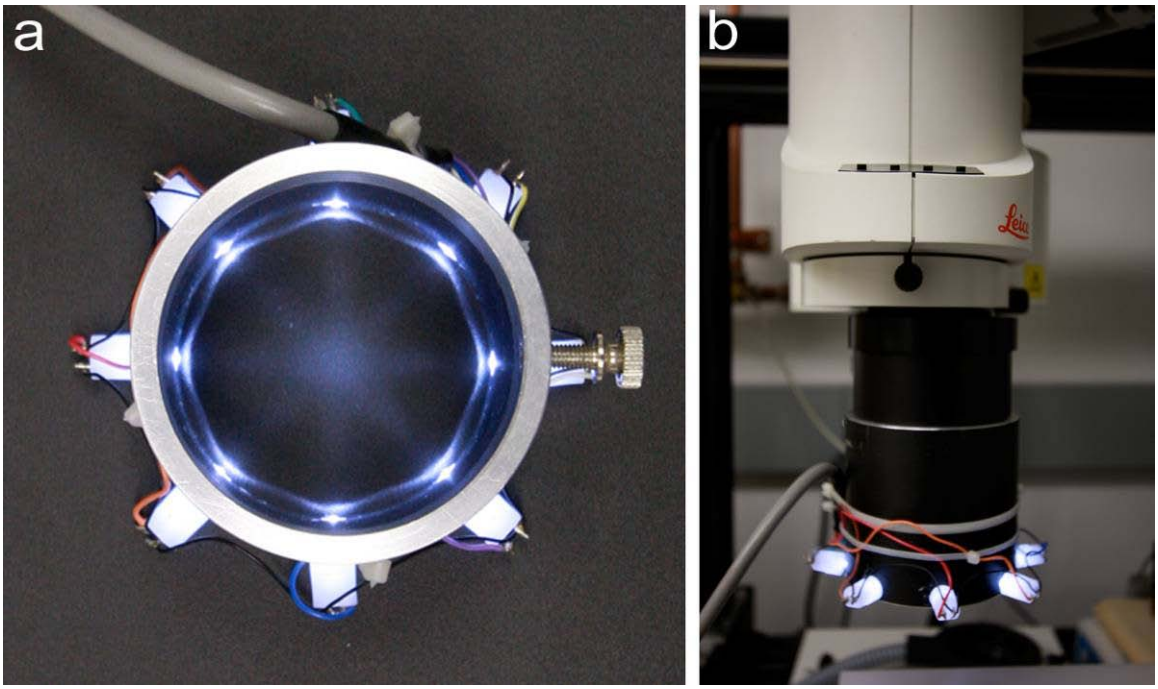

Figure 3.10: BFST illumination attachment for LIMA microscope. a) The eight LED's of the BFST provide oblique illumination of a highly sculptured specimen such as the lung for increased surface contrast. b) The BFST attachment is custom fit to directly mount to the LIMA microscope and can easily be interchanged with the standard ring light attachment.

CHAPTER 4

IMAGE PROCESSING AND ANALYSIS

4.1 Micro-CT Imaging

The micro-CT system is not a turn-key system that outputs image files in a standardized file format such as DICOM or ANALYZE. Therefore, the output files from the micro-CT undergo initial processing in order to be viewed and further processed as three-dimensional (3D) image files. Once the projection images have been acquired the micro-CT datasets are reconstructed using a cone beam back projection reconstruction algorithm [66] through the RVA software program provided with the Micro-CAT II scanner. Each reconstructed image is in a raw 16Bit Signed image file format that is 1536 pixels x 1536 pixels in size. A total of 1024 images are generated for each micro-CT scan with a voxel size for the dataset of 28 µm—creating a total size for these files of just over 4 GB. Since the area of interest—the lung—does not fill the entire region of the image set the files are cropped to a more manageable size to contain the lung volume and remove surrounding pixels that are non-lung regions. The individual cropped image files are then written to the ANALYZE file format. The size of the resulting cropped ANALYZE file for each micro-CT dataset varies in size based on the volume of the lung and generally is between 600-700 MB.

4.1.1 *In Vivo* Micro-CT Imaging

Initial image acquisition for the *in vivo* micro-CT scans were completed at a single airway pressure of 20 cmH_2O. Therefore, a total of six mice of each strain were imaged *in vivo* at this pressure. However, we were also interested in comparing the lung metrics that were extracted from the three strains of mice at multiple breath-hold pressures. We further collected *in vivo* micro-CT data for three mice of each strain at 10, 20, and 30 cmH_2O. Processing of this image data included many steps starting with the

conversion to a useable file format as discussed in section 4.1 and segmentation of the lung structures.

4.1.1.1 Lung Segmentation and Visualization

To calculate the volume of the lung at each of the three pressures for which scanning took place a software program, AMIRA (Visage Imaging, Inc., California), was used. The entire lung was segmented using a region growing technique where a seed pixel was specified and voxels within a specified threshold were labeled as lung. The resulting voxels were summed to give a total pixel volume and multiplied by the image resolution of 28 µm in all three dimensions. The same threshold was utilized for all lungs segmented for total lung volume calculation.

The lungs were also segmented into the four right lobes and single left lung at 20 cmH_2O. Currently no automated or semi-automated tools exist for segmentation of the lobes due to the difficulty in automatically detecting fissures in the mouse lung. Therefore, the individual lobe segmentation was completed via manual tracing of each slice with aid of a live wire tool that "locked" to the contrasting boundary features.

Following segmentation the lobe volumes were calculated and the lobes were rendered in 3D for visualization purposes. Each lobe was given a unique label and color, and visualized through a transparent three-dimensional voxel intensity projection. The output revealed the entire lung as well as the individual lobes overlaid onto an airway tree rendering (as described below), **Figure 4.1**. Using this visualization technique has provided, for the first time, the ability to compare these *in vivo* lung structures between mouse strains.

4.1.1.2 Airway Segmentation and Visualization

Defining the airway boundaries and segmenting the structures from the within the lung was necessary for characterization of the airway tree in the C57BL/6, A/J, and BALB/c inbred mouse strains. Initially, it was thought that it would be possible to segment the image data using a semi-automated technique that was already developed for extraction of human airways from CT images for the mouse. However, the image quality of the micro-CT images prevented the translation of existing techniques to the mouse lung. Major factors that contributed to this included poor density resolution and the thin-walled (little contrast) airways of the mouse lung. Therefore, manual segmentation of the airways was necessary. Using this technique enabled us to extract the airway segments for 3D visualization, quantification, and served as validation for an automated mouse airway segmentation approach that was being developed concurrently with this project [50].

The manual segmentation of the airways was completed using an in-house built software program for lung image analysis, Pulmonary Analysis Software Suite (PASS). The airways were segmented in each transverse image slice, approximately 700 slices per micro-CT scan. The airways for each mouse were segmented for the 10, 20, and 30 cmH_2O scans. The resulting segmentations were saved as binary image files as regions of interest. In addition to segmenting the visible airways from the micro-CT datasets, the bifurcations were further identified and five serial segmented slices at 50% of the branch length were isolated and extracted for regional quantitative analysis.

The complete airway segmented data was imported into AMIRA for 3D visualization that was necessary for identifying the branching structures in the inbred mouse strains, and development of a common nomenclature as discussed in section 5.1.

4.1.1.3 Airway Segmentation Validation

Since the airway tree of the mouse lung was segmented manually it was necessary to validate that the same tree could be reliably segmented between observers. We manually traced the same airway tree with three different observers. One of the three observers (Observer 1) served as the ground truth because they were responsible for the tracing of the airway trees throughout the project and were considered the 'expert'. The other two observers (Observer 2 and 3) were familiar with the mouse lung anatomy but had not previously traced a complete mouse airway tree. They were not shown any examples or given any specific instruction except to only trace airway segments that could be connected to a branch in a previous slice (except the starting slice), otherwise it was considered a point of termination.

We followed the technique utilized by Zehntner et al., and evaluated the manual segmentation results based on three measures including κ overlap, percentage of true positives, and percentage of false positives[67]. Three evaluations were completed for the manual segmentation results including comparing Observer 2 to the ground truth segmentation (Observer 1), Observer 3 to the ground truth segmentation (Observer 1), and comparing Observer 2 against Observer 3 (where Observer 3 was arbitrarily chosen as the ground truth between the two non-experienced manual segmenters). These measures were calculated based on the three specific regions that were defined: region 1—the region containing only the ground truth segmentation result, region 2—the region containing both the ground truth and the other segmentation result, and region 3—the region that contains only the non ground truth segmentation result. If we assign region A to the ground truth segmentation and region B to the other segmentation result then we can conclude:

- $Region_1$ = Contains A but not B (A & !B)
- $Region_2$ = Contains A and B (A & B)
- $Region_3$ = Contains B but not A (B & !A)

Once the regions were identified, a summation of the total number of voxels that existed in each region was completed for the entire segmented airway tree. We will further refer to the total voxels in each region as: V_1, V_2, and V_3.

The κ metric was used to assess the similarity that existed between the segmentation results, where:

$$\kappa = \frac{2V_2}{2V_2 + V_1 + V_3} \quad \textbf{4-1}$$

This technique has previously been shown to reward high levels of pixel agreement and penalize high levels of pixel disagreement and a κ metric value greater than 0.7 has been reported as an acceptable result for segmentation and classification results in image analysis[67]. In addition to the κ metric we also calculated the percentage of true positives (TP) and the percentage of false positives (FP) as:

$$TP = \frac{V_2}{V_1 + V_2} \bullet 100\% \quad \textbf{4-2}$$

$$FP = \frac{V_3}{V_2 + V_3} \bullet 100\% \quad \textbf{4-3}$$

Our measures of the segmentation result, **Table 4.1**, provide validation for the use of manual techniques for our mouse airway tree segmentation. We have been able to show that there is a strong agreement between the three observers with κ values greater than 0.9 in all cases. In addition, we have calculated the percentage of true positives to be greater than 90%, while the percentage of false positives is less than 10%. The main discrepancy that existed between the segmentation results was in the peripheral regions of the airway trees where inter-observer variation occurred because the small structures became less

clearly defined and therefore were hard to identify. However, all of the airway segments that were then quantified and presented in this project were consistently identified by all observers. The differences that exist between Observer 1 and 2, Observer 1 and 3, and Observer 2 and 3 are visually represented in **Figure 4.2**, **Figure 4.3**, and **Figure 4.4**, respectively.

4.1.1.4 Airway Measurement

Airway measurements were completed on the manual airway segmentation results obtained from the *in vivo* micro-CT datasets. From observations of mouse airway casts and 3D renderings of the mouse airway tree from micro-CT datasets of the C57BL/6, A/J, and BALB/c inbred mouse strains it can be seen that the major airways in the mouse have nearly a zero bifurcation angle at the carina which is almost perpendicular to the central axis of the imaging plane. However, the mouse airway tree cannot be modeled as an object with a circular cross section due to the unique geometrical properties, dependent upon the inbred strain, which would not be represented under this assumption.

Therefore, an ellipse was fitted to the perimeter of each airway segment and the area, major and minor diameters, as well as the centroid were recorded with respect to the inner airway wall. The area and major and minor diameters were measured at 50% of the branch length for each of the identified airway branches. Five segments were averaged to give a mean value of these airway metrics relative to a position within the branch.

The branch length was defined as the length between two bifurcations. The start of the branch was specified at the airway segment of interest within the slice at an identified bifurcation and the end of the branch was specified at the airway segment of interest within the slice at the subsequent bifurcation. The length of the branch was measured between the centroids of the two airway segments of interest using the 3D Euclidean distance metric where the distance (D) between centroid 1 (with coordinates (X_1, Y_1, Z_1)) and centroid 2 (with coordinates (X_2, Y_2, Z_2)) was:

$$D = \sqrt{(X_1 - X_2)^2 + (Y_1 - Y_2)^2 + (Z_1 - Z_2)^2} \quad \textbf{4-4}$$

4.1.2 *Ex Vivo* Micro-CT Imaging

For each mouse that was imaged *in vivo*, the lungs were fixed at full inflation of 20 cmH_2O and were re-imaged on the micro-CT system. Processing of the resulting image data included conversion to a useable file format as outlined in section 4.1 and segmentation of the lung structures.

4.1.2.1 Lung Segmentation

The segmentation of the lung boundary in the fixed lung micro-CT scan was necessary for calculation of the fixed lung volume. This was performed using the AMIRA software program. The entire lung was segmented manually and a mask file was generated. The resulting voxels were summed to give a total volume and multiplied by the image resolution of 28 µm in all three dimensions.

4.1.2.2 *Ex Vivo* Airway Segmentation and Measurement for Comparison to the LIMA Images

Manual segmentation of the airways in the *ex vivo* micro-CT dataset was completed using an in-house built software program for lung image analysis, Pulmonary Analysis Software Suite (PASS). Only the airways that were common to both the micro-CT and corresponding LIMA images were segmented for validation of the airway measurements, section 4.6. The resulting segmentations were saved as binary image files as regions of interest.

Again, an ellipse was fitted to the perimeter of each airway segment and the area, major and minor diameters, as well as the centroid were recorded with respect to the inner airway wall. The area and major and minor diameters were measured for each of the identified airway segments common to both the *ex vivo* micro-CT and LIMA images.

4.2 LIMA Imaging

The high resolution bright field LIMA images—acquired sequentially from apex to the base of the mouse lung—contained 36 subtile images at 20x magnification that were stitched together to form one composite image. Likewise, each high resolution BFST LIMA image—acquired at three locations apex, mid, and base of the lung—contained 144 subtile images at 60x magnification that were also stitched together to form one composite image. The composite images were generated using an automated photomerge algorithm in Adobe Photoshop (Adobe Systems Inc, California). Once the composite images were created the image files were cropped to the same size so they could be treated as a 3D image stack.

Analysis of the LIMA images included identification of the lung structures within the LIMA datasets as well as comparisons of the lung structures visible between the micro-CT, LIMA, and histology images, section 4.5. In addition, airways common to both the *ex vivo* micro-CT datasets and LIMA datasets were segmented and measured for validation of the airway measurements, section 4.6.

4.3 Histology Imaging

Histology is the gold standard for evaluating microscopic anatomical structures, such as the cellular and tissue content, of organs. Unlike the anatomical mouse lung structures visible in the micro-CT images, such as the major conducting airways, the smaller airspaces including the alveolar ducts and alveoli cannot be evaluated based on the resolution limitation of the Micro-CAT II. Therefore, characterization of the smaller airspaces in the C57BL/6, A/J, and BALB/c inbred mouse strains was performed on the histology images.

Previous research presented the differences in these smaller airspaces of inbred mice and made an evaluation of the size based on the mean chord length of the airspaces, on formalin fixed lungs. It was found that within the sampled region of the left lung there

was a significant difference between the mean chord length of the C57BL/6, A/J, and C3H/HeJ inbred mice [36]. However, this was limited to a very small region of sampled lung and did not take into account the possible heterogeneity effects that could influence the mean chord length of the airspace in different strains of mice or from the left or right side of the same lung.

The mean chord length technique is a stereological measure for quantifying lung airspace. It is defined as:

$$MCLa = \frac{\sum_{i=1}^{n} CLairS_i}{n}, CLairS = \left\{ s \in CLair \middle| s \geq 8 \wedge s \leq 300 \right\} \quad \textbf{4-5}$$

We acquired approximately 35 histology slides for each lung that was sectioned and imaged on the LIMA system. The sampling process we initiated for the resulting slides involved splitting the lung into three regions of the lung: the apex, mid, and base. The middle four histology slides within each region were chosen as the samples for the airspace analysis of the apex, mid, and base regions. Within each region, the left and right sides were sampled separately. This allowed us to investigate if there were any regional differences in the small airspaces of the C57BL/6, A/J, and BALB/c mice. For each slide, three subtile images from the left side and three subtile images from the right side were collected. These subtile images were chosen at semi-random locations within the lung tissue while avoiding any large vessels or airways and were 1072 x 932 pixels in size with a resolution of 0.504 µm per pixel. This resulted in a total of 216 images analyzed for each strain.

Each image was analyzed for mean chord length of alveolar airspace in an automated program developed in Matlab (Mathworks, Massachusetts). This was performed by placing evenly spaced parallel test lines throughout each image at a spacing of 10 µm. The start and end of each airspace wall were identified as the inflection points

on the intensity curve along each test line. Logging the start and end of each wall intersected enables the calculation of the mean chord length of the airspace, **Figure 4.5**. A maximum and minimum chord length condition was included in the assessment of the mouse airspaces and was established empirically. The maximum chord length was established as 400 µm and the minimum was 8 µm. The minimum was set to avoid the influence of red blood cells or small pieces of torn tissue that could potentially skew the data. The maximum was established because there were no chords longer than 400 µm recorded. The resulting data included the mean chord length for the airspace calculated for each strain at the apex, mid, and base regions for the left and right lungs. In addition, the frequency chord length distributions for each strain at the apex, mid, and base regions for the left and right lungs was also compiled.

4.4 Multi-Modal Image Registration

Image registration is the process of transforming different image sets into a common coordinate system. This is useful because it provides a means to quantitatively compare image content extracted from different image sets with respect to the same region. In this research, 3D image registration was completed for the *ex vivo* micro-CT to the LIMA datasets. We also aligned each histology slice in 2D to its respective LIMA image. This was important to compare lung structures visible in the micro-CT and LIMA and verify the smallest structures resolvable using micro-CT, validate that the airway measurements from the micro-CT images were repeatable in images that were not generated through the use of reconstruction algorithms, and provide a direct correspondence between histology sections and micro-CT images of the same lung for future radiologic and pathologic comparisons.

There are many metrics utilized in image registration. Mutual information is a common technique for registering image datasets acquired through different modalities [68, 69]. It is based on the concept that between two image sets with regions of similar

tissue there exists a relationship between grey values that is measured from the entropy between images. For example, the mutual information, *I*, between two images (*A* and *B*) can further be defined as:

$$I(A,B) = H(A) + H(B) - H(B,A) \qquad \textbf{4-5}$$

where the first two terms, *H(A)* and *H(B)*, are the Shannon entropies of image *A* and *B* calculated from the probability distributions of the grey values in images *A* and *B*. The final term, *H(B,A)* is the joint entropy between images *A* and *B* [69]. This equation can be summarized as maximizing the mutual information in any two images relates to minimizing their joint entropy while still taking into account the entropies of the separate images.

The AMIRA software package was utilized to perform registration between the *ex vivo* micro-CT and LIMA datasets. The 3D registration was performed with a rigid affine transformation utilizing the normalized mutual information metric. To begin, the lung parenchyma was manually segmented from both datasets. This enabled the registration algorithm to focus on the lung boundaries and internal structures such as vessels and airways, rather than the high contrast heart and catheter. The input *ex vivo* micro-CT image dataset was set as the model and transformed to the reference LIMA image dataset. Once the *ex vivo* micro-CT dataset was registered, it was resampled, maintaining its original voxel dimensions, into the coordinate system of the LIMA dataset. Finally, the resampled *ex vivo* micro-CT dataset was exported as a series of 16bit 2D tiffs.

4.5 The Smallest Resolvable Lung Structures in Micro-CT

We had previously established that the resolution limitation for the Micro-Cat II system was 55 µm using a tungsten wire phantom. However, this was under ideal conditions where there existed high contrast between the wire and surrounding phantom

material and there were no motion artifacts [40]. Assuming that in a fixed lung we can eliminate motion and resolve structures down to 55 µm there is still uncertainty as to what anatomical structure in the mouse lung this would constitute. Unlike the human airway system that transitions from the terminal bronchioles→ respiratory bronchioles→ alveolar ducts → alveoli, the mouse airway system transitions very quickly from the terminal bronchioles→ alveolar ducts → alveoli. Since the mouse airways are thin walled structures it is hard to distinguish the terminal bronchioles from the alveolar ducts using micro-CT. Therefore, we have utilized the high resolution LIMA and BFST images to verify lung structures of the same size within the micro-CT that can be resolved.

Registration of the *ex vivo* micro-CT to the LIMA datasets provides a means for verification of the lung structures that can be resolved in our micro-CT images using the Micro-CAT II system. The bright field LIMA images provide depth and color information with a resolution of 10x greater than the micro-CT images in the x-y plane. However, due to the nature of the lung tissue, it is difficult to clearly recognize boundaries at high resolutions using the bright field LIMA images as a result of the depth of field inherent to the microscope. Therefore, we have also utilized the bright field segmentation tomography (BFST) images which increase the surface contrast of the lung tissue and produce clearer boundaries of lung structures, **Figure 3.9**. In addition, the same regions of interest from the corresponding histology images were selected to serve as the ground truth for the identification of airways with visible airway walls, alveolar ducts, or individual alveoli.

In order to make sure that the smallest structures resolvable in the micro-CT images were the same across the C57BL/6, A/J, and BALB/c mice, a region of interest from the registered micro-CT and LIMA images of each strain was chosen. These were identified based on an airway or vessel landmark that was discernable between the different image sets as the starting position and the images were zoomed into the same

magnification. Manual segmentation of multiple structures, which reached the observers' threshold for identification in the micro-CT image within the specified region of interest was completed and the same structures within the bright field LIMA and BFST LIMA were also segmented. The corresponding histology slice from the LIMA was utilized to verify that a structure of similar size was an airway (if it had a defined wall), alveolar duct, or alveoli.

For each of the three inbred strains investigated, it was found that no lung structure smaller than approximately 100 µm in diameter could be resolved in the *ex vivo* micro-CT scan. These structures were identified and confirmed using the registered LIMA images. However, not every 100 µm structure that was identifiable within the LIMA images could be defined in the corresponding micro-CT. This can be attributed to reaching the resolution limitation of the Micro-CAT II in combination with the partial volume effects. Due to the partial volume effects, the CT number for pixels containing structures smaller than the resolution limit would contain a mixture of both lung tissue and air. This would contribute to the blurred edges and inconsistent intensity of these small structures and explain why some are not distinguishable depending on their shape and where they were located.

From comparison of the registered micro-CT and LIMA mouse lung images we have concluded that the smallest structures we have identified are the alveolar ducts, **Figure 4.6** and **Figure 4.7**. From the BFST images, verified through histology, the alveolar ducts can be seen as the structures ranging between 100-200 µm and the alveoli can be visualized as the structures adjacent to the alveolar ducts and the tissue surrounding the ducts ranging between 30-45 µm. Comparing the registered BFST images to the micro-CT images at the same magnification, **Figure 4.7**, we have identified that some alveolar ducts are visible (yellow box) while no alveoli can be discerned. These structures could also potentially be terminal bronchioles (red box) transitioning into alveolar ducts. We have, based on the corresponding histology, identified both

alveolar ducts and terminal airways to be between 100-200 µm. However, the most "terminal" lung units we can define in the micro-CT images are alveolar ducts.

4.6 Micro-CT Airway Measurement Validation

The LIMA system was used to serve as the ground truth for the airway measurements made in the micro-CT images since it is not reliant upon reconstruction algorithms for generating the image data. We segmented the major conducting airways in the registered micro-CT and LIMA images and calculated the major diameters and minor diameters. The percentage error between the micro-CT and LIMA images of the segmented airway measurements was then calculated.

The smallest difference was found to be 8 µm, which was 0.5% error between the micro-CT and LIMA images. This would be equivalent to less than one pixel in the micro-CT image. The largest difference was found to be 124 µm, which was 7% error and equivalent to approximately four pixels in the micro-CT image. Overall, from the quantified small differences, **Table 4.2**, between the image data we can conclude that the micro-CT images can be used to extract accurate airway measures of the mouse lung. The variation seen between the airway measures in the LIMA and micro-CT images can be attributed to the differences in image content between the LIMA and micro-CT images and the manual observers' ability to clearly distinguish the airway boundaries within four pixels of the micro-CT dataset.

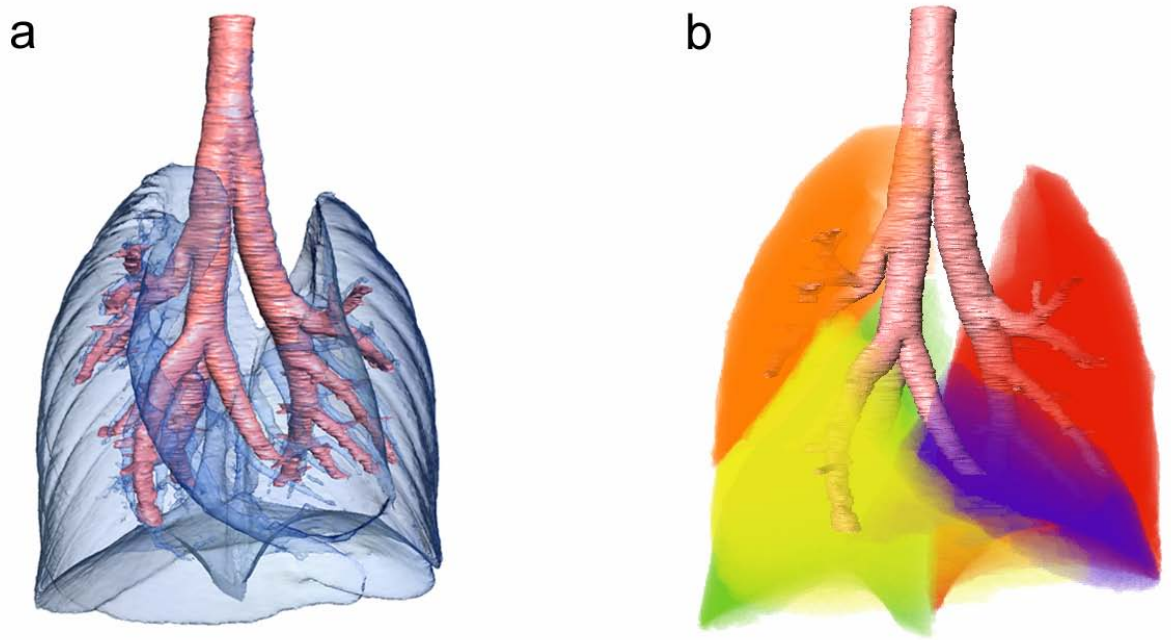

Figure 4.1: **3D Reconstruction of the mouse lung.** a) The entire lung is rendered including the airway tree. b) The individual lobes are color coded and rendered with the airway tree for separate visualization purposes.

	Obs.1 vs. Obs. 2	Obs. 1 vs. Obs. 3	Obs. 2 vs. Obs. 3
Region 1 (voxels)	226,682	310,139	250,623
Region 2 (voxels)	4,265,083	4,181,623	4,319,165
Region 3 (voxels)	392,742	388,165	334,366
K	0.932	0.923	0.936
TP	95.0%	93.1%	94.5%
FP	8.4%	8.5%	7.2%

Table 4.1: Comparison of the manual airway segmentation agreement between three observers.

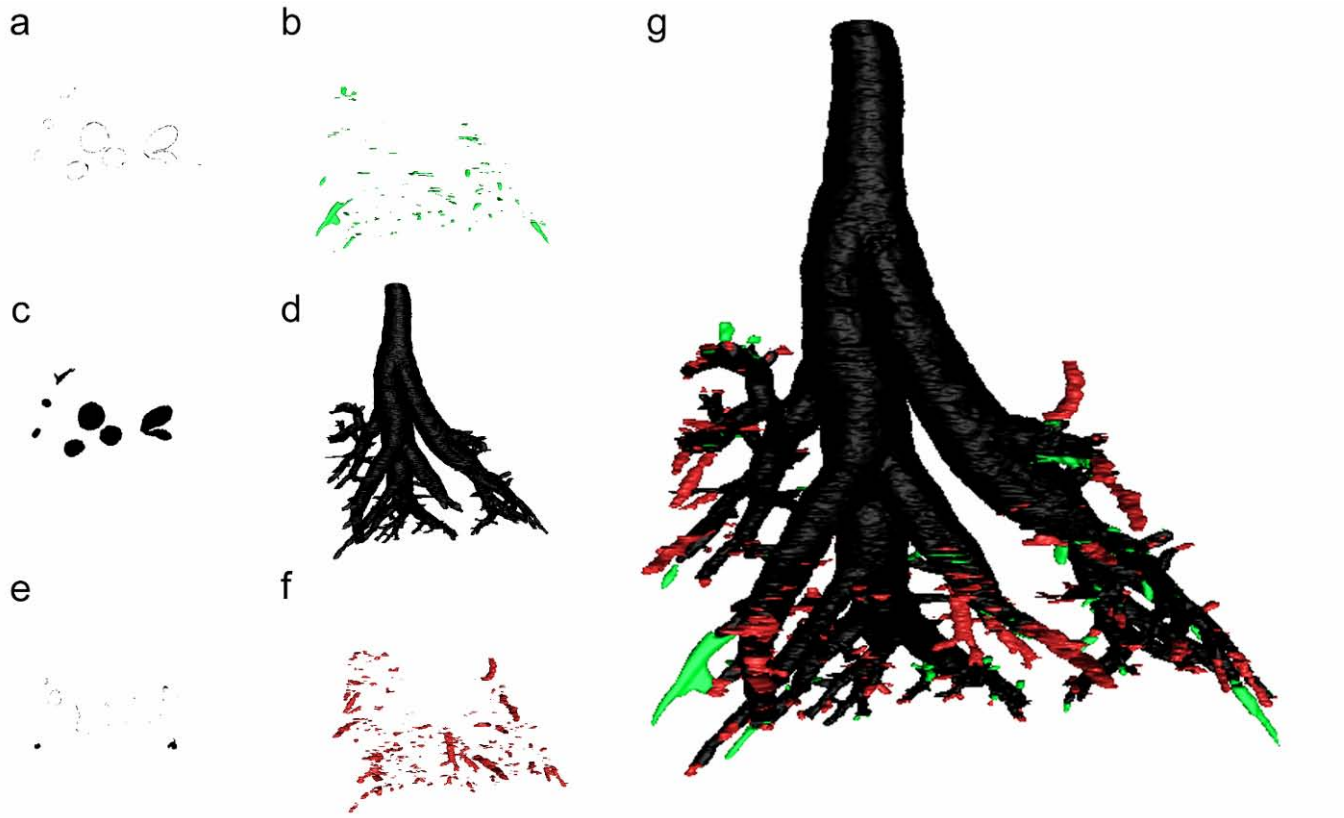

Figure 4.2: Observer 1 vs Observer 2 Airway Segmentation Validation. a) The region identified only by observer 1 on an individual 2D image. b) 3D reconstruction of region identified only by observer 1 over the entire micro-CT dataset. c) The region identified by observers 1 and 2 on an individual 2D image. d) 3D reconstruction of region identified by observers 1 and 2 over the entire micro-CT dataset. e) The region identified only by observer 2 on an individual 2D image. f) 3D reconstruction of region identified only by observer 2 over the entire micro-CT dataset. g) Overlap of all three regions

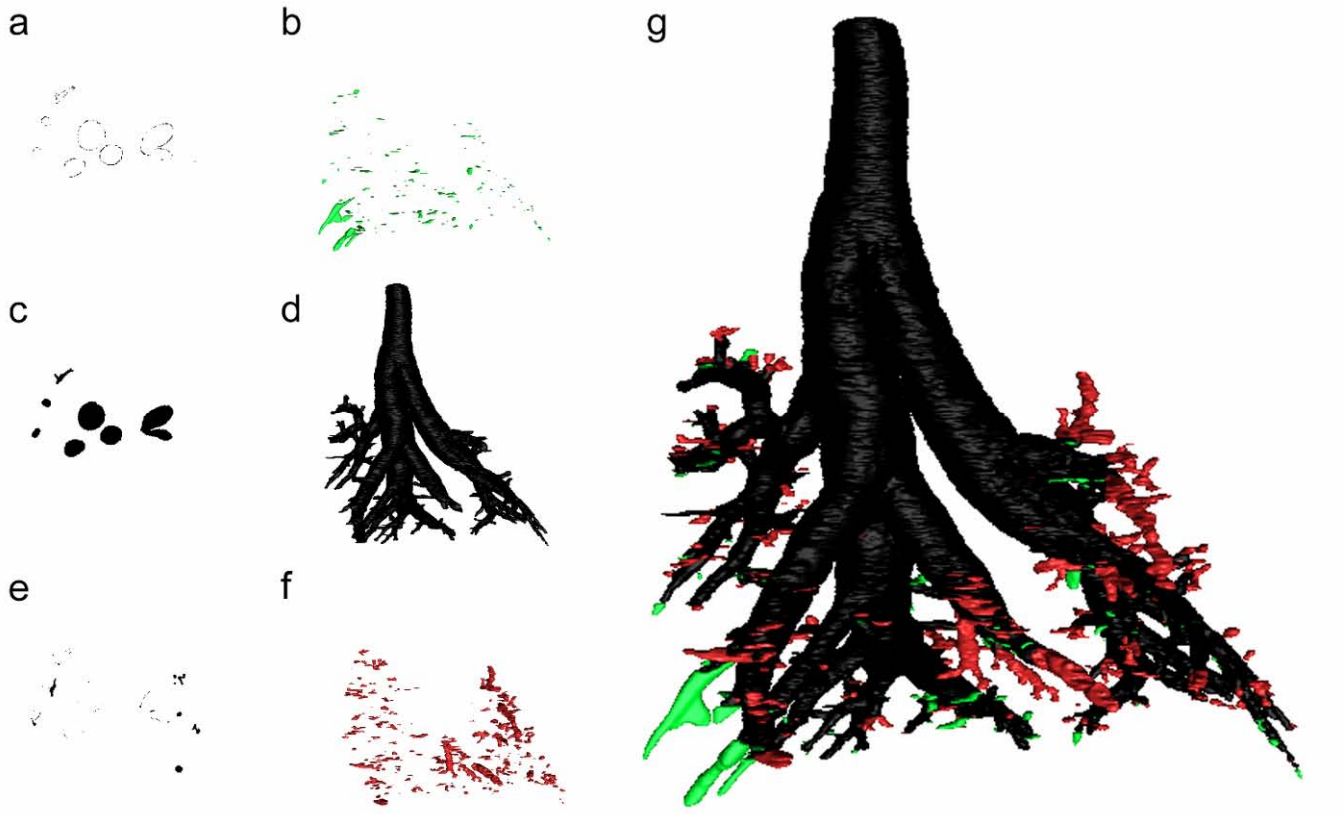

Figure 4.3: Observer 1 vs Observer 3 Airway Segmentation Validation. a) The region identified only by observer 1 on an individual 2D image. b) 3D reconstruction of region identified only by observer 1 over the entire micro-CT dataset. c) The region identified by observers 1 and 3 on an individual 2D image. d) 3D reconstruction of region identified by observers 1 and 3 over the entire micro-CT dataset. e) The region identified only by observer 3 on an individual 2D image. f) 3D reconstruction of region identified only by observer 3 over the entire micro-CT dataset. g) Overlap of all three regions.

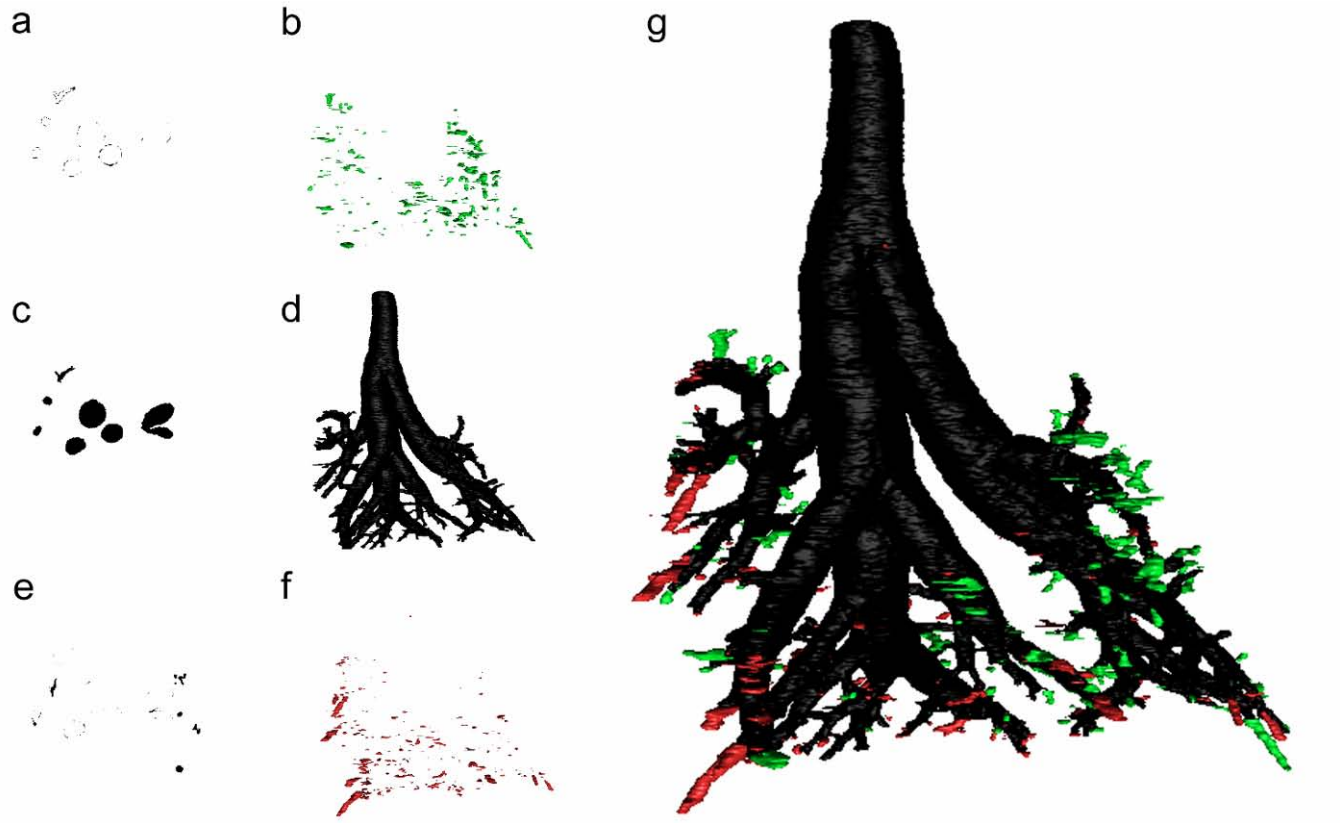

Figure 4.4: Observer 2 vs Observer 3 Airway Segmentation Validation. a) The region identified only by observer 2 on an individual 2D image. b) 3D reconstruction of region identified only by observer 2 over the entire micro-CT dataset. c) The region identified by observers 2 and 3 on an individual 2D image. d) 3D reconstruction of region identified by observers 1 and 3 over the entire micro-CT dataset. e) The region identified only by observer 3 on an individual 2D image. f) 3D reconstruction of region identified only by observer 3 over the entire micro-CT dataset. g) Overlap of all three regions.

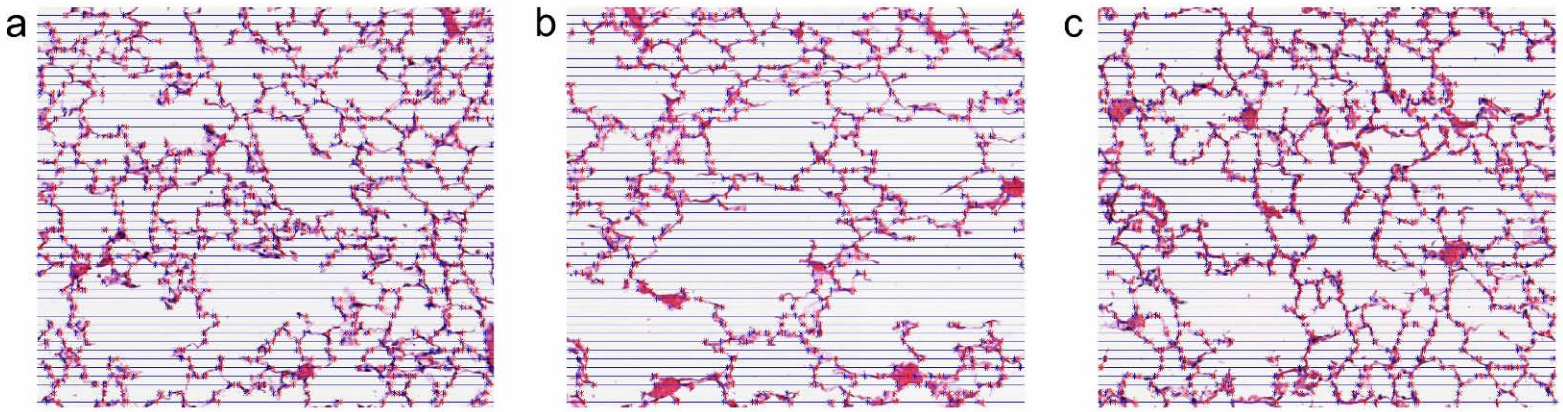

Figure 4.5: Histology subtile images with intercepts along the equally spaced test lines. The red markers indicate the start of a airspace and the blue markers indicate the end of an airspace. An example subtile image is given for each of the strains in a) C57BL/6, b) A/J, and c) BALB/c.

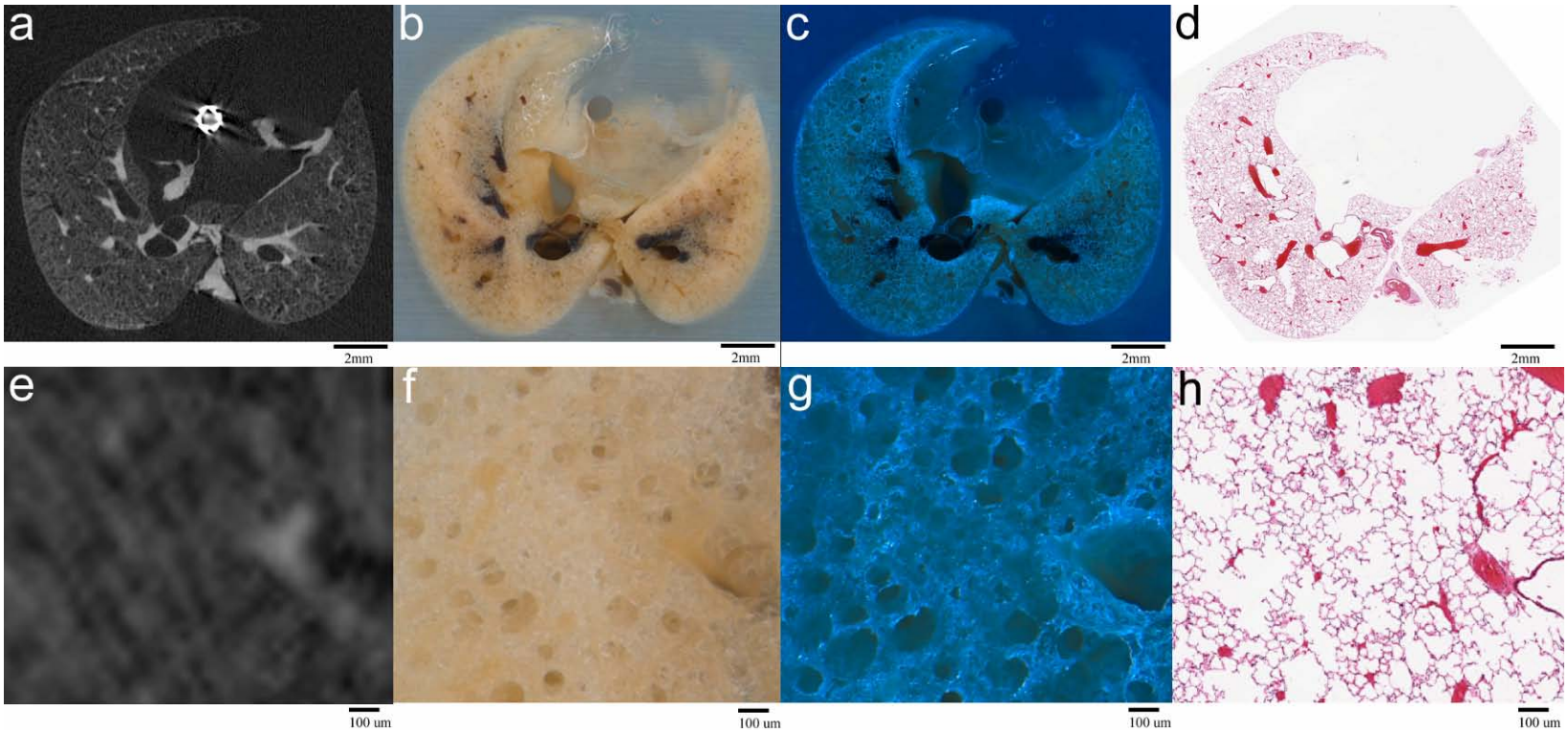

Figure 4.6: Registered *ex vivo* micro-CT, bright field LIMA, BFST LIMA, and histology of a BALB/c mouse lung. An example a) 2D slice of the registered *ex vivo* micro-CT image, b) corresponding bright field LIMA, c) BFST LIMA, and d) histology image. In addition a zoomed in region of interest is given for the e) *ex vivo* micro-CT from the right lung , f) corresponding bright field LIMA, g)BFST LIMA, and h) histology.

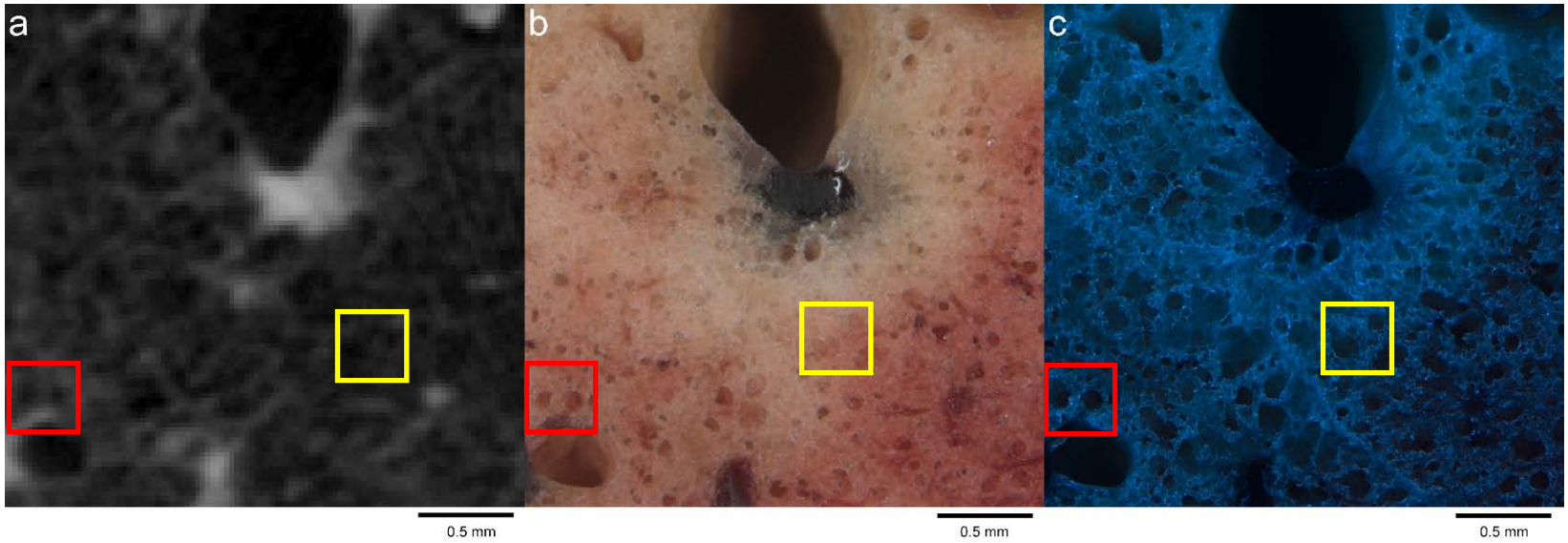

Figure 4.7: Region of interest from the registered *ex vivo* micro-CT, bright field LIMA, and BFST LIMA lung used to verify the smallest lung structure visible in micro-CT. An example of two structures visible in all three images is highlighted by the red and yellow boxes in a) the micro-CT, b) bright field LIMA, and c)BFST LIMA. The two structures within the red box were verified as terminal airways and the structure in the yellow box were verified as alveolar ducts in the BFST and histology images

	Slice Number	Airway Label	Measurements (mm)	
			Max. Diameter	Min. Diameter
	4	TRACHEA	1.939	1.201
	13	RMB2	1.753	1.500
		LMB1	1.599	0.912
LIMA	17	DiRMB3	1.251	0.917
		AzRMB3	1.137	0.819
	21	DiRMB5	0.983	0.594
		LMB5	0.681	0.437
	79	TRACHEA	1.880	1.110
	241	RMB2	1.629	1.528
		LMB1	1.607	0.940
Micro-CT	313	DiRMB3	1.234	0.873
		AzRMB3	1.162	0.769
	385	DiRMB5	0.961	0.585
		LMB5	0.629	0.475
Difference (% error)	4-79	TRACHEA	0.059 (3.0%)	0.091 (7.6%)
	13-241	RMB2	0.124 (7.0%)	0.028 (1.9%)
		LMB1	0.008 (0.5%)	0.028 (3.1%)
	17-313	DiRMB3	0.017 (1.3%)	0.044 (4.8%)
		AzRMB3	0.025 (2.1%)	0.050 (6.1%)
	21-385	DiRMB5	0.019 (1.9%)	0.009 (1.5%)
		LMB5	0.052 (7.6%)	0.038 (8.7%)

Table 4.2: Airway measurements between corresponding LIMA and micro-CT airway segments.

CHAPTER 5

LUNG PHENOTYPES IN THE C57BL/6, A/J, AND BALB/C INBRED MOUSE STRAINS

5.1 Mouse Airway Nomenclature

Development of a systematic nomenclature for labeling the airways is essential for anatomical investigation, comparative and quantitative analysis, as well as facilitating the interpretation of physiological studies based on the knowledge of lung structure. Existing methods include clinically relevant anatomical labeling schemes as well as numerical methods that are more appropriate for analysis of relationships between the number of branches, the radius of the branches, and path lengths in symmetrical versus asymmetrical dichotomous systems [35, 70-73]. In this section a background investigation into the development and application of these techniques will be laid out to create a foundation for the rationale and development of a new mouse airway nomenclature.

Historically, the bronchi have been labeled anatomically in order to aid clinicians in identifying and locating disease conditions that are localized to certain regions within the lung. For instance, bronchogenic carcinoma, which most commonly occurs in the lobar and segmental bronchi, produces characteristic patterns on chest radiographs that are based on their anatomical location [71]. In addition, other disease conditions are more likely to affect specific segmental bronchi such as aspiration pneumonia. This indicates the importance of having a naming system that can be used collectively among clinicians and researchers when making assessments based on airway location.

The nomenclature systems developed for the human airways include that of Jackson and Huber and Boyden [70, 71]. Both systems are based on division of the lobes into sub lobes and classifying the bronchial segments into the sub lobe regions in which they occupy. **Table 5.1**, shows the correspondence between the Jackson-Huber and

Boyden nomenclatures. The nomenclature system of Boyden, has been particularly useful in imaging applications of airway analysis since it is based on numbering of the bronchi from their lobe and sub lobe locations and it has thus been applied to an automated approach of locating and labeling the human airway tree [74].

The Boyden nomenclature is based on the three lobes of the right lung and the two lobes of the left lung in the human pulmonary system. The three right lobes are referred to as the right upper (RU), the middle lobe (ML), and right lower (RL); the two left lobes are the left upper (LU) and left lower (LL). These lobes are further broken down into sub lobe regions and the numbering of the bronchi corresponds to the anatomical positioning of the bronchi within these sub lobes [70]. **Figure 5.1**, shows the Boyden nomenclature applied to a schematic of the human airway tree and a table for numbering of the airways for the left and right sides of the lung. Although the development of the Jackson-Huber and Boyden nomenclatures have aided in classifying the anatomy of the human airways, it is still difficult to count the total number of airways and their generation number as the bronchial tree divides dichotomously and becomes more complex. Therefore, numbering approaches have been developed for the analysis of relationships between airway generation and the geometrical properties of the airways.

In 1963 Weibel published his analysis of the human bronchial tree [73]. In this work the author generated a resin cast and measured the airways completely up to generation 5 and incompletely up to the 10^{th} generation. Anything beyond the 10^{th} generation was then examined by conventional histological techniques. In order to successfully analyze the airway tree, a binary numbering scheme from the top down was developed, making the assumption that the airway tree follows a symmetric dichotomous branching pattern. In this model, if n is the generation number and n=0 at the trachea then the total number of branches at any given generation would be 2^n –with the assumption that each parent branch gave rise to two daughter branches of equal length and diameter. From this model, each bronchial segment could be labeled based on its location with

respect to the trachea (origin) and its generation [73]. The labels started with A—the reference to the origin or the trachea and were followed by an a or b at each generation. For instance, at the first generation (2^1) the two branches would be: Aa and Ab. **Figure 5.2**, shows the code for the branches for generations 0-3. The development of this system by Weibel and the resulting analysis greatly expanded the knowledge of the human lung structure and served as the basis for future research on the morphology of the human lung.

However there were still unanswered questions on certain assumptions made about the human lung structure and function, so in 1968 Horsfield and Cumming proposed a new method for numbering the airway tree in order to study the morphology and asymmetry of the bronchial tree in the human lung. Unlike Weibel, Horsfield and Cumming found the assumption of symmetrical dichotomy to be problematic because it did not group like with like in terms of the flow carried through the airways and it was therefore a poor means of classification of the branches from a functional point of view [72]. Although they still regarded the human bronchial tree as a dichotomously branching structure they wanted to incorporate the validity of asymmetry in their analysis of the morphology of the bronchial tree. Their new numbering technique of the airway tree, which allowed for asymmetry, was developed to order branches with similar function (size) by numbering the airway tree from the bottom upward. Utilizing this technique, an asymmetrical branching system became a symmetrical system with some branches missing, **Figure 5.3**. Therefore, asymmetrical systems that do not have the same branches on both sides of the lung are numbered in a way that branches similar in respect to structure and function are labeled with the same number.

The branching pattern of the airway tree has been a point of interest in the human for many generations; however, there are still many animals for which we do not have a concrete understanding of the airway structure. Direct application of the techniques used for labeling the human airways is not always practical for other mammalian species due

to variations in branching patterns including: trichotomy, polychotomy, and monopody. As research continues to utilize animal models, in particular mice, for studying human disease conditions in the lung it is also vital to have a useful nomenclature customized for the mouse airway tree.

Wallau et al. in 2000 created a nomenclature for the entire rodent mammalian order. The goal was to develop a nomenclature that described and classified rodent lungs in order to assess relationships between species using biological systematics (i.e. phylogenetic analysis). The new nomenclature of the bronchi and lung lobes was created to denote as many homologous structures as possible across multiple species. The author followed the rules that have been established for generating order numbers for branches stemming from bifurcations and trifurcations. Branches that exhibited a monopodial branching pattern were considered as stem bronchi with an order of zero and all the side branches that projected off of the stem were assigned an order of 1.

Labeling of bronchi was based on regional locations relative to the pulmonary artery and was broken up into two categories: the eparterial region and the hyparterial region. The eparterial region lies cranial to the point where the pulmonary artery crosses the stem bronchus and the hyparterial region lies caudal to the crossing. The bronchi were further classified based on being stem bronchi or row bronchi. The stem bronchi consist of one on the right and left side and traverse to the base of the lung. The row bronchi are modeled as a helical pattern around the stem bronchi and are labeled as lateral, dorsal, medial, and ventral, **Figure 5.5**.

Application of this nomenclature to the mouse airway tree revealed many drawbacks to using this technique for morphometric analysis. First and foremost the system only considers two main stems, one on the left lung and one for the four lobes of the right lung. The other branches which feed into the other lobes on the right lung are factored as row branches and compared with other row branches rather than main stems. This is problematic in morphometric studies because a comparison of branches with

similar structure and function is crucial and using this system would classify dissimilar branches as similar. Second, main stems do not have specific labels given to them in between row bronchi. Finally, no specified rules were given to deal with airways that branched after the first order bronchi.

Through visualization of the 3D airway tree from the three strains of mice analyzed in this work, it was clear that the mouse airway tree required a new nomenclature to allow for meaningful cross-correlative studies. Therefore, we developed a nomenclature specifically for the mouse airway tree, taking into account the accepted airway nomenclatures that exist, and developed an anatomically significant nomenclature that is a hybrid of the previous techniques and can be used for identification of the anatomical structures and comparative analysis to reveal intra-strain and inter-strain variability. In addition, the nomenclature has a numbering scheme built in to keep track of the generation number as well as anatomical position.

The normal mouse lung consists of four lobes of the right lung and a single left lung as seen in, **Figure 2.4**. Therefore, the labels for the airway segment of interest begin with an indicator of the lobe in which they occupy namely: Left (L), Apical (Ap), Azygous (Az), Diaphramatic (Di), and Cardiac (Ca). Due to the monopodial branching of the mouse airways a main bronchus (MB) stem was assigned to traverse to the base of each lobe. For instance, in the Apical lobe the Apical Right Main Bronchus (ApRMB) traverses to the base of the lobe, **Figure 5.5**. The first generation of bronchi (B) that offshoot from the lobar main bronchus are split into divisions denoted by capital letters such as A, B, and C, and preceded by the letter B indicating a bronchi as opposed to MB for the main bronchus. For example, the first offshoot from ApRMB2, would be labeled as ApRBA3, where this segment is from the Right Apical lobe (ApR), it is a bronchi (B) and is the first offshoot (A). In addition, it is the 3rd generation from the trachea. Divisions off of these bronchi are further distinguished by assignment of a lower case letter a,b,c. For example, the first division off ApRBA3 would be labeled ApRBA4a,

where this refers to the Right Apical lobe (ApR), it is the first offshoot bronchi (BA) and the first division (a). Here we can see that the generation number is 4, and its location in the label is now fixed after the first offshoot (BA). The next generation is labeled using roman numerals such as i, ii, and iii. For example, the first sub division off ApRBA4a would be labeled ApRBA5ai. In all segments, the assigned number represents the generation of that segment with respect to the pathway from the trachea which is defined as generation 0. An example of the nomenclature applied to a mouse airway schematic is shown in **Figure 5.5**. **Table 5.2** represents the label, anatomical name, and generation number, through the fourth generation, for the labels that are depicted in the schematic.

This nomenclature is sufficiently expandable for the current capabilities of *in vivo* micro-CT imaging as utilized in this work. However, with further development and improvement in the resolution of such imaging systems, this nomenclature may need to be adapted to allow for previously indiscernible airways in addition to extension of the number of generations that are then visible.

5.2 *In Vivo* Lung Characterization

As described in section 3.2 *in vivo* micro-CT imaging was performed at three positive airway pressures (PAP) (10, 20 & 30cmH_2O) on each mouse strain. Two groups of mice were scanned to obtain the datasets used in this work. The first group was scanned at 20 cmH_2O with an n=3 per strain, while the second group of mice was scanned at 10, 20 and 30 cmH_2O with an n=3 per strain. In total there are six *in vivo* micro-CT scans at 20 cmH_2O and three at 10 and 30 cmH_2O for each mouse strain.

5.2.1 Mouse Airway Tree Phenotypes

Segmentation of the airway tree from the C57BL/6, A/J, and BALB/c mice has been performed using the image processing techniques described in section 4.1. Visualization of these airways in 3D is important and has revealed the distinct branching pattern in the mouse lung. Through the use of such 3D models we have developed an

appropriate mouse airway nomenclature, section 5.1, in order to make quantitative comparisons across inbred mouse strains at multiple PAP's.

5.2.1.1 Qualitative Assessment

The lung in the C57BL/6, A/J, and BALB/c inbred mouse strains we investigated contained a single left lung and four lobes in the right lung as previously reported. These mouse strains were also confirmed to exhibit a monopodial airway branching pattern that feeds the right and left lungs. Each lobe is fed by a main stem that traverses to the base of the lobe. Side branches can be identified off of these main stems and are most prominent in the Diaphragmatic lobe and the Left lung where motion artifact is not as significant as in the Azygous and Cardiac lobes due to their close proximity to the heart. Using the *in vivo* micro-CT datasets, identification of airways down to 200 µm can be made, where we believe this is the transition point into terminal bronchioles. However, such identification, as discussed in section 4.5, was not reliable for each airway path and quantitative assessment has been limited to structures no smaller than 500 µm. Using the *in vivo* datasets we have also confirmed that the mouse airway tree quickly diverges from large airways (main bronchi) to small airways (terminal bronchioles) in a non-dichotomous fashion within a few generations. In addition, we know that the terminal bronchioles do not transition into respiratory bronchioles. Instead, the terminal bronchioles feed straight into the alveolar ducts. This has also been confirmed using the *in vivo* to *ex vivo* mouse lung acquisition techniques as detailed in section 4.5. This fast transition further increases the difficulty to reliably identify airway paths between 200-500 µm.

Visually, a substantial difference is observed in the airway dimensions between the C57BL/6 mouse strain and the A/J and BALB/c mouse strains, **Figure 5.6**. The main bronchi in the C57BL/6 display enlarged regions around points where the branches split whereas the main bronchi in the A/J and BALB/c do not seem to exhibit the same

characteristics. Also, from qualitative assessment of the 2D transverse images of the main bronchi in the C57BL/6 mouse, the airways appear significantly larger.

5.2.1.2 Quantitative Assessment

In addition to qualitative assessment of the airway tree, quantitative measurements at three PAP's of 10 (n=3), 20 (n=6), and 30 (n=3) cmH_2O for each mouse strain have also been made as described in section 4.1.1.4. Tabulated values for the area, major and minor diameters, and branch length for the C57BL/6, A/J, and BALB/c strains at the three PAP's have been compiled and reported, **Table 5.3**, **Table 5.4**, and **Table 5.5**. This is the first comprehensive report of mouse airway metrics (encompassing both central and peripheral) using *in vivo* imaging techniques [39].

To visualize the trends in the data tabulated in **Table 5.3**, **Table 5.4**, and **Table 5.5**, plots were generated using a 'pathway' approach where each graph represents measurements at each PAP for multiple generations leading to an endpoint/branch segment. For example, **Figure 5.7(a)** represents the relationship of mean airway area versus generation for the DiRMB path in the C57BL/6 mouse strain. This plot includes the right main bronchus for generation one and two (RMB1, RMB2), the Diaphragmatic lobe segments including DiRMB3, DiRMB4, DiRMB5, DiRMB6, and finally the end of the measured path-DiRMB7. Plots for each metric, including major and minor diameters and branch length have also been compiled for this path as shown in **Figure 5.7(b-c).** In addition, plots for all of the measured paths (RMB, ApRMB, AzRMB, CaRMB, DiRMB, DiRBA, DiRBB, DiRBC, DiRBD, LMB, LBA, LBB, LBC, LBD) for each strain at 10-30 cmH_2O PAP's have been compiled and included in Appendix A, figures A1-A36.

C57BL/6 Airway Evaluation

The mean area measurements of the C57BL/6 strain confirm the 'bulging' pattern of the airways in the right and left lungs as initially identified through the qualitative assessment. As presented in Appendix A figures A1-A3 there is an increase in the mean

airway area from RMB1 to RMB2 and LMB1 to LMB2 at all three PAP's of 10, 20, and 30 cmH_2O. Also, on the right side of the lung this change in size is greater between 10 and 20 cmH_2O, when compared to the change between 20 and 30 cmH_2O. This trend is only observed between the first and second generation. While generation 3, 4, 5, and 6 on the right lung exhibit a greater increase between 20 and 30 cmH_2O. The left side differs from the right where there is a smaller increase in area between 10 and 20 cmH_2O and a larger increase in area between 20 and 30 cmH_2O from generations 2 to 4. This suggests there is a difference in the airway distensibility of the left and right lungs at these measured PAP's.

In both the right and left lungs the smallest airways measured, which include DiRMB7, DiRBD7, and LBD5, do not reach a plateau and the airway dimensions (area, major and minor diameter, Appendix A figures A4-A12) continue to decrease. This is to be expected as we have not measured the terminal airways due to the resolution limit of the micro-CT scans.

Finally, the trend for branch length measurements does not appear to have as a dramatic difference with respect to the airway pressure at each generation as does the area and diameter values.

A/J Airway Evaluation

In contrast to the C57BL/6 there is a decrease in mean airway area from RMB1 to RMB2 as seen in Appendix A figure A13(a). This trend follows our visual assessment where there does not appear to be any 'bulging' of the airway regions. However, in the left lung, we do observe an increase between LMB1 to LMB2, although not as dramatic as in the C57BL/6 strain. Through the qualitative assessment this observation was not apparent and further emphasizes the importance of quantitative assessment.

In the A/J strain, in both the left and right lungs the trends for the pathways indicate that there is a limiting increase in mean airway area past 20 cmH_2O. This can be seen in Appendix A figures A13-A15 where there exists a substantial increase in the

mean airway area between 10 and 20 cmH_2O, while there is only a small difference between 20 and 30 cmH_2O. This indicates that the airways cannot be distended significantly past the 20 cmH_2O positive airway pressure. This is an important observation, and could potentially be used to define the total lung capacity of the mouse lung, a variable which is debated [33] and currently unknown. In addition, the total lung capacity of the mouse lung may be dependant upon the strain as this relationship varies in the results found here.

Similar to the C57BL/6 the trend for branch length measurements does not appear to have a dramatic difference with respect to the airway pressure at each generation as does the area and diameter values.

BALB/c Airway Evaluation

Similar to the A/J but in contrast to the C57BL/6, the airway measurements for the BALB/c inbred mouse strain as seen in Appendix A figure A25(a) reveals a decrease in mean airway area in the right lung between RMB1 and RMB2. This trend is also confirmed by our visual assessment where no enlarged airway regions appear. However, similar to both the C57BL/6 and A/J strains, there is an increase in mean airway area between LMB1 and LMB2, Appendix A figure 27(c). This increase in the BALB/c strain is not as dramatic as the C57BL/6 strain, however it is an important finding that is missed through visual inspection.

In the BALB/c strain, in both the left and right lungs the trends for the pathways indicate that there is a greater increase in mean airway area between 10 and 20 cmH_2O than between 20 and 30 cmH_2O. This limited increase that was also observed in the A/J indicates that the airways cannot be distended significantly past the 20 cmH_2O positive airway pressure. However, unlike the A/J strain, the BALB/c has a different rate of change between the 20 and 30 cmH_2O for the DiRMB pathway at generation 3 and 4. Here there is a greater increase in mean area between 20 and 30 cmH_2O when compared to 10 to 20 cmH_2O. This is a counterintuitive observation, as it indicates an increase in

compliance. This is likely due to the error in measuring the major diameter using the manual segmentation approach from airways that may not be perpendicular to the imaging plane. It also appears that, like both the C57BL/6 and A/J strains, the trend for branch length measurements is not as dramatic with respect to the airway pressure at each generation.

Statistical Analysis

Linear mixed model analysis was used to compare mean airway measures (area, major and minor diameters) among the 3 strains at PAP's of 10, 20, and 30 cmH_2O. The fixed effects in the model were strain, PAP, generation, and strain*PAP interaction. A significant strain*PAP interaction indicates that the magnitude of differences among the strains varies significantly with PAP level. Thus, pairwise mean comparisons between strains have to be tested at each level of PAP. This was done using test of mean contrasts with the p-values adjusted using Bonferroni's method to account for the number of tests performed (i.e. 3 pairwise mean comparisons between strains at 3 PAP levels = 9 tests). This analysis was performed for the main bronchus pathways of each lobe. The mean (SE) estimates and results of the test of the strain comparisons at each of the lung lobes are shown in **Table 5.6** for area, **Table 5.7** for major diameter, and **Table 5.8** for minor diameter.

Significant differences were found for multiple main bronchi pathways in certain lung regions between the C57BL/6 inbred strain and both the A/J and BALB/c strains. For instance, at 10, 20, and 30 cmH_2O the CaRMB pathway of the C57BL/6 was significantly different ($p < 0.001$) for area, major, and minor diameters compared to both the A/J and BALB/c strains. In addition, the RMB pathway of the C57BL/6 was significantly different ($p < 0.0002$) for area and major diameter compared to the A/J and BALB/c strains. However, there were no significant differences found for the RMB pathway of the C57BL/6 compared to the A/J and BALB/c strains based on the minor diameters. This indicates that the major diameter measure is more sensitive to the

'bulging' region which is non-circular. The DiRMB and LMB pathways for the C57BL/6 were also found to be significantly different ($p < 0.05$) compared to the A/J and BALB/c strains.

No significant differences ($p > 0.99$) were found between the A/J and BALB/c strains at 10, 20, or 30 cmH_2O for the airway measures of area, major, or minor diameters. Also, there were no significant differences detected for any of the PAP's between the three strains in the ApRMB and AzRMB pathways.

5.2.1.3 Interstrain Airway Distensibility

Due to the significant differences found in the mean airway measures between the inbred mouse strains under investigation at each airway pressure, an analysis of the rate of change or the distensibility of the airways from 10-30 cmH_2O was investigated. Distensibility was defined for the airways as:

$$D = \frac{\Delta A}{\Delta P} \quad , \qquad \textbf{5-1}$$

where ΔA is the change in area for the change in pressure ΔP.

We measured and graphed the distensibility in both the left main bronchus and right diaphragmatic lobe bronchus, **Figure 5.9 (a-b)**. In the left lung we measured distensibility for the 6 generations of LMB and found that the C57BL/6 has a greater distensibility for generations 1-6 than the BALB/c and A/J inbred mouse strains. The difference in distensibility was the greatest at generation 2 with 0.058 mm^2/cmH_2O for the C57BL/6 and 0.022 mm^2/cmH_2O and 0.033 mm^2/cmH_2O for the A/J and BALB/c respectively. Distensibility of the BALB/c airways was found to be greater than the A/J airways in generations 1-3, while distensibility of the A/J airways was greater than the BALB/c for generations 5 and 6. On the right lung we measured the distensibility for the 5 generations of DiRMB and again found that the C57BL6 has a greater distensibility for generations 1-5 than the BALB/c and A/J mice. The difference in distensibility was the

greatest at generation 2 with 0.070 mm^2/cmH_2O for the C57BL/6, and 0.020 mm^2/cmH_2O and 0.025 mm^2/cmH_2O for the A/J and BALB/c respectively. Distensibility of the BALB/c airways was found to be greater than the A/J airways in generations 1-4, while distensibility of the A/J airways was greater for generation 5.

5.2.2 Mouse Lung Volumes

The mouse lung was segmented to assess the total lung volumes at the multiple PAP's using the techniques described in section 4.1.1.1. In addition, the four right lobes and the single left lung were segmented, **Figure 5.8** and the lobe volumes were calculated for the C57BL/6, A/J, and BALB/c mouse strains.

5.2.2.1 Total Lung Volume

The mean total lung volumes for the C57BL/6, A/J, and BALB/c mouse strains were calculated at 10, 20, and 30 cmH_2O PAP, using the techniques described in section 4.1.1.1. At 10 cmH_2O the mean lung volumes (SE) for the C57BL/6, A/J, and BALB/c mice were 844.7 (57.0) µL, 831.8 (77.5) µL, and 897.3 (39.1) µL, respectively. As the PAP increased to 20 cmH_2O the total volume of the lungs of the C57BL/6, A/J, and BALB/c mice increased to 992.5 (39.7) µL, 965.5 (50.2) µL, and 1152.5 (62.5) µL. At the final PAP of 30 cmH_2O the C57BL/6, A/J, and BALB/c were 1356.1 (27.8) µL, 1332.6 (61.3) µL, and 1738.3 (54.4) µL, respectively as shown in **Figure 5.10**. This finding reveals a substantial rate of increase in the lung volume with respect to PAP for the BALB/c with respect to both the C57BL/6 and A/J mice. However, there does not appear to be a distinguishable difference between the A/J and C57BL/6 strains, as confirmed by the literature measuring the pressure and volume relationship at multiple airway pressures [30].

Statistical Analysis

A linear mixed model analysis was used to compare the mean total lung volumes among the three strains at the PAP's of 10, 20, and 30 cmH_2O. The fixed effects in the

model were strain, PAP, and strain*PAP interaction. A significant strain*PAP interaction indicates that the magnitude of differences among the strains varies significantly with PAP level. Thus, pairwise mean comparisons between strains have to be tested at each level of PAP. This was done using test of mean contrasts with the p-values adjusted using Bonferroni's method to account for the number of tests performed (i.e. 3 pairwise mean comparisons between strains at 3 PAP levels = 9 tests). A significant difference ($p < 0.005$) was observed at the PAP of 30 cmH_2O between the BALB/c strain and both the C57BL/6 and A/J inbred strains. There were no significant differences observed for the PAP's of 10 and 20 cmH_2O.

Since a difference in body weight was observed between the A/J (25.1 ± 0.71 g) mice at 20-22 weeks old as compared to the C57BL/6 (29.5 ± 0.05 g) and BALB/c (30.9 ± 1.53 g) mice we made the assumption that body weight and lung volume were linked. With this assumption the lung volumes were normalized with respect to body weight, **Figure 5.11**.

We again performed a linear mixed model analysis to compare the mean normalized total lung volumes among the three strains at the three PAP levels studied. The fixed effects in the model remained the same and were strain, PAP, and the strain*PAP interaction. The linear mixed model analysis showed a significant strain*PAP interaction effect ($p=0.0003$). The mean lung volume differences among the strains were significantly larger at the PAP of 30 cmH_2O, where we found significant differences among the strains. The normalized mean lung volume of the C57BL/6 versus the BALB/c was significant ($p< 0.005$). Although there was a significant difference between the mean total lung volumes of the A/J and BALB/c ($p > 0.003$), the differences in the normalized mean lung volumes of the A/J vs. the BALB/c was not significant ($p > 0.05$). If the assumption of body weight has a link to total lung volume then the significant difference between the A/J and BALB/c of the non-normalized mean total lung volumes may have been due to the difference in size of the animals. There were still

no significant differences between the C57BL/6 and A/J strains ($p>0.05$). In addition, there were no significant differences in the normalized mean total lung volumes among the strains at PAP of 10 and 20 cmH_2O. The mean lung volume (SE) estimates and results of the test comparing the strains are shown, **Figure 5.11**.

Table 5.9 compiles the body weight, lung, and lobe volumes that have been calculated from the lungs of the C57BL/6, A/J, and BALB/c inbred mouse strains.

5.2.2.2 Lobe Volumes

The mean lobe volumes were calculated for the C57BL/6, A/J, and BALB/c inbred mouse strains at the single PAP of 20 cmH_2O using the techniques described in section 4.1.1.1. The left lung in all three strains comprised of the greatest mean volume with a total of 326.7 µL, 300.9 µL, and 396.5 µL for the C57BL/6, A/J, and BALB/c respectively. The right lobe with the greatest mean volume in all three strains was the Diaphragmatic with 284.7 µL, 294.8 µL, and 296.3 µL for the C57BL/6, A/J, and BALB/c respectively. The total mean volume of the right lobes combined for the three strains were 665.8 µL, 664.5 µL, and 755.9 µL for the C57BL/6, A/J, and BALB/c respectively.

Statistical Analysis

A comparison of the mean lobe volumes among the strains was completed using a one-way ANOVA followed by Tukey's test for the pairwise comparison of means between the strains. The comparison revealed that no significant differences ($p>0.05$) were found between the Azygous, Diaphragmatic, or Cardiac lobes in all three strains. However in the Apical lobe a significant difference was found between the A/J (135.1 µL) and BALB/c (208.1 µL) mice ($p< 0.05$). In addition, a significant difference ($p< 0.05$) in the left lung between the A/J (300.9 µL) and BALB/c (396.5 µL) mice was also found. **Figure 5.12** graphs the lobe volumes and compiles the mean lobe volume and the results of the pairwise comparisons.

5.2.3 Pulmonary Function Testing

Pulmonary function tests were carried out on a subset of mice investigated in this work (n=3 per strain) as described in section 3.2.2. Mean values for the resistance (R) and compliance (C) were obtained using a custom flexivent script which performed the appropriate pulmonary function tests six times per mouse prior to micro-CT imaging. Mean and standard deviations for each mouse strain have been compiled and presented in **Table 5.10**. In addition, compiled values from the Mouse Phenome Database (MPD) for lung function have also been included in **Table 5.10** for comparison.

As seen from this data, the values obtained using the *flexivent* sytem prior to imaging are not consistent with the values found in the MPD. There are several variables that differ between the acquisition of these values. In the empirical data obtained in this work, we used mice that were 20-22 weeks of age vs 12-14 weeks used in the MPD. Also, we performed the pulmonary function tests on a SCIREQ *flexivent* computer controlled ventilator, while the MPD data was obtained using an un identified possibly in-house built system. Furthermore, the pulmonary function tests were performed as an adjunct to the *in vivo* imaging, and hence were executed on the same long length of inspiratory and expiratory tubing needed for the imaging ventilation. Although the *flexivent* system is calibrated for tube resistance and compliance prior to the tests, the increase in tube length reduces the sensitivity and increases our error. Finally, we performed the pulmonary function tests on a subset of mice with an n=3 per strain, while the MPD data was averaged from 12-16 mice per strain. With this in mind, we will make some observations based on our sensitive imaging results with respect to the MPD lung function data.

The reported difference in resistance between the C57BL/6, A/J and BALB/c are not statistically significant, which is counter intuitive to our anatomical results where there is a significant difference between the C57BL/6 airway dimensions compared to the A/J and BALB/c. We would expect from our airway measures that the C57BL/6 mouse

strain would show a lowered respiratory resistance. However, there maybe significant peripheral airspace differences in the C57BL/6 compared to the A/J and BALB/c mice that may account for the discrepancy between central airway dimensions and respiratory resistance.

The reported compliance for the C56BL/6 is significantly lower than the A/J mouse strain while no significant difference is found with the BALB/c mouse strain. However, from the airway distensibility measures obtained in this work as presented in section 5.2.1.3, the C57BL/6 strain has a significantly higher distensibility as compared to both the A/J and BALB/c strain. Again this seems counterintuitive that the pulmonary function tests do not follow the same order as those determined using the airway distensibility values. However, the compliance measure obtained using pulmonary function tests would also incorporate the influence of the parenchyma tissue. This suggests that there is a difference in the peripheral airspace between these inbred mouse strains.

5.3 *Ex Vivo* Lung Characterization

5.3.1 Airway Wall Composition

To investigate the 'bulging' regions of the central airways found in the C57BL/6 mice, a series of H&E histology slides were assessed for differences in airway wall composition. The tissue types we were interested in comparing included, airway epithelium, cartilage, and smooth muscle.

We located tissue sections for the C57BL/6, A/J, and BALB/c strains that contained the left and right main bronchi where the greatest difference in size was observed (RMB2 and LMB2). Within these histology samples, there were no apparent differences between the epithelium and cartilage among the strains. However, there were obvious visual differences in the amount of smooth muscle surrounding the airway lumen. This is clearly seen in **Figure 5.13**. Previous analysis of the airway smooth

muscle in the C57BL/6, A/J, and C3H/HeJ mice investigated the smooth muscle content only in a sample of the trachea. It was found that the C57BL/6 mice had less tracheal smooth muscle than the A/J and C3H/HeJ strains [75]. This indicates that the smooth muscle composition varies between strains within regions of the airway tree. Additional analysis quantifying the amount of smooth muscle within the 'bulging' region of the airway tree compared to other airway regions such as the trachea needs to be completed with special consideration to the tissue sampling and preparation, orientation of sections, staining, and image analysis techniques applied [76].

5.3.2 Airspace of the Peripheral Lung

The mean chord length was calculated for each strain using the automated image processing and analysis techniques described in section 4.3. A total of 648 images were analyzed (n=3 per strain), representing subtiles from the apex, mid and base of the right and left lung. **Table 5.11** represents the compiled chord length data for this study. The mean chord length was the greatest in the A/J (48 ± 2.55 µm) strain compared to the C57BL/6 (39 ± 1.74 µm) and BALB/c (39 ± 1.80 µm). This commonly used metric is best described as an indicator of peripheral airspace size. We were not able to detect differences in the chord lengths throughout different regions of the lung, and this may be expected as they are quadrupeds and the effects of gravity would be negligible on such a small lung. In a previous study by Soutiere, et al a significant difference between the size of chord length for the A/J was also found when compared to the C57BL/6 [36]. However the BALB/c was not assessed in their study.

In addition to the mean chord length for each mouse, the distribution of chord lengths at the apex, mid, and base for the left and right lung, as well as the overall distribution for the left and right lung has also been compiled and presented in **Figure 5.14**-**Figure 5.21**. A difference in the frequency of the chord lengths from both the right and left lungs can be seen across the mouse strains. In particular, there exist a greater

number of chords between 10-70 µm in size for the C57BL/6 and BALB/c when compared to the A/J strain. This indicates that the A/J mice have less peripheral airspace structures in the range of 10-70 µm. Since this is the range we would expect mouse alveoli to fall within, this suggests fewer alveoli within a specified area in the A/J as compared to the C57BL/6 and BALB/c mice. In addition the frequency of chord lengths greater than 70 µm, is greater for the A/J than the C57BL/6 and BALB/c strains. Although the difference is small, the ratio between the strains over this region is significant (as discussed below). We believe these differences indicate that the A/J strain has a greater proportion of alveolar ducts vs. alveoli when compared to the C57BL/6 and BALB/c strains. A similar trend is also observed in the BFST images where there is a clear difference in the number of alveoli vs. alveolar ducts in each field of view, **Figure 5.22**.

Statistical Analysis

A generalized logistic model fitted using the generalized estimating equations (GEE) method was used to compare the distribution of chord lengths among the 3 strains (C57BL/6, A/J, and BALB/c). Chord lengths were divided into 3 intervals, <10, 10-65, and ≥70, with the outcome measure being the chord length category. Since the observations comprised of chord lengths from the same animal, the GEE analysis was used to account for the correlation of chord lengths from the same animal. This analysis was performed for each of the 2 sides (right and left) and 3 regions (apex, mid, and base). The strain comparisons are based on the odds of having chord length ≥70 µm relative to chord length <10 µm, and chord length 10-65 µmrelative to chord length <10 µm, with the pairwise differences between strains expressed as odds ratios. **Table 5.12** gives the percentage distribution of chord lengths and the odds ratios (95% confidence limits) for the pairwise strain comparisons. For all the regions, there was a significantly greater proportion of ≥70 µm chord lengths in the A/J strain compared to BALB/c and C57BL/6. There was no significant difference between BALB/c and C57BL/6.

5.4 Implications for the Anatomical Lung Phenotypes of the C57BL/6, A/J, and BALB/c Inbred Mouse Strains

Phenotyping the lung function in the mouse has revealed strain specific differences between parameters such as lung volumes, compliance of the lung, respiratory system resistance, and ventilatory responses [26, 27, 29, 30, 77-79], to name a few. However, as reported by Reinhard et al., there have been no reports that show obvious evidence that any one strain exhibits the smallest or largest values for lung function phenotypes [26]. In addition, there has been an increased interest in the role that interstrain variation in lung morphology may play in lung function. We have, through our developed techniques for imaging the mouse lung, uncovered significant differences in lung structure that may play a substantial role in understanding the lung function in the normal mouse. Phenotype characterization of the lung structure within three normal inbred mouse strains has further confirmed that the "normal mouse lung" consists of a spectrum of characteristics. We have in this body of work focused on the differences in the structural lung phenotypes in three of the most commonly utilized mouse strains. Our findings lead us to believe that just as lung function varies between other strains, lung structure varies among those strains.

The differences in airway structures revealed in this work could potentially indicate variable functional requirements of the normal mouse lung between inbred mouse strains. For instance, if we take into account the conflicting requirements for movement of gas down the bronchial tree and the diffusion of gas across the alveolar capillary membrane, as stated by Horsfield, we find that as the airway cross sectional area and volume increases the resistance to flow would decrease. However, with an increase in the volume of the conducting airways there is a decrease in the volume that is available for gas transfer (dead airspace). Therefore, if we assume that the functional requirements for a normal mouse lung to be the same across the inbred strains, we would expect that the C57BL/6 inbred mouse strain, which has an increase in airway volume, would also

have a larger overall lung volume compared to the A/J and BALB/c mice. However, this is not the case as shown in this work. In fact, the BALB/c strain has a significantly larger lung volume compared to the C57BL/6 strain while the A/J strain shows no significant difference. This finding suggests that there could be a significant difference in the functional requirements of the lung across strains, and/or there are significant parenchyma differences that account for the airway / lung volume difference. In this study we have seen that there are significant differences in the parenchyma across these mouse strains, however they do not necessarily correlate to airway or lung volume.

In addition, it has been reported that the C57BL/6 strain has a significantly increased respiratory rate compared to both the A/J and BALB/c strains [29]. The C57BL/6 strain has a respiratory rate of 163.2 breaths/min, while the A/J and BALB/c have respiratory rates of 144.6 breaths/min and 148.2 breaths/min, respectively. Again this leads us to believe there are other factors that need to be investigated in order to make stronger correlations between the structure and function relationships.

The C57BL/6 mouse strain was found to have larger airways in several of the main pathways **Table 5.3-Table 5.5** and an increase in distensibility in the left LMB pathway and the right DiRMB pathway as compared to the BALB/c and A/J strains. This would suggest that there exists a significant difference between the composition of the airway wall in the airways of the C57BL/6 strain. Through investigation of the histology it seems that there are certain regional differences in the amount of smooth muscle surrounding the airway lumen between these inbred mouse strains. The C57BL/6 appears to have an increase of smooth muscle, which seems counterintuitive considering the airways were found to be more compliant. Further investigation of the amount, distribution and orientation of smooth muscle between the different strains of mice must be performed.

The variation of lung function parameters for both normal and diseased mice has been evaluated using pulmonary function tests [27]. These lung function parameters can

include lung volume, lung elascticity and airway resistance. In this work we have measured such parameters using the *flexivent* system. Comparison of measured resistance (R) and compliance (C) using the *flexivent* data with airway metrics obtained through the imaging approach has revealed that there may not be a direct relationship between structure and function. This may be due to the limitation in the sensitivity of the measurement equipment on small samples such as the mouse lung. However in either case, further investigation into the relationship between structural and functional measurements for evaluation of normal and diseased conditions in the mouse lung needs to be undertaken.

Using the BFST imaging system, a difference in the peripheral airspace between the three strains of mice was identified, where the A/J strain appeared to have more alveolar ducts in any one field of view when compared to the BALB/c and C57BL/6 mice. This observation was further confirmed through the corresponding histology where a significant difference between the frequency of the airspace chord lengths greater than 70 µm was found. The chord length analysis was performed excluding large airways (including terminal) and vessels. In addition, it has been reported, and we have confirmed through our BFST and histology imaging, that alveoli in the mice range from 30-50 µm. Therefore, this strongly suggests that the observed analytical difference in the mean chord lengths greater than 70 µm are due to an increase in the number of alveolar ducts in the A/J mouse. Again, these structural differences could play a role in the variation in lung function that has been detected between these inbred mouse strains.

Finally, the structural variations we have identified in the normal mouse lung are important during development of new respiratory disease models in the mouse. In addition, investigation into the genetic basis of disease may be further advanced through our characterization of the normal lung phenotypes identified within this body of research.

Jackson-Huber	**Boyden**
Right upper lobe	
Apical	B1
Anterior	B2
Posterior	B3
Right middle lobe	
Lateral	B4
Medial	B5
Right lower lobe	
Superior	B6
Medial basal	B7
Anterior basal	B8
Lateral basal	B9
Posterior basal	B10
Left upper lobe	
Upper division	
Apical-posterior	B1,B3
Anterior	B2
Lower (lingular) division	
Superior lingular	B4
Inferior lingular	B5
Left lower lobe	
Superior	B6
Anteriormedical	B7,B8
Lateral basal	B9
Posterior basal	B10

Table 5.1: The nomenclature developed by Jackson-Huber and the corresponding nomenclature developed by Boyden.

Source: R. B. George, *Chest Medicine: Essentials of Pulmonary and Critical Care Medicine*, 2000.

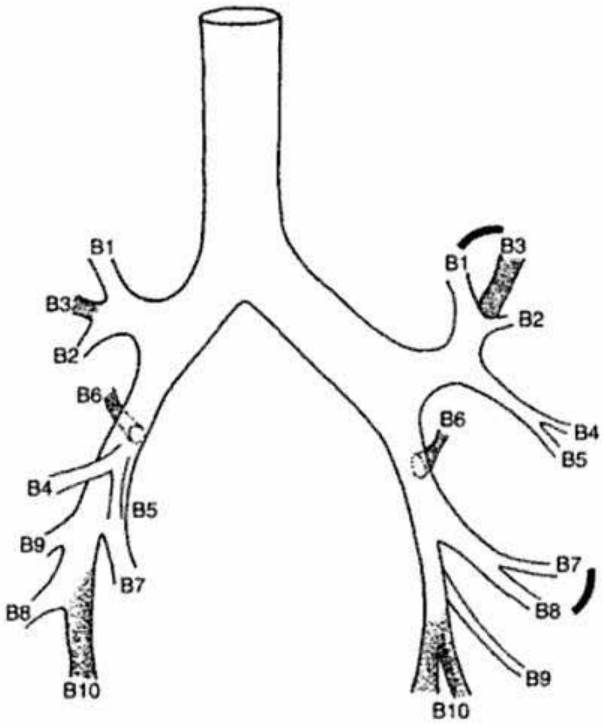

Right	Left
B1. apical	B1. apicoposterior
B2. posterior	B2. apicoposterior
B3. anterior	B3. anterior
B4. lateral	B4. superior
B5. medial	B5. inferior
B6. apical	B6. apical
B7. medial basal (cardiac)	B7. (omitted)
B8. anterior basal	B8. anterior basal
B9. lateral basal	B9. lateral basal
B10. posterior basal	B10. posterior basal

Figure 5.1: Bronchial tree diagram showing Boyden nomenclature. The bronchial tree schematic is labeled using the Boyden system where the main segments are numbered from apex to base. The numbers are given to bronchi feeding into the right and left lungs and signify the anatomical location of the segments within the lobe the bronchi.

Reproduced from Boyden. 1955 [70].

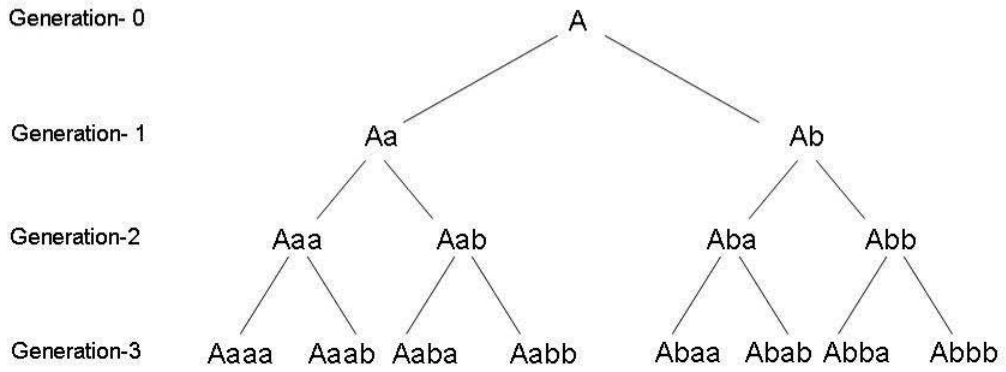

Figure 5.2: Weibel airway labeling for generations 0-3. The binary scheme developed by Weibel for labeling the airways allows for comparative analysis between different airway structures under the assumption of a symmetric dichotomous branching structure.

Reproduced from Weibel. 1963 [73].

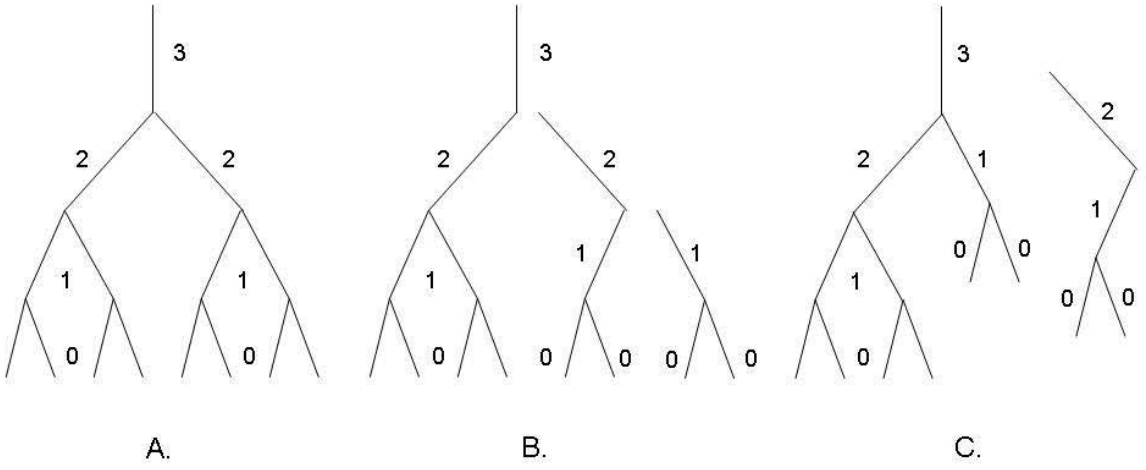

Figure 5.3: Branching diagrams numbered with technique by Horsfield and Cumming. The reverse numbering method of Horsfield and Cumming (bottom up) demonstrating the numbering of a symmetrical and asymmetrical dichotomy. a) A simple structure with dichotomous symmetrical branching. b) An example where a portion of the airway tree has been removed with the same numbering sequence. c) The resulting asymmetrical dichotomous tree remains labeled for comparison of similar airway segments.

Reproduced from Horsfield and Cumming. 1968 [72].

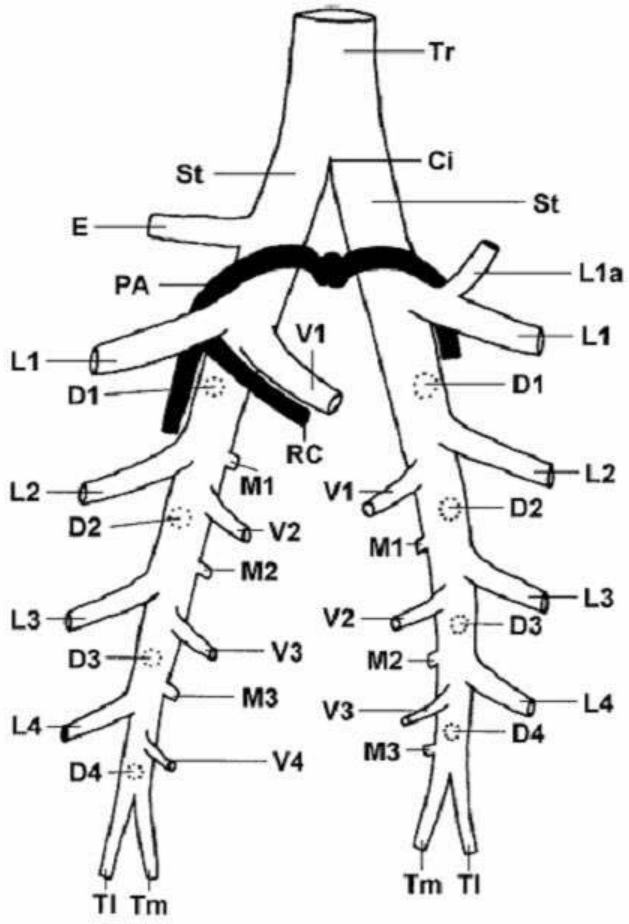

Figure 5.4: Rodent airway schematic with Wallau nomenclature. The airways have been labeled to classify similar structures of the airways between different species of rodent. The nomenclature is based on two main stems traversing to the left and right lungs with lateral branches being labeled in a helical fashion with respect to their position anatomically including: medial, dorsal, lateral, and ventral.

Reproduced from Wallau. 2000 [35].

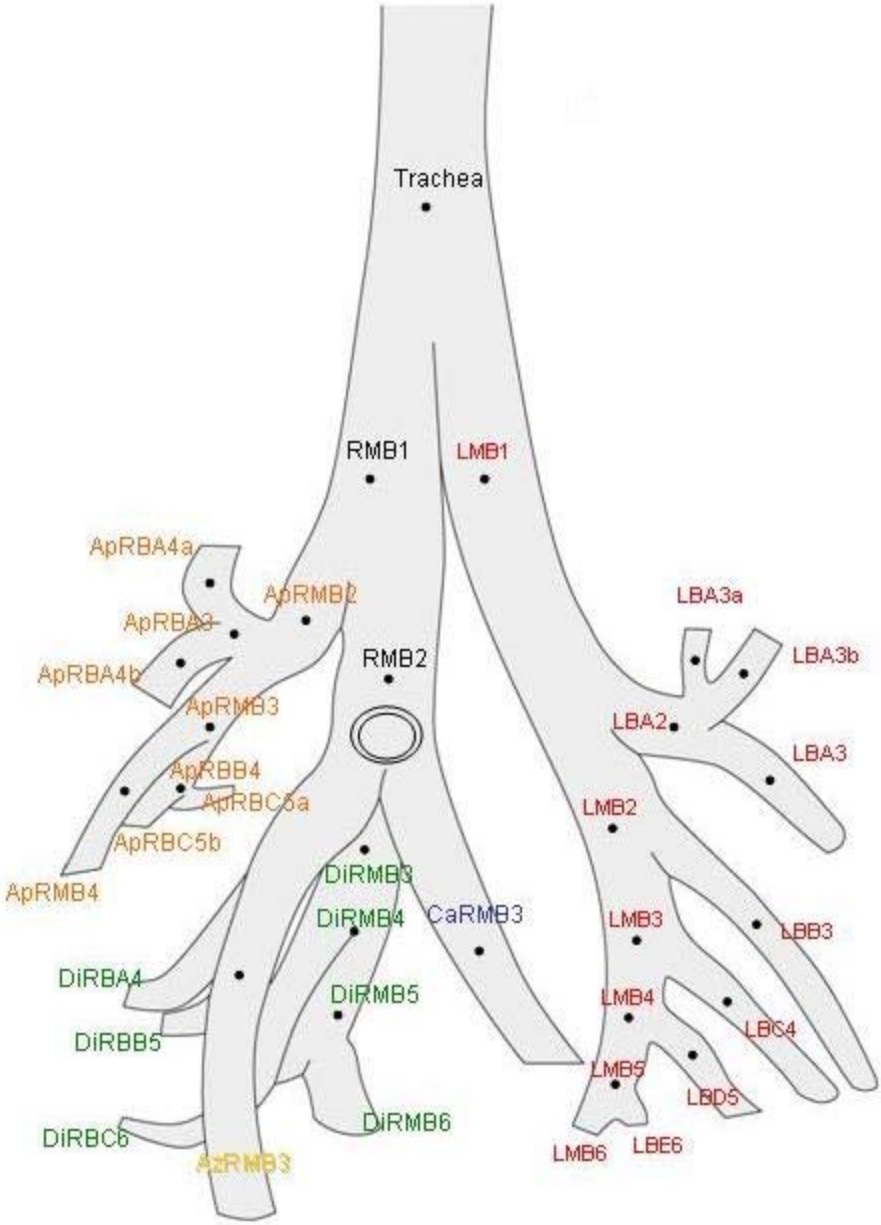

Figure 5.5: Mouse airway schematic with Thiesse nomenclature. The nomenclature specific to the mouse airway tree is labeled with a single main stem for the left lung and four main stems feeding each lobe of the right lung. Lateral branches off of each main stem are labeled with respect to the main stem from which they originate. Inclusion of generation number allows for comparative analysis of airway metrics within and across subjects.

Label	Anatomical Name	Generation
Trachea	Trachea	0
LMB1	Left Main Bronchus	1
LBA2	Left Bronchus First Division	2
LBA3a,b,c	Left Bronchus First Division Sub Branches	3
LMB2	Left Main Bronchus	2
LBB3	Left Bronchus Second Division	3
LMB3	Left Main Bronchus	3
LBC4	Left Bronchus Third Division	4
LMB4	Left Main Bronchus	4
RMB1	Right Main Bronchus	1
ApRMB2	Apical Lobe Right Main Bronchus	2
ApRBA3	Apical Lobe Right First Division	3
ApRBA4a,b	Apical Lobe Right First Division Sub Branches	4
ApRMB3	Apical Lobe Right Main Bronchus	3
ApRBB4	Apical Lobe Right Second Division	4
ApRMB4	Apical Lobe Right Main Bronchus	4
RMB2	Right Main Bronchus	2
DiRMB3	Diaphramatic Lobe Right Main Bronchus	3
DiRBA4	Diaphramatic Lobe Right First Division	4
DiRMB4	Diaphramatic Lobe Right Main Bronchus	4
CaRMB3	Cardiac Lobe Right Main Bronchus	3
AzRMB3	Azygous Lobe Right Main Bronchus	3

Table 5.2: Breakdown of the Thiesse nomenclature including the airway label, the full anatomical name, and the corresponding generation number.

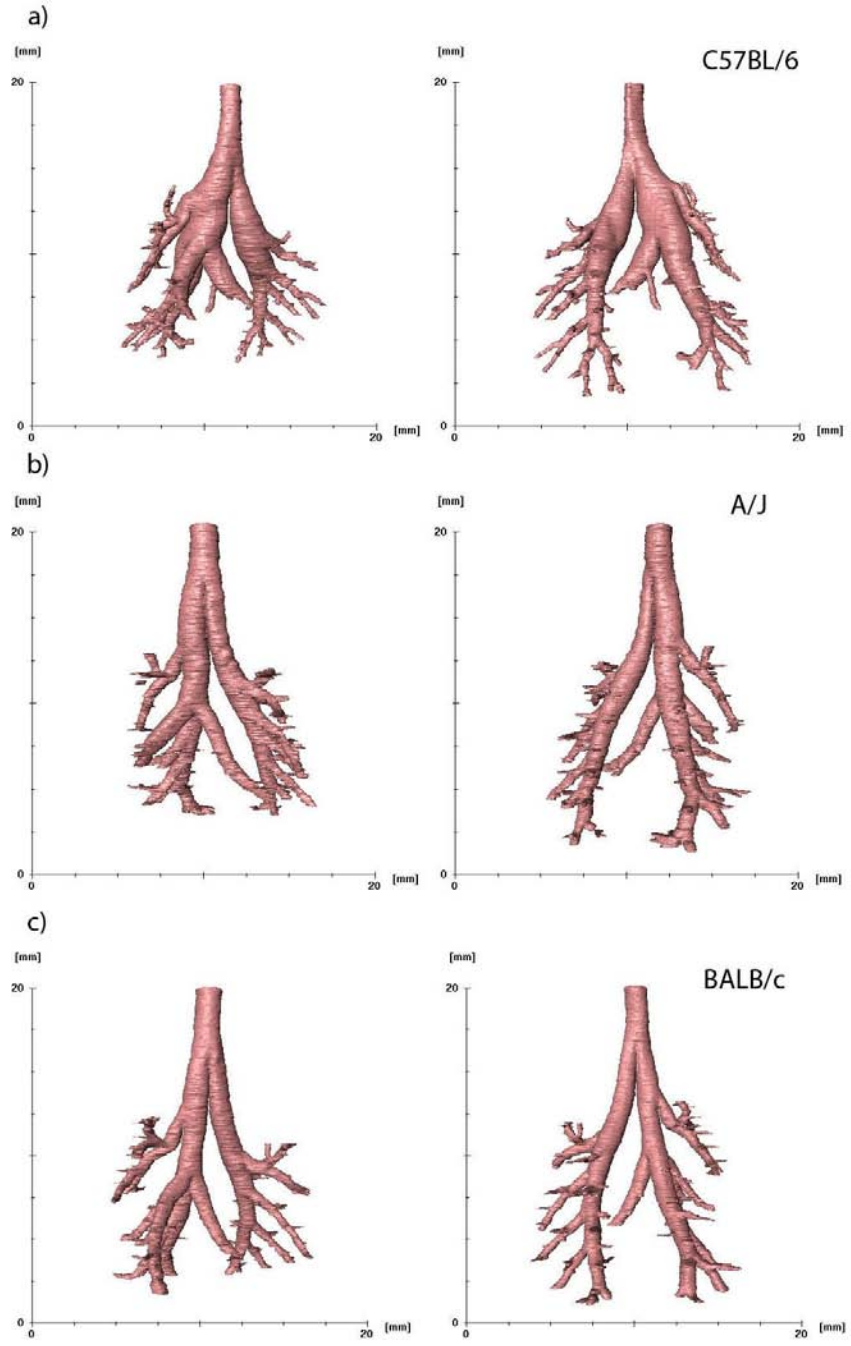

Figure 5.6: Anterior and posterior views of 3D airway rendering for the C57BL/6, A/J, and BALB/c inbred mouse strains. A difference in the size of the airway lumen can be visually detected for the a) C57BL/6 inbred mouse strain compared to the b) A/J and c) BALB/c strains.

Strains	**C57BL/6**			**A/J**			**BALB/c**		
Airway Measures (mm)	*Area*	*Diameter (Maj/Min)*	*Branch Length*	*Area*	*Diameter (Maj/Min)*	*Branch Length*	*Area*	*Diameter (Maj/Min)*	*Branch Length*
Trachea	1.877 ± 0.054	1.824 ± 0.107/ 1.313 ± 0.069	--	1.854 ± 0.356	1.618 ± 0.174/ 1.450 ± 0.132	--	1.524 ± 0.201	1.485 ± 0.097/ 1.303 ± 0.087	--
RMB1	3.440 ± 0.756	2.277 ± 0.346/ 1.910 ± 0.154	3.258 ± 0.130	1.988 ± 0.842	1.689 ± 0.318/ 1.451 ± 0.387	3.562 ± 0.698	1.865 ± 0.280	1.685 ± 0.111/ 1.408 ± 0.168	3.118 ± 0.508
RMB2	4.061± 0.789	2.376 ± 0.263/ 2.162 ± 0.198	1.953 ± 0.251	1.671 ± 0.298	1.508 ± 0.131/ 1.403 ± 0.134	3.224 ± 0.077	1.333 ± 0.094	1.380 ± 0.090/ 1.230 ± 0.024	3.024 ± 0.462
ApRMB2	--	--	--	0.581 ± 0.242	0.945 ± 0.201/ 0.758 ± 0.181	0.599 ± 0.297	0.809 ± 0.127	1.102 ± 0.073/ 0.932 ± 0.085	0.519 ± 0.254
ApRMB3	0.681 ± 0.052	1.102 ± 0.084/ 0.788 ± 0.031	1.711 ± 0.366	0.512 ± 0.109	0.968 ± 0.177/ 0.674 ± 0.059	1.569 ± 0.089	0.499 ± 0.080	0.943 ± 0.083/ 0.673 ± 0.079	1.863 ± 0.313
ApRMB4	0.233 ± 0.009	0.588 ± 0.022/ 0.504 ± 0.040	1.677 ± 0.590	0.234 ± 0.114	0.692 ± 0.211/ 0.418 ± 0.084	1.293 ± 0.476	0.205 ± 0.046	0.577 ± 0.072/ 0.449 ± 0.046	1.767 ± 0.129
AzRMB3	1.101 ± 0.416	1.403 ± 0.292/ 0.980 ± 0.168	3.132 ± 0.676	1.108 ± 0.314	1.475 ± 0.175/ 0.946 ± 0.160	1.669 ± 0.779	0.937 ± 0.089	1.295 ± 0.090/ 0.921 ± 0.050	1.789 ± 0.078
AzRMB4	--	--	--	0.840 ± 0.270	1.224 ± 0.241/ 0.862 ± 0.111	--	--	--	--
CaRMB3	1.458 ± 0.257	1.494 ± 0.170/ 1.237 ± 0.074	1.594 ± 0.352	0.682 ± 0.110	1.032 ± 0.038/ 0.839 ± 0.106	1.209 ± 0.136	0.792 ± 0.096	1.113 ± 0.080/ 0.903 ± 0.047	1.551 ± 0.044
CaRMB4	--	--	--	0.529 ± 0.070	0.885 ± 0.067/ 0.759 ± 0.052	1.400 ± 00.900	--	--	--
DiRMB3	2.833 ± 0.440	2.226 ± 0.328/ 1.619 ± 0.019	2.320 ± 0.264	1.456 ± 0.187	1.450 ± 0.121/ 1.276 ± 0.074	1.665 ± 0.240	1.514 ± 0.267	1.622 ± 0.327/ 1.192 ± 0.032	2.090 ± 0.251

Table 5.3: Airway measurements at 10 cmH_2O for the C57BL/6, A/J, and BALB/c strains.

DiRMB4	2.373 ± 0.341	2.292 ± 0.324/ 1.318 ± 0.069	1.970 ± 0.157	1.150 ± 0.156	1.305 ± 0.118/ 1.120 ± 0.086	1.918 ± 0.138	1.350 ± 0.349	1.617 ± 0.454/ 1.068 ± 0.047	1.787 ± 0.077
DiRMB5	1.822 ± 0.393	1.868 ± 0.235/ 1.244 ± 0.205	1.432 ± 0.240	0.856 ± 0.116	1.133 ± 0.094/ 0.959 ± 0.054	1.748 ± 0.311	1.262 ± 0.502	1.467 ± 0.333/ 1.074 ± 0.179	1.420 ± 0.218
DiRMB6	1.040 ± 0.124	1.423 ± 0.068/ 0.928 ± 0.067	1.440 ± 0.157	0.470 ± 0.087	0.824 ± 0.074/ 0.722 ± 0.078	1.647 ± 0.093	0.551 ± 0.057	0.905 ± 0.057/ 0.773 ± 0.035	1.322 ± 0.155
DiRBA4	0.532 ± 0.132	1.043 ± 0.266/ 0.650 ± 0.027	1.153 ± 0.819	0.479 ± 0.158	0.945 ± 0.150/ 0.634 ± 0.116	1.188 ± 0.562	0.454 ± 0.023	0.902 ± 0.024/ 0.640 ± 0.031	0.658 ± 0.253
DiRBB5	0.669 ± 0.180	1.237 ± 0.330/ 0.689 ± 0.002	0.714 ± 0.467	0.584 ± 0.126	0.981 ± 0.080/ 0.756 ± 0.122	--	0.469 ± 0.067	0.938 ± 0.086/ 0.635 ± 0.032	0.371 ± 0.186
DiRBC6	0.409 ± 0.032	0.858 ± 0.074/ 0.607 ± 0.029	1.479 ± 0.380	0.300 ± 0.053	0.786 ± 0.105/ 0.484 ± 0.023	1.310 ± 0.485	0.296 ± 0.052	0.698 ± 0.070/ 0.538 ± 0.052	1.732 ± 0.361
DiRBD7	0.360 ± 0.017	0.853 ± 0.018/ 0.536 ± 0.016	0.954 ± 0.454	--	--	--	0.219 ± 0.037	0.600 ± 0.095/ 0.465 ± 0.015	1.491 ± 0.074
LMB1	1.757 ± 0.278	1.713 ± 0.250/ 1.305 ± 0.020	4.637 ± 0.235	0.892 ± 0.445	1.203 ± 0.231/ 0.905 ± 0.311	5.645 ± 1.026	1.036 ± 0.157	1.265 ± 0.116/ 1.040 ± 0.069	5.150 ± 0.371
LMB2	3.704 ± 0.071	2.736 ± 0.099/ 1.725 ± .0031	2.518 ± 0.115	1.547 ± 0.229	1.465 ± 0.098/ 1.340 ± 0.107	1.896 ± 0.227	1.585 ± 0.122	1.593 ± 0.225/ 1.275 ± 0.096	2.263 ± 0.101
LMB3	1.730 ± 0.247	1.852 ± 0.231/ 1.194 ± 0.151	1.557 ± 0.120	0.929 ± 0.066	1.143 ± 0.081/ 1.034 ± 0.000	1.732 ± 0.326	1.010 ± 0.104	1.263 ± 0.195/ 1.024 ± 0.065	1.942 ± 0.176
LMB4	1.085 ± 0.237	1.346 ± 0.249/ 1.022 ± 0.093	2.133 ± 0.053	0.747 ± 0.048	1.067 ± 0.049/ 0.891 ± 0.020	1.914 ± 0.240	0.813 ± 0.133	1.126 ± 0.212/ 0.923 ± 0.021	1.774 ± 0.098
LMB5	0.837 ± 0.231	1.498 ± 0.535/ 0.724 ± 0.052	1.315 ± 0.122	0.522 ± 0.100	0.948 ± 0.076/ 0.697 ± 0.080	1.548 ± 0.245	0.737 ± 0.089	1.188 ± 0.148/ 0.798 ± 0.131	1.326 ± 0.195
LMB6	0.391 ± 0.186	0.922 ± 0.362/ 0.526 ± 0.074	0.927 ± 0.202	0.228 ± 0.062	0.637 ± 0.067/ 0.453 ± 0.076	1.260 ± 0.642	0.379 ± 0.158	0.737 ± 0.183/ 0.636 ± 0.122	1.044 ± 0.050

Table 5.3: Continued.

LBA2	--	--	--	--	--	--	--	--	
LBB3	0.518 ± 0.200	1.163 ± 0.266/ 0.551 ± 0.132	1.514 ± 0.933	0.493 ± 0.138	1.119 ± 0.229/ 0.555 ± 0.137	--	0.407 ± 0.112	0.930 ± 0.148/ 0.555 ± 0.096	0.450 ± 0.189
LBC4	0.473 ± 0.094	1.163 ± 0.202/ 0.520 ± 0.086	0.901 ± 0.150	0.238 ± 0.012	0.634 ± 0.037/ 0.480 ± 0.052	--	0.419 ± 0.044	0.914 ± 0.069/ 0.588 ± 0.106	0.378 ± 0.296
LBD5	0.427 ± 0.14	1.023 ± 0.281/ 0.526 ± 0.041	1.356 ± 1.152	0.228 ± 0.016	0.604 ± 0.019/ 0.480 ± 0.018	1.345 ± 0.050	0.249 ± 0.092	0.735 ± 0.194/ 0.425 ± 0.047	0.764 ± 0.585
LBE6	0.404 ± 0.106	0.988 ± 0.180/ 0.518 ± 0.045	0.888 ± 0.084	--	--	--	0.226 ± 0.027	0.51 ± 0.161/ 0.416 ± 0.030	1.837 ± 0.637-

Table 5.3: Continued.

Strains		**C57BL/6**			**A/J**			**BALB/c**	
Airway Measures (mm)	*Area*	*Diameter (Max/Min)*	*Branch Length*	*Area*	*Diameter (Max/Min)*	*Branch Length*	*Area*	*Diameter (Max/Min)*	*Branch Length*
Trachea	2.322 ± 0.085	1.927 ± 0.117/ 1.536 ± 0.041	--	2.165 ± 0.321	1.715 ± 0.157/ 1.602 ± 0.99	--	1.983 ± 0.200	1.585 ± 0.234/ 1.520 ± 0.045	--
RMB1	4.219 ± 0.514	2.641 ± 0.330/ 2.041 ± 0.183	3.519 ± 0.057	2.680 ±0.698	1.932 ± 0.278/ 1.741 ± 0.225	3.700 ± 0.634	2.215 ± 0.475	1.769 ± 0.155/ 1.580 ± 0.220	3.347 ± 0.458
RMB2	4.864 ± 0.581	2.717 ± 0.249/ 2.278 ± 0.161	1.982 ± 0.228	2.181 ± 0.578	1.699 ± 0.209/ 1.613 ± 0.220	3.352 ± 0.013	1.699 ± 0.491	1.508 ± 0.237/ 1.407 ± 0.217	3.177 ± 0.465
ApRMB2	0.881 ± 0.110	1.315 ± 0.139/ 0.853 ± 0.017	--	0.751 ± 0.201	1.077 ± 0.177/ 0.877 ± 0.103	0.581 ± 0.235	0.888 ± 0.109	1.125 ± 0.078/ 1.003 ± 0.070	--
ApRMB3	0.819 ± 0.156	1.177 ± 0.178/ 0.881 ± 0.052	1.961 ± 0.515	0.621 ± 0.059	1.052 ± 0.111/ 0.757 ± 0.089	--	1.146 ± 0.203	1.411 ± 0.160/ 1.029 ± 0.095	1.952 ± 0.336
ApRMB4	0.286 ± 0.043	0.672 ± 0.080/ 0.541 ± 0.030	1.791 ± 0.127	0.413 ± 0.289	0.967 ± 0.479/ 0.510 ± 0.103	1.175 ± 0.682	0.296 ± 0.046	0.709 ± 0.066/ 0.530 ±0.039	1.799 ± 0.195
AzRMB3	1.399 ± 0.315	1.543 ± 0.213/ 1.144 ± 0.124	2.901 ± 0.221	1.440 ± 0.288	1.659 ± 0.187/ 1.097 ± 0.119	1.392 ± 0.420	1.146 ± 0.203	1.411 ± 0.160/ 1.029 ± 0.095	1.855 ± 0.135
AzRMB4	0.716 ± 0.413	1.177 ± 0.489/ 0.729 ± 0.163	--	0.680 ± 0.402	1.103 ± 0.392/ 0.724 ± 0.260	1.488± 0.127	0.591 ± 0.227	0.990 ± 0.240/ 0.741 ± 0.150	2.016 ± 0.233
CaRMB3	1.777 ± 0.188	1.645 ± 0.127/ 1.373 ± 0.049	1.733 ± 0.356	0.955 ± 0.263	1.153 ± 0.149/ 1.041 ± 0.145	1.278 ± 0.088	0.928 ± 0.114	1.166 ± 0.080/ 1.011 ± 0.062	1.727 ± 0.051
CaRMB4	--	--	--	0.637 ± 0.077	0.954 ± 0.073/ 0.848 ± 0.049	1.415 ± 0.691	0.625 ± 0.200	1.013 ± 0.186/ 0.775 ± 0.102	1.263 ± 0.197
DiRMB3	3.182 ± 0.590	2.194 ± 0.392/ 1.845 ± 0.068	2.654 ± 0.258	1.750 ± 0.190	1.560 ± 0.088/ 1.425 ± 0.080	1.675 ± 0.262	1.689 ± 0.421	1.626 ± 0.361/ 1.316 ± 0.113	2.321 ± 0.180

Table 5.4: Airway measurements at 20 cmH_2O for the C57BL/6, A/J, and BALB/c strains.

DiRMB4	2.310 ± 0.713	2.021 ± 0.576/ 1.448 ± 0.068	2.071 ± 0.144	1.373 ± 0.114	1.415 ± 0.037/ 1.235 ± 0.080	2.019 ± 0.097	1.481 ± 0.467	1.642 ± 0.425/ 1.132 ± 0.129	1.985 ± 0.134
DiRMB5	1.782 ± 0.653	1.799 ± 0.486/ 1.239 ± 0.172	1.486 ± 0.406	1.192 ± 0.152	1.410 ± 0.104/ 1.073 ± 0.068	--	1.341 ± 0.612	1.439 ± 0.396/ 1.133 ± 0.249	1.575 ± 0.349
DiRMB6	0.885 ± 0.393	1.211 ± 0.332/ 0.898 ± 0.157	1.205 ± 0.053	0.647 ± 0.155	0.962 ± 0.128/ 0.847 ± 0.101	--	0.692 ± 0.125	1.035 ± 0.139/ 0.849 ± 0.058	1.315 ± 0.075
DiRBA4	0.624 ± 0.196	1.045 ± 0.268/ 0.732 ± 0.141	1.249 ± 0.984	0.636 ± 0.107	1.048 ± 0.152/ 0.771 ± 0.036	0.588 ± 0.080	0.499 ± 0.109	0.902 ± 0.114/ 0.699 ± 0.086	0.512 ± 0.088
DiRBB5	0.699 ± 0.156	1.194 ± 0.217/ 0.742 ± 0.043	0.730 ± 0.360	0.539 ± 0.096	0.956 ± 0.107/ 0.714 ± 0.055	0.826 ± 0.610	0.602 ± 0.127	1.059 ± 0.187/ 0.720 ± 0.025	0.698 ± 0.511
DiRBC6	0.480 ± 0.017	0.969 ± 0.031/ 0.632 ± 0.035	1.516 ± 0.214	0.416 ± 0.131	0.864 ± 0.168/ 0.604 ± 0.069	1.636 ± 0.080	0.450 ± 0.120	0.925 ± 0.228/ 0.619 ± 0.051	1.827 ± 0.301
DiRBD7	--	--	--	0.212 ± 0.038	0.600 ± 0.069/ 0.449 ± 0.037	--	0.292 ± 0.042	0.731 ± 0.086/ 0.508 ± 0.015	1.714 ± 0.149
LMB1	2.275 ± 0.214	1.896 ± 0.135/ 1.526 ± 0.057	4.805 ± 0.382	1.380 ± 0.424	1.447 ± 0.166/ 1.193 ± 0.235	5.843 ± 0.888	1.334 ± 0.274	1.390 ± 0.172/ 1.209 ± 0.126	5.330 ± 0.201
LMB2	3.980 ± 0.787	2.753 ± 0.467/ 1.833 ± 0.060	2.864 ± 0.385	1.870 ± 0.425	1.640 ± 0.167/ 1.438 ± 0.182	1.961 ± 0.322	1.992 ± 0.342	1.773 ± 0.247/ 1.427 ± 0.105	2.504 ± 0.330
LMB3	1.803 ± 0.426	1.736 ± 0.395/ 1.322 ± 0.083	1.626 ± 0.236	1.155 ± 0.095	1.289 ± 0.050/ 1.140 ± 0.071	1.831 ± 0.369	1.312 ± 0.337	1.455 ± 0.260/ 1.136 ± 0.098	1.990 ± 0.103
LMB4	1.129 ± 0.420	1.338 ± 0.402/ 1.057 ± 0.093	2.238 ± 0.097	0.956 ± 0.142	1.232 ± 0.089/ 0.984 ± 0.078	2.071 ± 0.341	1.004 ± 0.287	1.296 ± 0.268/ 0.975 ± 0.085	2.005 ± 0.261
LMB5	0.799 ± 0.375	1.284 ± 0.649/ 0.799 ± 0.043	1.329 ± 0.189	0.623 ± 0.084	1.030 ± 0.069/ 0.769 ± 0.063	1.665 ± 0.196	0.813 ± 0.223	1.198 ± 0.210/ 0.852 ± 0.118	1.396 ± 0.240
LMB6	0.494 ± 0.193	1.057 ± 0.351/ 0.586 ± 0.047	1.112 ± 0.403	0.371 ± 0.061	0.801 ± 0.069/ 0.587 ± 0.050	0.633 ± 0.405	0.449 ± 0.183	0.804 ± 0.206/ 0.692 ± 0.119	1.075 ± 0.237

Table 5.4: Continued.

LBA2	--	--	--	--	--	--	--	--	--
LBB3	0.580 ± 0.155	1.151 ± 0.220/ 0.634 ± 0.064	2.256 ± 0.891	0.406 ± 0.072	0.938 ± 0.101/ 0.548 ± 0.043	1.759 ± 0.638	0.617 ± 0.120	1.118 ± 0.168/ 0.701 ± 0.063	0.589 ± 0.263
LBC4	0.624 ± 0.135	1.197 ± 0.231/ 0.661 ± 0.045	0.703 ± 0.218	0.277 ± 0.027	0.633 ± 0.016/ 0.555 ± 0.041	1.146 ± 0.903	0.495 ± 0.016	0.992 ± 0.048/ 0.636 ± 0.012	0.608 ± 0.192
LBD5	0.512 ± 0.147	1.176 ± 0.308/ 0.554 ± 0.051	0.574 ± 0.083	0.341 ± 0.115	0.804 ± 0.178/ 0.532 ± 0.060	0.640 ± 0.574	0.325 ± 0.043	0.768 ± 0.157/ 0.544 ± 0.044	0.749 ± 0.594
LBE6	--	--	--	0.239 ± 0.020	0.651 ± 0.083/ 0.470 ± 0.026	1.518 ± 0.296	0.252 ± 0.050	0.713 ± 0.069/ 0.448 ± 0.047	--

Table 5.4: Continued.

Strains		**C57BL/6**			**A/J**			**BALB/c**	
Airway Measures (mm)	*Area*	*Diameter (Max/Min)*	*Branch Length*	*Area*	*Diameter (Max/Min)*	*Branch Length*	*Area*	*Diameter (Max/Min)*	*Branch Length*
Trachea	2.505 ± 0.166	1.957 ± 0.114/ 1.630 ± 0.432	--	2.662 ± 0.705	2.040 ± 0.377/ 1.650 ± 0.135	--	2.100 ± 0.173	1.719 ± 0.055/ 1.553 ± 0.080	--
RMB1	4.340 ± 0.713	2.552 ± 0.236/ 2.156 ± 0.179	3.813 ± 0.029	2.629 ± 0.654	1.939 ± 0.288/ 1.709 ± 0.183	3.772 ± 0.486	2.655 ± 0.157	1.943 ± 0.086 1.739 ± 0.030	3.286 ± 0.512
RMB2	5.466 ± 0.783	2.769 ± 0.222/ 2.505 ± 0.177	2.076 ± 0.204	2.074 ± 0.392	1.703 ± 0.146/ 1.541 ± 0.174	3.608 ± 0.082	1.839 ± 0.045	1.605 ± 0.064/ 1.460 ± 0.025	3.585 ± 0.469
ApRMB2	--	--	--	0.871 ± 0.312	1.152 ± 0.249/ 0.940 ± 0.172	0.584 ± 0.260	--	--	--
ApRMB3	0.916 ± 0.134	1.282 ± 0.161/ 0.908 ± 0.034	2.346 ± 0.563	0.705 ± 0.060	1.227 ± 0.071/ 0.732 ± 0.052	1.872 ± 0.010	0.762 ± 0.106	1.221 ± 0.039/ 0.796 ± 0.118	2.328 ± 0.282
ApRMB4	0.314 ± 0.030	0.688 ± 0.014/ 0.580 ± 0.054	2.160 ± 0.166	--	--	--	0.291 ± 0.055	0.687 ± 0.100/ 0.538 ± 0.036	1.969 ± 0.348
AzRMB3	1.421 ± 0.378	1.468 ± 0.224/ 1.219 ± 0.133	3.091 ± 0.264	1.442 ± 0.298	1.694 ± 0.232/ 1.079 ± 0.122	1.327 ± 0.470	1.299 ± 0.128	1.435 ± 0.094/ 1.151 ± 0.044	1.644 ± 0.234
AzRMB4	0.941 ± 0.284	1.325 ± 0.321/ 0.898 ± 0.059	2.071 ± 0.259	1.029 ± 0.076	1.353 ± 0.142/ 0.970 ± 0.030	1.469 ± 0.029	0.819 ± 0.130	1.207 ± 0.177/ 0.863 ± 0.013	2.289 ± 0.355
CaRMB3	3.984 ± 0.527	2.597 ± 0.306/ 1.951 ± 0.030	1.904 ± 0.365	0.841 ± 0.130	1.090 ± 0.065/ 0.978 ± 0.095	1.374 ± 0.166	1.059 ± 0.046	1.199 ± 0.013/ 1.124 ± 0.042	2.023 ± 0.095
CaRMB4	1.260 ± 0.451	1.363 ± 0.236/ 1.159 ± 0.221	--	0.684 ± 0.084	0.993 ± 0.044/ 0.875 ± 0.071	1.553 ± 0.889	0.662 ± 0.035	0.964 ± 0.026/ 0.874 ± 0.029	1.884 ± 0.246
DiRMB3	3.984 ± 0.527	2.597 ± 0.306/ 1.951 ± 0.030	2.997 ± 0.243	1.887 ± 0.191	1.608 ± 0.071/ 1.492 ± 0.089	1.847 ± 0.307	2.048 ± 0.372	1.835 ± 0.378/ 1.426 ± 0.051	2.821 ± 0.334

Table 5.5: Airway measurements at 30 cmH2O for the C57BL/6, A/J, and BALB/c strains.

DiRMB4	3.140 ± 0.502	2.615 ± 0.414/ 1.529 ± 0.066	2.222 ± 0.167	1.425 ± 0.072	1.462 ± 0.014/ 1.241 ± 0.072	2.223 ± 0.206	1.799 ± 0.676	1.930 ± 0.822/ 1.205 ± 0.104	2.157 ± 0.125
DiRMB5	2.341 ± 0.251	2.212 ± 0.148/ 1.350 ± 0.144	1.685 ± 0.318	1.128 ± 0.097	1.372 ± 0.049/ 1.046 ± 0.055	1.921 ± 0.252	1.324 ± 0.362	1.486 ± 0.301/ 1.124 ± 0.075	1.803 ± 0.286
DiRMB6	1.229 ± 0.141	1.513 ± 0.087/ 1.033 ± 0.060	1.316 ± 0.160	0.612 ± 0.114	0.961 ± 0.100/ 0.806 ± 0.081	1.922 ± 0.278	0.629 ± 0.048	0.976 ± 0.015/ 0.820 ± 0.051	1.555 ± 0.162
DiRBA4	0.676 ± 0.098	1.099 ± 0.160/ 0.784 ± 0.008	1.293 ± 0.920	0.627 ± 0.135	1.062 ± 0.183/ 0.751 ± 0.072	0.711 ± 0.183	0.572 ± 0.025	0.959 ± 0.013/ 0.760 ± 0.038	0.841 ± 0.090
DiRBB5	0.872 ± 0.296	1.394 ± 0.393/ 0.790 ± 0.048	--	0.571 ± 0.121	0.955 ± 0.155/ 0.758 ± 0.071	0.472 ± 0.200	0.624 ± 0.135	1.059 ± 0.172/ 0.747 ± 0.042	0.633 ± 0.136
DiRBC6	0.532 ± 0.020	0.993 ± 0.092/ 0.684 ± 0.038	1.912 ± 0.215	0.374 ± 0.062	0.825 ± 0.119/ 0.577 ± 0.012	2.007 ± 0.087	0.388 ± 0.059	0.832 ± 0.110/ 0.593 ± 0.013	2.222 ± 0.478
DiRBD7	0.401 ± 0.059	0.898 ± 0.060/ 0.566 ± 0.045	1.518 ± 0.543	0.278 ± 0.009	0.718 ± 0.034/ 0.492 ± 0.007	1.147 ± 0.714	0.255 ± 0.059	0.653 ± 0.096/ 0.493 ± 0.043	2.001 ± 0.166
LMB1	2.631 ± 0.294	2.051 ± 0.146/ 1.631 ± 0.079	5.158 ± 0.157	1.392 ± 0.230	1.445 ± 0.132/ 1.222 ± 0.095	5.789 ± 0.948	1.641 ± 0.250	1.549 ± 0.157/ 1.344 ± 0.069	5.146 ± 0.388
LMB2	4.870 ± 0.107	3.086 ± 0.117/ 2.010 ± 0.036	2.857 ± 0.208	1.981 ± 0.276	1.755 ± 0.111/ 1.434 ± 0.124	2.242 ± 0.462	2.254 ± 0.372	1.878 ± 0.325/ 1.530 ± 0.048	2.654 ± 0.178
LMB3	2.481 ± 0.283	2.318 ± 0.396/ 1.376 ± 0.158	1.878 ± 0.212	1.183 ± 0.006	1.364 ± 0.024/ 1.105 ± 0.022	2.032 ± 0.372	1.457 ± 0.224	1.600 ± 0.251/ 1.161 ± 0.017	2.461 ± 0.213
LMB4	1.530 ± 0.369	1.691 ± 0.356/ 1.147 ± 0.082	2.458 ± 0.237	0.971 ± 0.037	1.333 ± 0.017/ 0.928 ± 0.029	2.399 ± 0.307	1.030 ± 0.163	1.334 ± 0.219/ 0.983 ± 0.006	2.129 ± 0.241
LMB5	1.031 ± 0.357	1.604 ± 0.677/ 0.835 ± 0.057	1.694 ± 0.225	0.641 ± 0.114	1.102 ± 0.078/ 0.739 ± 0.093	2.037 ± 0.294	0.797 ± 0.123	1.153 ± 0.110/ 0.878 ± 0.066	1.599 ± 0.186
LMB6	0.529 ± 0.235	1.144 ± 0.475/ 0.582 ± 0.038	1.338 ± 0.589	0.354 ± 0.049	0.808 ± 0.021/ 0.556 ± 0.064	1.071 ± 0.548	0.446 ± 0.139	0.826 ± 0.136/ 0.678 ± 0.107	0.883 ± 0.564

Table 5.5: Continued.

LBA2	--	--	--	--	--	--	--	--	--
LBB3	0.670 ± 0.219	1.203 ± 0.266/ 0.698 ± 0.018	2.775 ± 1.003	0.574 ± 0.089	1.122 ± 0.103/ 0.650 ± 0.146	--	0.745 ± 0.049	1.303 ± 0.106/ 0.729 ± 0.071	0.490 ± 0.266
LBC4	0.691 ± 0.072	1.275 ± 0.157/ 0.692 ± 0.066	1.050 ± 0.258	0.360 ± 0.088	0.761 ± 0.161/ 0.601 ± 0.021	--	0.558 ± 0.115	1.082 ± 0.284/ 0.663 ± 0.040	0.539 ± 0.124
LBD5	0.591 ± 0.073	1.332 ± 0.009/ 0.565 ± 0.074	0.753 ± 0.413	0.428 ± 0.167	1.049 ± 0.456/ 0.525 ± 0.026	--	0.388 ± 0.113	0.924 ± 0.176/ 0.528 ± 0.059	0.496 ± 0.256
LBE6	--	--	0.464 ± 0.406	0.234 ± 0.002	0.624 ± 0.067/ 0.479 ± 0.055	--	0.316 ± 0.058	0.805 ± 0.094/ 0.498 ± 0.038	0.931 ± 0.678

Table 5.5: Continued.

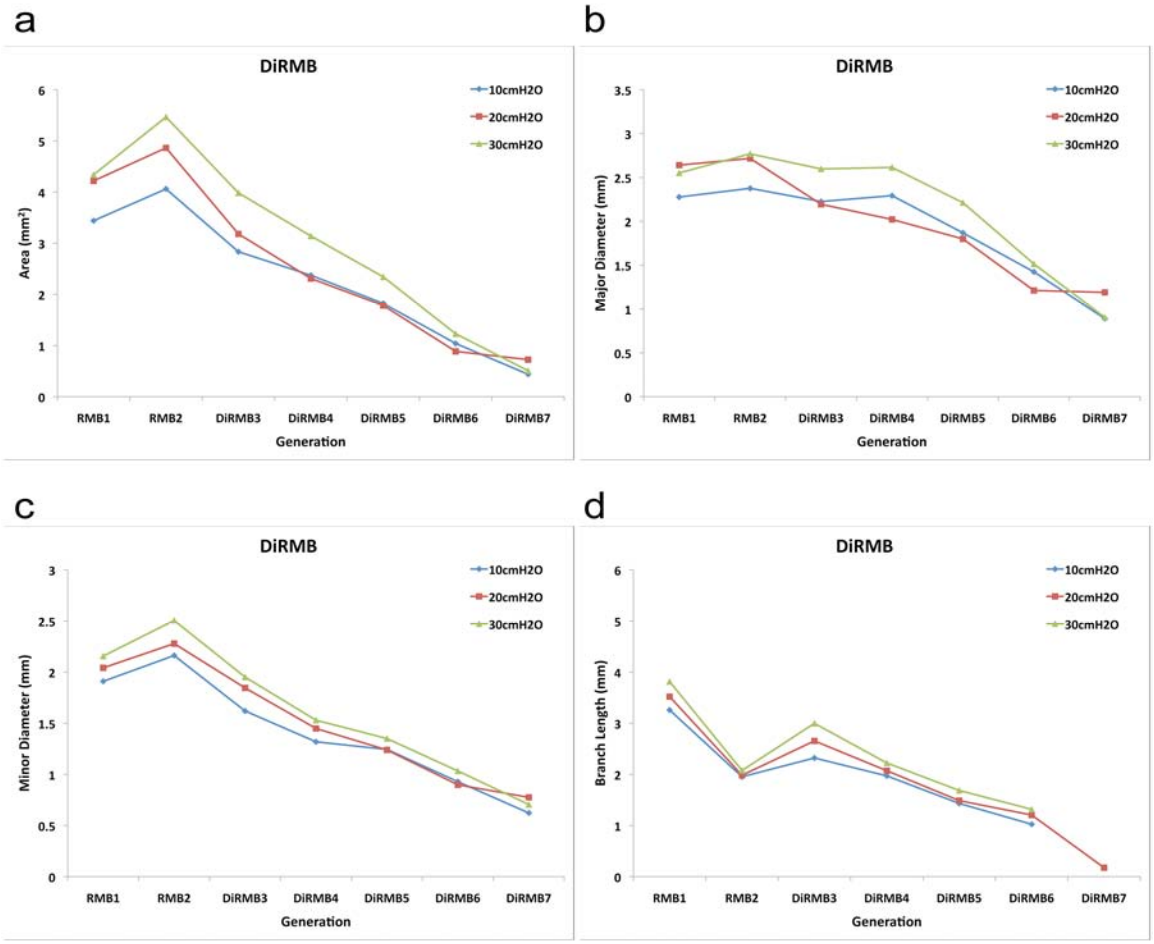

Figure 5.7: C57BL/6 DiRMB pathway airway measures including area, major and minor diameter, and branch length. The a) area, b) major diameter, c) minor diameter, and d) branch length for the DiRMB pathway at PAP's from 10-30 cmH_2O.

Lobe	PAP	Strain -- Mean (SE)			Compare Strains p-value	Pairwise mean comparisons
		A/J	BALB/c	C57		
ApR-MB **Str* PAP p=0.238** **Strain p=0.336**	10	0.48 (0.09)	0.49 (0.03)	0.57 (0.02)	0.506	--
	20	0.58 (0.07)	0.61 (0.02)	0.68 (0.04)	>0.99	--
	30	0.68 (0.08)	0.66 (0.02)	0.70 (0.05)	>0.99	--
AzR-MB **Str* PAP p=0.854** **Str p=0.049 A/J>BALB/c**	10	1.03 (0.10)	0.69 (0.10)	0.93 (0.10)	0.226	--
	20	1.20 (0.09)	0.92 (0.08)	1.16 (0.08)	0.217	--
	30	1.31 (0.09)	1.02 (0.08)	1.24 (0.09)	0.208	--
CaR-MB **Str* PAP p=0.0004**	10	0.68 (0.08)	0.55 (0.07)	1.24 (0.08)	<0.0001	C57 vs. A/J p=0.0007 C57 vs. BALB/c p<0.0001 A/J vs. BALB/c p>0.99
	20	0.81 (0.08)	0.76 (0.08)	1.53 (0.08)	<0.0001	C57 vs. A/J p<0.0001 C57 vs. BALB/c p<0.0001 A/J vs. BALB/c p>0.99
	30	0.83 (0.07)	0.82 (0.07)	1.58 (0.07)	<0.0001	C57 vs. A/J p<0.0001 C57 vs. BALB/c p<0.0001 A/J vs. BALB/c p>0.99
Cont'd…						

Table 5.6: Comparison of mean area among A/J, BALB/c, and C57BL/6 by PAP at each lobe.

DiR-MB **Str* PAP p=0.790** **Str p=0.015 C57>A/J C57>BALB/c**	10	0.83 (0.07)	0.91 (0.10)	1.53 (0.15)	0.009	C57 vs. A/J p=0.015 C57 vs. BALB/c p=0.039 A/J vs. BALB/c p>0.99
	20	1.07 (0.06)	1.09 (0.13)	1.85 (0.21)	0.050	C57 vs. A/J p=0.074 C57 vs. BALB/c p=0.080 A/J vs. BALB/c p>0.99
	30	1.16 (0.11)	1.14 (0.18)	1.91 (0.26)	0.187	--
L-MB **Str* PAP p=0.130** **Str p=0.001 C57>A/J C57>BALB/c**	10	0.77 (0.08)	0.79 (0.11)	1.31 (0.10)	0.007	C57 vs. A/J p=0.015 C57 vs. BALB/c p=0.048 A/J vs. BALB/c p>0.99
	20	0.96 (0.07)	1.03 (0.08)	1.67 (0.14)	0.003	C57 vs. A/J p=0.006 C57 vs. BALB/c p=0.014 A/J vs. BALB/c p>0.99
	30	1.02 (0.06)	1.09 (0.11)	1.81 (0.15)	0.006	C57 vs. A/J p=0.006 C57 vs. BALB/c p=0.016 A/J vs. BALB/c p>0.99
R-MB **Str* PAP p=0.022**	10	2.02 (0.21)	1.46 (0.20)	3.68 (0.20)	<0.0001	C57 vs. A/J p=0.0002 C57 vs. BALB/c p<0.0001 A/J vs. BALB/c p=0.634
	20	2.43 (0.23)	1.96 (0.21)	4.54 (0.21)	<0.0001	C57 vs. A/J p<0.0001 C57 vs. BALB/c p<0.0001 A/J vs. BALB/c p>0.99
	30	2.60 (0.27)	2.07 (0.24)	4.81 (0.24)	<0.0001	C57 vs. A/J p=0.0002 C57 vs. BALB/c p<0.0001 A/J vs. BALB/c p>0.99

Table 5.6: Continued.

Lobe	PAP	Strain -- Mean (SE)			Compare Strains p-value	Pairwise mean comparisons
		A/J	BALB/c	C57		
ApR-MB **Str*PAP p=0.232** **Strain p=0.344**	10	0.93 (0.11)	0.86 (0.02)	0.93 (0.02)	0.517	--
	20	1.01 (0.09)	0.98 (0.02)	1.03 (0.03)	>0.99	--
	30	1.11 (0.09)	1.04 (0.02)	1.07 (0.04)	>0.99	--
AzR-MB **Str* PAP p=0.660** **Str p=0.036 A/J>BALB/c**	10	1.38 (0.07)	1.16 (0.07)	1.36 (0.07)	0.162	--
	20	1.51 (0.07)	1.29 (0.06)	1.44 (0.06)	0.187	--
	30	1.59 (0.08)	1.33 (0.07)	1.43 (0.07)	0.212	--
CaR-MB **Str* PAP** **Strain p<0.0001**	10	1.00 (0.04)	0.98 (0.04)	1.38 (0.04)	<0.0001	C57 vs. A/J p=0.0003 C57 vs. BALB/c p<0.0001 A/J vs. BALB/c p>0.99
	20	1.07 (0.05)	1.07 (0.05)	1.53 (0.05)	<0.0001	C57 vs. A/J p<0.0001 C57 vs. BALB/c p<0.0001 A/J vs. BALB/c p>0.99
	30	1.07 (0.04)	1.06 (0.04)	1.49 (0.04)	<0.0001	C57 vs. A/J p<0.0001 C57 vs. BALB/c p<0.0001 A/J vs. BALB/c p>0.99

Table 5.7: Comparison of mean major diameter among A/J, BALB/c, and C57 by PAP at each lobe

DiR-MB **Str* PAP p=0.875** **Str p=0.014 C57>A/J**	10	1.06 (0.04)	1.18 (0.09)	1.59 (0.14)	0.060	C57 vs. A/J p=0.086 C57 vs. BALB/c p=0.339 A/J vs. BALB/c p>0.99
	20	1.22 (0.03)	1.28 (0.10)	1.69 (0.14)	0.072	C57 vs. A/J p=0.081 C57 vs. BALB/c p=0.271 A/J vs. BALB/c p>0.99
	30	1.25 (0.03)	1.27 (0.18)	1.71 (0.17)	0.215	--
L-MB **Str* PAP p=0.585** **Str p=0.006 C57>A/J C57>BALB/c**	10	0.99 (0.03)	1.06 (0.07)	1.38 (0.10)	0.034	C57 vs. A/J p=0.040 C57 vs. BALB/c p=0.169 A/J vs. BALB/c p>0.99
	20	1.14 (0.03)	1.22 (0.07)	1.57 (0.11)	0.033	C57 vs. A/J p=0.049 C57 vs. BALB/c p=0.187 A/J vs. BALB/c p>0.99
	30	1.21 (0.02)	1.25 (0.07)	1.66 (0.12)	0.045	C57 vs. A/J p=0.045 C57 vs. BALB/c p=0.090 A/J vs. BALB/c p>0.99
R-MB **Str* PAP p=0.081**	10	1.67 (0.09)	1.48 (0.08)	2.41 (0.08)	<0.0001	C57 vs. A/J p=0.0001 C57 vs. BALB/c p<0.0001 A/J vs. BALB/c p=0.634
	20	1.82 (0.09)	1.64 (0.08)	2.68 (0.08)	<0.0001	C57 vs. A/J p<0.0001 C57 vs. BALB/c p<0.0001 A/J vs. BALB/c p>0.99
	30	1.90 (0.10)	1.72 (0.09)	2.75 (0.09)	<0.0001	C57 vs. A/J p<0.0001 C57 vs. BALB/c p<0.0001 A/J vs. BALB/c p>0.99

Table 5.7: Continued.

Lobe	PAP	Strain -- Mean (SE)			Compare Strains p-value	Pairwise mean comparisons
		A/J	BALB/c	C57		
ApR-MB **Str*PAP p=0.897** **Strain p=0.261**	10	0.64 (0.03)	0.67 (0.03)	0.70 (0.03)	>0.99	--
	20	0.71 (0.03)	0.76 (0.02)	0.78 (0.02)	0.476	--
	30	0.75 (0.03)	0.78 (0.03)	0.81 (0.03)	>0.99	--
AzR-MB **Str* PAP p=0.061** **Str p=0.144**	10	0.95 (0.06)	0.75 (0.06)	0.84 (0.06)	0.305	--
	20	0.98 (0.04)	0.91 (0.03)	0.99 (0.03)	0.563	--
	30	1.04 (0.04)	0.96 (0.04)	1.08 (0.04)	0.404	--
CaR-MB **Str* PAP p=0.100** **Strain p<0.0001**	10	0.84 (0.04)	0.75 (0.04)	1.13 (0.04)	<0.0001	C57 vs. A/J p=0.0001 C57 vs. BALB/c p<0.0001 A/J vs. BALB/c p>0.99
	20	0.95 (0.04)	0.89 (0.03)	1.24 (0.04)	<0.0001	C57 vs. A/J p=0.0002 C57 vs. BALB/c p<0.0001 A/J vs. BALB/c p>0.99
	30	0.96 (0.04)	0.98 (0.04)	1.31 (0.04)	<0.0001	C57 vs. A/J p<0.0001 C57 vs. BALB/c p=0.0002 A/J vs. BALB/c p>0.99

Table 5.8: Comparison of mean minor diameter among A/J, BALB/c, and C57 by PAP at each lobe.

DiR-MB **Str* PAP p=0.826** **Str p<0.0001**	10	0.91 (0.03)	0.89 (0.04)	1.13 (0.02)	<0.0001	C57 vs. A/J p=0.001 C57 vs. BALB/c p=0.002 A/J vs. BALB/c p>0.99
	20	1.03 (0.03)	0.99 (0.04)	1.25 (0.03)	<0.0001	C57 vs. A/J p=0.013 C57 vs. BALB/c p<0.0001 A/J vs. BALB/c p>0.99
	30	1.06 (0.04)	1.01 (0.03)	1.30 (0.03)	0.0009	--
L-MB **Str* PAP p=0.329** **Str p=0.0002 C57>A/J C57>BALB/c**	10	0.85 (0.05)	0.83 (0.05)	0.99 (0.01)	0.026	C57 vs. A/J p=0.040 C57 vs. BALB/c p=0.169 A/J vs. BALB/c p>0.99
	20	0.93 (0.04)	0.95 (0.03)	1.11 (0.01)	0.0005	C57 vs. A/J p=0.018 C57 vs. BALB/c p=0.004 A/J vs. BALB/c p>0.99
	30	0.93 (0.03)	0.99 (0.02)	1.16 (0.01)	0.0007	C57 vs. A/J p<0.0001 C57 vs. BALB/c p=0.005 A/J vs. BALB/c p=0.655
R-MB Str* PAP p=0.477 **Str p=0.011 C57>A/J C57>BALB/c**	10	1.56 (0.13)	1.17 (0.17)	1.94 (0.10)	0.117	--
	20	1.68 (0.08)	1.49 (0.08)	2.16 (0.10)	0.006	C57 vs. A/J p<0.087 C57 vs. BALB/c p<0.019 A/J vs. BALB/c p>0.99
	30	1.69 (0.07)	1.58 (0.02)	2.22 (0.12)	0.010	C57 vs. A/J p<0.167 C57 vs. BALB/c p<0.122 A/J vs. BALB/c p>0.99

Table 5.8: Continued.

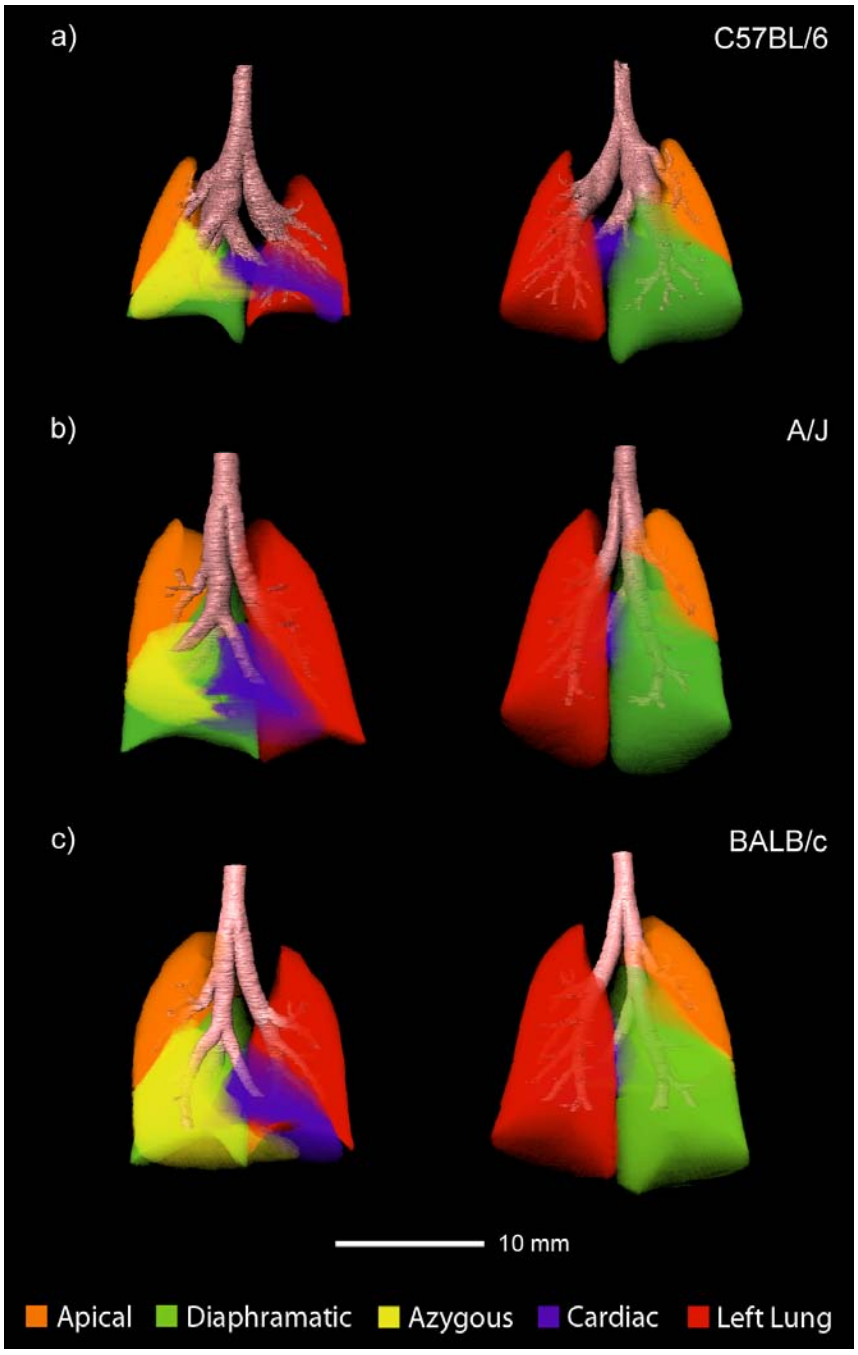

Figure 5.8: Anterior and posterior view of the rendered lobe segmentations overlaid on the airway tree. The lobes of the right lung and the left lung can be visually identified using this technique and compared for the a) C57BL/6, b) A/J, and c) BALB/c strains.

a

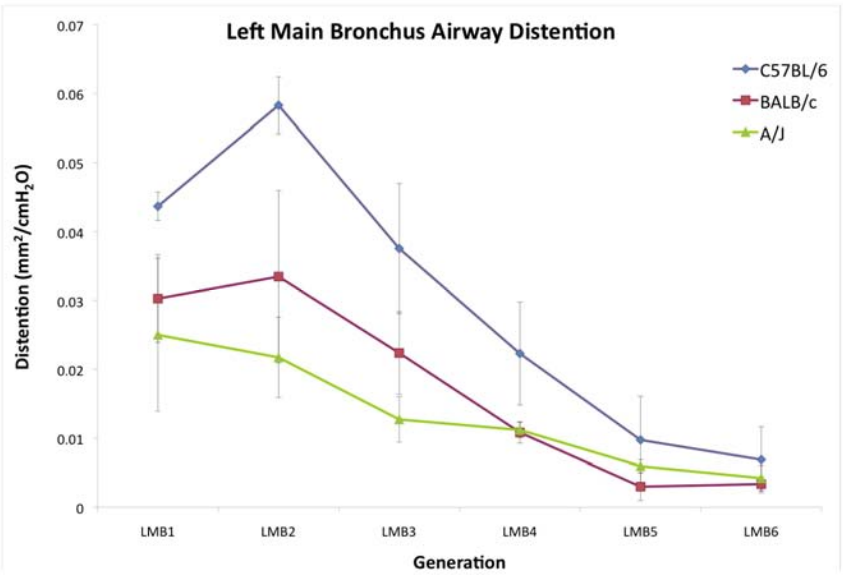

b

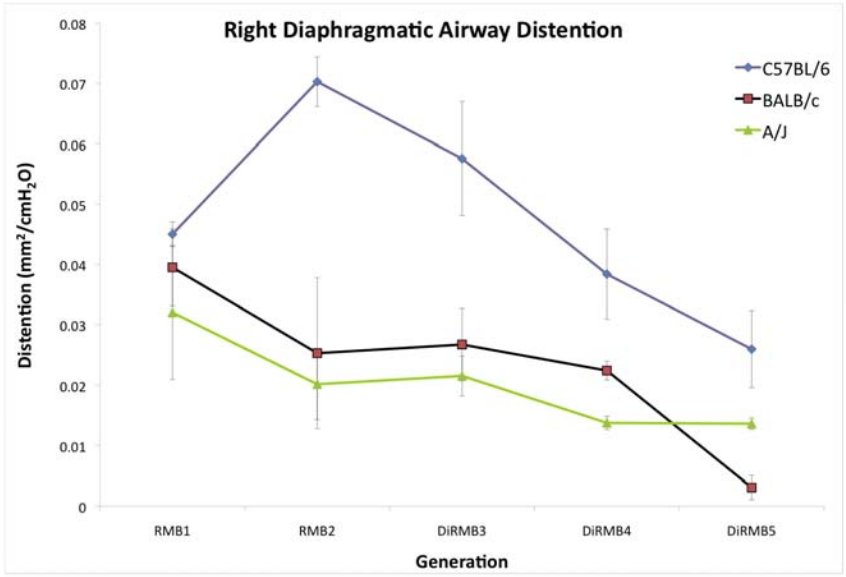

Figure 5.9: Distensibility measure for the left main bronchus and right diaphragmatic pathways. a) Distensibility of the left main brochus pathway for generations 1-6. b) Distensibility of the right diaphragmatic main bronchus pathway for generation 3-5 including right main bronchi for the C57BL/6, A/J, and BALB/c strains.

Strains	C57BL/6	A/J	BALB/c
Body weight (g)	29.5 ± 0.05	25.1 ± 0.71	30.9 ± 1.53
Lung volumes (µL)			
Total lung volume			
10 cmH_2O	844.7 ± 57.0	831.8 ± 77.5	897.3 ± 39.1
20 cmH2O	992.5 ± 39.7	965.5 ± 50.2	1152.5 ± 62.5
30 cmH2O	1356.1 ± 27.8	1332.6 ± 61.3	1738.3 ± 54.4
Normalized Lung volumes (µL/g)			
Total lung volume			
10 cmH_2O	28.6 ± 1.9	33.1 ± 2.9	29.0 ± 0.5
20 cmH2O	33.6 ± 1.3	38.5 ± 1.5	37.3 ± 0.9
30 cmH2O	46.0 ± 0.9	53.1 ± 1.6	56.3 ± 0.1
Lobe volume$_{20\ cmH2O}$ (uL)			
Apical	166.7 ± 14.4	135.8 ± 15.6	208.1 ± 3.0
Azygous	127.8 ± 5.2	142.7 ± 8.2	155.8 ± 11.2
Diaphragmatic	284.7 ± 22.4	294.8 ± 11.1	296.3 ± 22.9
Cardiac	86.6 ± 3.4	91.2 ± 9.0	95.7 ± 1.4
Left	326.7 ± 9.7	300.9 ± 22.9	396.5 ± 25.3
Normalized Lobe volume$_{20\ cmH2O}$ (uL/g)			
Apical	5.7 ± 0.5	5.4 ± 0.6	6.7 ± 0.05
Azygous	4.3 ± 0.2	5.7 ± 0.3	5.0 ± 0.01
Diaphragmatic	9.7 ± 0.8	11.7 ± 0.4	9.6 ± 0.04
Cardiac	2.9 ± 0.1	3.6 ± 0.3	3.1 ± 0.05
Left	11.1 ± 0.3	12.0 ± 0.9	12.8 ± 0.01

Table 5.9: Average ± SE of overall lung volumes and individual lobe volumes for the C57BL/6, A/J, and BALB/c inbred mouse strains.

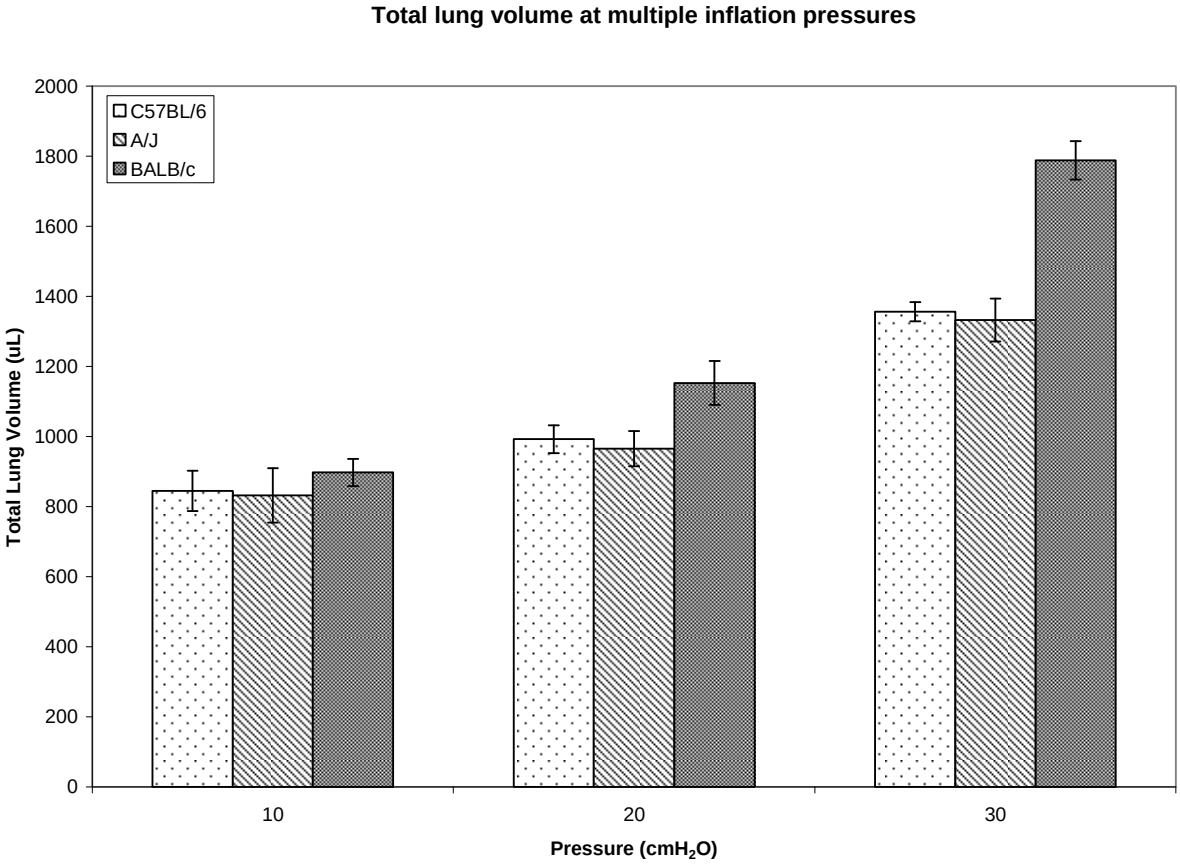

PAP (cmH_2O)	Strain -- Mean (SE)			Compare Strains p-value	Pairwise mean comparisons
	A/J	BALB/c	C57		
10	831.8 (77.5)	897.3 (39.1)	844.7 (57.0)	>0.99	--
20	965.5 (50.2)	1152.5 (62.5)	992.5 (39.7)	0.244	--
30	1332.6 (61.3)	1787.6 (54.4)	1356.1 (27.8)	0.001	C57 vs. A/J p>0.99 C57 vs. BALB/c p=0.004 A/J vs. BALB/c p=0.003

Figure 5.10: Total lung volume measures at 10, 20 and 30 cmH2O for the C57BL/6, A/J, and BALB/c inbred mouse strains and the resulting statistical significance. The total lung volume at 30 cmH_2O is significantly greater in the BALB/c compared to the C57BL/6 and A/J strains.

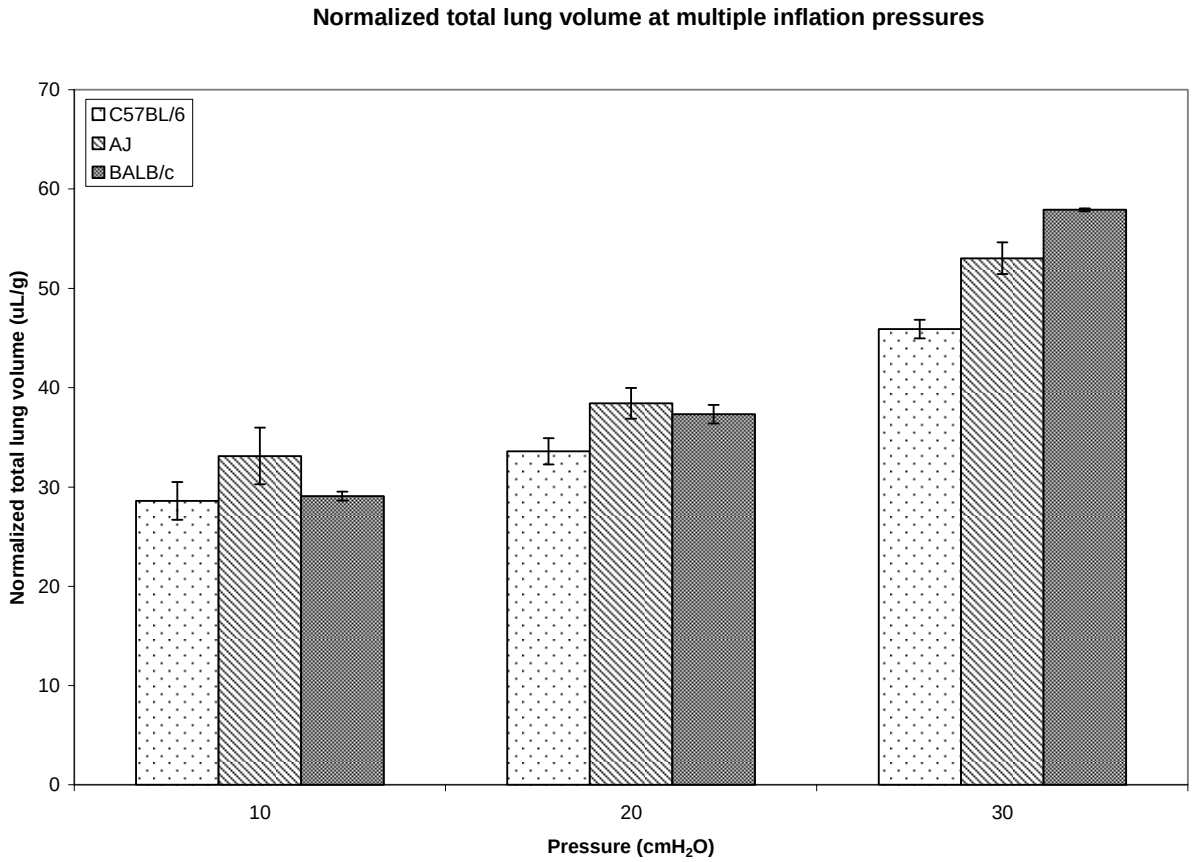

PAP (cmH_2O)	Strain -- Mean (SE)			Compare Strains p-value	Pairwise mean comparisons
	A/J	BALB/c	C57		
10	33.1 (2.9)	29.0 (0.5)	28.6 (1.9)	0.373	--
20	38.4 (1.5)	37.3 (0.9)	33.6 (1.3)	0.348	--
30	53.0 (1.6)	57.9 (0.1)	45.9 (0.9)	0.002	C57 vs. A/J p=0.077 C57 vs. BALB/c p=0.002 A/J vs. BALB/c p=0.431

Figure 5.11: Normalized (with respect to body weight) total lung volume measures at 10, 20 and 30 cmH2O for the C57BL/6, A/J, and BALB/c inbred mouse strains and the resulting statistical significance. There is no significance between the BALB/c and the A/J strain when the lung volumes are normalized with respect to body weight, although there is still significance between the C57BL/6 and BALB/c strains.

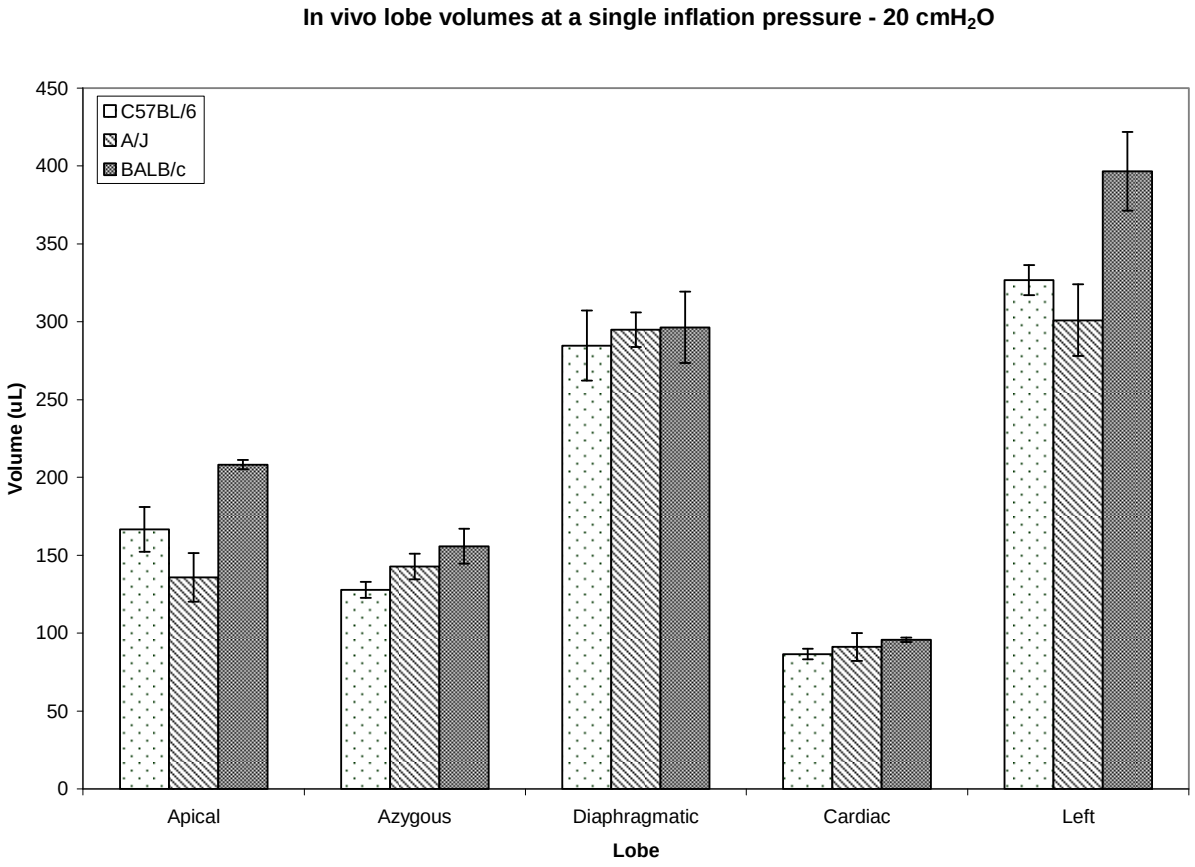

Lobe	Strain -- Mean (SE)			Compare Strains p-value	Pairwise mean comparisons
	A/J	BALB/c	C57		
Apical	135.1 (15.6)	208.1 (3.0)	166.7 (14.4)	0.018	C57 vs. A/J p=0.261 C57 vs. BALB/c p=0.122 A/J vs. BALB/c p=0.015
Azygous	142.8 (8.2)	155.8 (11.3)	127.8 (5.2)	0.148	--
Diaphragmatic	294.8 (11.1)	296.3 (22.9)	284.7 (22.4)	0.903	--
Cardiac	91.2 (9.0)	95.7 (1.4)	86.6 (3.4)	0.552	--
Left	300.9 (22.9)	396.5 (25.3)	326.7 (9.7)	0.039	C57 vs. A/J p=0.666 C57 vs. BALB/c p=0.115 A/J vs. BALB/c p=0.038

Figure 5.12: Lobe volume measures at 20 cmH2O for the C57BL/6, A/J, and BALB/c inbred mouse strains and the resulting statistical significance. For both the apical lobe and left lung there is significance between the A/J and BALB/c strains.

	Strain	C57BL/6			A/J			BALB/c		
Source	**Measure**	**Average**	**STD**	**n**	**Average**	**STD**	**n**	**Average**	**STD**	**n**
Empirical Flexivent Data	**Resistance** ($cmH_2O \cdot s/mL$)	0.797	0.014	3	0.941	0.097	3	0.849	0.04	3
	Compliance (uL/cmH_2O)	55.7	6.17	3	50.4	6.83	3	60.8	3.2	3
Mouse Phenome Database (MPD)	**Resistance** ($cmH_2O \cdot s/mL$)	0.741	0.086	12	0.827	0.173	15	0.84	0.203	16
	Compliance (uL/cmH_2O)	38.1	2.01	12	45.5	3.85	15	42.4	3.14	16

Table 5.10: Resistance and compliance values for the C57BL/6, A/J, and BALB/c inbred mouse strains obtained from empirical pulmonary function testing and the MPD [57].

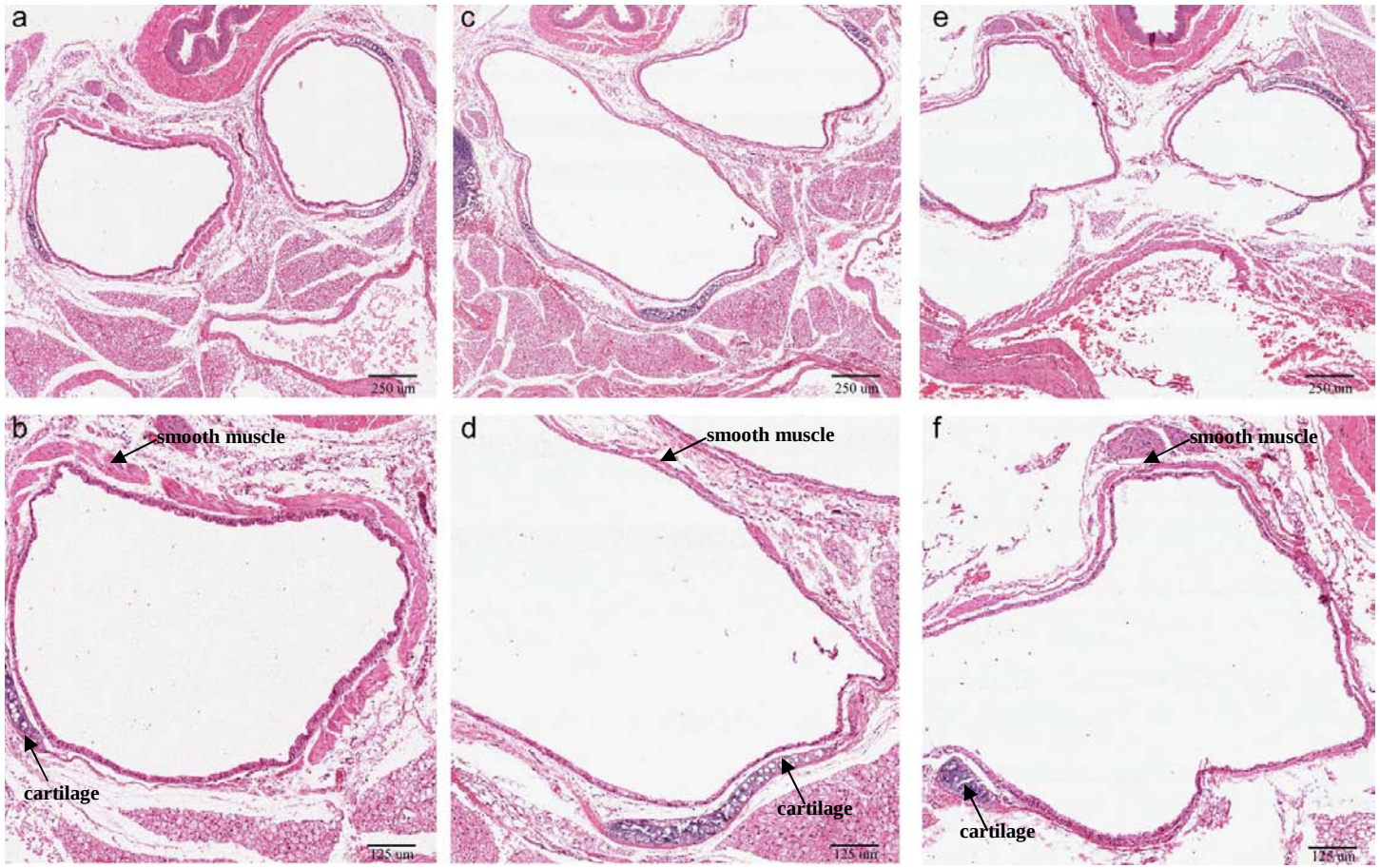

Figure 5.13: H&E histology comparison of C57BL/6, A/J, and BALB/c central airways. The left and right main bronchi from the region following RMB1 at low magnification a) C57BL/6, c) A/J, and e) BALB/c. At higher magnification the smooth muscle and cartilage is easier to distinguish and it appears the b) C57BL/6 has more smooth muscle than the d) A/J, and e) BALB/c.

	C57BL/6 Mean Chord Length (µm)		A/J Mean Chord Length (µm)		BALB/c Mean Chord Length (µm)	
	LEFT	**RIGHT**	**LEFT**	**RIGHT**	**LEFT**	**RIGHT**
Overall	39.5 (1.7)	41.4 (1.9)	48.1 (2.6)	48.3 (2.5)	39.7 (1.8)	40.3 (1.8)
Apex	38.4 (1.6)	37.9 (1.7)	45.5 (2.3)	49.2 (2.6)	37.4 (1.7)	33.2 (1.3)
Mid	39.3 (1.7)	41.9 (1.9)	48.8 (2.5)	49.1 (2.6)	39.5 (1.8)	40.4 (1.8)
Base	38.3 (1.6)	41.9 (1.9)	49.1 (2.8)	49.7 (2.7)	40.8 (1.9)	40.9 (1.9)

Table 5.11: Mean chord lengths for the C57BL/6, A/J, and BALB/c strains based on lung region.

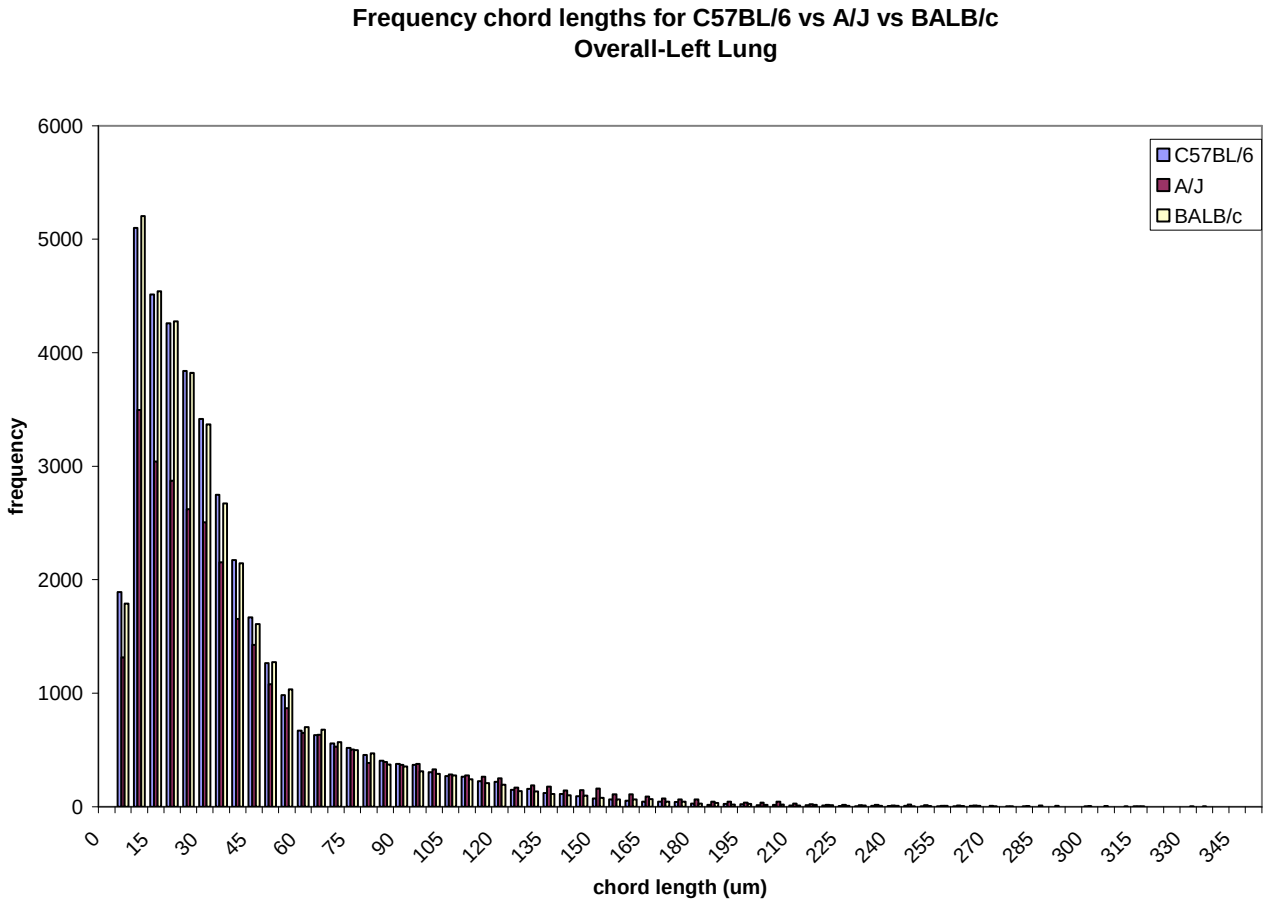

Figure 5.14: Airspace chord length distribution for C57BL/6, A/J, and BALB/c for the left lung. Visible differences in the frequency of chords of the A/J compared to the C57BL/6 and BALB/c strains.

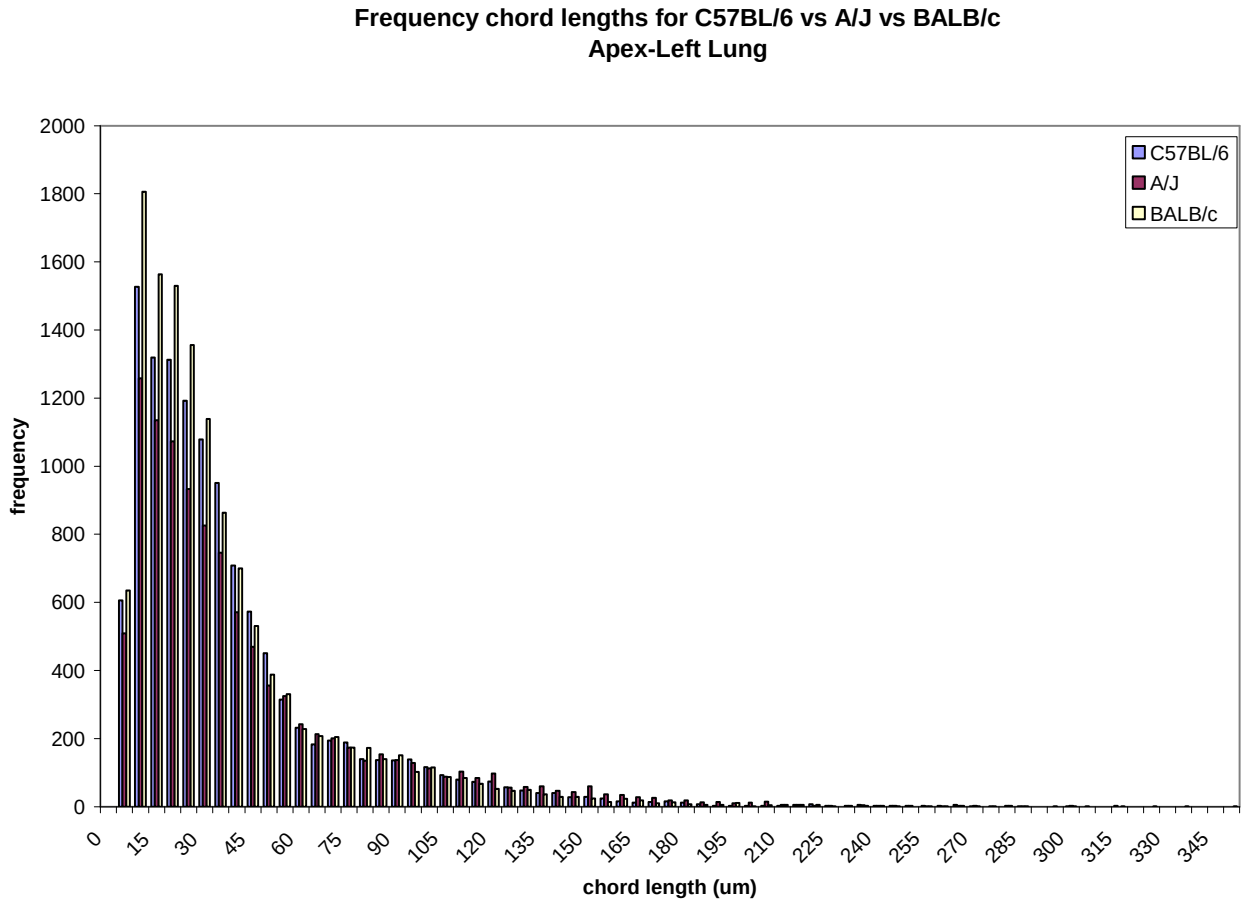

Figure 5.15: Airspace chord length distribution for C57BL/6, A/J, and BALB/c for the apex of the left lung. Visible differences in the frequency of chords of the A/J compared to the C57BL/6 and BALB/c strains.

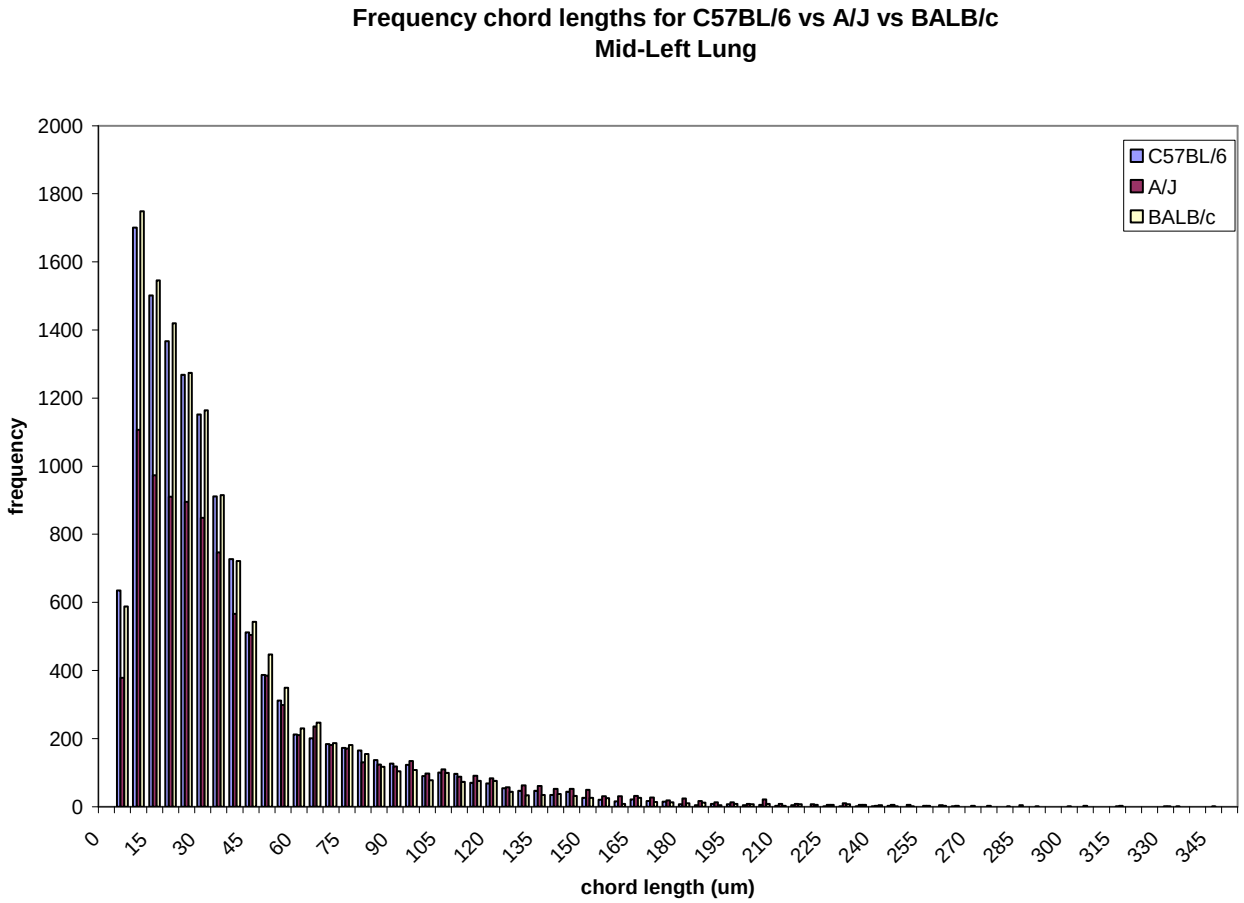

Figure 5.16: Airspace chord length distribution for C57BL/6, A/J, and BALB/c for the middle of the left lung. Visible differences in the frequency of chords of the A/J compared to the C57BL/6 and BALB/c strains.

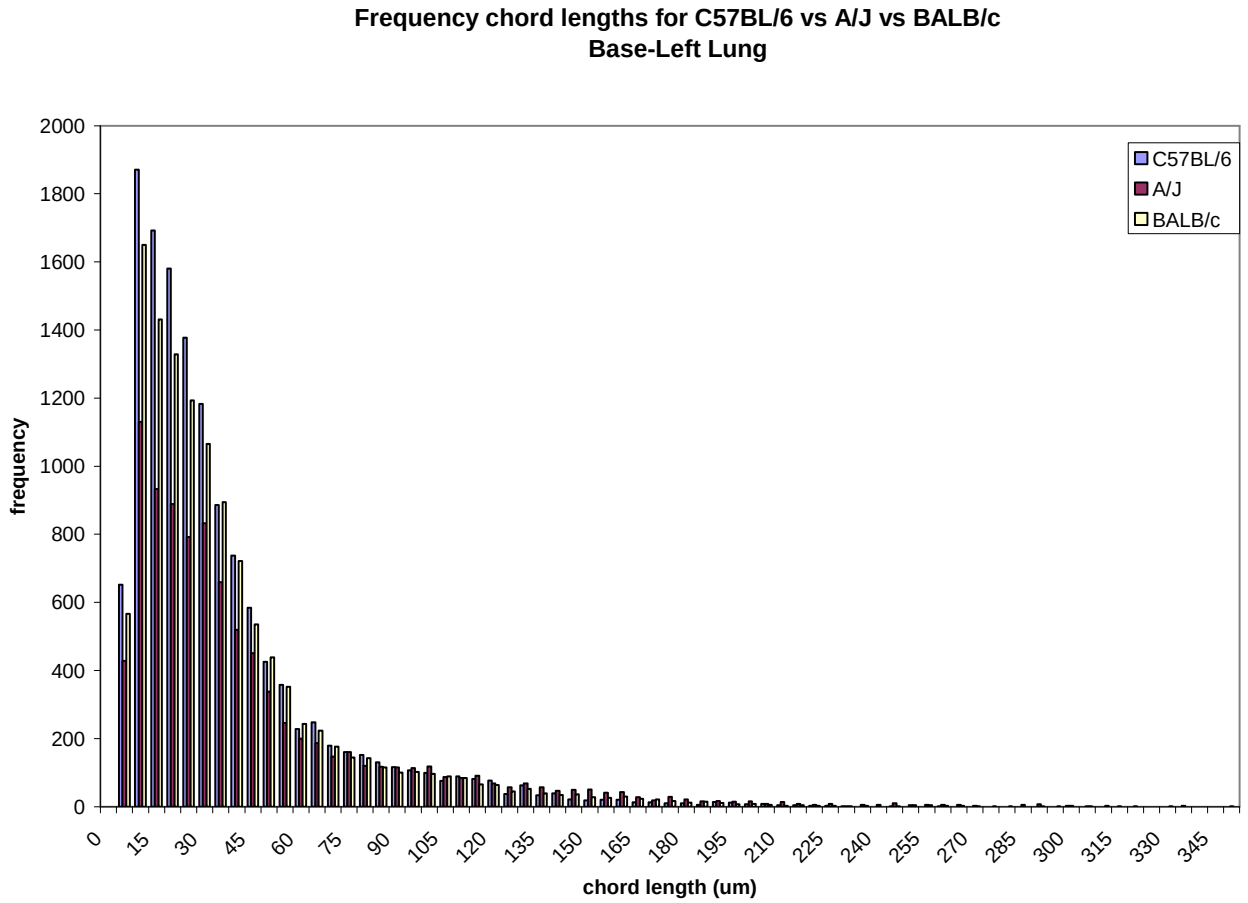

Figure 5.17: Airspace chord length distribution for C57BL/6, A/J, and BALB/c for the base of the left lung. Visible differences in the frequency of chords of the A/J compared to the C57BL/6 and BALB/c strains.

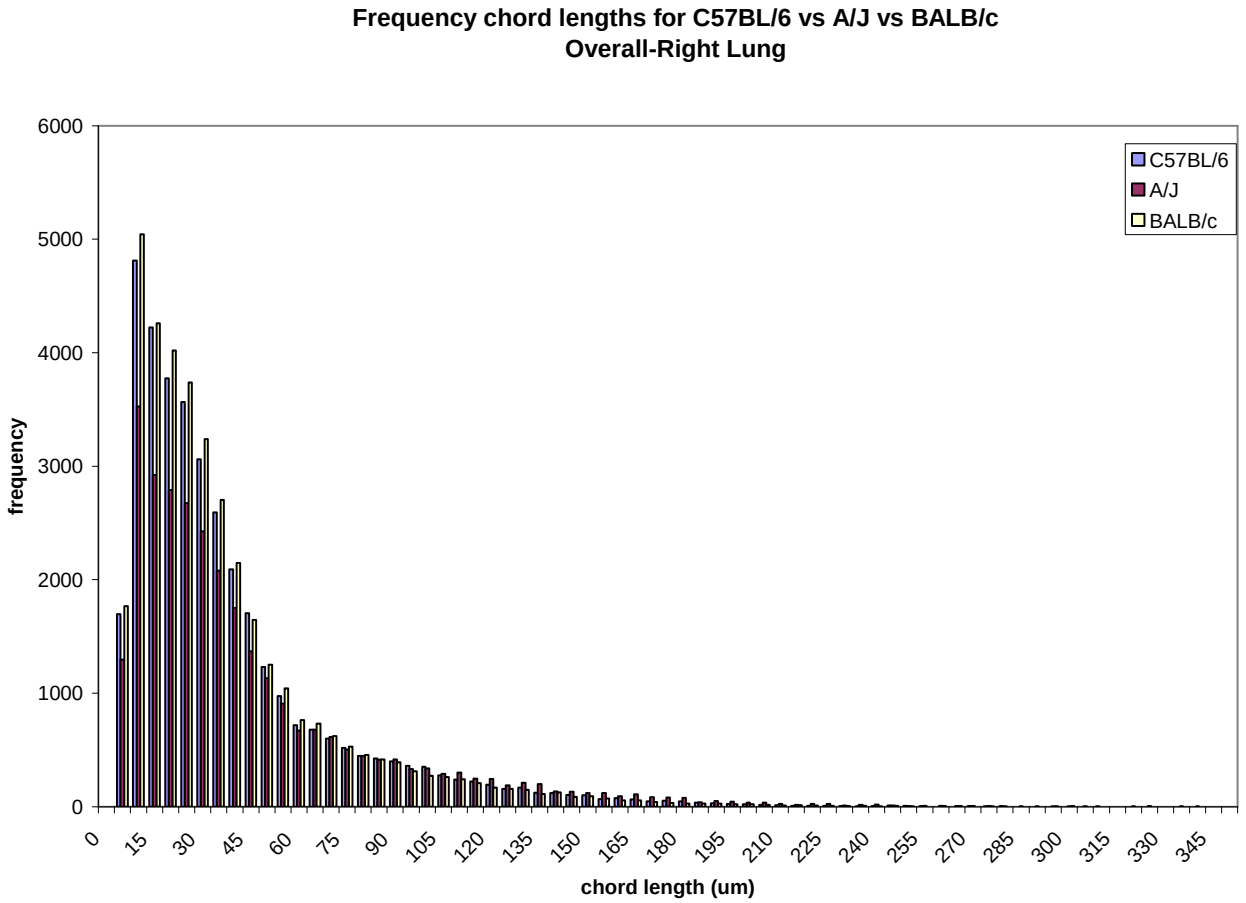

Figure 5.18: Airspace chord length distribution for C57BL/6, A/J, and BALB/c for the right lung. Visible differences in the frequency of chords of the A/J compared to the C57BL/6 and BALB/c strains.

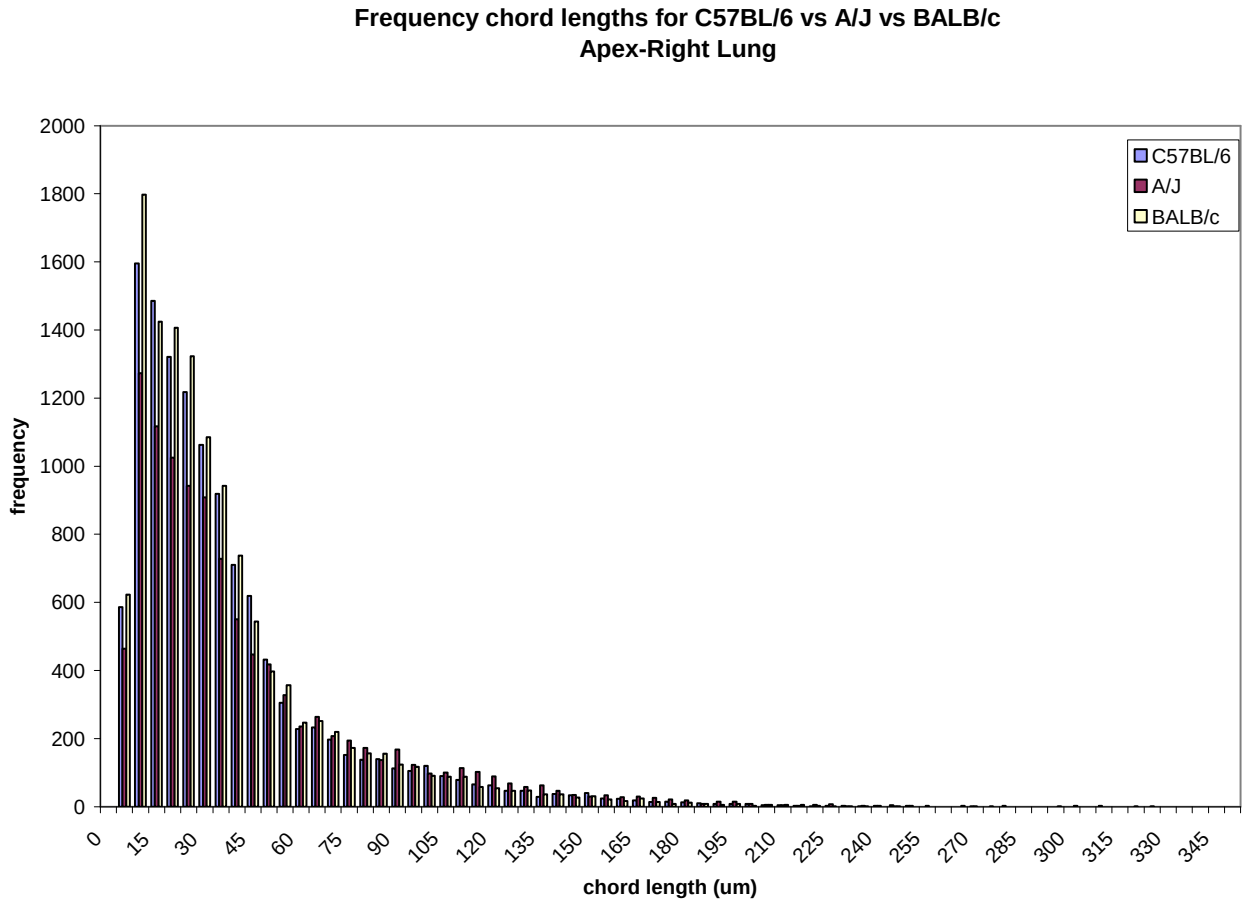

Figure 5.19: Airspace chord length distribution for C57BL/6, A/J, and BALB/c for the apex of the right lung. Visible differences in the frequency of chords of the A/J compared to the C57BL/6 and BALB/c strains.

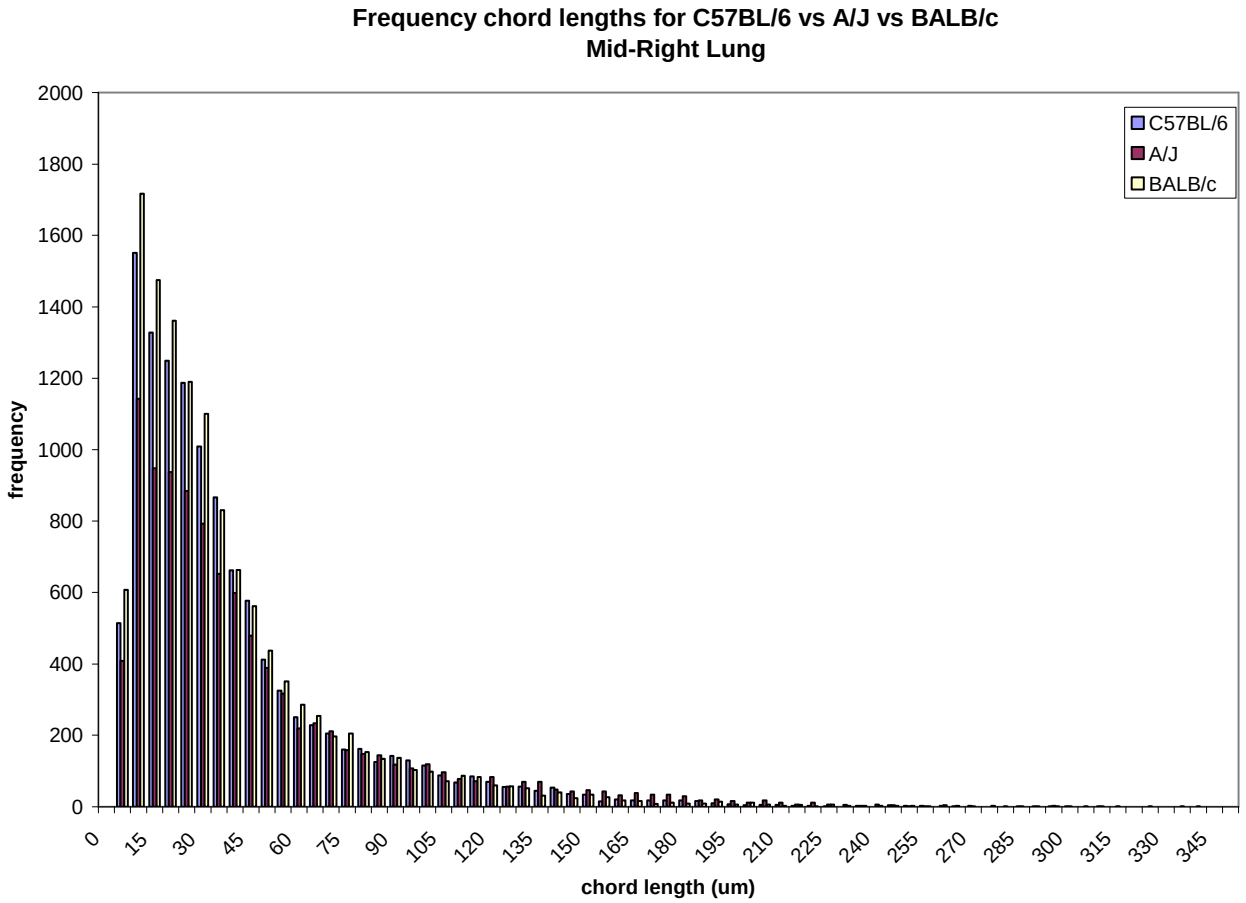

Figure 5.20: Airspace chord length distribution for C57BL/6, A/J, and BALB/c for the middle of the right lung. Visible differences in the frequency of chords of the A/J compared to the C57BL/6 and BALB/c strains.

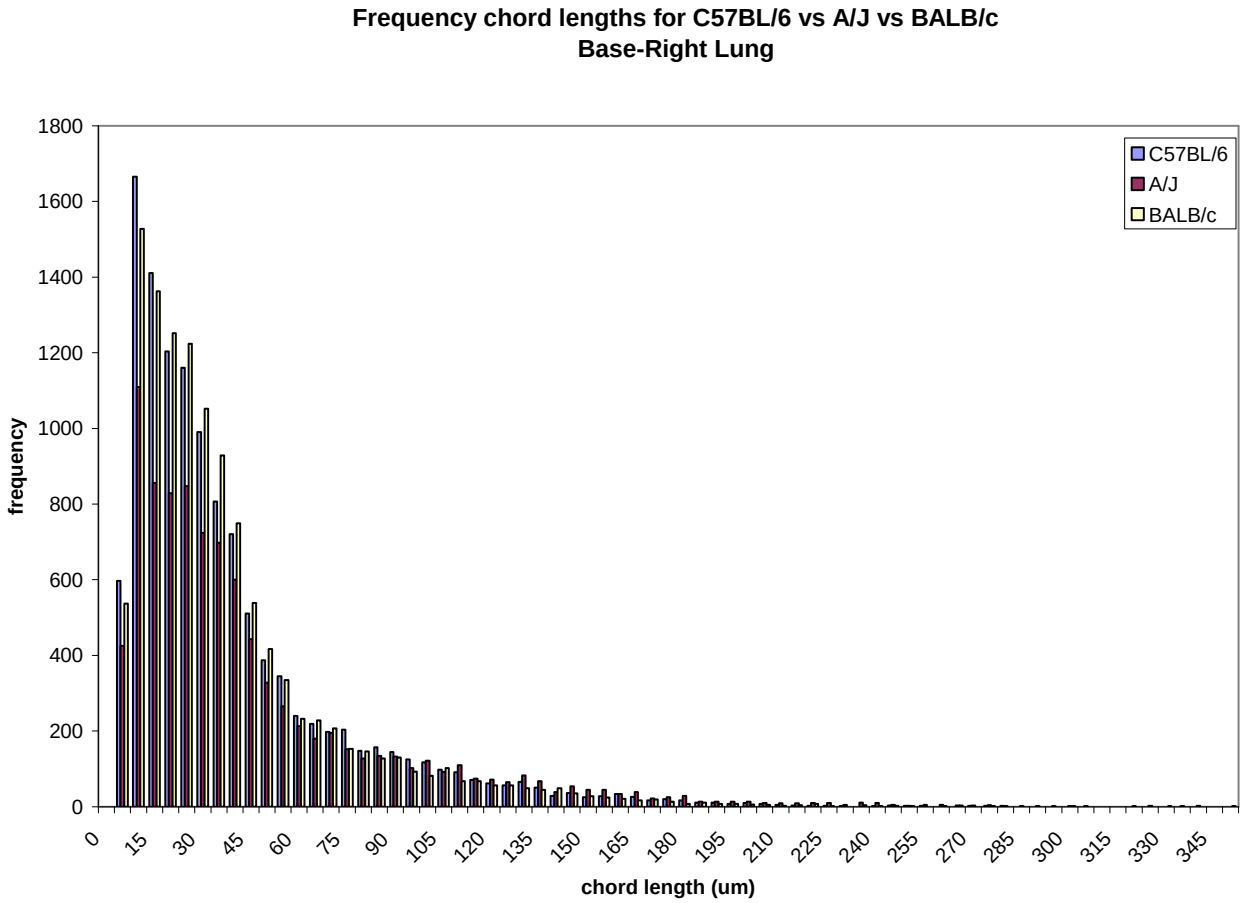

Figure 5.21: Airspace chord length distribution for C57BL/6, A/J, and BALB/c for the base of the right lung. Visible differences in the frequency of chords of the A/J compared to the C57BL/6 and BALB/c strains.

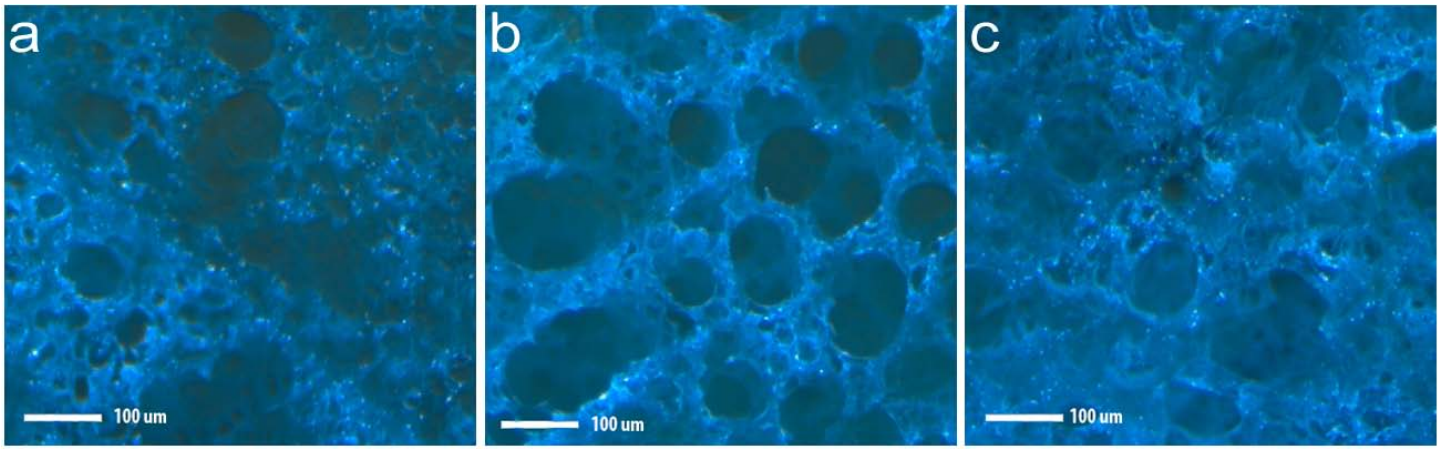

Figure 5.22: Single BFST field of view of the parenchyma for the C57BL/6, A/J, and BALB/c strains. The parenchyma in a) the C57BL/6 appears to have less alveolar ducts than in b) the A/J. Likewise, the parenchyma in c) the BALB/c also appears to have less alveolar ducts than the A/J.

Region	Cord length	Percentage distribution of chord lengths			Odds Ratio (95% Confidence Limits)		
		A/J	BALB/c	C57	A/J vs. BALB/c	A/J vs. C57	BALB/c vs. C57
Right Apex	> 70	19.2	13.4	13.5	1.63 (1.14, 2.34) p=0.007	1.55 (1.17, 2.04) p=0.002	0.95 (0.64, 1.41) p=0.794
	10-65	76.5	81.8	81.8	1.05 (0.91, 1.21) p=0.508	1.02 (0.88, 1.19) p=0.747	0.98 (0.82, 1.16) p=0.793
	<10	4.3	4.8	4.7	-ref-	-ref-	-ref-
Right Mid	> 70	20.3	14.0	15.0	1.74 (1.43, 2.12) p<0.0001	1.65 (1.38, 1.99) p<0.0001	0.95 (0.73, 1.24) p=0.710
	10-65	75.6	81.2	80.0	1.10 (0.98, 1.24) p=0.109	1.16 (0.97, 1.37) p=0.102	1.05 (0.87, 1.27) p=0.630
	<10	4.1	4.8	5.0	-ref-	-ref-	-ref-
Right Base	> 70	21.3	14.0	15.6	1.54 (1.14, 2.09) p=0.005	1.50 (1.23, 1.84) p<0.0001	0.98 (0.69, 1.37) p=0.885
	10-65	74.3	81.5	79.5	0.91 (0.83, 0.99) p=0.038	1.03 (0.92, 1.16) p=0.604	1.13 (0.99, 1.29) p=0.054
	<10	4.5	4.5	4.9	-ref-	-ref-	-ref-
Left Apex	> 70	19.0	13.3	14.5	1.46 (1.15, 1.86) p=0.002	1.36 (1.08, 1.72) p=0.010	0.93 (0.78, 1.12) p=0.435
	10-65	76.3	81.8	80.6	0.95 (0.84, 1.08) p=0.446	0.98 (0.87, 1.11) p=0.789	1.03 (0.99, 1.08) p=0.151
	<10	4.8	4.9	5.0	-ref-	-ref-	-ref-
Left Mid	> 70	19.8	12.9	13.7	1.87 (1.46, 2.38) p<0.0001	1.91 (1.52, 2.40) p<0.0001	1.02 (0.82, 1.28) p=0.837
	10-65	76.5	82.5	81.3	1.12 (0.99, 1.28) p=0.080	1.25 (1.02, 1.55) p=0.033	1.12 (0.93, 1.35) p=0.247
	<10	3.8	4.6	5.0	-ref-	-ref-	-ref-
Left Base	> 70	20.2	13.4	12.1	1.56 (1.17, 2.07) p=0.002	1.79 (1.53, 2.10) p<0.0001	1.15 (0.89, 1.49) p=0.278
	10-65	75.3	82.0	83.0	0.95 (0.89, 1.02) p=0.154	0.98 (0.92, 1.04) p=0.471	1.03 (0.98, 1.08) p=0.307
	<10	4.5	4.6	4.9	-ref-	-ref-	-ref-

Table 5.12: Percentage distribution of chord lengths and the odds ratios of chord length ≥ 70 µm (and 10-65 µm) relative to chord length < 10 µm between strains.

CHAPTER 6

SUMMARY AND FUTURE DIRECTIONS

6.1 Summary of Contributions

In this research, we confirmed our hypothesis that the 'normal' mouse lung anatomy consists of a spectrum of characteristics and that significant differences in lung structure exist between the C57BL/6, A/J, and BALB/c inbred mouse strains. As an outcome, we have characterized the lung structure phenotypes including the lobes, tracheobronchial tree, and peripheral airspace.

We have successfully completed the specific aims of this research which include:

Specific Aim 1: The development of an image acquisition sequence for collection of the *in vivo* micro-CT, *ex vivo* micro-CT, LIMA, and histology datasets for the mouse lung.

Specific Aim 2: Define the smallest anatomical structure of the mouse lung that can be resolved using the Siemens Micro-CAT II micro-CT system

Specific Aim 3: Characterize the normal mouse lung anatomy including the lobes and tracheobronchial tree in the C57BL/6, A/J, and BALB/c inbred mouse strains using *in vivo* micro-CT.

Specific Aim 4: Assess the lung parenchyma airspace in the C57BL/6, A/J, and BALB/c strains.

In this work we have developed the experimental methods necessary for *in vivo* and *ex vivo* mouse lung imaging, as described in Chapter 3. This spanned developing animal handling, anesthesia protocols, and micro-surgical techniques to undertaking *in vivo* micro-CT imaging utilizing a novel breath hold approach for acquiring high resolution images. The development of a tissue fixation protocol was necessary for successful *ex vivo* imaging between the micro-CT, LIMA, and histology. The incorporation of the LIMA system in this study provided a means to directly correlate the

ex vivo micro-CT image data to histology since it maintains spatial correspondence. In addition, specific hardware modifications were developed in order to improve image acquisition and detection of lung structures. This included: a mouse lung orientation device custom fit to the micro-CT bed and the LIMA specimen stage, a dynamic embedment container for successful sectioning of the mouse lung using the LIMA system, and the development of a unique illumination device, BFST, for increased surface contrast of lung tissue for improved identification of lung structure boundaries in the LIMA images. Finally, the modification of protocols for processing and embedding mouse lung tissue sections with agarose from the LIMA system for histology was perfromed (Specific aim 1).

Image processing and analysis techniques were implemented for visualization and quantification of the normal lung structure in the C57BL/6, A/J, and BALB/c mice, as discussed in Chapter 4. For each imaging modality, including *in vivo* and *ex vivo* micro-CT, LIMA and histology, processing and analysis of images was completed for extraction of lung structures including the entire lung, individual lobes, and the airway tree as well as identification of the airspaces of the parenchyma (alveoli and alveolar ducts). In order to compare image information between datasets, registration techniques were employed, while the LIMA system served as the reference. This important imaging tool provided a means for defining the smallest lung structures in the micro-CT images through registration with the LIMA, BFST, and histology image data (Specific aim 2). Validation of the manual airway segmentation technique was completed through assessment of overlapping regions using the κ metric with three observers. Finally, micro-CT measured airway structures were validated using the LIMA system.

The micro-CT image data was compiled (Chapter 5) to characterize the *in vivo* lung structure phenotypes. This included anatomical and volume analysis of the total lung, individual lobar structures, and visualization and comprehensive quantification of the airway tree. The development of a mouse airway nomenclature was also necessary

for the characterization of the *in vivo* airway tree structures as well as for comparative analysis of the airway structures between the inbred mouse strains utilized in this research (Specific aim 3).

Finally, the assessment of the peripheral airspace was made through the development of an automated airspace analysis program for evaluation of the mean chord length metric from digitized H&E histology slides (Specific aim 4).

6.2 Research Limitations

The greatest limitation that we encountered in this research was the extremely time intensive processes that prevented high throughput analysis of the mouse lung structure phenotypes. The acquisition time for collecting the data for a single mouse lung was over 70 hours (conservative estimate) and this did not include the processing and analysis time that was necessary for extracting the lung structure information. For instance, on average a micro-CT scan is 8x's larger in size than a standard CT scan. Since manual techniques were utilized for many of the processing and analysis techniques for these large datasets, the number of samples that could be completed was limited. The potential for high throughput analysis ultimately lies in the availability of automated techniques.

Successful imaging the mouse lung *in vivo* included a gating technique that would improve the image quality of the micro-CT system. The IIBH technique used during the imaging process utilized a forced airway pressure which may or may not represent the true inflation state of a spontaneously breathing mouse. In addition, the accurate pressure range in the spontaneously breathing mouse is unknown and it is uncertain if the positive pressure (rather than negative pressure) induced any error in the airway metrics.

Finally, the manual segmentation of the airways provides valuable first pass data and we have shown that the variability is low enough to identify significant differences between the normal airways in these three strains of mice. However, measurements were

not generated perpendicular to the centerline of the airway and several of the segments could not be measured since they were parallel to the imaging plane and were omitted (ApRMB2 and LBA2).

Although these limitations exist, the knowledge of the normal mouse lung anatomy has been greatly expanded through this research. Advancements in the techniques for imaging the mouse lung have been made and the potential for developing automated techniques for analyzing the current image data with manual segmentations and measurements for validation are now available.

6.3 Future Directions

There are many future directions that would lead to the advancement of the research that was undertaken in this thesis. First, improvements to the micro-CT image reconstruction algorithms could potentially increase the image quality and the ability to distinguish lung structures. The improvements would include reduction of ring artifacts, beam hardening, and thermal noise variations in and across datasets. This would also aid in the development of automated segmentation algorithms, which leads to the second direction that should be undertaken—the development of multiple automated lung structure segmentation algorithms. The extremely time intensive process of manually segmenting and analyzing such large datasets prevents the ability to perform high throughput analysis. Therefore, the development of automated mouse lung, lobe and airway segmentation algorithms would be the first step in decreasing processing time. In addition, the development an automated lung, lobe and airway analysis package would be necessary for improved lung structure quantitative analysis. This would include an airway centerline and the ability to output airway diameters perpendicular to the airway segment. In addition, branch length and volume as well as lung, lobe volume and density measurements would be extremely valuable.

The development of automated techniques for processing and analysis of the image data would allow a high throughput investigation of inbred mouse strains that we have not looked at in this research. Some additional strains of interest include the C3H/HeJ, FVB/nJ, 129Sv/ImJ, and the SWR/J where lung function values have been collected but lung structure is still unknown.

A comprehensive knowledge of the airway wall composition would also prove highly valuable as a future direction. We have preliminarily identified differences in the amount of smooth muscle between these inbred mouse strains. Further investigation of the amount, distribution and orientation of smooth muscle between the different strains of mice must be performed

We have identified significant differences in the peripheral airspace between the A/J and C57BL/6 and BALB/c strains. Further investigation of the peripheral airspace differences between the three strains of mice studied is necessary. This would include calculating the number of alveoli as well as alveolar ducts in the C57BL/6, A/J, and BALB/c inbred strains through unbiased stereological techniques.

Finally, the compilation of the mouse lung structure phenotype metrics into the Jackson Lab's MPD would be highly useful to future researchers interested in studying the structure and function relationship in the lungs of normal and diseased inbred mouse strains. The data we have acquired in this research is the most comprehensive analysis undertaken on the same mouse lung and includes *in vivo* and *ex vivo* lung metrics. In addition, the availability of these image datasets for future research including the development of automated processing and analysis techniques, education for biomedical scientists interested in pulmonary research, and development of new pulmonary imaging modalities for the mouse including optical tomography.

REFERENCES

[1] JAX, "Mouse Genome Informatics," vol. 2007, 2007.

[2] J. M. Drazen, P. W. Finn, and G. T. De Sanctis, "Mouse models of airway responsiveness: physiological basis of observed outcomes and analysis of selected examples using these outcome indicators," *Annu Rev Physiol*, vol. 61, pp. 593-625, 1999.

[3] J. Gil, *Models of Lung Disease. Lung Biology in Health and Disease*, vol. 47. New York: Marcel Dekker, 1990.

[4] E. J. a. T. Jacks, "Murine Lung Cancer Models," in *MMHCC the Mouse Models of Human Cancers Consortium*, 2007.

[5] S. D. Shapiro, "Transgenic and gene-targeted mice as models for chronic obstructive pulmonary disease," *Eur Respir J*, vol. 29, pp. 375-8, 2007.

[6] N. L. Ford, M. M. Thornton, and D. W. Holdsworth, "Fundamental image quality limits for microcomputed tomography in small animals," *Med Phys*, vol. 30, pp. 2869-77, 2003.

[7] E. L. Ritman, "Micro-computed tomography of the lungs and pulmonary-vascular system," *Proc Am Thorac Soc*, vol. 2, pp. 477-80, 501, 2005.

[8] E. L. Ritman, "Micro-computed tomography-current status and developments," *Annu Rev Biomed Eng*, vol. 6, pp. 185-208, 2004.

[9] E. L. Ritman, "Molecular imaging in small animals--roles for micro-CT," *J Cell Biochem Suppl*, vol. 39, pp. 116-24, 2002.

[10] T. Sera, N. Yagi, and K. Uesugi, "Three-dimensional visualization of intact mouse lung by synchrotron radiation CT," presented at 26th Annual International Conference of the IEEE EMBS, San Francisco, CA, USA, 2004.

[11] J. Sijbers and A. Postnov, "Reduction of ring artefacts in high resolution micro-CT reconstructions," *Phys Med Biol*, vol. 49, pp. N247-53, 2004.

[12] D. Cavanaugh, E. Johnson, R. E. Price, J. Kurie, E. L. Travis, and D. D. Cody, "In vivo respiratory-gated micro-CT imaging in small-animal oncology models," *Mol Imaging*, vol. 3, pp. 55-62, 2004.

[13] J. B. West, *Respiratory Physiology: The Essentials*, Seventh ed: Lippincott Williams & Wilkins, 2005.

[14] M. A. Bedell, N. A. Jenkins, and N. G. Copeland, "Mouse models of human disease. Part I: techniques and resources for genetic analysis in mice," *Genes Dev*, vol. 11, pp. 1-10, 1997.

[15] P. L. a. D. K. Altman, D, *Inbred and genetically defined strains of laboratory animals*. Bethesda, 1979.

[16] H. Hedrich, *The Laboratory Mouse*: Elsevier Academic Press, 2004.

[17] L. M. Silver, *Mouse Genetics: Concepts and Applications*: Oxford University Press, 1995.

[18] J. A. Beck, S. Lloyd, M. Hafezparast, M. Lennon-Pierce, J. T. Eppig, M. F. Festing, and E. M. Fisher, "Genealogies of mouse inbred strains," *Nat Genet*, vol. 24, pp. 23-5, 2000.

[19] R. P. Erickson, "Mouse models of human genetic disease: which mouse is more like a man?," *Bioessays*, vol. 18, pp. 993-8, 1996.

[20] N. L. Ford, "Optimization of micro-computed tomography techniques for *in vivo* small-animal imaging," in *Medical Biophysics*, vol. Doctor of Philosophy. London, Ontario: The University of Western Ontario, 2005, pp. 126.

[21] J. M. Arbeit and R. Hirose, "Murine mentors: transgenic and knockout models of surgical disease," *Ann Surg*, vol. 229, pp. 21-40, 1999.

[22] K. Shinagawa and M. Kojima, "Mouse model of airway remodeling: strain differences," *Am J Respir Crit Care Med*, vol. 168, pp. 959-67, 2003.

[23] J. N. Kline, K. Kitagaki, T. R. Businga, and V. V. Jain, "Treatment of established asthma in a murine model using CpG oligodeoxynucleotides," *Am J Physiol Lung Cell Mol Physiol*, vol. 283, pp. L170-9, 2002.

[24] M. Lomask, "Further exploration of the Penh parameter," *Exp Toxicol Pathol*, vol. 57 Suppl 2, pp. 13-20, 2006.

[25] L. K. Lundblad, C. G. Irvin, A. Adler, and J. H. Bates, "A reevaluation of the validity of unrestrained plethysmography in mice," *J Appl Physiol*, vol. 93, pp. 1198-207, 2002.

[26] C. Reinhard, G. Eder, H. Fuchs, A. Ziesenis, J. Heyder, and H. Schulz, "Inbred strain variation in lung function," *Mamm Genome*, vol. 13, pp. 429-37, 2002.

[27] H. Schulz, C. Johner, G. Eder, A. Ziesenis, P. Reitmeier, J. Heyder, and R. Balling, "Respiratory mechanics in mice: strain and sex specific differences," *Acta Physiol Scand*, vol. 174, pp. 367-75, 2002.

[28] K. Takeda, A. Haczku, J. J. Lee, C. G. Irvin, and E. W. Gelfand, "Strain dependence of airway hyperresponsiveness reflects differences in eosinophil localization in the lung," *Am J Physiol Lung Cell Mol Physiol*, vol. 281, pp. L394-402, 2001.

[29] C. G. Tankersley, R. S. Fitzgerald, and S. R. Kleeberger, "Differential control of ventilation among inbred strains of mice," *Am J Physiol*, vol. 267, pp. R1371-7, 1994.

[30] C. G. Tankersley, R. Rabold, and W. Mitzner, "Differential lung mechanics are genetically determined in inbred murine strains," *J Appl Physiol*, vol. 86, pp. 1764-9, 1999.

[31] C. G. Irvin and J. H. Bates, "Measuring the lung function in the mouse: the challenge of size," *Respir Res*, vol. 4, pp. 4, 2003.

[32] M. J. Oldham and R. F. Phalen, "Dosimetry implications of upper tracheobronchial airway anatomy in two mouse varieties," *Anat Rec*, vol. 268, pp. 59-65, 2002.

[33] S. E. Soutiere and W. Mitzner, "On defining total lung capacity in the mouse," *J Appl Physiol*, vol. 96, pp. 1658-64, 2004.

[34] K. P. Valerius, "Size-dependent morphology of the conductive bronchial tree in four species of myomorph rodents," *J Morphol*, vol. 230, pp. 291-7, 1996.

[35] B. R. Wallau, A. Schmitz, and S. F. Perry, "Lung morphology in rodents (Mammalia, Rodentia) and its implications for systematics," *J Morphol*, vol. 246, pp. 228-48, 2000.

[36] S. E. Soutiere, C. G. Tankersley, and W. Mitzner, "Differences in alveolar size in inbred mouse strains," *Respir Physiol Neurobiol*, vol. 140, pp. 283-91, 2004.

[37] V. E. Fernandez, V. McCaskill, N. D. Atkins, and A. Wanner, "Variability of airway responses in mice," *Lung*, vol. 177, pp. 355-66, 1999.

[38] D. P. Schuster, A. Kovacs, J. Garbow, and D. Piwnica-Worms, "Recent advances in imaging the lungs of intact small animals," *Am J Respir Cell Mol Biol*, vol. 30, pp. 129-38, 2004.

[39] N. L. Ford, E. L. Martin, J. F. Lewis, R. A. Veldhuizen, M. Drangova, and D. W. Holdsworth, "In vivo characterization of lung morphology and function in anesthetized free-breathing mice using micro-computed tomography," *J Appl Physiol*, vol. 102, pp. 2046-55, 2007.

[40] E. Namati, D. Chon, J. Thiesse, E. A. Hoffman, J. de Ryk, A. Ross, and G. McLennan, "In vivo micro-CT lung imaging via a computer-controlled intermittent iso-pressure breath hold (IIBH) technique," *Phys Med Biol*, vol. 51, pp. 6061-75, 2006.

[41] S. K. Carlson, K. L. Classic, C. E. Bender, and S. J. Russell, "Small animal absorbed radiation dose from serial micro-computed tomography imaging," *Mol Imaging Biol*, vol. 9, pp. 78-82, 2007.

[42] J. Thiesse, E. Namati, J. De Ryk, E. A. Hoffman, J. M. Reinhardt, and G. McLennan, "Three dimensional anatomical description of the normal airway tree in three strains of mice " presented at American Thoracic Society, San Francisco, CA, 2007.

[43] J. Thiesse, J. M. Reinhardt, J. De Ryk, E. Namati, E. A. Hoffman, and G. McLennan, "Three dimensional visual truth of the normal airway tree for use as a quantitative comparison to micro-CT reconstructions," presented at SPIE Medical Imaging, 2005.

[44] L. Junqueira and J. Carneiro, "Basic Histology: Text & Atlas, 11th edition," McGraw Hill 2005.

[45] M. Ochs, "A brief update on lung stereology," J Microsc, vol. 222, pp. 188-200, 2006.

[46] E. Namati, J. de Ryk, J. Thiesse, Z. Towfic, E. Hoffman, and G. McLennan, "Large Image Microscope Array for the Compilation of Multimodality Whole Organ Image Databases," *Anat Rec (Hoboken)*, vol. 290, pp. 1377-1387, 2007.

[47] D. Aykac, E. A. Hoffman, G. McLennan, and J. M. Reinhardt, "Segmentation and analysis of the human airway tree from three-dimensional X-ray CT images," *IEEE Trans Med Imaging*, vol. 22, pp. 940-50, 2003.

[48] A. P. Kiraly, W. E. Higgins, G. McLennan, E. A. Hoffman, and J. M. Reinhardt, "Three-dimensional human airway segmentation methods for clinical virtual bronchoscopy," *Acad Radiol*, vol. 9, pp. 1153-68, 2002.

[49] J. Tschirren, E. A. Hoffman, G. McLennan, and M. Sonka, "Intrathoracic airway trees: segmentation and airway morphology analysis from low-dose CT scans," *IEEE Trans Med Imaging*, vol. 24, pp. 1529-39, 2005.

[50] L. Shi, J. Thiesse, G. McLennan, E. A. Hoffman, and J. M. Reinhardt, "Three dimensional murine airway segmentation in micro-CT images," presented at SPIE Medical Imaging, San Diego, CA, 2007.

[51] A. Chaturvedi and Z. Lee, "Three-dimensional segmentation and skeletonization to build an airway tree data structure for small animals," *Phys Med Biol*, vol. 50, pp. 1405-19, 2005.

[52] E. R. Weibel, C. C. Hsia, and M. Ochs, "How much is there really? Why stereology is essential in lung morphometry," *J Appl Physiol*, vol. 102, pp. 459-67, 2007.

[53] D. M. Hyde, N. K. Tyler, and C. G. Plopper, "Morphometry of the respiratory tract: avoiding the sampling, size, orientation, and reference traps," *Toxicol Pathol*, vol. 35, pp. 41-8, 2007.

[54] J. D. Escolar, M. A. Escolar, J. Guzman, and M. Roques, "Pressure volume curve and alveolar recruitment/de-recruitment. A morphometric model of the respiratory cycle," *Histol Histopathol*, vol. 17, pp. 383-92, 2002.

[55] H. Lum, I. Huang, and W. Mitzner, "Morphological evidence for alveolar recruitment during inflation at high transpulmonary pressure," *J Appl Physiol*, vol. 68, pp. 2280-6, 1990.

[56] W. Mitzner, "Use of mean airspace chord length (Lm) to assess emphysema," *J Appl Physiol*, 2008.

[57] JAX, "Mouse Phenome Database," vol. 2007, 2007.

[58] D. E. a. M. M. M. I. Project, "Pulmonary Airway Tree," vol. 2008, 2006.

[59] NIH, "Comparative Medicine Branch: Mouse Necropsy," 2006.

[60] J. H. Bates and C. G. Irvin, "Measuring lung function in mice: the phenotyping uncertainty principle," *J Appl Physiol*, vol. 94, pp. 1297-306, 2003.

[61] JAX, "Mouse Anesthesia and Analgesia," presented at Phenotyping Mouse Models of Human Lung Disease, Bar Harbor, ME, 2008.

[62] E. R. Heitzman, *The Lung: Radiologic-pathologic correlations*, 2nd edition ed. St. Louis, Missouri: Mosby, 1984.

[63] P. Blumler, R. H. Acosta, A. Thomas-Semm, and S. Reuss, "Lung fixation for the preservation of air spaces," *Exp Lung Res*, vol. 30, pp. 73-82, 2004.

[64] R. Renne, X. Fouillet, J. Maurer, A. Assaad, K. Morgan, F. Ha, K. Nikula, N. Gillet, and M. Copley, "Recommendation of optimal method for formalin fixation of rodent lungs in routine toxicology studies," *Toxicol Pathol*, vol. 29, pp. 587-9, 2001.

[65] M. L. Crosfill and J. G. Widdicombe, "Physical characteristics of the chest and lungs and the work of breathing in different mammalian species," *J Physiol*, vol. 158, pp. 1-14, 1961.

[66] D. L. C. Feldkamp L A, and Kress J W, "Practical cone-beam algorithm," *J Opt. Soc. Am.*, vol. 1, pp. 612-619, 1984.

[67] S. P. Zehntner, M. M. Chakravarty, R. J. Bolovan, C. Chan, and B. J. Bedell, "Synergistic tissue counterstaining and image segmentation techniques for accurate, quantitative immunohistochemistry," *J Histochem Cytochem*, vol. 56, pp. 873-80, 2008.

[68] S. K. Boyd, S. Moser, M. Kuhn, R. J. Klinck, P. L. Krauze, R. Muller, and J. A. Gasser, "Evaluation of three-dimensional image registration methodologies for in vivo micro-computed tomography," *Ann Biomed Eng*, vol. 34, pp. 1587-99, 2006.

[69] J. P. Pluim, J. B. Maintz, and M. A. Viergever, "Mutual-information-based registration of medical images: a survey," *IEEE Trans Med Imaging*, vol. 22, pp. 986-1004, 2003.

[70] E. A. Boyden, *Segmental Anatomy of the Lungs: A Study of the Patterns of the Segmental Bronchi and Related Pulmonary Vessels*: McGraw-Hill Book Company, 1955.

[71] R. B. George, *Chest Medicine: Essentials of Pulmonary and Critical Care Medicine*, Fifth Edition ed: Lippincott Williams & Wilkins.

[72] K. Horsfield and G. Cumming, "Morphology of the bronchial tree in man," *J Appl Physiol*, vol. 24, pp. 373-83, 1968.

[73] E. R. Weibel, *Morphometry of the human lung.* Berlin: Springer, 1963.

[74] J. Tschirren, G. McLennan, K. Palagyi, E. A. Hoffman, and M. Sonka, "Matching and anatomical labeling of human airway tree," *IEEE Trans Med Imaging*, vol. 24, pp. 1540-7, 2005.

[75] A. Duguet, K. Biyah, E. Minshall, R. Gomes, C. G. Wang, M. Taoudi-Benchekroun, J. H. Bates, and D. H. Eidelman, "Bronchial responsiveness among inbred mouse strains. Role of airway smooth-muscle shortening velocity," *Am J Respir Crit Care Med*, vol. 161, pp. 839-48, 2000.

[76] A. James and N. Carroll, "Airway smooth muscle in health and disease; methods of measurement and relation to function," *Eur Respir J*, vol. 15, pp. 782-9, 2000.

[77] C. G. Tankersley, D. A. DiSilvestre, A. E. Jedlicka, H. M. Wilkins, and L. Zhang, "Differential inspiratory timing is genetically linked to mouse chromosome 3," *J Appl Physiol*, vol. 85, pp. 360-5, 1998.

[78] J. T. Heverhagen, H. K. Hahn, M. Wegmann, U. Herz, C. D. Shaffer Whitaker, V. Matschl, and H. Alfke, "Volumetric analysis of mice lungs in a clinical magnetic resonance imaging scanner," *Magma*, vol. 17, pp. 80-5, 2004.

[79] W. Mitzner, R. Brown, and W. Lee, "In vivo measurement of lung volumes in mice," *Physiol Genomics*, vol. 4, pp. 215-21, 2001.

APPENDIX

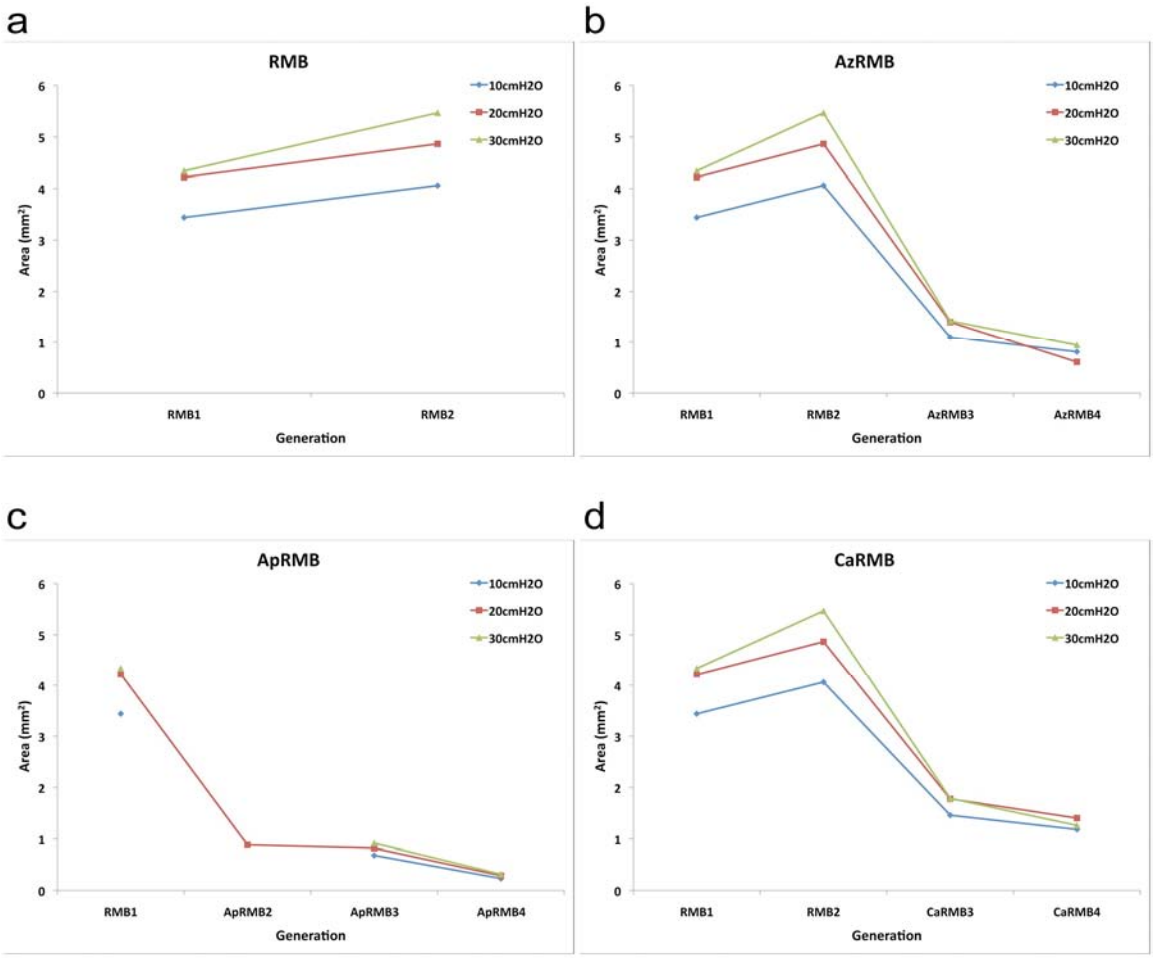

Figure A1: C57BL/6 Area vs Generation for RMB, AzRMB, ApRMB and CaRMB.

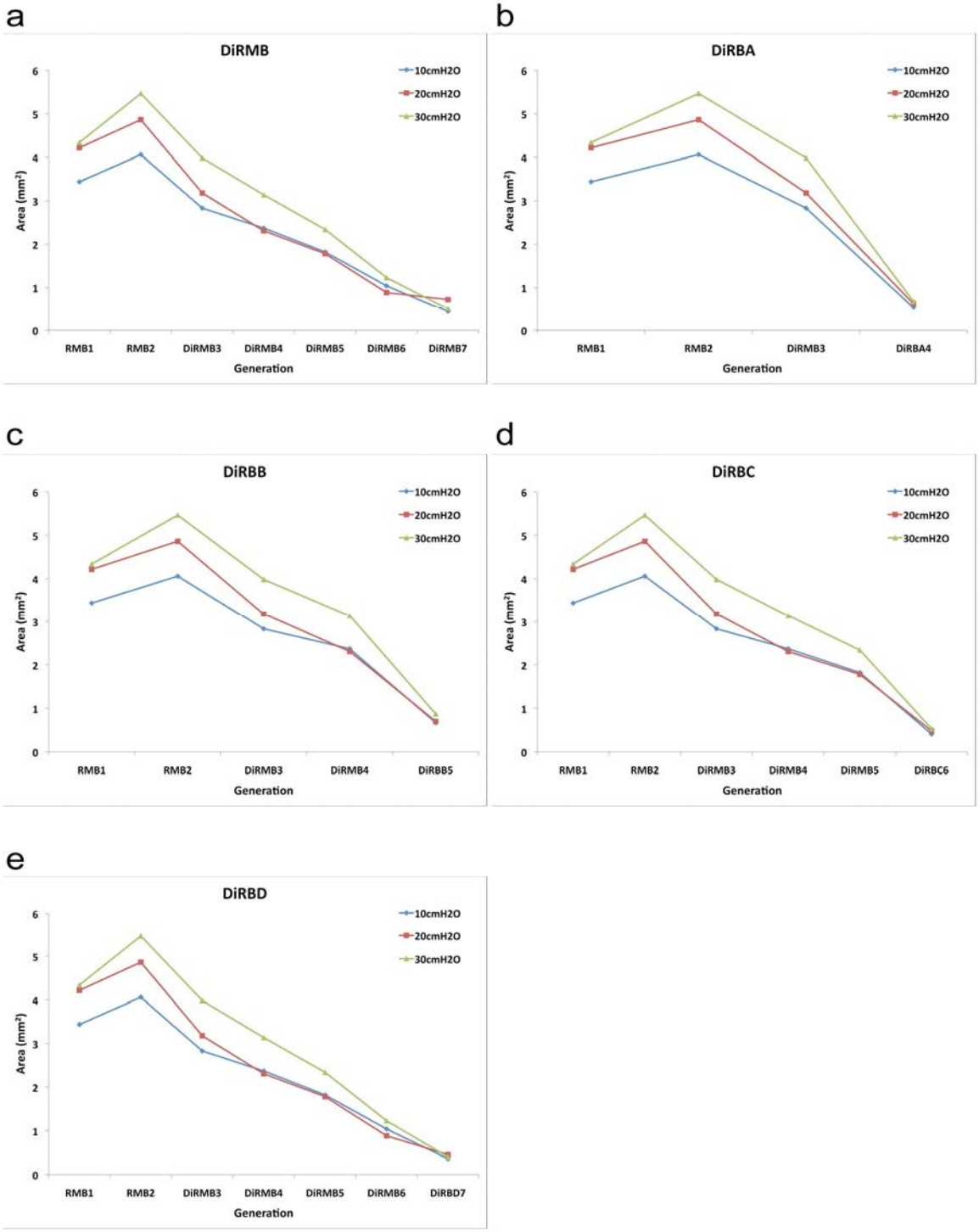

Figure A2: C57Bl/6 Area vs Generation for DiRMB, DiRBA, DiRBB, DiRBC, and DiRBD.

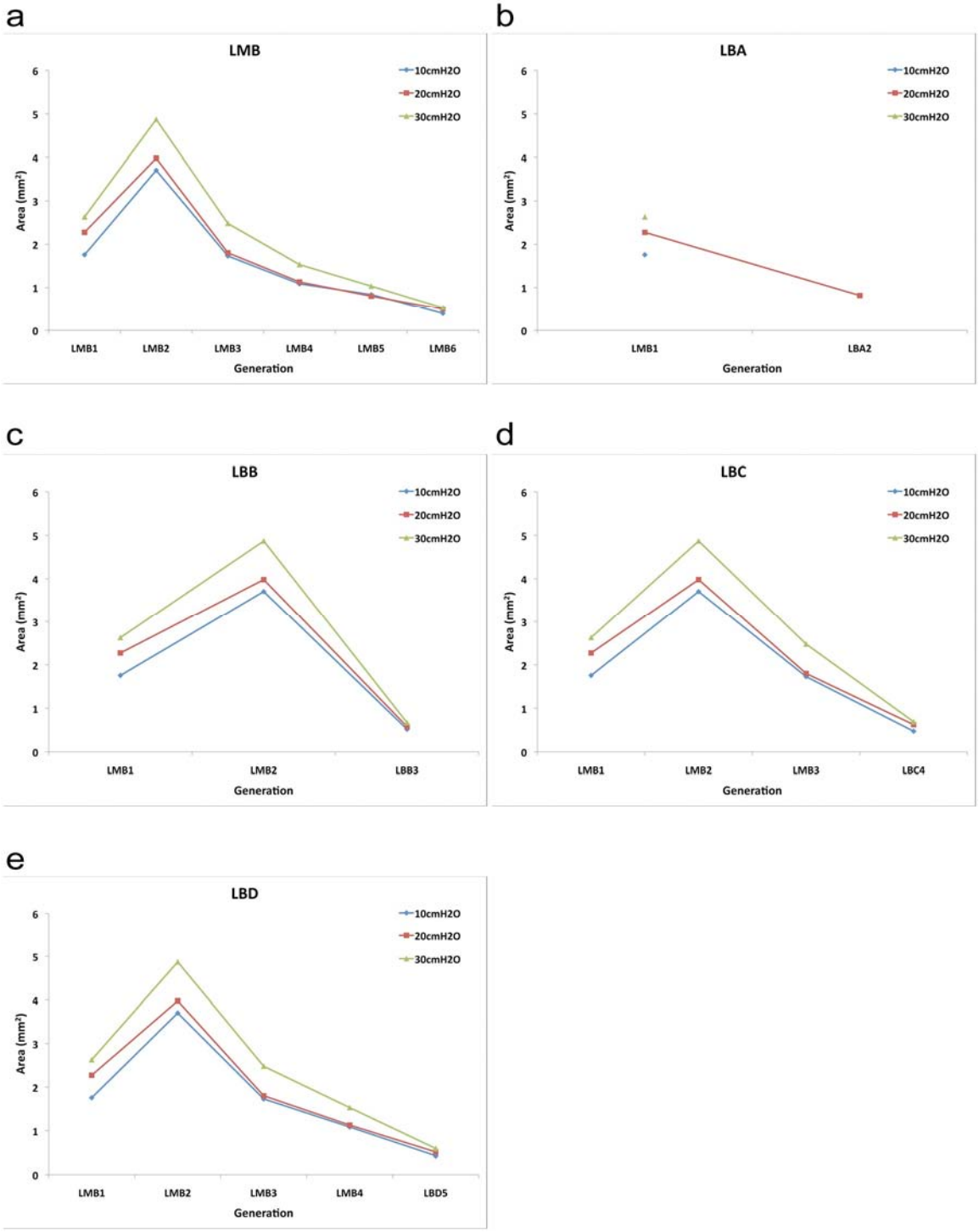

Figure A3: C57Bl/6 Area vs Generation for LMB, LBA, LBB, LBC and LBD.

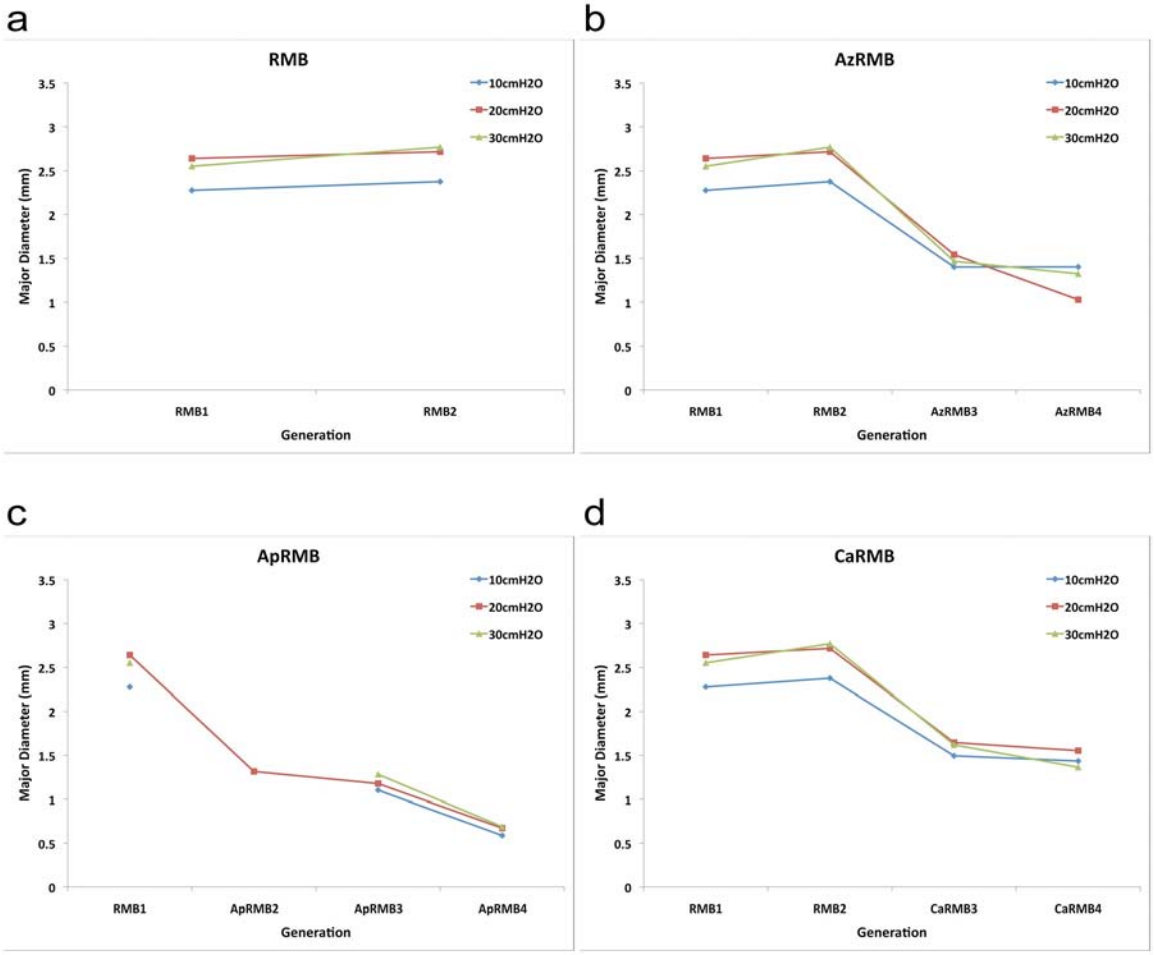

Figure A4: C57BL/6 Major Diameter vs Generation for RMB, AzRMB, ApRMB and CaRMB.

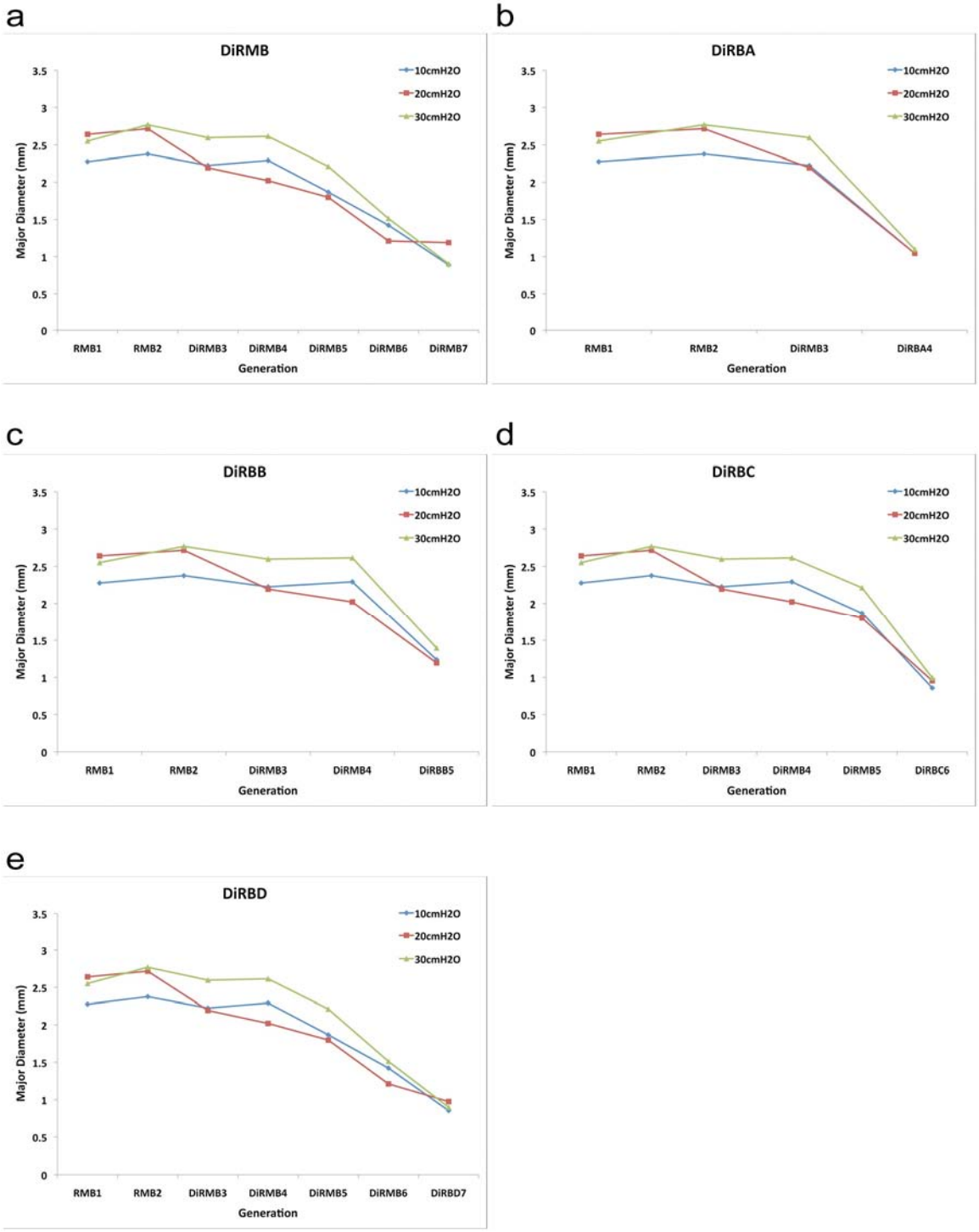

Figure A5: C57Bl/6 Major Diameter vs Generation for DiRMB, DiRBA, DiRBB, DiRBC, and DiRBD.

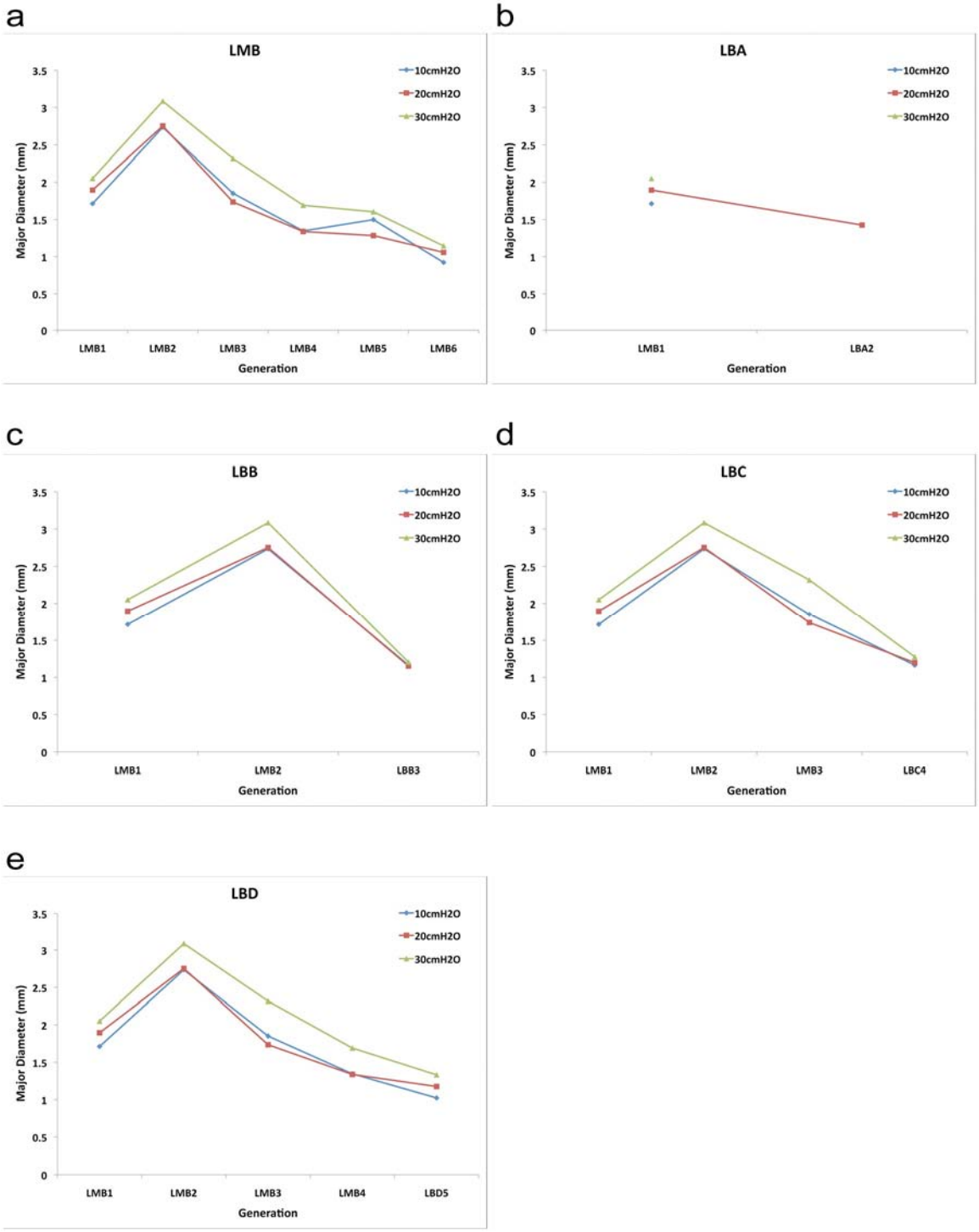

Figure A6: C57Bl/6 Major Diameter vs Generation for LMB, LBA, LBB, LBC and LBD.

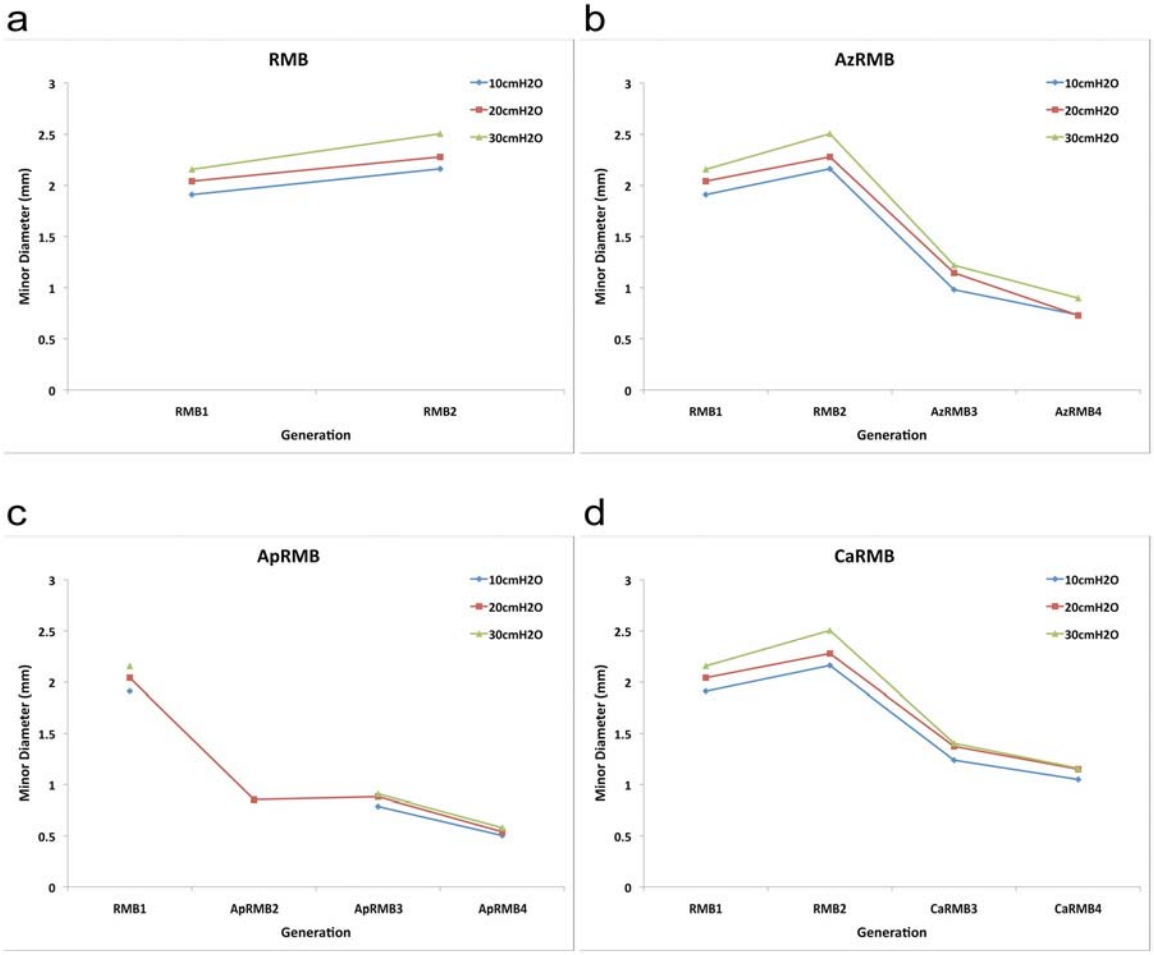

Figure A7: C57BL/6 Minor Diameter vs Generation for RMB, AzRMB, ApRMB and CaRMB

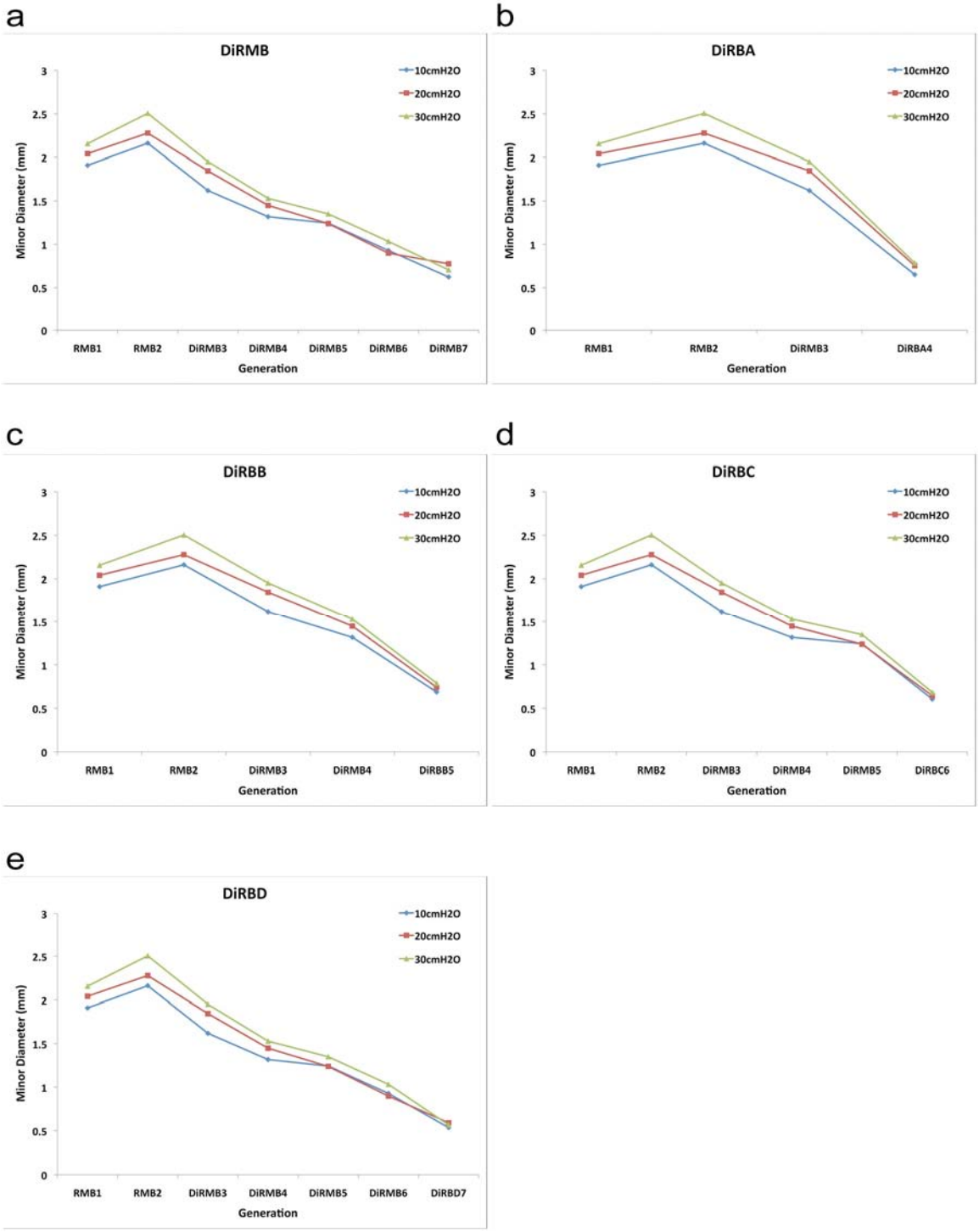

Figure A8: C57Bl/6 Minor Diameter vs Generation for DiRMB, DiRBA, DiRBB, DiRBC, and DiRBD

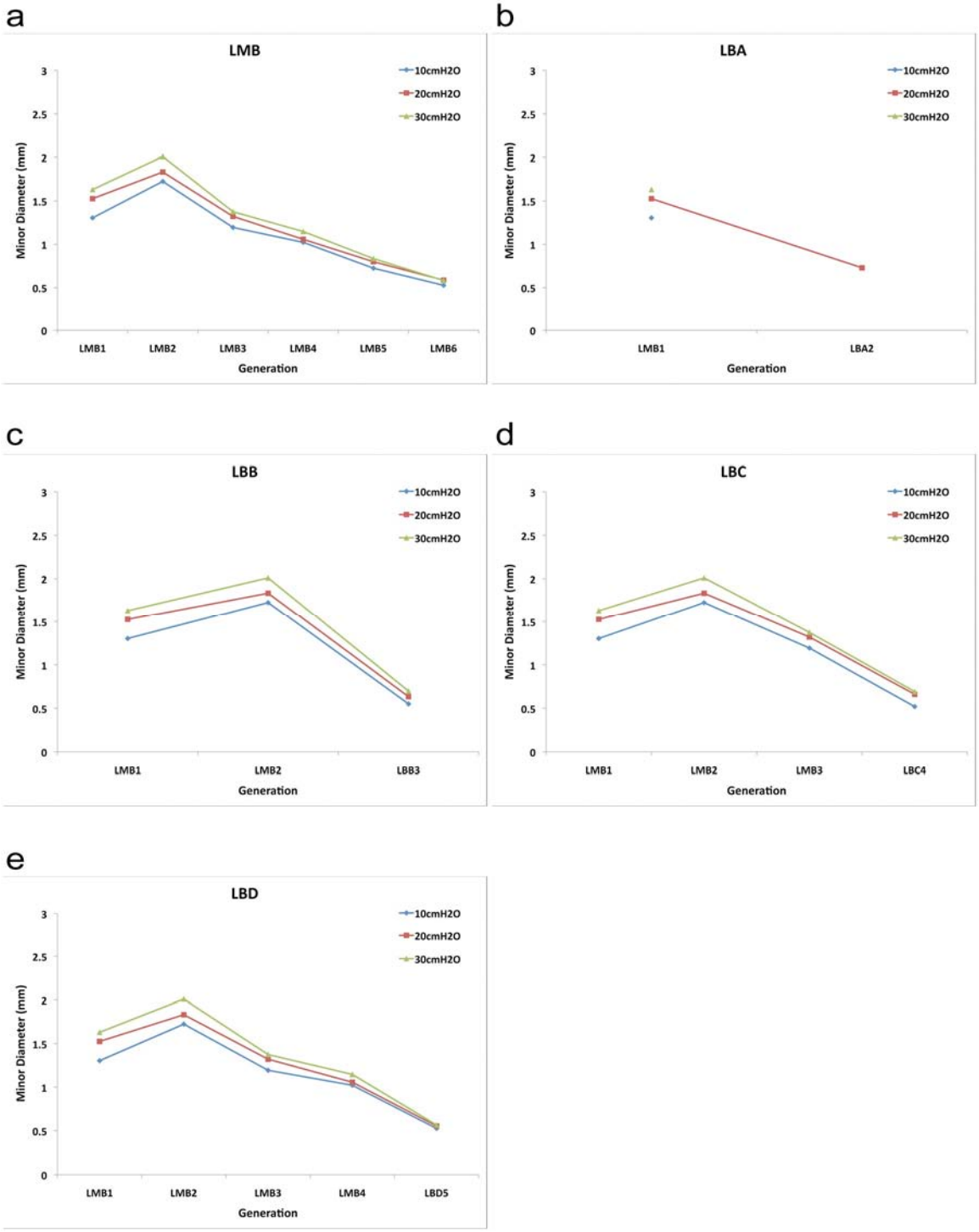

Figure A9: C57Bl/6 Minor Diameter vs Generation for LMB, LBA, LBB, LBC and LBD.

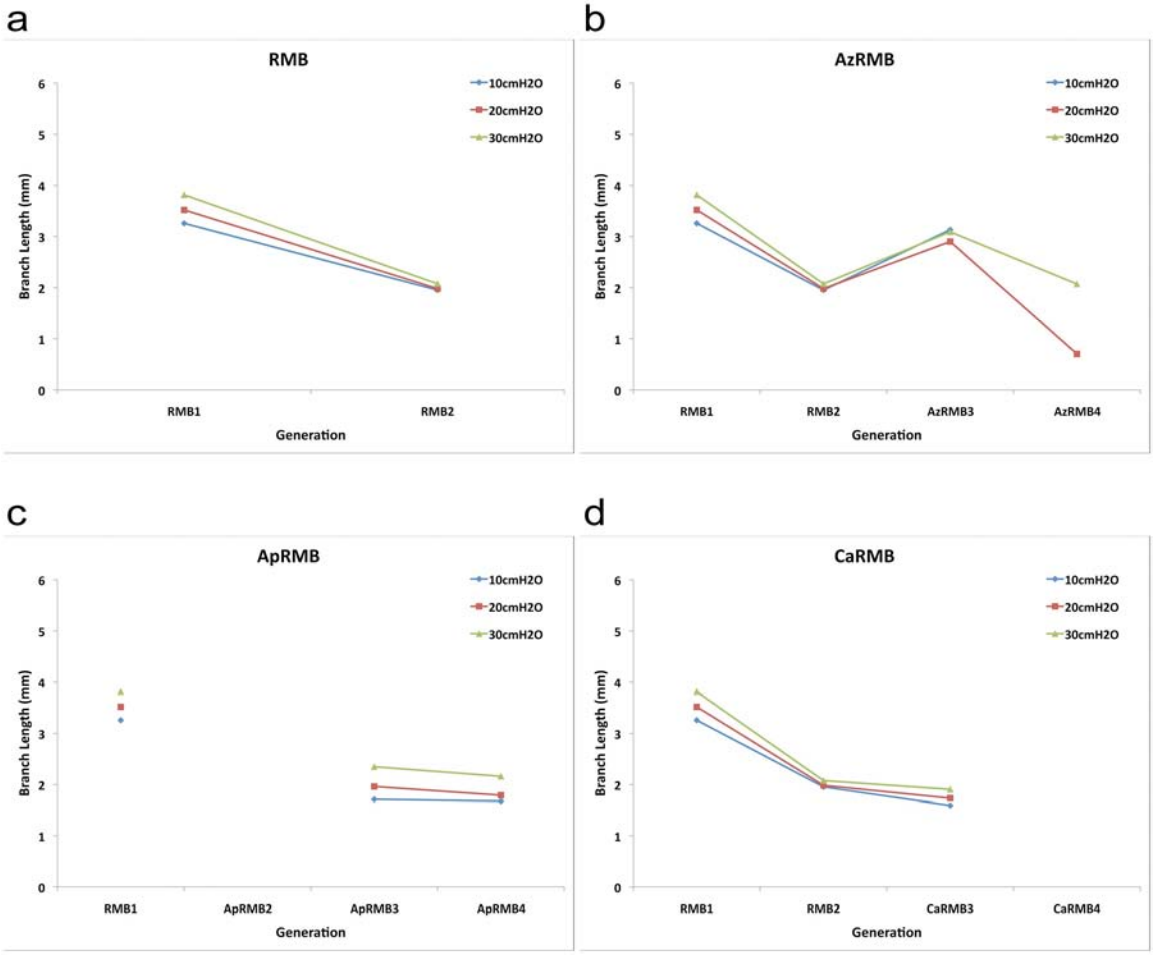

Figure A10: C57BL/6 Branch Length vs Generation for RMB, AzRMB, ApRMB and CaRMB.

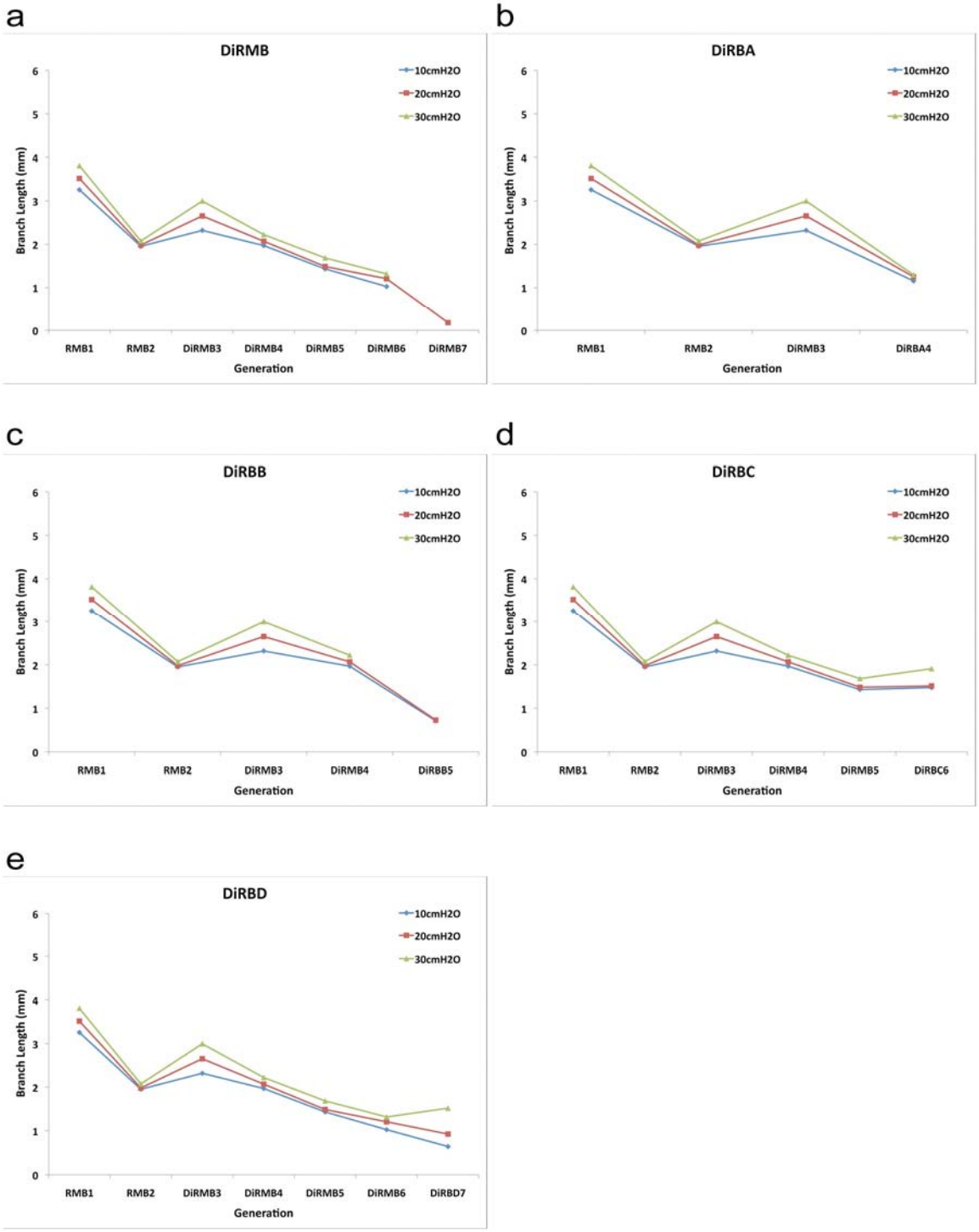

Figure A11: C57Bl/6 Branch Length vs Generation for DiRMB, DiRBA, DiRBB, DiRBC, and DiRBD.

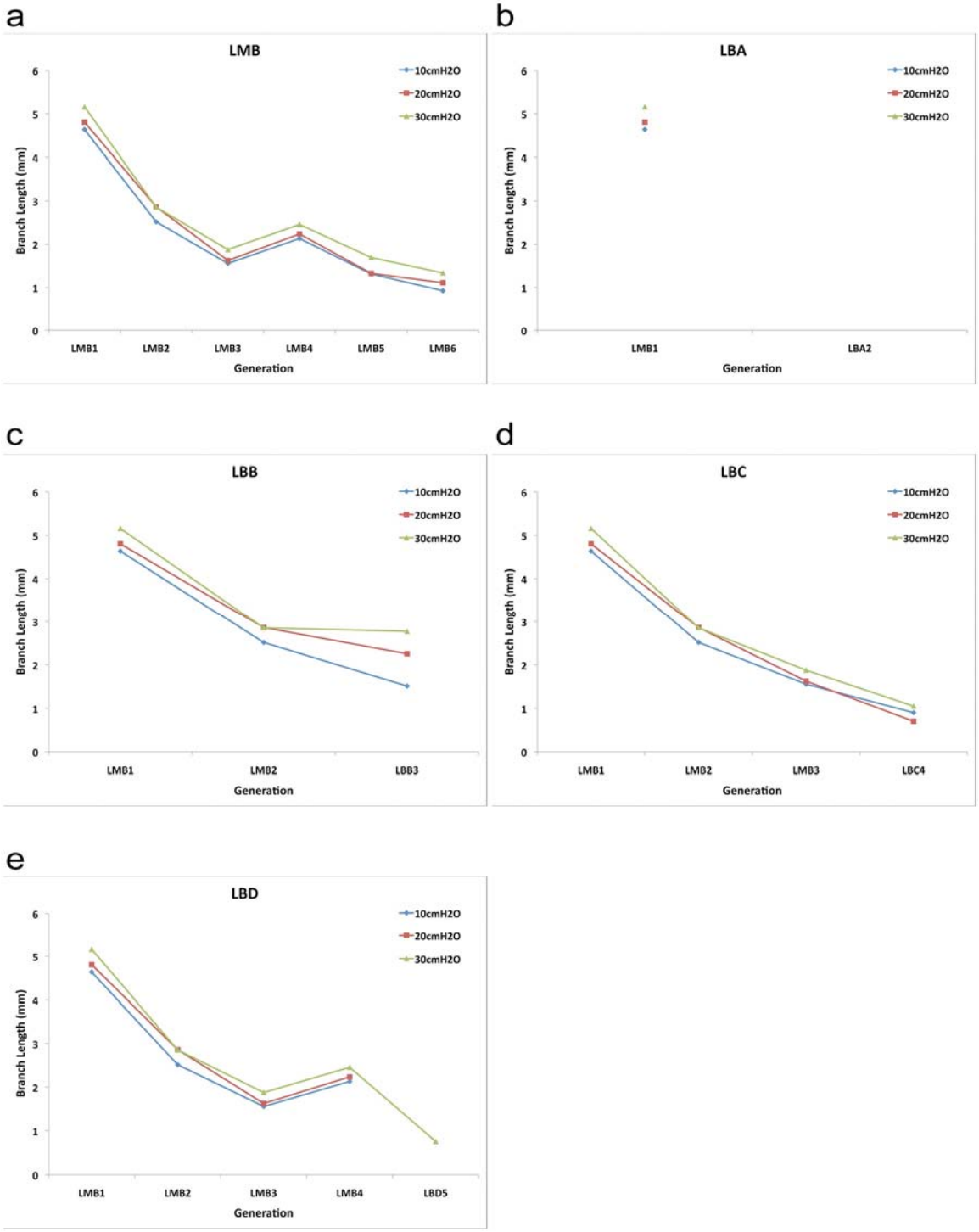

Figure A12: C57Bl/6 Branch Length vs Generation for LMB, LBA, LBB, LBC and LBD.

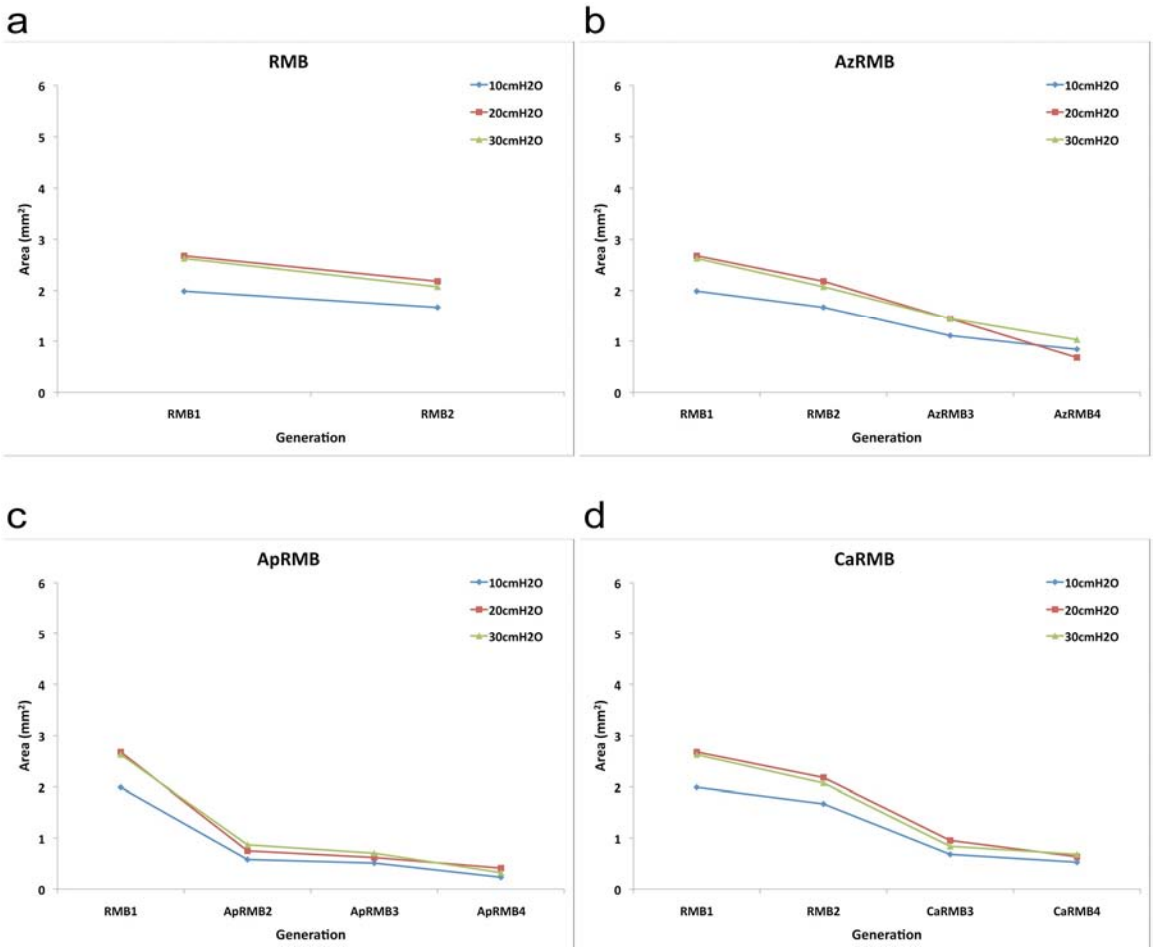

Figure A13: A/J Area vs Generation for RMB, AzRMB, ApRMB and CaRMB.

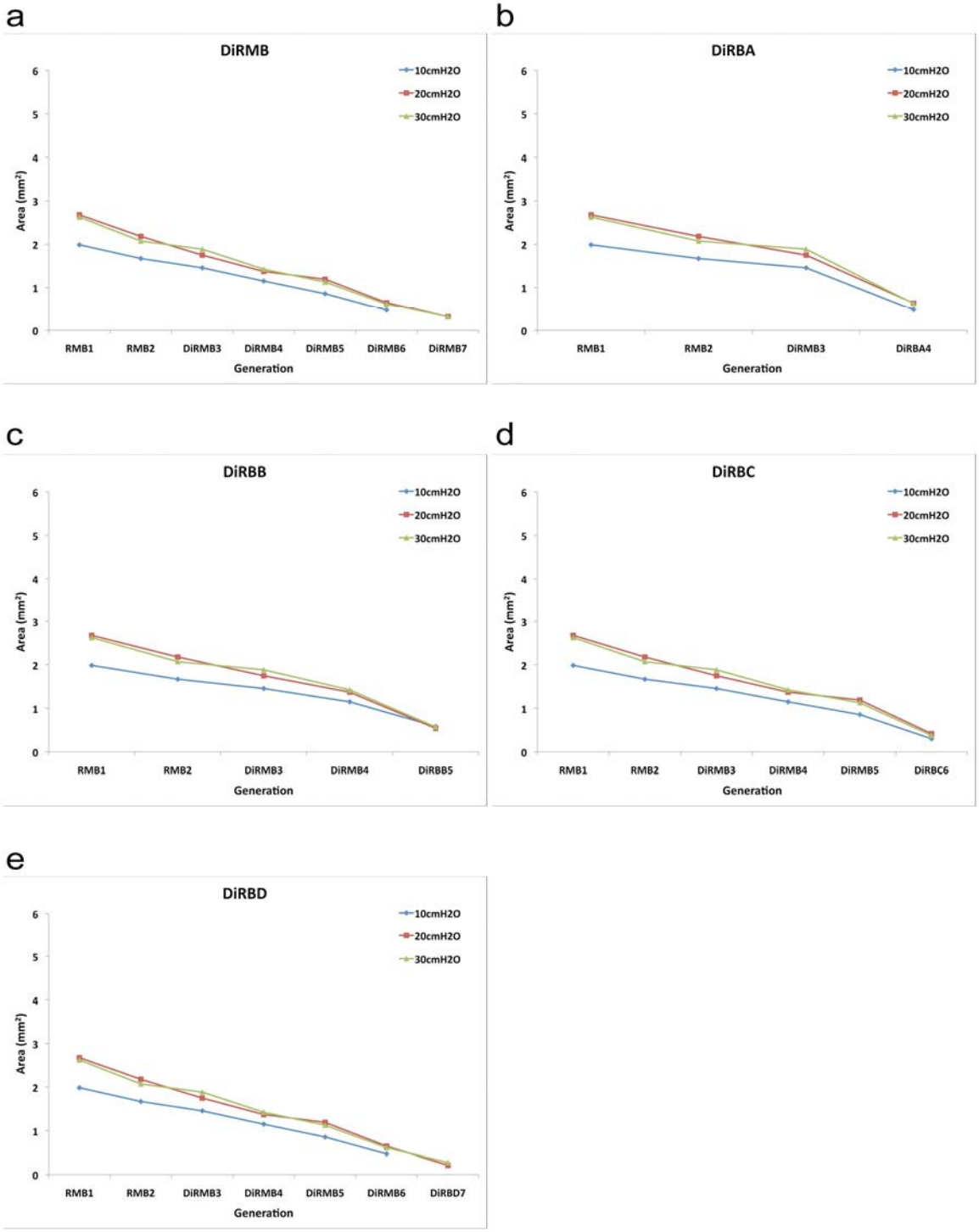

Figure A14: A/J Area vs Generation for DiRMB, DiRBA, DiRBB, DiRBC, and DiRBD.

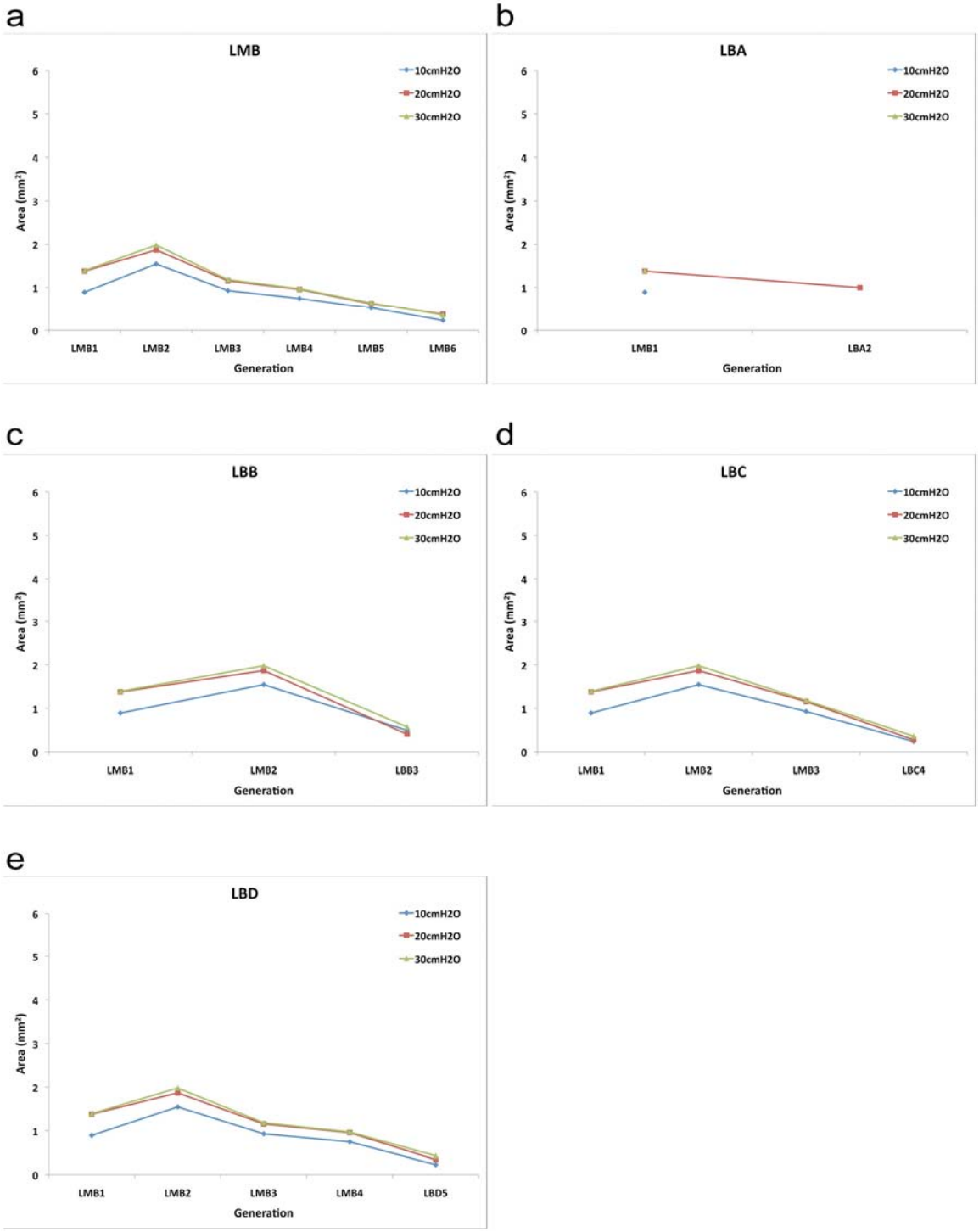

Figure A15: A/J Area vs Generation for LMB, LBA, LBB, LBC and LBD.

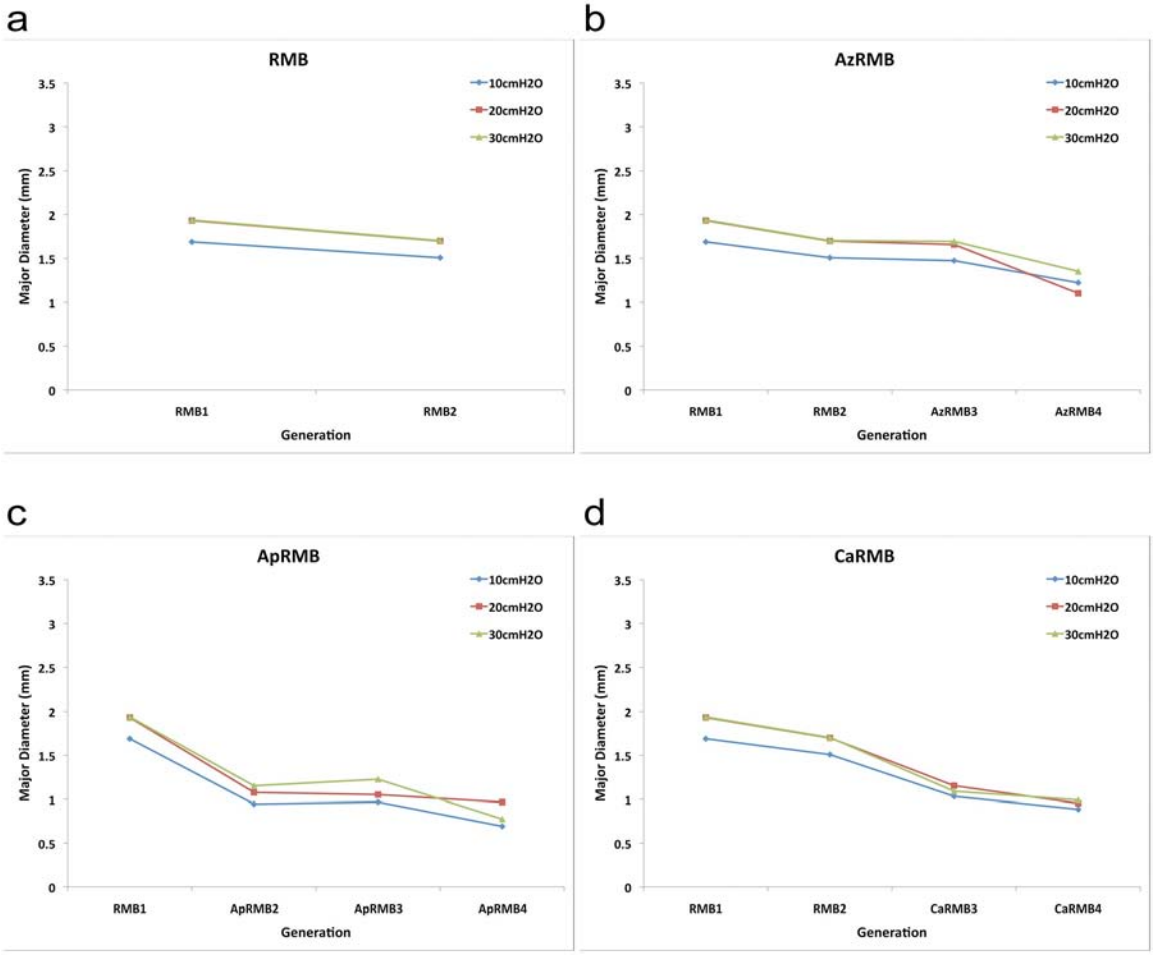

Figure A16: A/J Major Diameter vs Generation for RMB, AzRMB, ApRMB and CaRMB.

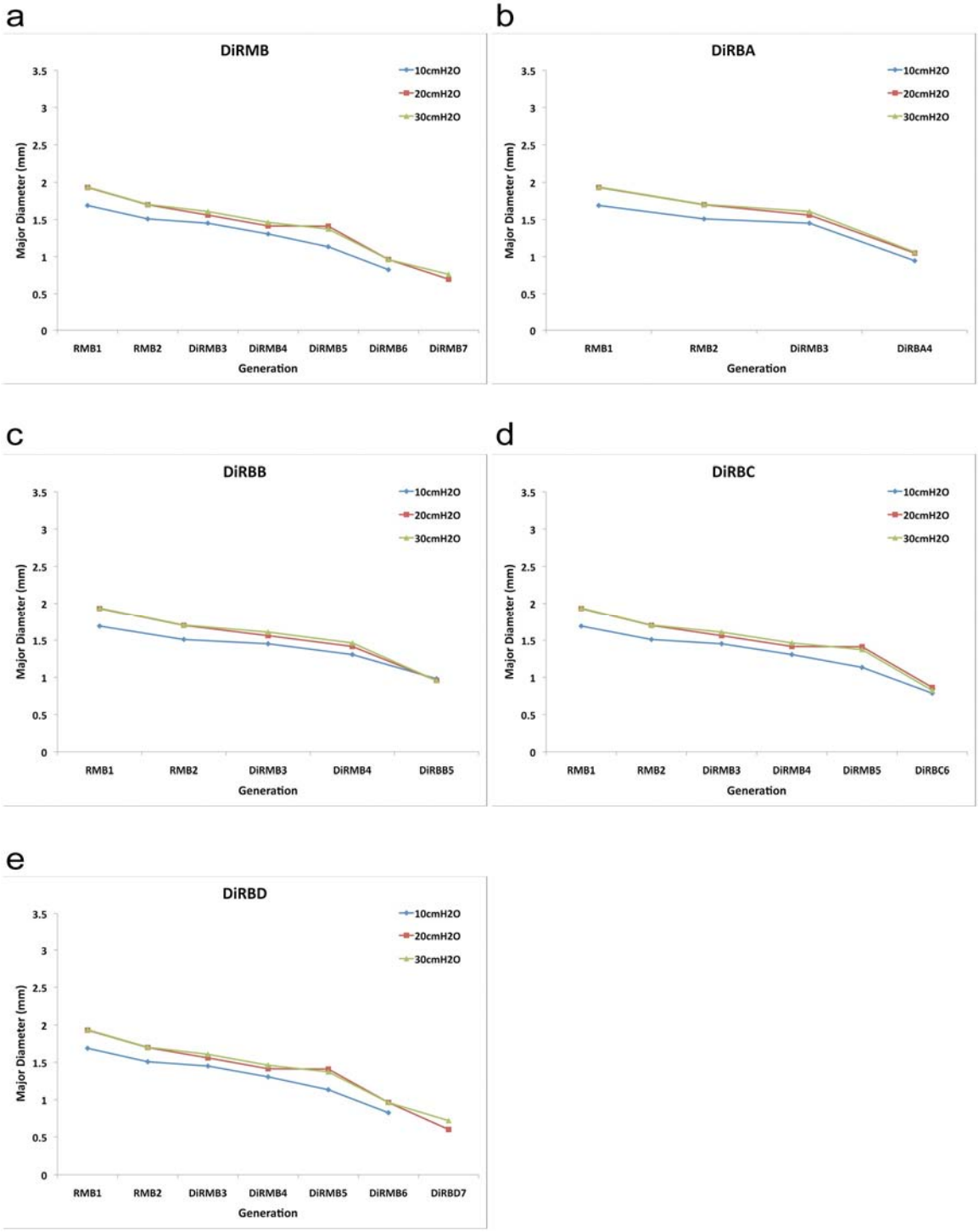

Figure A17: A/J Major Diameter vs Generation for DiRMB, DiRBA, DiRBB, DiRBC, and DiRBD.

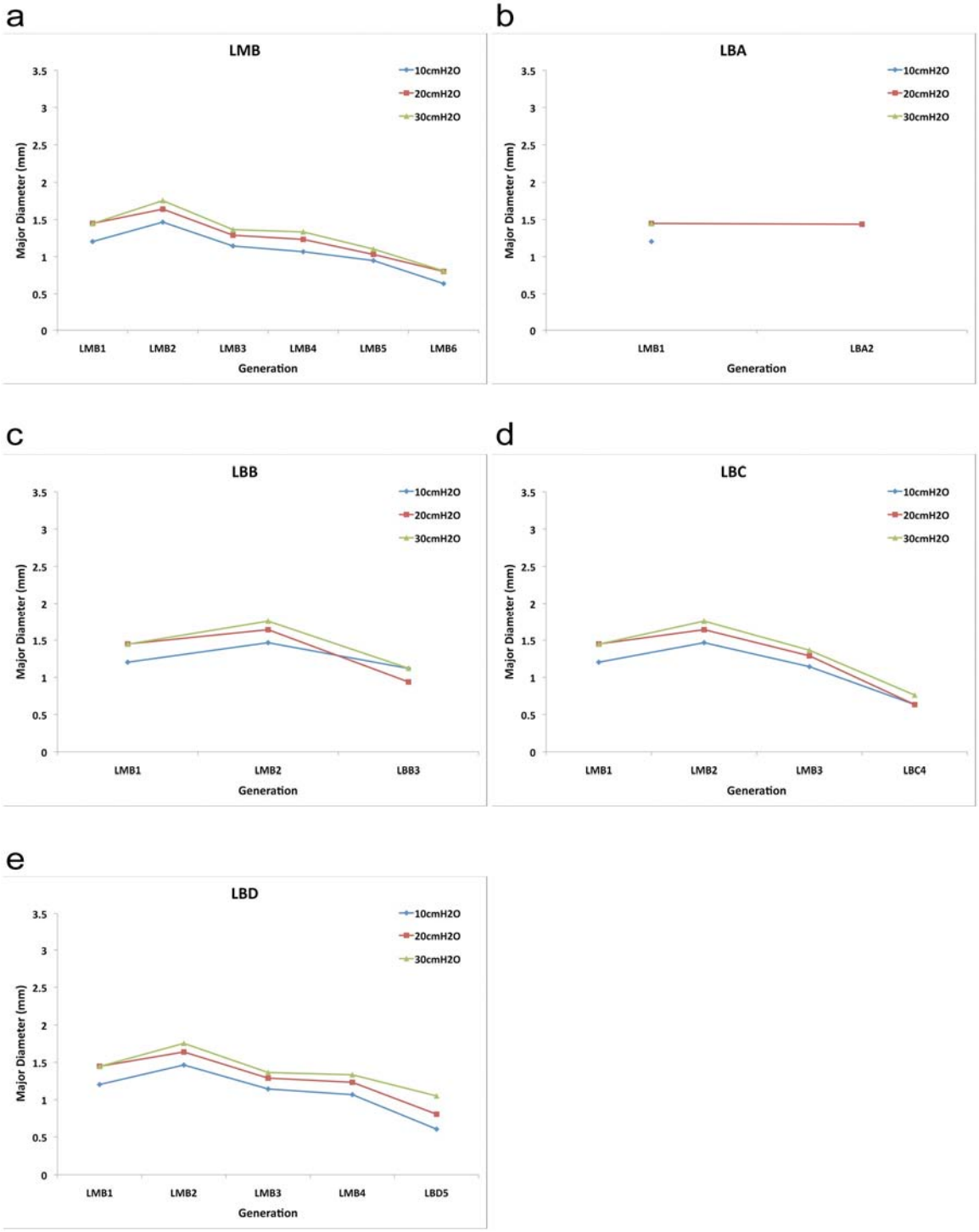

Figure A18: A/J Major Diameter vs Generation for LMB, LBA, LBB, LBC and LBD.

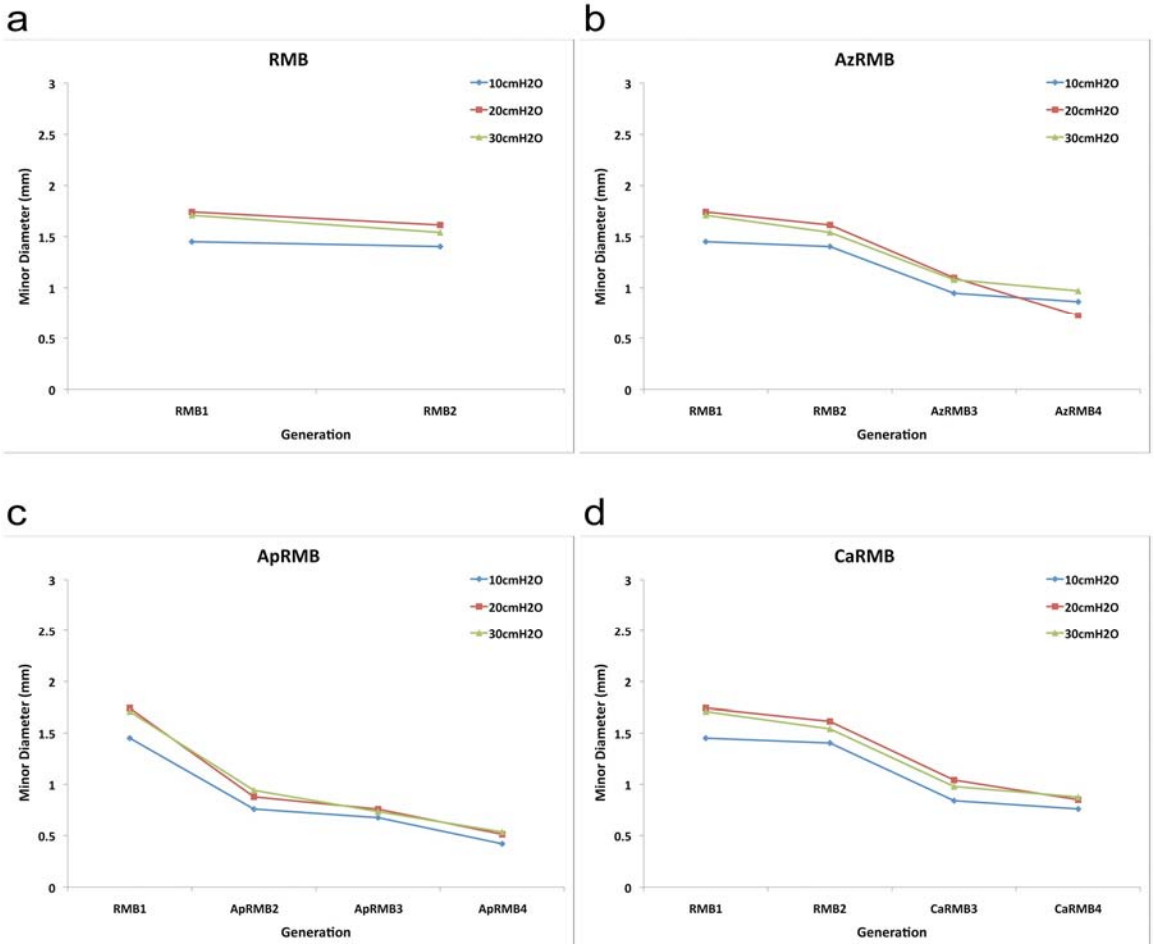

Figure A19: A/J Minor Diameter vs Generation for RMB, AzRMB, ApRMB and CaRMB.

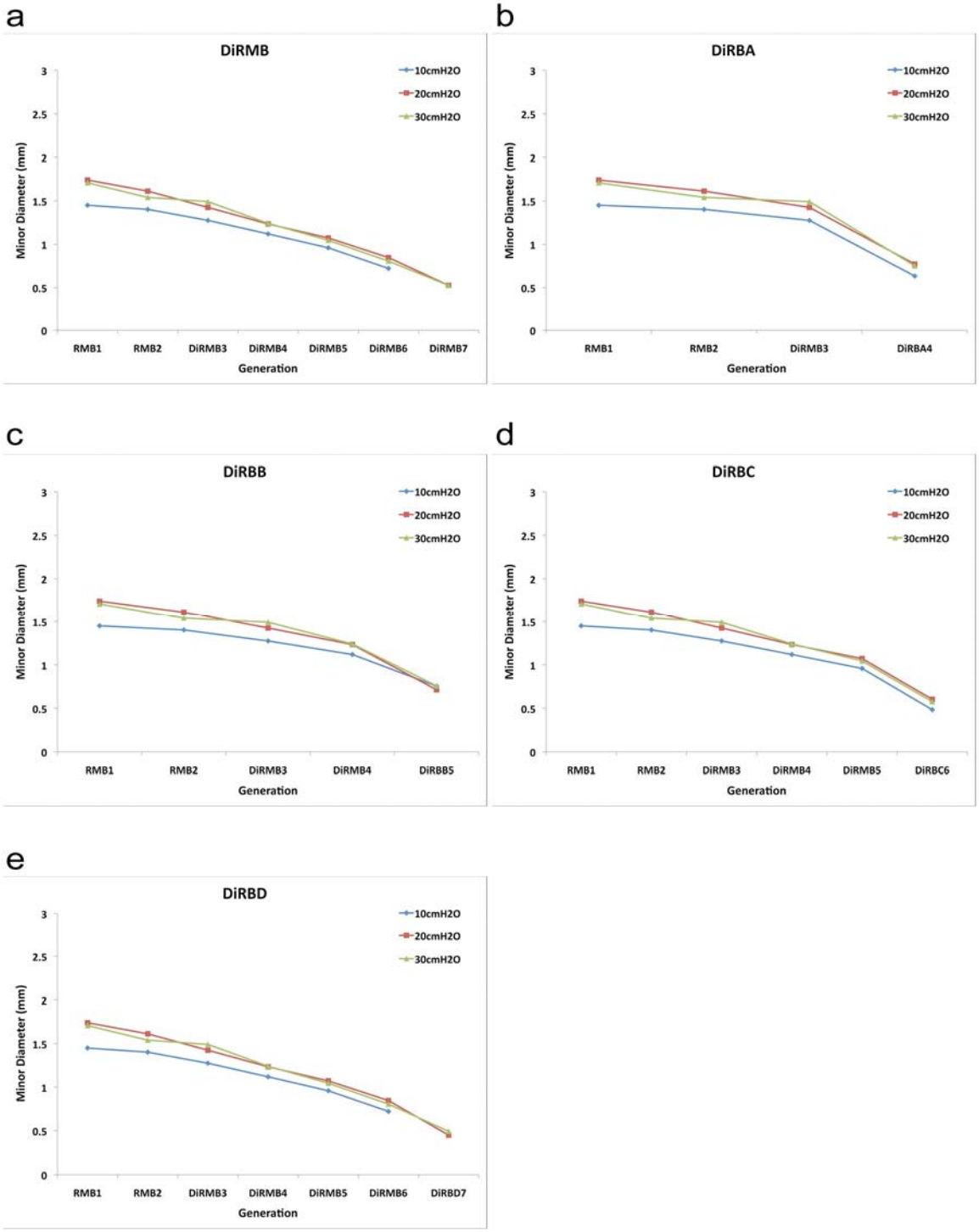

Figure A20: A/J Minor Diameter vs Generation for DiRMB, DiRBA, DiRBB, DiRBC, and DiRBD.

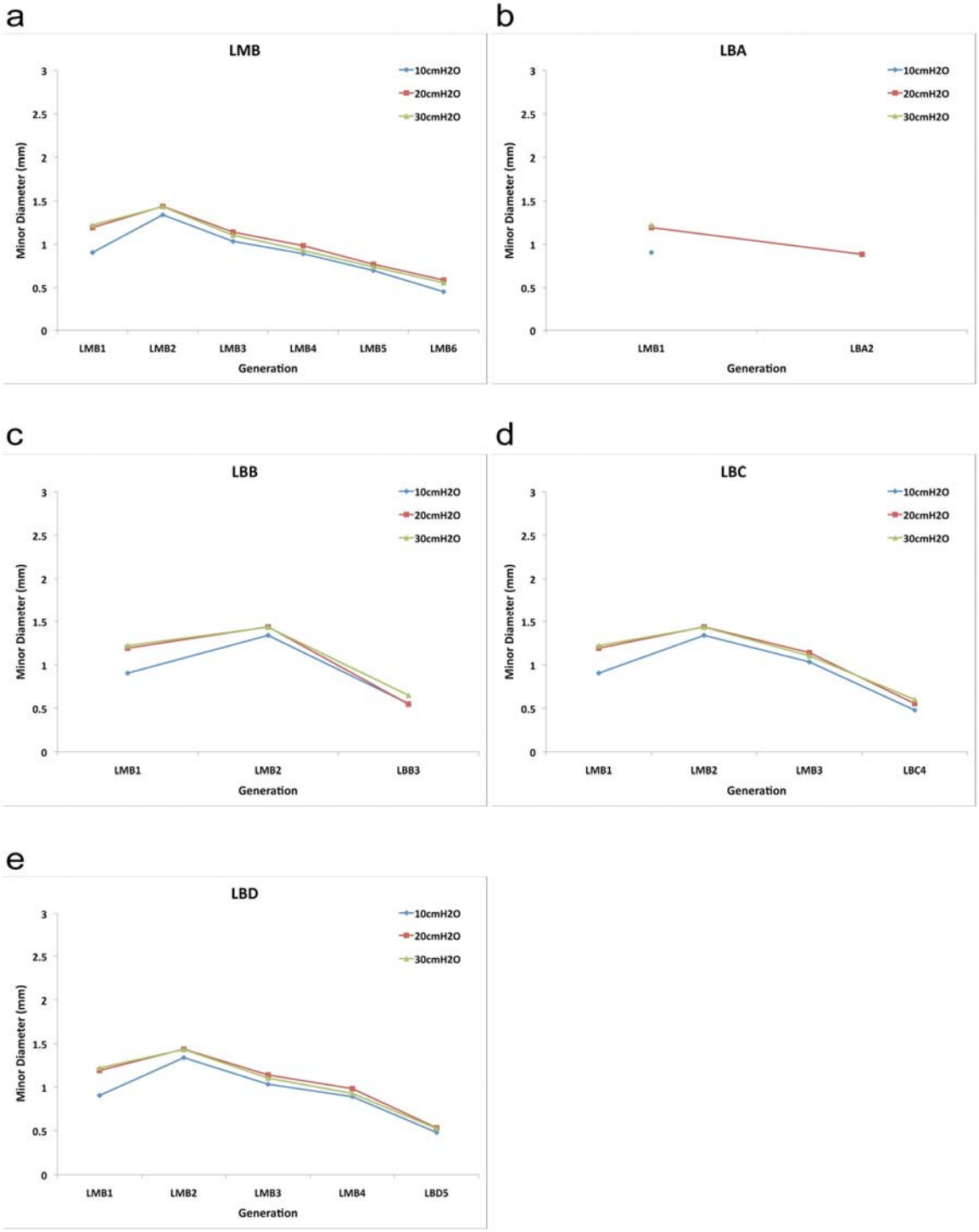

Figure A21: A/J Minor Diameter vs Generation for LMB, LBA, LBB, LBC and LBD.

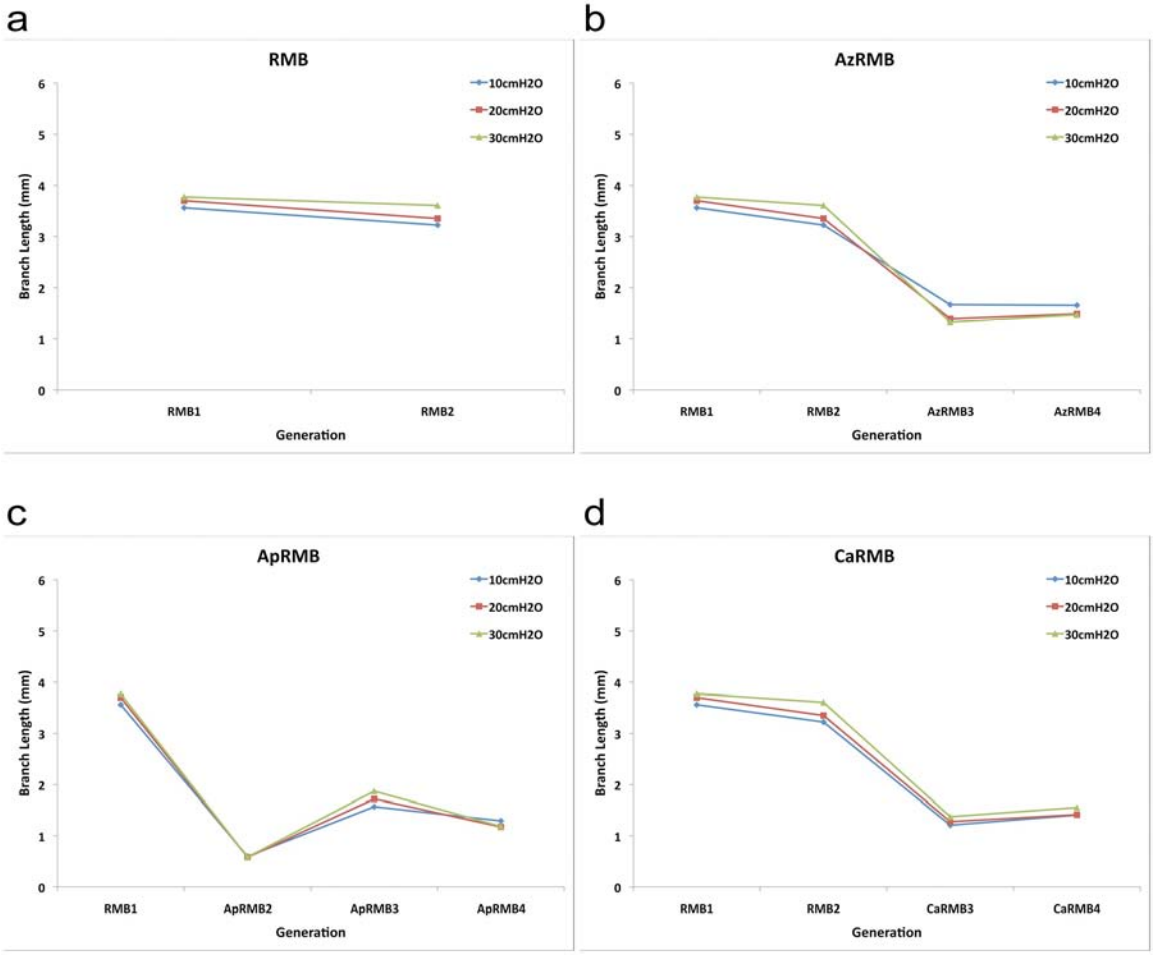

Figure A22: A/J Branch Length vs Generation for RMB, AzRMB, ApRMB and CaRMB.

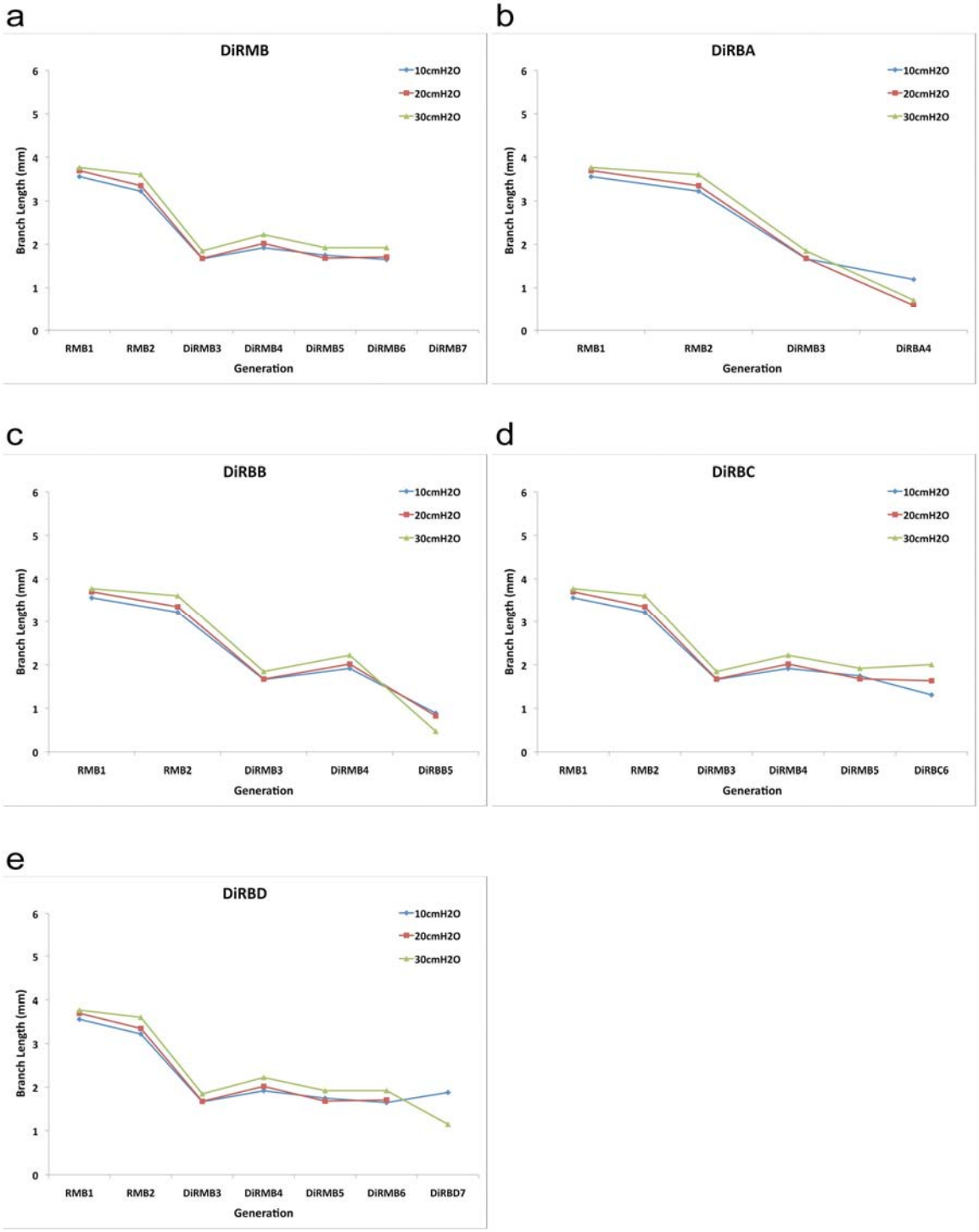

Figure A23: A/J Branch Length vs Generation for DiRMB, DiRBA, DiRBB, DiRBC, and DiRBD.

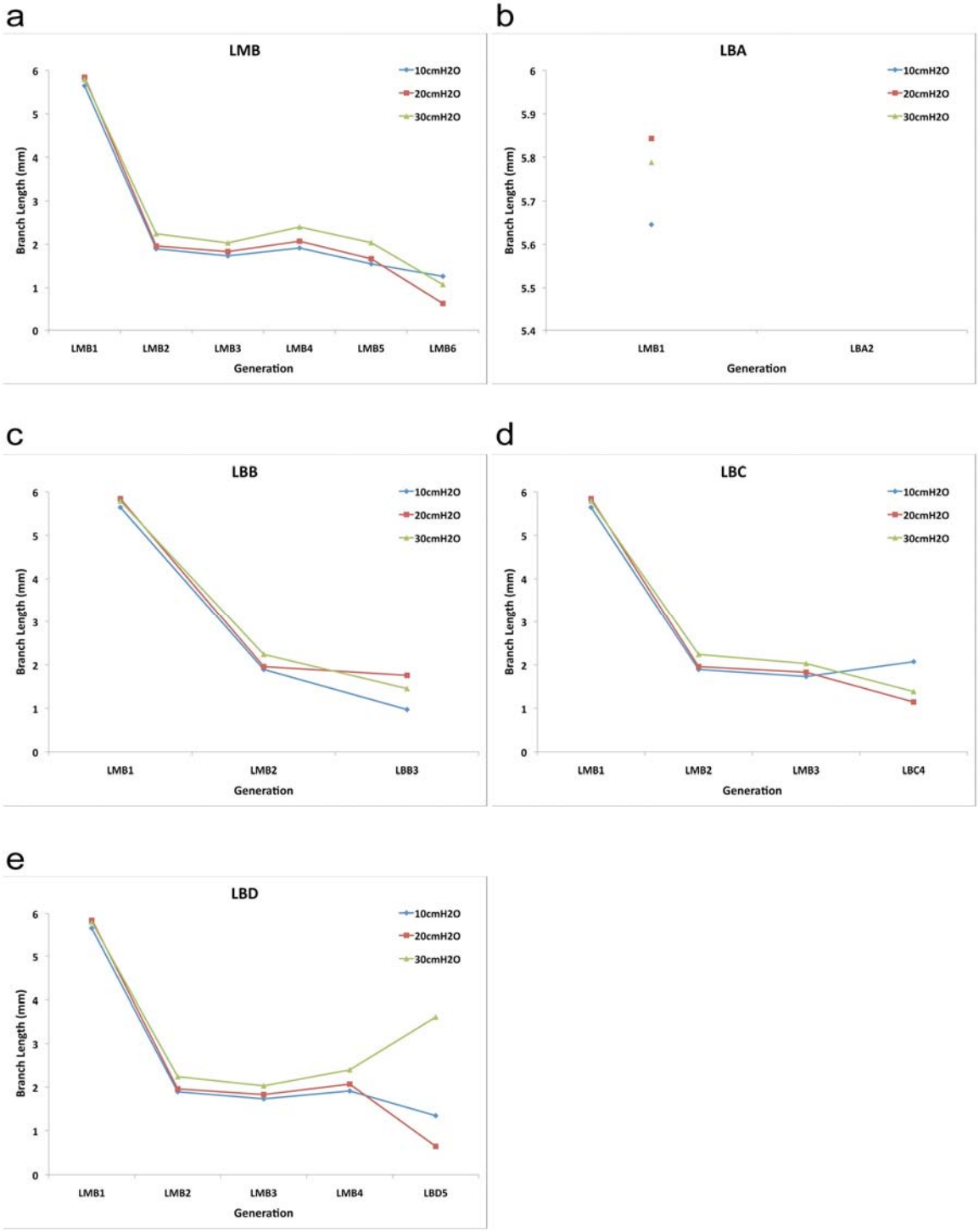

Figure A24: A/J Branch Length vs Generation for LMB, LBA, LBB, LBC and LBD.

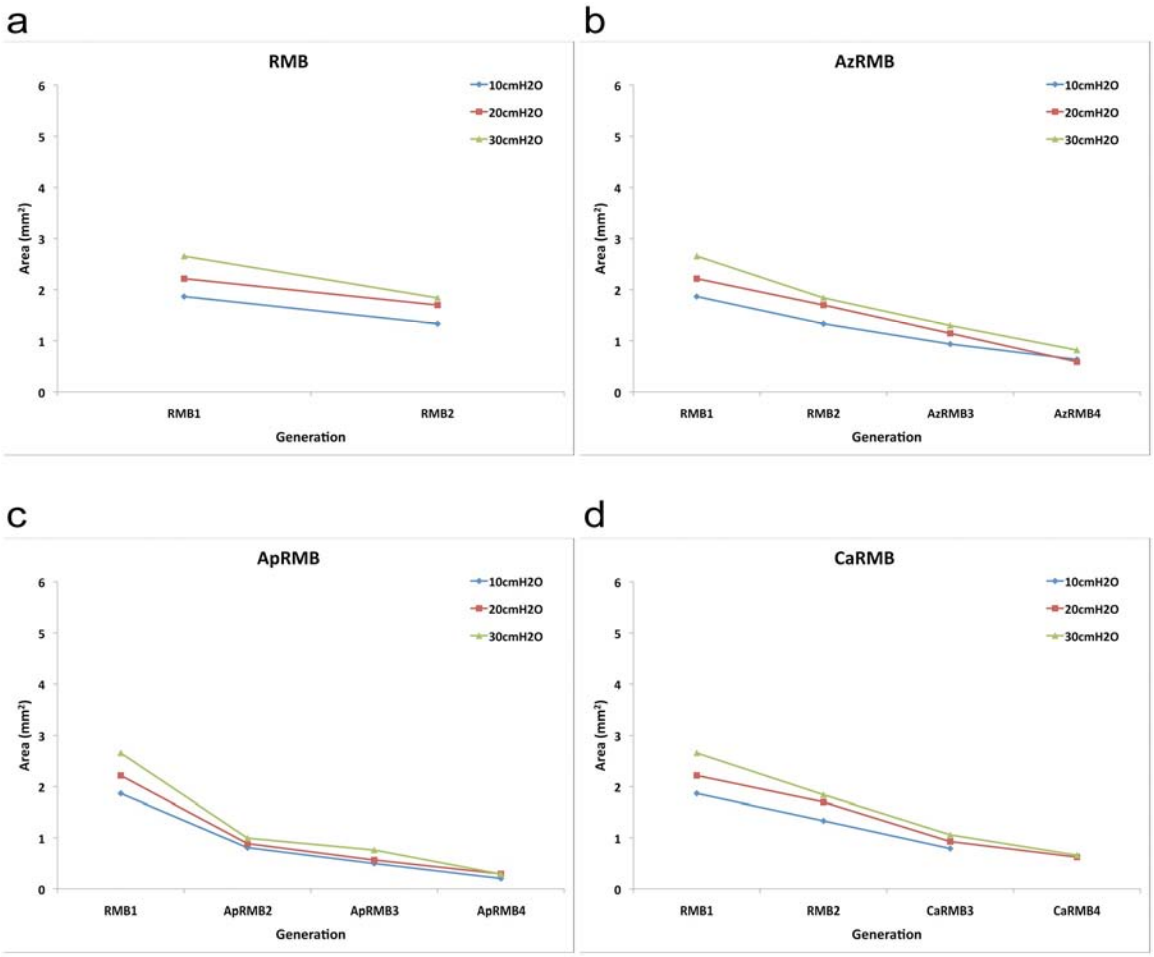

Figure A25: BALB/C Area vs Generation for RMB, AzRMB, ApRMB and CaRMB.

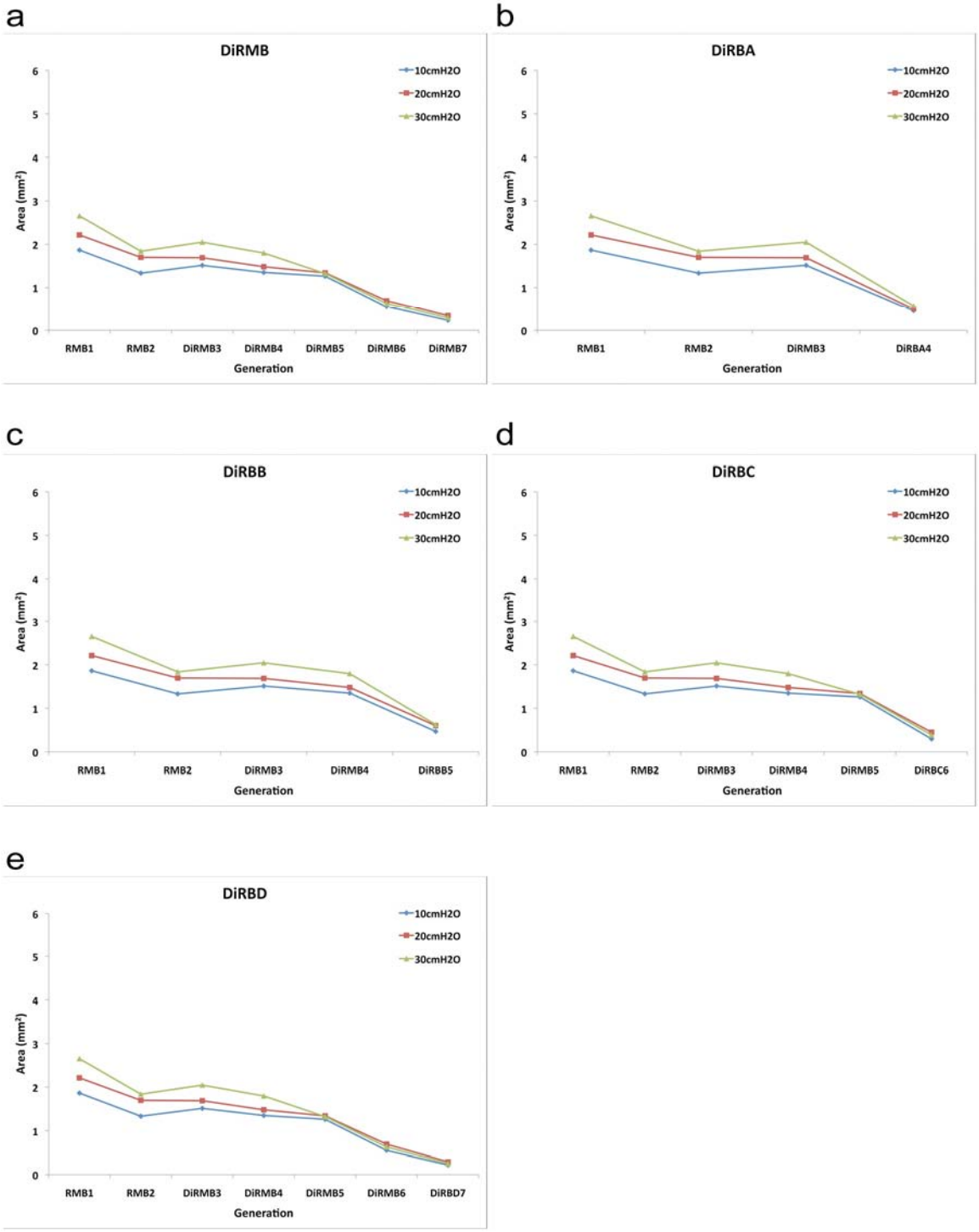

Figure A26: BALB/C Area vs Generation for DiRMB, DiRBA, DiRBB, DiRBC, and DiRBD.

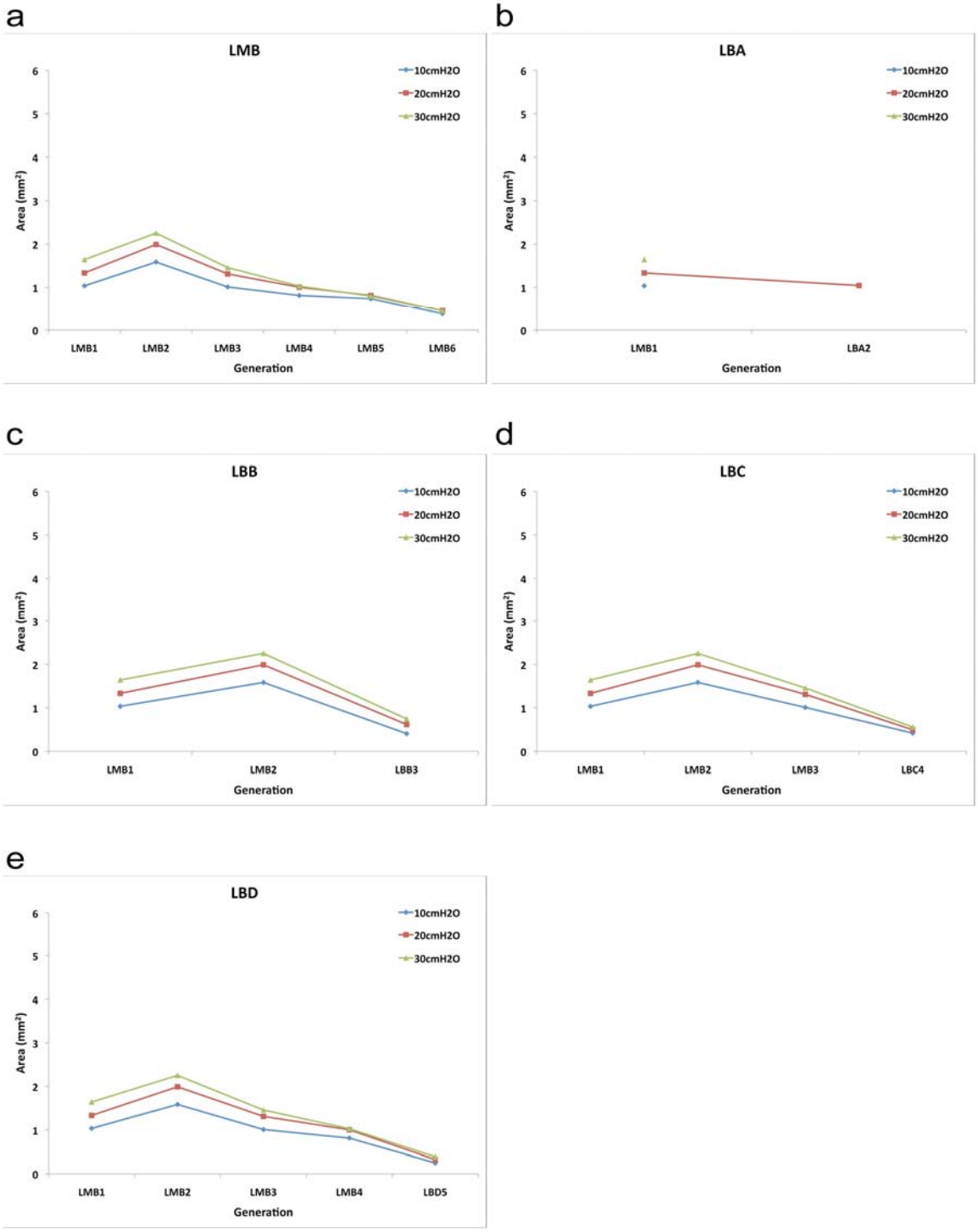

Figure A27: BALB/C Area vs Generation for LMB, LBA, LBB, LBC and LBD.

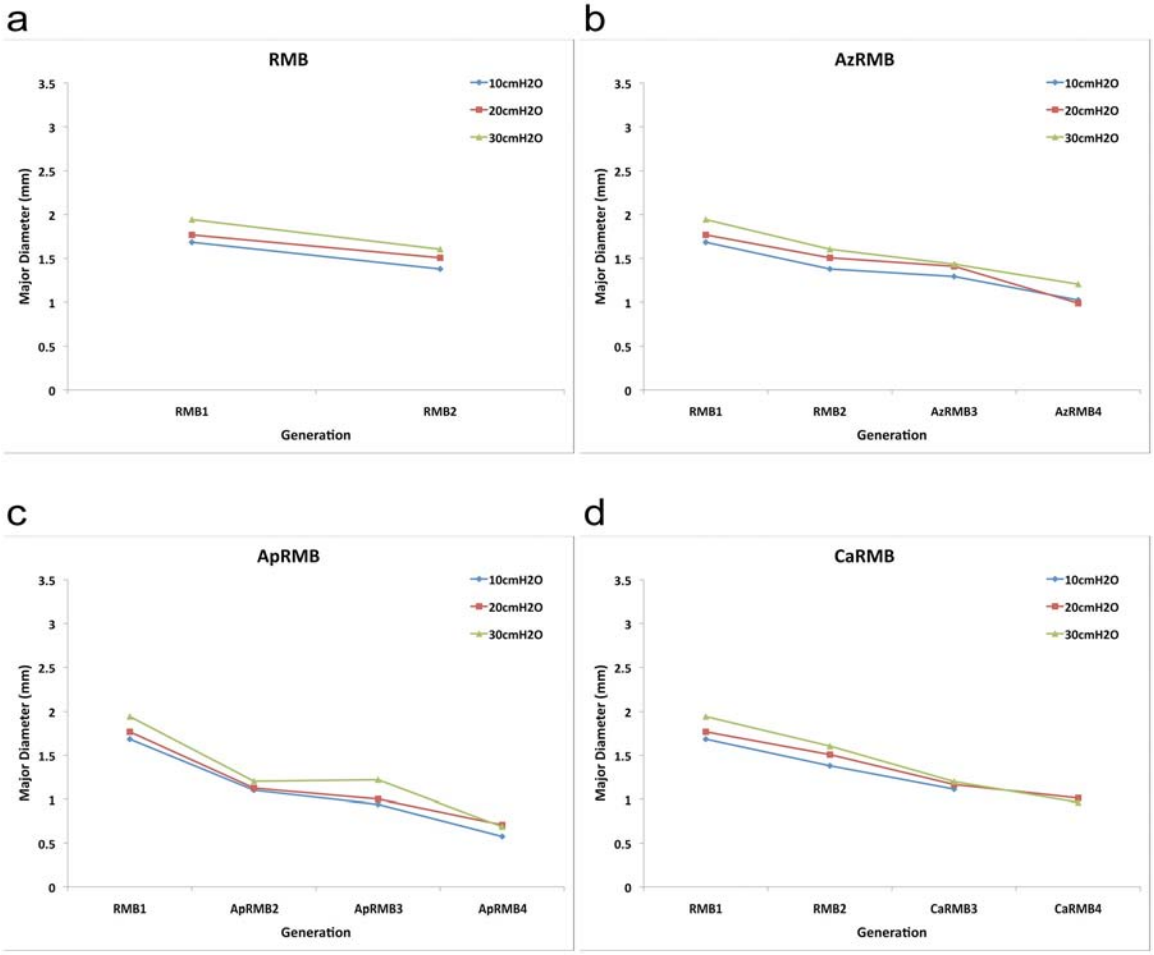

Figure A28: BALB/C Major Diameter vs Generation for RMB, AzRMB, ApRMB and CaRMB.

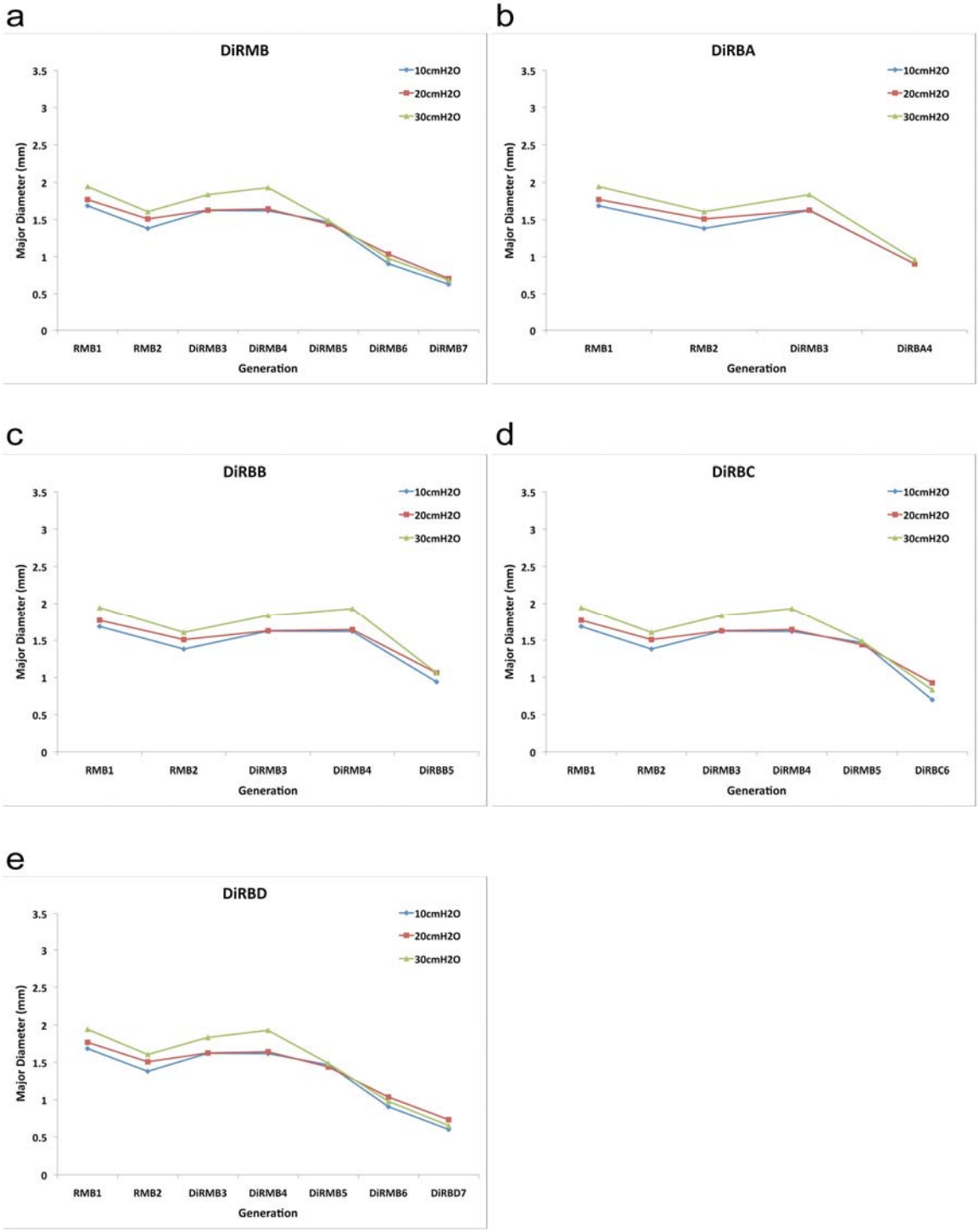

Figure A29: BALB/C Major Diameter vs Generation for DiRMB, DiRBA, DiRBB, DiRBC, and DiRBD.

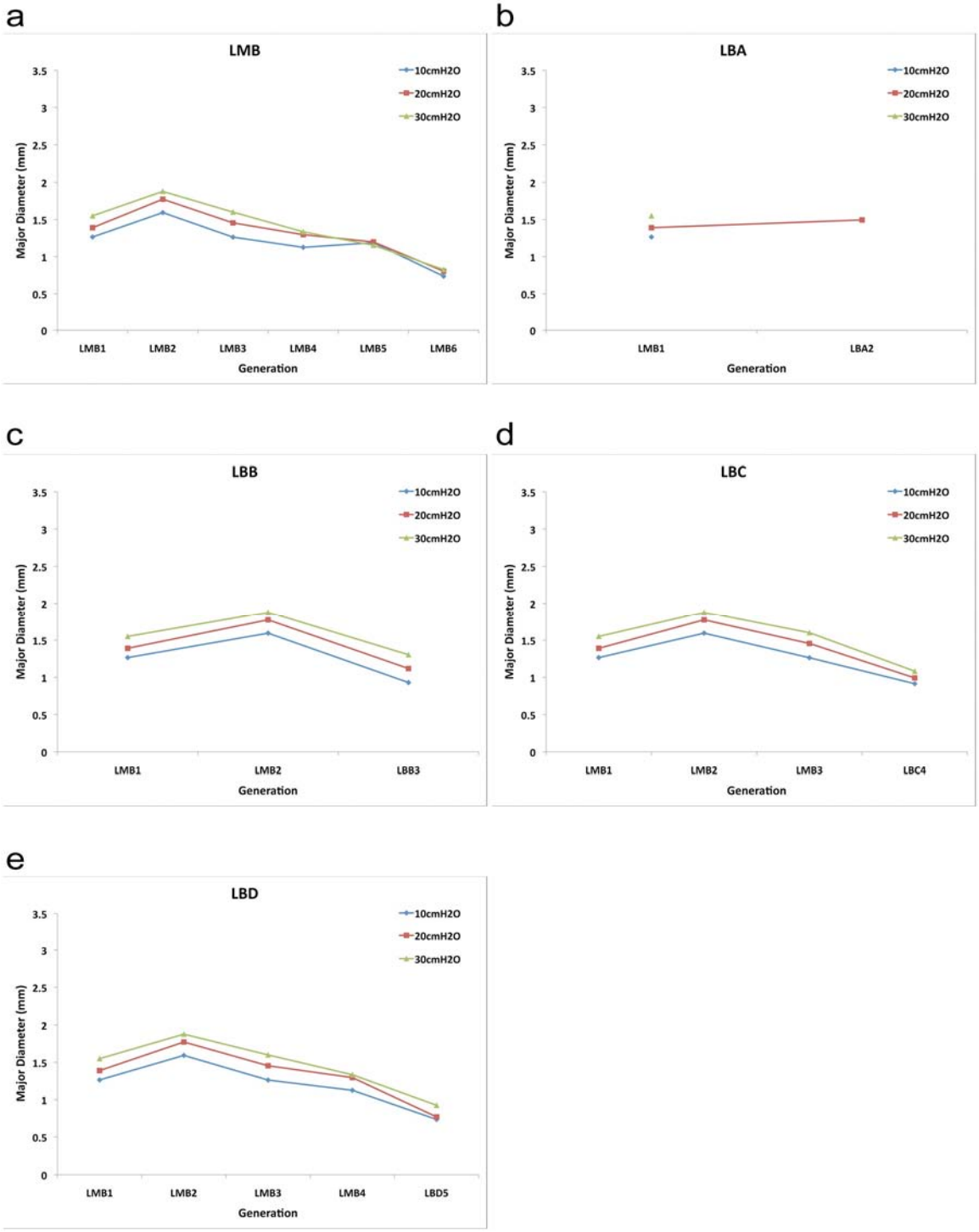

Figure A30: BALB/C Major Diameter vs Generation for LMB, LBA, LBB, LBC and LBD.

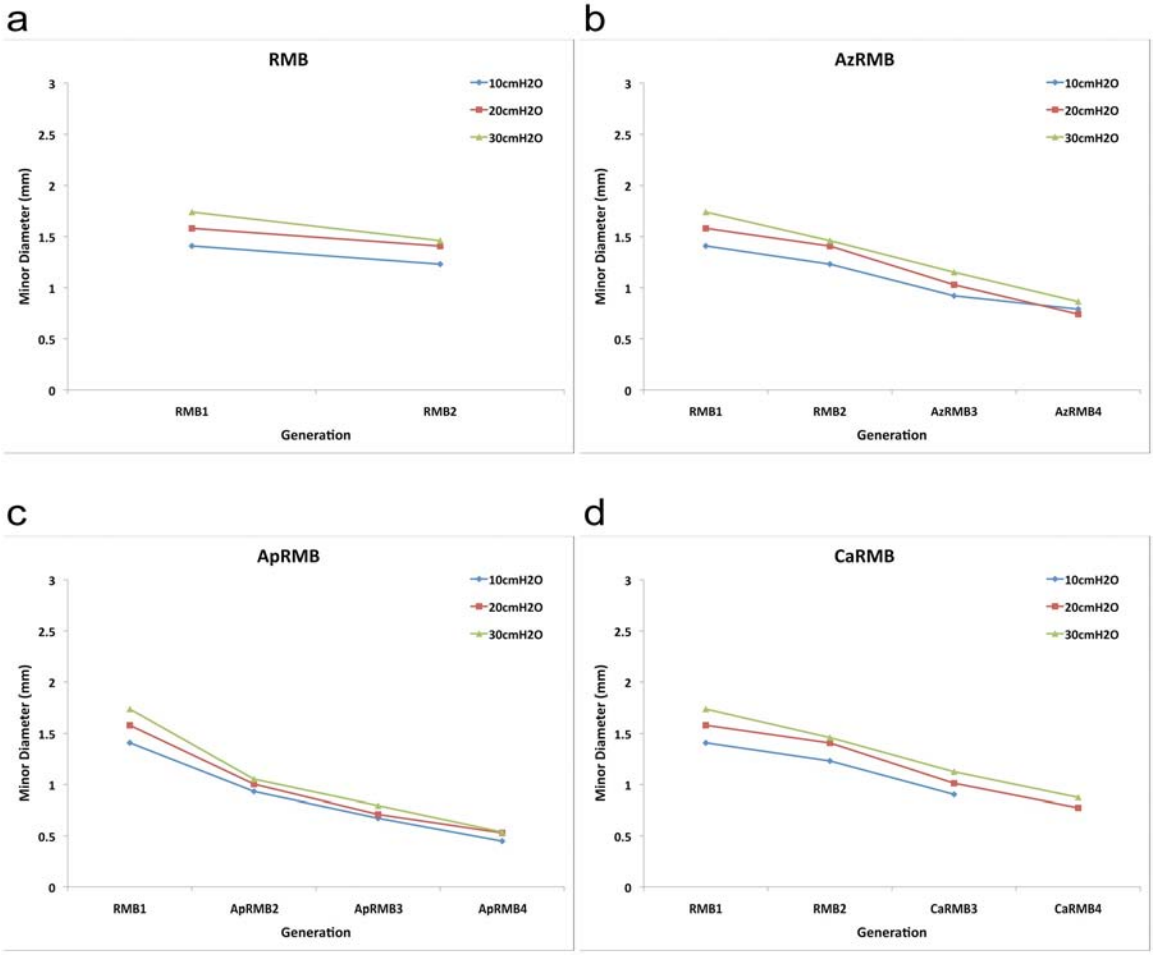

Figure A31: BALB/C Minor Diameter vs Generation for RMB, AzRMB, ApRMB and CaRMB.

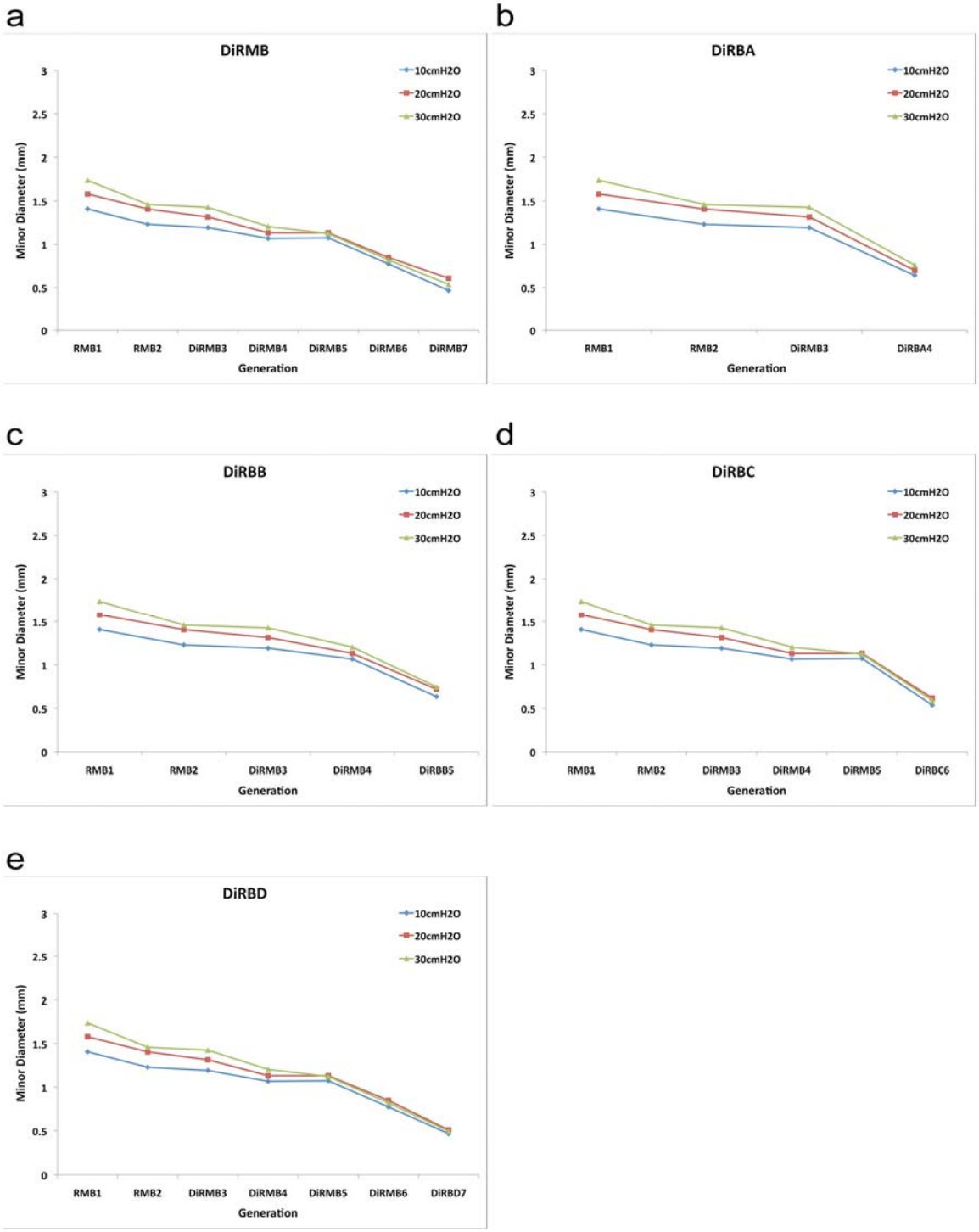

Figure A32: BALB/C Minor Diameter vs Generation for DiRMB, DiRBA, DiRBB, DiRBC, and DiRBD.

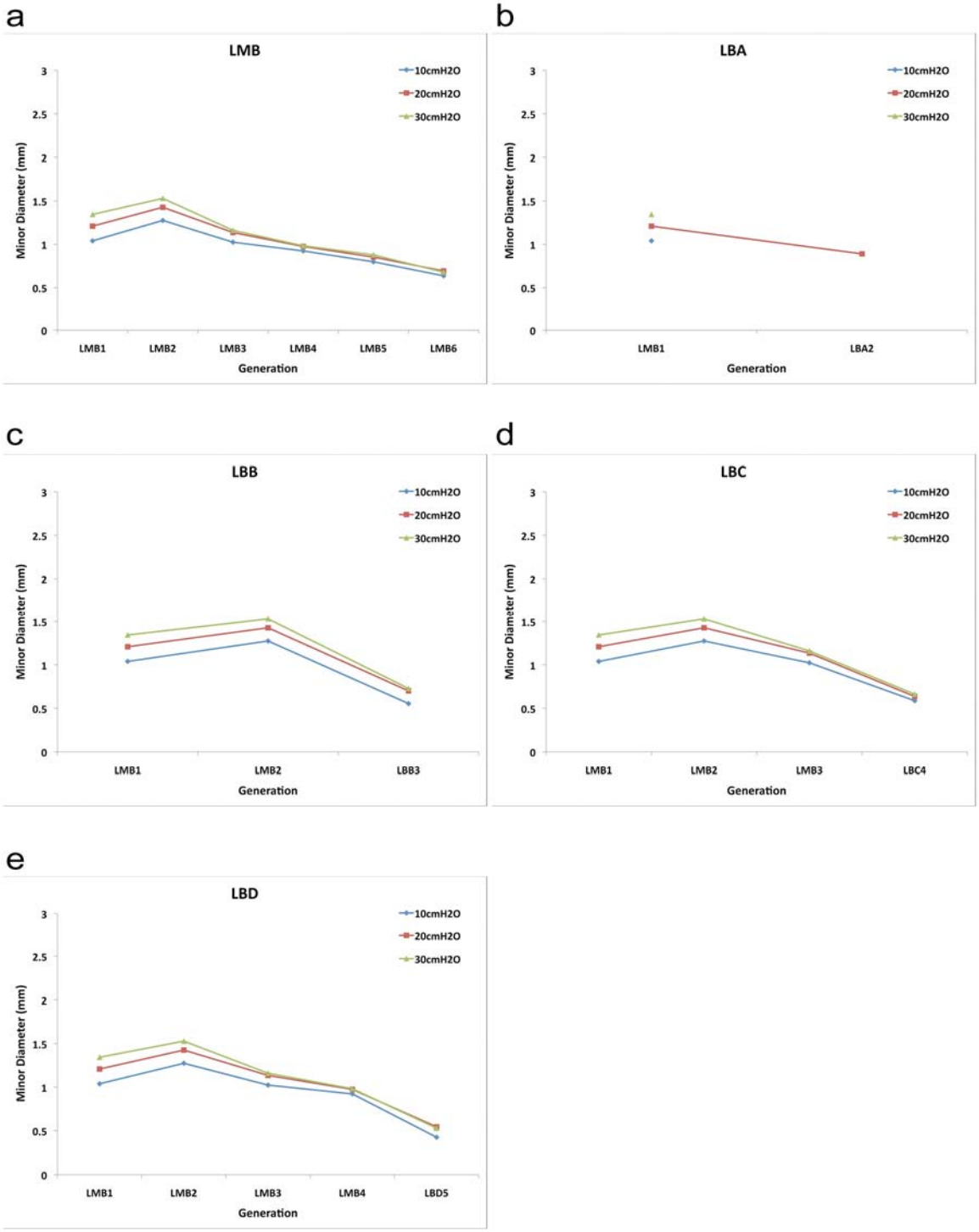

Figure A33: BALB/C Minor Diameter vs Generation for LMB, LBA, LBB, LBC and LBD.

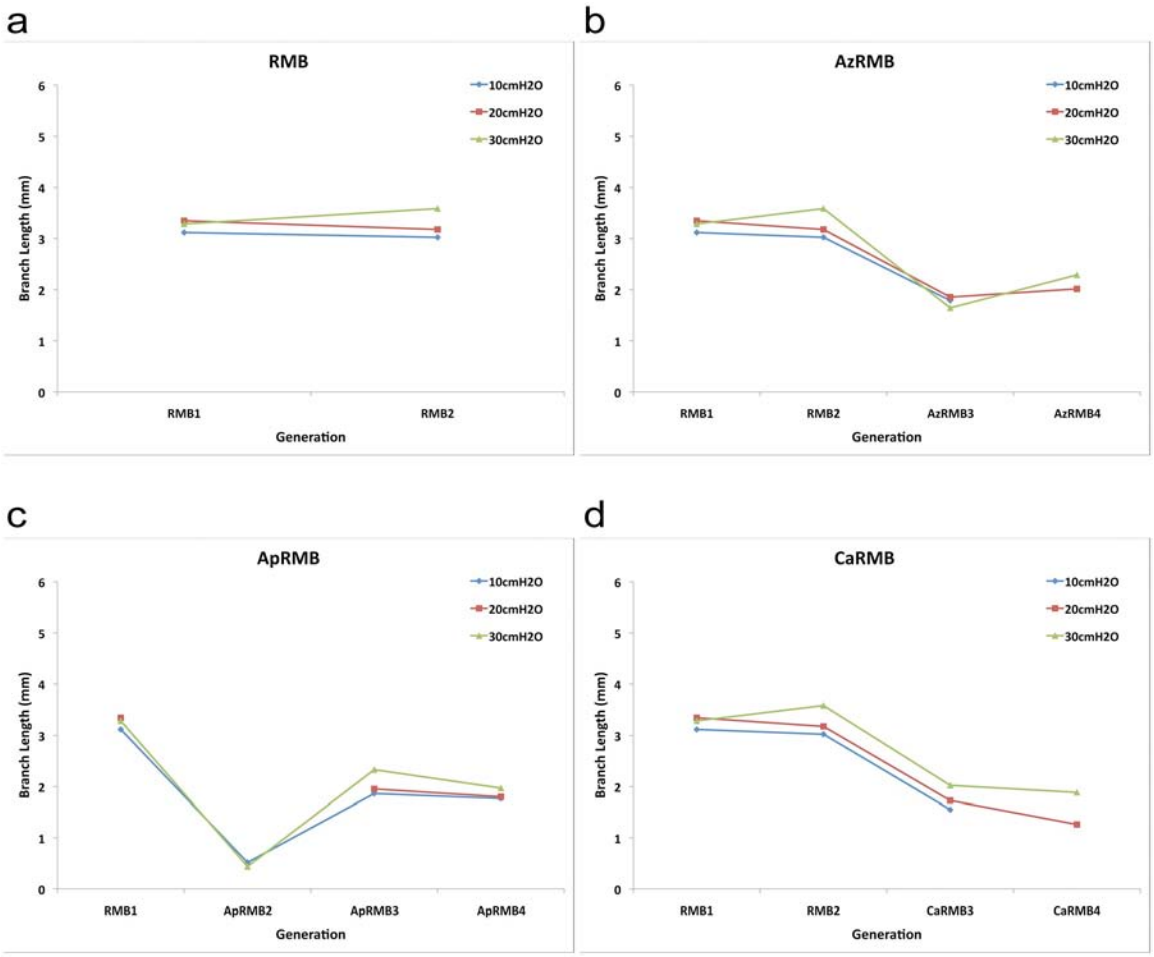

Figure A34: BALB/C Branch Length vs Generation for RMB, AzRMB, ApRMB and CaRMB.

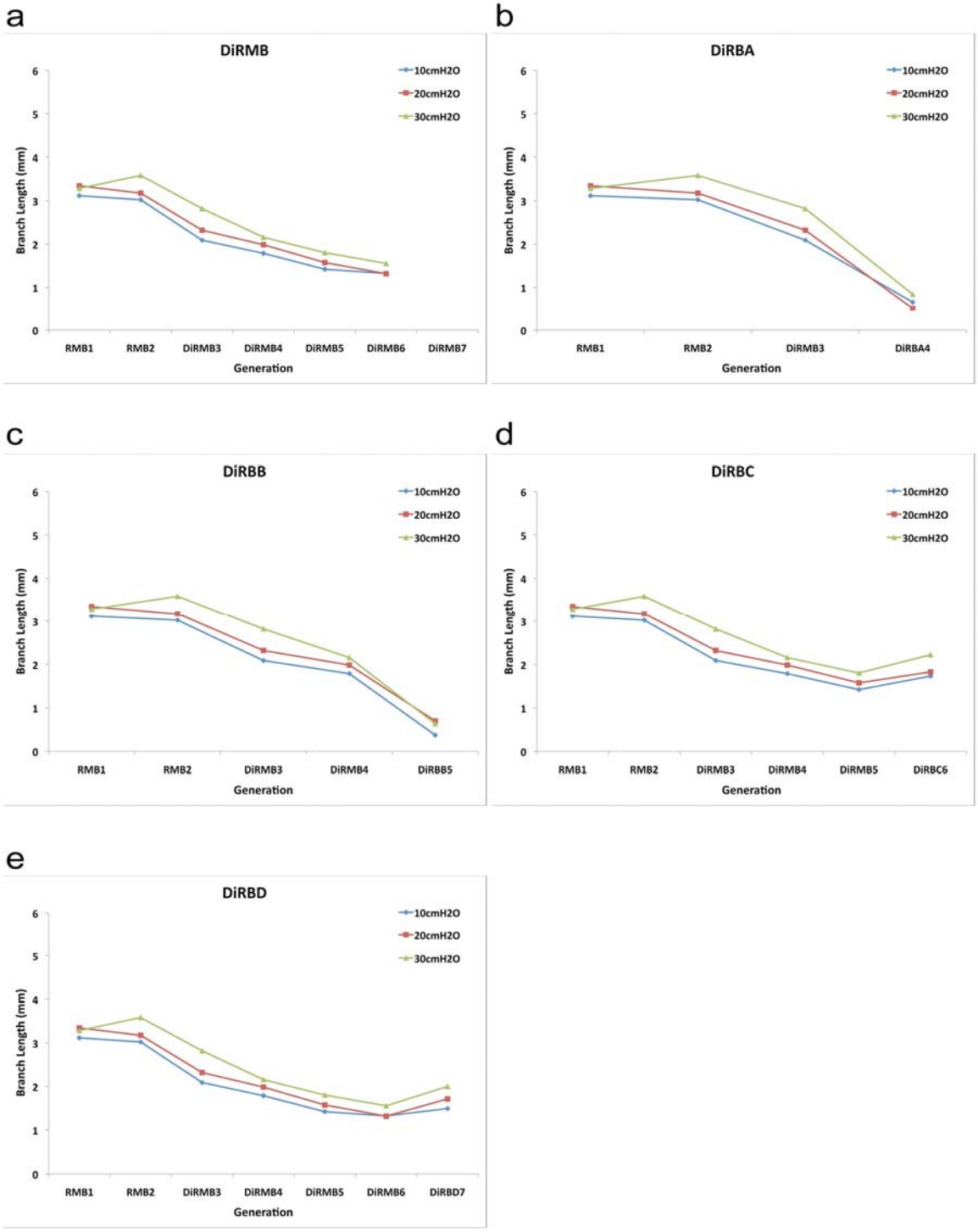

Figure A35: BALB/C Branch Length vs Generation for DiRMB, DiRBA, DiRBB, DiRBC, and DiRBD.

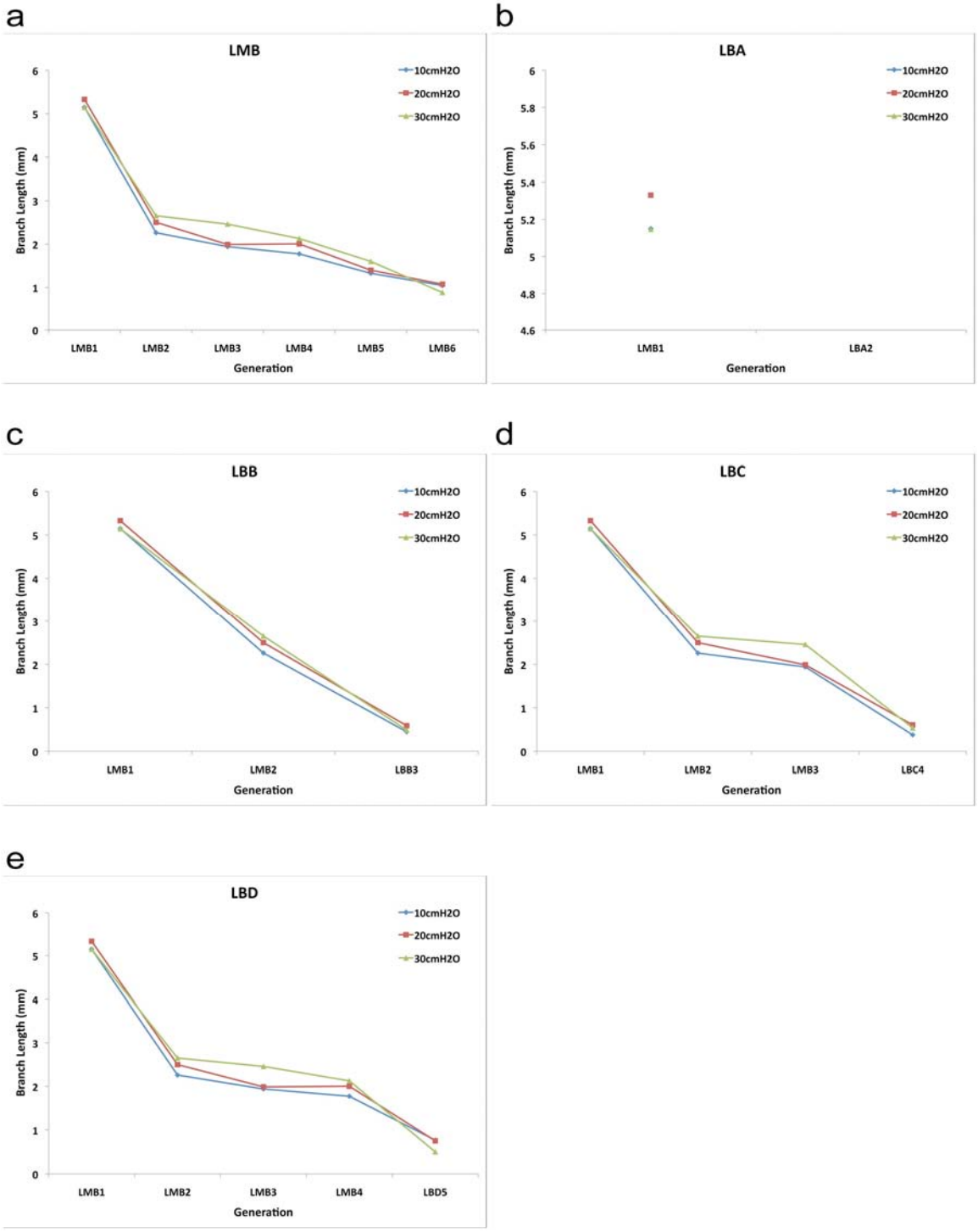

Figure A36: BALB/C Branch Length vs Generation for LMB, LBA, LBB, LBC and LBD.